



Provided by the author(s) and University of Galway in accordance with publisher policies. Please cite the published version when available.

Title	A computational and experimental investigation of the in-vivo biomechanics of the human aorta
Author(s)	Concannon, Jamie
Publication Date	2020-07-06
Publisher	NUI Galway
Item record	<a href="http://hdl.handle.net/10379/16050">http://hdl.handle.net/10379/16050</a>

Downloaded 2024-04-19T10:55:12Z

Some rights reserved. For more information, please see the item record link above.



# A COMPUTATIONAL AND EXPERIMENTAL INVESTIGATION OF THE IN-VIVO BIOMECHANICS OF THE HUMAN AORTA

Jamie Concannon, B.E. (2015)



**NUI Galway**  
**O'É Gaillimh**

A thesis submitted to the National University of Ireland as  
fulfilment of the requirements for the Degree of Doctor of  
Philosophy

January 2020

Discipline of Biomedical Engineering,  
School of Engineering,  
College of Science and Engineering,  
National University of Ireland Galway

Supervisor of Research:

Dr. J. Patrick McGarry

Co-Supervisor of Research:

Prof. Peter E. McHugh



*Go Mom, Dad, Aaron agus Gemma, do bhur grá agus tacaíocht i gcónaí.*

## ABSTRACT

The overall objective of this thesis is to provide a new understanding of the degree of biomechanical heterogeneity that exists along the human aorta, against the backdrop of clinical literature reporting that patient outcomes depend on the distance of aortic repair from the heart.

Spatial variance in human aortic bioarchitecture responsible for the elasticity of the vessel is poorly understood. We present a quantification of the constituents responsible for aortic compliance, namely, elastin, collagen and smooth muscle cells, using histological and stereological techniques along the vessel length. Using donated cadaveric tissue, a series of samples were excised between the proximal ascending aorta and the distal abdominal aorta, for five cadavers, each of which underwent various staining procedures to enhance specific constituents of the wall. Using polarised light microscopy techniques, the orientation of collagen fibres was studied for each location and each tunical layer of the aorta. Significant transmural and longitudinal heterogeneity in collagen fibre orientations were uncovered throughout the vessel. It is shown that a von Mises mixture model is required accurately to fit the complex collagen fibre distributions that exist along the aorta. Additionally, collagen and smooth muscle cell density was observed to increase with increasing distance from the heart, whereas elastin density decreased. Evidence clearly demonstrates that the aorta is highly heterogeneous in terms of bioarchitecture along its length, providing a microstructural basis for varying biomechanical properties spatially.

Several limitations exist with the *ex-vivo* approach to aortic mechanical property characterization including; (i) sample dimensions are generally small, presenting difficulty in terms of tensile testing, (ii) medical legislation prevents extension of the operative field for the purposes of obtaining ‘healthy’ samples, essentially rendering all tissue excised surgically to be either diseased or dead, and (iii) samples are generally from isolated segments of the aorta which cannot be taken to represent the properties of the entire vessel. As an alternative, we adopt an *in-vivo* approach to investigate the spatial variance in biomechanics of the healthy human aorta. Accurate measurement of the kinematics and haemodynamics of the aorta however, presents a considerable challenge. We present a dual-VENC 4D Flow MRI protocol capable of capturing the unsteady non-uniform blood flow throughout the entire vessel and cardiac cycle, in addition to measurement of the dynamically changing geometry of the aortic wall. Cross sectional area change, volumetric flow rate, and compliance are observed to decrease with increasing distance from the heart, while pulse wave velocity is observed to increase. A non-linear aortic lumen pressure-area relationship is observed throughout the aorta, such that a high vessel compliance occurs at low pressures, and a low vessel compliance occurs at high pressures. Results show that the biomechanical behaviour of the aorta is highly dependent on the time-point of the cardiac cycle and on the spatial location relative to the heart.

We then turn our focus to characterizing the spatially varying non-linear compliance of the aorta *in-vivo* using a combined MRI/FEA framework and a novel physically motivated constitutive law. It is shown that in order to accurately capture the biomechanics of the aorta, the contractile elements of the vessel wall must be incorporated in the material model. The pre-stretch of elastin and the contraction of smooth muscle cells (SMCs) are applied, resulting in a reduction in the reference lumen area to a new equilibrium area. The novel constitutive law is also demonstrated to capture the key features of both elastin and SMC knockout experiments. A subject-specific FE model is generated directly from the MRI data presented in Chapter 5, and the volume fractions of the constituent components of the aortic material model (i.e. non-linear elastic collagen, pre-stretched elastin, and contractile SMCs) were computed so that the *in-silico* pressure-area curves accurately predict the corresponding MRI data at each location. This leads to the prediction that collagen and smooth muscle volume fractions increase distally, while elastin volume fraction decreases distally. This finding is supported by the histological analyses presented in Chapter 4. The current study validates the inaccuracy in the assumption that the aorta exhibits a spatially uniform compliance along its length and a temporally uniform stiffness throughout the cardiac cycle.

The effect of repair techniques on the biomechanics of the human aorta has not been rigorously investigated to date, resulting in significant levels of postoperative complications for patients worldwide. Furthermore, several studies show that cardiac death is dependent on the location of the aortic repair. We show using our combined MRI/FEA framework, that both endovascular aortic repair (EVAR) and open surgical repair (OSR) significantly alter the biomechanics of the human aorta. Following an EVAR, the aorta reaches a new equilibrium configuration due to the outward force of the implant being balanced by increased tension in the vessel wall. This additional strain being imparted on the aortic wall results in the material transition from the high compliance regime (HCR) into the low compliance regime (LCR). The stent-graft unloads from the crimped configuration during deployment and operates along the unloading plateau between diastole and systole. The direct effective stiffness of the implant is negligible compared to the high-stiffness of the artery wall in the LCR. As a result, the pressure-area relationship post-stenting between diastole and systole follows that of the local LCR slope of the aorta. The stented section follows the local LCR slope for the entire cardiac cycle, and as a result the effective change in diastole is more pronounced proximally versus distally where the bi-linearity of the pressure-area curve is more pronounced. Finally, we also show that OSR results in a profound change in both the HCR and LCR slope, where a near zero compliance is observed throughout the entire cardiac cycle. The link between aortic heterogeneity and compliance mismatch uncovered may significantly advance the current understanding of the efficacy of aortic devices and their impact on the cardiovascular system.

## ACKNOWLEDGEMENTS

First and foremost, I would like to sincerely thank my academic supervisor Dr. Patrick McGarry for his guidance, time, and discussions over the past few years, and for awaking an enthusiasm for mechanics that I never knew I had. I would also like to sincerely thank my academic co-supervisor Prof. Peter McHugh for his support, motivation and insights, from which I have learnt so much.

I would also like to thank my collaborators both nationally and internationally; Prof. Peter Dockery and Alex Black of anatomy, NUI Galway for their support and guidance in all matters cadaveric and anatomical, and Dr. Christof Karmonik of The Houston Methodist, TX, USA, for his incredible support and knowledge in the field of MRI.

To my clinical supervisors Prof. Sherif Sultan and Ms. Niamh Hynes, thank you for your invaluable insight and your relentless drive to ensure research is always patient-focused.

To all the McHugh and McGarry group members, past and present thank you all for the help and guidance over the years. To Brian and Sarah thank you both for the last 8 years of friendship and craic. To Donnacha, thank you for your time and patience and for all the knowledge you passed down to me. To Kevin (Caoimhín), thank you for all your help and for showing me the endless capabilities of MATLAB.

Thank you to Jane, for everything you do and always welcoming me with a smile even when you knew I was coming with hassle for you! and to William for all our great chats about Mayo and Galway football.

I would like to thank my funding sources; the Irish Research Council and the Western Vascular Institute along with the Irish Centre for High-End Computing (ICHEC) for the provision of essential computational facilities and technical support.

And finally, to my family; Mom, Dad, Aaron and Gemma, thank you for all your love and support throughout the years, none of this would be possible without you all.

## **DECLARATION OF ORIGINALITY**

I certify that the work presented in this thesis is my own.

*Jamie Concannon*



## TABLE OF CONTENTS

<b>Abstract</b>	<b>ii</b>
<b>Acknowledgements</b>	<b>iv</b>
<b>Declaration of Originality</b>	<b>v</b>
<b>Table of Contents</b>	<b>vii</b>
<b>1 Introduction</b>	<b>1</b>
1.1 Introduction to Thesis and Structure .....	1
1.1.1 Objectives .....	2
1.1.2 Thesis Structure .....	2
1.2 Bibliography .....	5
<b>2 Background to the Literature</b>	<b>6</b>
2.1 The Aorta .....	6
2.1.1 Aortic Morphology .....	8
2.1.2 Tissue Microarchitecture.....	8
2.1.3 Aortic Wall Layers.....	10
2.1.4 Aortic Disease.....	12
2.1.5 Aortic Repair.....	15
2.1.6 Postoperative Complications.....	16
2.2 Background and Literature.....	18
2.2.1 Histological analysis of Aortic Tissue .....	18
2.2.2 Experimental Testing of Aortic Tissue .....	20
2.2.3 4D Flow MRI in the Aorta.....	23
2.2.4 Computational Modelling of the Aorta.....	27
2.3 Bibliography .....	31
<b>3 Theory</b>	<b>43</b>
3.1 Continuum Mechanics .....	43
3.1.1 Deformation and motion .....	43
3.1.2 Strain and strain rate measures.....	44
3.1.3 Stress measures .....	45
3.1.4 Forms of Strain Energy Density Functions for Soft Tissue .....	46
3.2 Finite Element Method (FEM).....	50
3.2.1 Implicit Integration Scheme.....	52
3.2.2 User defined material subroutines.....	53
3.3 Optimization Methods .....	55
3.4 Magnetic Resonance Imaging .....	58

3.5 Bibliography .....	64
<b>4 Quantification of the Regional Bioarchitecture in the Human Aorta</b>	<b>67</b>
Abstract .....	67
4.1 Introduction .....	68
4.2 Methodology .....	69
4.2.1 Tissue Harvesting.....	69
4.2.2 Staining Procedures.....	71
4.2.3 Postprocessing.....	71
4.3 Results.....	74
4.3.1 Elastin .....	74
4.3.2 Collagen .....	75
4.3.3 Layer Thickness .....	76
4.3.4 Collagen Fiber Orientations .....	77
4.4 Discussion .....	82
4.5 Conclusion .....	85
4.6 Acknowledgements.....	85
4.7 Bibliography .....	86
<b>5 A dual-VENC 4D Flow MRI Framework to Uncover Spatiotemporal Compliance and Pulse Wave Velocity in the Human Aorta</b>	<b>94</b>
Abstract .....	94
5.1 Introduction.....	95
5.2 Methodology .....	97
5.2.1 Theoretical Background.....	97
5.2.2 Proposed dual-VENC protocol for complete characterisation of aortic flow .....	101
5.2.3 Imaging Parameters.....	101
5.2.4 Postprocessing.....	102
5.2.5 Compliance .....	105
5.3 Results.....	107
5.3.1 Dual-VENC protocol for complete characterisation of aortic flow .....	107
5.3.2 Spatial Deformation .....	108
5.3.3 Spatial Haemodynamics.....	110
5.3.4 Spatial and Temporal Compliance .....	112
5.4 Discussion .....	114
5.4.1 Spatial Deformation .....	114
5.4.2 Spatial Haemodynamics.....	115
5.4.3 Spatial and Temporal Compliance .....	116
5.4.4 Limitations .....	116

5.4.5 Implications.....	117
5.5 Conclusions.....	118
5.6 Acknowledgements.....	118
5.7 Bibliography .....	119
<b>6 Characterization of the <i>in-vivo</i> Biomechanics of the Human Aorta</b>	<b>127</b>
Abstract.....	127
6.1 Introduction.....	128
6.2 Methodology .....	130
6.2.1 Novel Constitutive Law .....	130
6.2.2 Experimental/clinical motivation for constitutive model.....	131
6.2.3 Model Parameter Sensitivity Study.....	136
6.2.4 Construction of Subject-Specific finite element model .....	139
6.2.5 Simulation of subject specific aorta biomechanical behaviour .....	140
6.3 Results.....	141
6.4 Discussion.....	145
6.5 Bibliography .....	150
<b>7 An Investigation of Repair Techniques on the Biomechanics of the Human Aorta</b>	<b>159</b>
Abstract.....	159
7.1 Introduction.....	160
7.2 Model Development.....	162
7.2.1 Mechanical behaviour of Aortic Stent-Grafts .....	162
7.2.2 Comparison of ESM and Stent-Graft on Artery Compliance .....	164
7.2.3 Effect of Implant Oversizing and Positioning on Compliance .....	167
7.2.4 Investigation of Open Surgical Repair on Vessel Compliance .....	173
7.3 Discussion.....	174
7.4 Bibliography .....	179
<b>8 Concluding Remarks</b>	<b>186</b>
8.1 Summary of Key Contributions .....	186
8.2 Future perspectives .....	189
8.3 Bibliography .....	191



# CHAPTER 1

## INTRODUCTION



### 1.1 Introduction to Thesis and Structure

The *aorta* was first baptised by Aristotle in the 4<sup>th</sup> century BC, a term which derives from the Greek form *ἀορτέω*, meaning ‘to lift’. The first known function of the aorta was simply to hang the heart (Antoniou *et al.*, 2011). It is now known that its function is far more complex, and it represents an integral part of the cardiovascular system. Not only does the aorta serve as a conduit for blood transfer from the heart to the entire systemic vasculature, it also acts as an elastic chamber resulting in a reduction in left ventricular afterload, and an improvement in coronary blood flow and left ventricular relaxation (Belz, 1995). Otto Frank used the analogy of an old-fashioned fire hose in 1899 to formulate the Windkessel theory and illustrate the buffering effect of the aorta (Kassab, 2006).

In recent years, high levels of cardiac failure have been reported in patients that have undergone aortic repair close to the heart (Martín *et al.*, 2008; Beach *et al.*, 2017; Conrad *et al.*, 2017), irrespective of the device used or the disease being treated. Patients who undergo repair of the distal aorta however, seldom suffer from such postoperative complications (Barakat *et al.*, 2015; Atti *et al.*, 2018). These findings warrant an investigation into the fundamental differences in the biomechanics of the aorta that could result in such drastic location dependent postoperative outcomes within the same vessel.

The spatial variance in biomechanics of the aorta today remains poorly understood. Testing of surgically excised tissue is limited due to both sample size and legal constraints surrounding multiple excision sites. Testing of cadaveric tissue provides an alternative in the form of histological analyses, however tensile testing of the same is subject to questions regarding the effects of fixative on the mechanical properties.

*In-vivo* characterization through advanced medical imaging platforms and finite element analysis (FEA) provides the best possible platform for patient-specific characterization and preoperative planning. To date no clinically derived FE model of the entire human aorta has been developed and its mechanical properties characterised using a physically motivated constitutive law. In order to develop next generation devices for the treatment of aortic disease that minimise cardiac complications, an understanding of the regional biomechanics of the aorta must first be established.

### **1.1.1 Objectives**

The overall objective of this thesis is to provide advance on the current understanding of aortic biomechanics, with particular focus on the importance of mechanical heterogeneity of the system. Novel complex diagnostic and computational methodologies are developed that ultimately combine to result in a framework for *in-vivo* material characterization and preoperative planning capabilities. The specific aims are as follows:

- Characterize the spatial variation in area fractions of the constituents of the aortic wall responsible for compliance in the human cadaveric aorta.
- Develop and implement a novel non-invasive MRI framework for characterizing the regional biomechanics of the human aorta *in-vivo*.
- Develop a framework for generating patient-specific FE models of the human aorta directly from the aforementioned MRI dataset.
- Develop and implement a novel physically based anisotropic hyperelastic constitutive law and calibrate the mechanical properties of the aorta using the *in-vivo* deformation of the system.
- Investigate the regional effects of stent deployment and Dacron repair on the mechanical properties of the patient-specific aorta.

### **1.1.2 Thesis Structure**

Four studies form the backbone of the thesis. A brief outline of each chapter is outlined below.

#### **1.1.2.1 Chapter 1**

The remaining sections of the current chapter provide an outline of each chapter in the thesis.

#### **1.1.2.2 Chapter 2**

Chapter 2 presents an overview of the relevant literature to the proceeding work. Section 2.1 describes the form and function of the aorta, providing detail on the microarchitecture and wall layers of the vessel in addition to disease states, treatment options and postoperative complications. Section 2.2 provides detail on the literature to date on the regional biomechanics of the aorta, including histological studies, experimental testing, *in-vivo* imaging studies using 4D Flow MRI and existing computational models of the human aorta, providing insights and motivation for the work to follow in this thesis. In addition to the broad review of the literature provided

in Chapter 2, a more detailed analysis of the literature is also provided within each technical chapter (Chapters 4-7).

### **1.1.2.3 Chapter 3**

Chapter 3 outlines the relevant theory that encompasses this thesis. An introduction to continuum mechanics is provided in Section 3.1, the principles of which are used to solve the simulations performed in this thesis. Section 3.2 describes the finite element method (FEM) in general, in addition to common integration schemes which are used in solving the boundary value problems outlined in Chapters 6 and 7. In Section 3.3, the theory surrounding optimization methods is discussed to motivate the work performed in Chapter 6. Finally, Section 3.4 details both the classical and quantum magnetic resonance theory required in order to provide a foundation for the work undertaken in Chapter 5.

### **1.1.2.4 Chapter 4**

The spatial variance in bioarchitectural components of the wall responsible for compliance are quantified in 5 adult human cadavers with no previous history of aortic disease, in order to investigate whether or not microstructural heterogeneity exists along the human aorta. Elastin is the dominant protein in the wall proximally, whereas collagen dominates distally. With increasing distance from the heart elastin content decreases while both collagen and smooth muscle cell (SMC) content increases. Additionally, significant heterogeneity in collagen fiber orientation density is evident along the length of the aorta, with two families of perfectly symmetric fibers absent as commonly assumed in the majority of FE models to date.

### **1.1.2.5 Chapter 5**

A novel dual-VENC 4D Flow MRI framework is developed and implemented in a commercial scanner, whereby the regional kinematics and haemodynamics of the entire aorta is characterised throughout the entire cardiac cycle. The aorta is most compliant proximally and stiffness increases with increasing distance from the heart. The pulse wave velocity forms an inverse relationship with compliance and increases distally. Furthermore, by plotting instantaneous pressure versus area, a non-linear compliance is uncovered *in-vivo*, whereby the aorta is highly compliant at low pressures and stiffens at high pressures. The framework developed provides both a novel methodology for characterising aortic biomechanics and new insights into the *in-vivo* behaviour of the healthy human aorta.

### **1.1.2.6 Chapter 6**

A novel physically based constitutive law is developed that is capable of capturing the true biomechanics of the aorta *in-vivo*. It is shown that in order to accurately capture the mechanical behaviour of the aorta, the contractile elements of the vessel wall must be incorporated in the material model. The pre-stretch of elastin and the contraction of SMCs are applied, resulting in a reduction in the reference lumen area to a new equilibrium area. The novel constitutive law is also demonstrated to capture the key features of both elastin and SMC knockout experiments. A subject-specific FE model is generated directly from the MRI dataset presented in Chapter 5 and the novel

constitutive law is used to calibrate the regional material properties along the length of the aorta over a full cardiac cycle. Finally, in order to simulate the spatially varying heterogeneous pressure-area relationships uncovered in Chapter 5, our modelling framework predicts that the volume fraction of collagen and SMCs increases while the volume fraction of elastin decreases with distance from the heart. These computed spatial variations in collagen, elastin and SMC are strongly supported by histological analyses from Chapter 4.

### **1.1.2.7 Chapter 7**

It is shown in the subject-specific finite element model developed in Chapter 6, that both endovascular aortic repair (EVAR) and open surgical repair (OSR) significantly alter the biomechanics of the aorta. Following an EVAR, the aorta reaches a new equilibrium configuration due to the outward force of the implant being balanced by increased tension in the vessel wall. This additional strain being imparted on the aortic wall results in the material transition from the high compliance regime (HCR) into the low compliance regime (LCR). The stent-graft unloads from the crimped configuration during deployment and operates along the unloading plateau between diastole and systole. The direct effective stiffness of the implant is negligible compared to the high-stiffness of the artery wall in the LCR. As a result, the pressure-area relationship post-stenting between diastole and systole follows that of the local LCR slope of the aorta. The stented section follows the local LCR slope for the entire cardiac cycle, and as a result the effective change in diastole is more pronounced proximally versus distally where the bi-linearity of the pressure-area curve is more pronounced. Finally, we also show that OSR results in a profound change in both the HCR and LCR slope, where a near zero compliance is observed throughout the entire cardiac cycle.

### **1.1.2.8 Chapter 8**

A discussion of key thesis contributions and future perspectives is provided.

## 1.2 Bibliography

- Antoniou, G. A., Antoniou, A. I., Antoniou, S. A. and Lazarides, M. K. (2011) 'A historical perspective of medical terminology of aortic aneurysm', *Journal of Vascular Surgery. Mosby Inc.*, 54(5), pp. 1527–1528. doi: 10.1016/j.jvs.2011.04.036.
- Atti, V., Nalluri, N., Kumar, V., Tabet, R., Yandrapalli, S., Edla, S., Tripathi, A., Patel, N. J., Dave, M., Aronow, W. S., Basir, M. B., Davis, T. P., Drachman, D. E. and Bhatt, D. L. (2018) 'Frequency of 30-Day Readmission and Its Causes After Endovascular Aneurysm Intervention of Abdominal Aortic Aneurysm (from the Nationwide Readmission Database)', *The American Journal of Cardiology. Excerpta Medica*. doi: 10.1016/J.AMJCARD.2018.12.006.
- Barakat, H. M., Shahin, Y., McCollum, P. T. and Chetter, I. C. (2015) 'Prediction of organ-specific complications following abdominal aortic aneurysm repair using cardiopulmonary exercise testing', *Anaesthesia*, 70(6), pp. 679–685. doi: 10.1111/anae.12986.
- Beach, J. M., Kuramochi, Y., Brier, C., Roselli, E. E. and Eagleton, M. J. (2017) 'Durable outcomes of thoracic endovascular aortic repair with Zenith TX1 and TX2 devices.', *Journal of vascular surgery. Elsevier*, 65(5), pp. 1287–1296. doi: 10.1016/j.jvs.2016.11.029.
- Belz, G. G. (1995) 'Elastic Properties and of the Human Aorta Windkessel Function', *Cardiovascular Drugs and Therapy*, 9, pp. 73–83. Available at: <https://link.springer.com/content/pdf/10.1007%2F00877747.pdf> (Accessed: 19 September 2018).
- Conrad, M. F., Tucheck, J., Freezor, R., Bavaria, J., White, R. and Fairman, R. (2017) 'Results of the VALOR II trial of the Medtronic Valiant Thoracic Stent Graft', *Journal of Vascular Surgery. Mosby*, 66(2), pp. 335–342. doi: 10.1016/J.JVS.2016.12.136.
- Kassab, G. S. (2006) 'Biomechanics of the cardiovascular system: the aorta as an illustratory example.', *Journal of the Royal Society, Interface / the Royal Society. The Royal Society*, 3(11), pp. 719–40. doi: 10.1098/rsif.2006.0138.
- Martín, C. E., Forteza, A., Pérez, E., López, M. J., Centeno, J., Blázquez, J. A., de Diego, J., García, D. and Cortina, J. M. (2008) 'Predictors of Mortality and Reoperation in Acute Type-A Aortic Dissection Surgery: 18 Years of Experience', *Revista Española de Cardiología (English Edition). Elsevier*, 61(10), pp. 1050–1060. doi: 10.1016/S1885-5857(09)60008-6.

# CHAPTER 2

## BACKGROUND TO THE LITERATURE

---



### 2.1 The Aorta

The aorta is the largest artery in the body and plays the role of connecting the left ventricle of the heart to the entire systemic vasculature. Arteries can generally be subdivided into two categories; '*elastic*' and '*muscular*', based on their morphology, location and composition (Rhodin, 1980). Elastic arteries include the aorta, carotid and pulmonary arteries, and are closer to the heart. Muscular arteries include femoral, plantar and coronary arteries, and are closer to the capillaries (Humphrey, 1995). Significant variance in terms of their underlying tissue structure is evident in Table 2.1, where elastic arteries exhibit a higher content of elastin and muscular arteries a higher density of smooth muscle. This architectural heterogeneity is associated with the distinct roles of both types of artery. Elastic arteries dilate and recoil, whereas muscular arteries undergo vasoconstriction to control pressure and blood flow. In this section, a detailed introduction to the aorta is described, including details of its morphology, its wall layers, common diseases that affect the vessel and common complications that follow the repair such diseases.

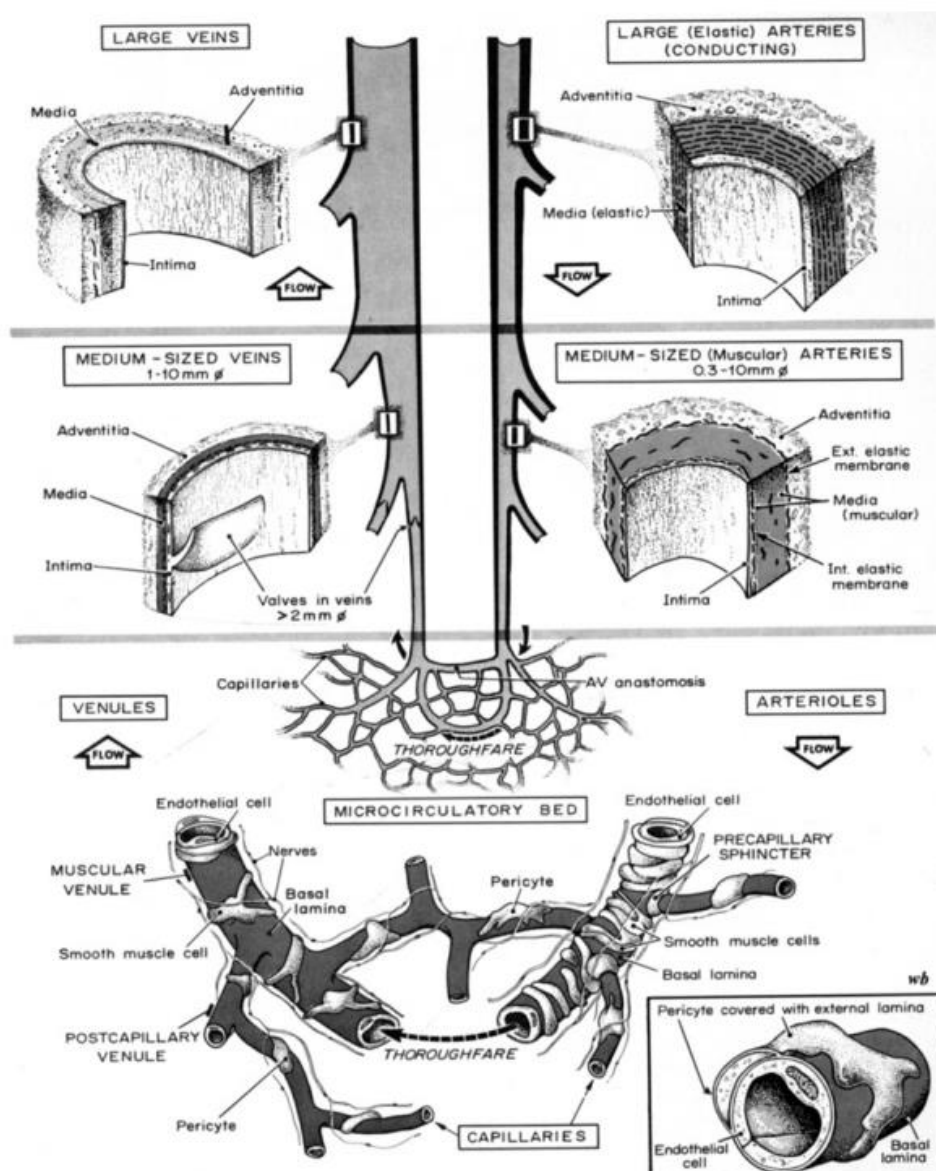


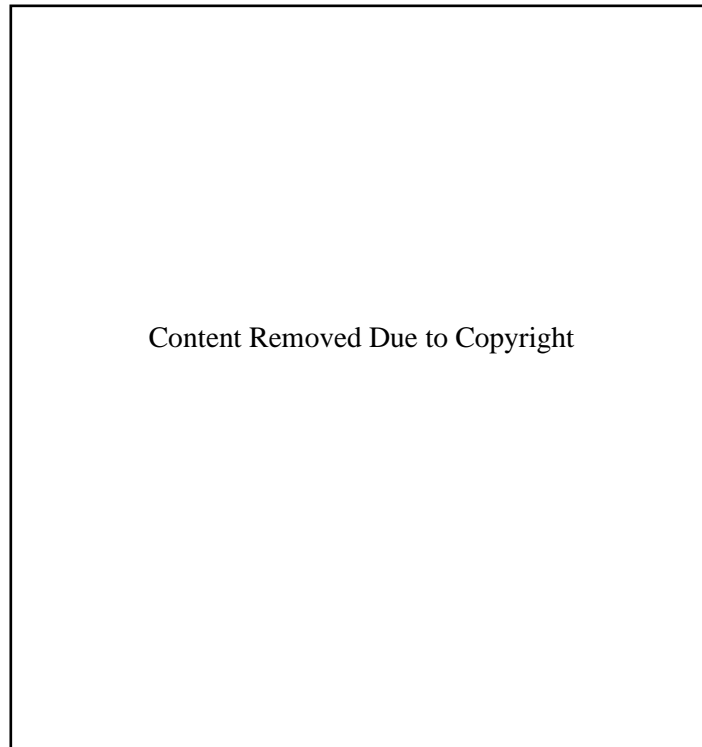
Figure 2.1: Schematic of major structural characteristics of principal segments of blood vessels in mammals (Rhodin, 1980). Permission granted by John Wiley and Sons.

Table 2.1: Breakdown of medial layer of thoracic aorta and plantar artery (Fung, 1993).

	Thoracic Aorta	Plantar Artery
Smooth muscle (%)	33.5 $\pm$ 10.4	60.5 $\pm$ 6.5
Ground substance (%)	5.6 $\pm$ 6.7	26.4 $\pm$ 6.4
Elastin (%)	24.3 $\pm$ 7.7	1.3 $\pm$ 1.1
Collagen (%)	27.4 $\pm$ 13.2	11.9 $\pm$ 8.4

### 2.1.1 Aortic Morphology

The candy cane shape of the aorta (Figure 2.2) facilitates both cranial and caudal perfusion of oxygenated blood following ventricular ejection. Its compliant nature allows for a portion of the kinetic energy associated with systole to be stored within the walls during extension. This is then released during diastole, forming a pressure wave transmission and converting the pulsatile flow profile of the left ventricular outflow tract (LVOT) to a steady flow downstream. The microarchitectural components of the wall that govern this compliance are outlined below.



**Figure 2.2: Morphology of human aorta. Real Anatomy, M. Nielsen, S. Miller, Wiley (2008).**

### 2.1.2 Tissue Microarchitecture

#### 2.1.2.1 *Connective Tissue*

The primary function of connective tissue is to provide structural and mechanical support for other types of tissue (Young, O'Dowd and Woodford, 2013). It also mediates the exchange of nutrients and waste products between tissues (Ovalle, Nahirney and Netter, 2013), however this is outside the scope of the current work as we focus here only on the kinematics of the wall. In the context of the aortic wall, there are two main connective tissue components which contribute to the mechanical behaviour of the tissue; (i) extracellular matrix (ECM) components, and (ii) cellular components (Gasser, 2017). The ECM includes protein fibers such as elastin and collagen and a surrounding amorphous component known as the ground matrix which consists of proteoglycans, glycoproteins and glycosaminoglycans (Ross and Pawlina, 2015). The cellular components consist of endothelial cells, smooth muscle cells, macrophages and fibroblasts among others, each of which play highly specialised roles

within the vessel wall. The wall can be regarded as having passive (elastin and collagen) and active (smooth muscle cell) systems which contribute to its mechanical properties. The passive components provide elasticity and tensile strength respectively, while the active component is concerned with the production of ECM components and vessel tone (Ross, 1971).

Elastin, collagen and smooth muscle cells can constitute between 50% and 90% of the material of the wall, the rest is largely water, which governs the compressibility of the tissue (Y. Fung, 1993; Pedley, 2003). A number of studies have held ECM components responsible for changes in arterial stiffness (Brozovich *et al.*, 2016), however SMCs are also accountable, in that they have been shown to play a major role in the overall arterial stiffness (Xu and Shi, 2014). We provide a focused summary below of the primary structural components of the ECM; collagen and elastin, as well as the primary cellular component that contributes to arterial stiffness; SMCs, in order to understand their roles in the kinematics of the system.

### **2.1.2.2 Collagen**

Collagen is the most abundant protein in the human body and the main fiber found in most supporting tissues (Ovalle, Nahirney and Netter, 2013; Young, O'Dowd and Woodford, 2013). Its primary function is to provide tensile strength to connective tissues and resist pulling, stretching or tearing. In blood vessels and specifically in the aorta its function is to limit distension (Xu and Shi, 2014). Collagen consists of three polypeptide (or  $\alpha$ ) chains bound together to form helical structures that are 300 nm long and 1.5 nm in diameter which make up collagen fibrils. Collagen fibrils then bundle together to form collagen. There are over 28 different types of collagen, however collagen types I, II and III are arranged as rope-like fibrils and are the main forms of fibrillar collagen found in the arterial wall (Trelstad, 1974; Ross and Pawlina, 2015). Fibers typically form a helical bundle around the elastin-SMC unit (Rhodin, 1980; Shadwick, 1999; Agrawal *et al.*, 2013a) and appear wavy under light microscopy. The unfolding of their naturally crimped configuration during extension describes the material non-linearity observed during *ex-vivo* tensile testing (Clark and Glagov, 1985).

### **2.1.2.3 Elastin**

Elastin, like collagen, is also a protein but is responsible for the elasticity of vessels, i.e., the passive return to their reference configuration following distension. The random distribution of glycines make elastin hydrophobic and allows for random coiling of its fibers. This permits elastic fibers to slide over one another in both loading and unloading (Xu and Shi, 2014). Microscopy studies also indicate that elastin is made up of repeating self-similar structures at many length scales (Gasser, 2017). In arteries, elastin is arranged into fibers (100-500nm) and sheets (1-2.2 $\mu$ m) interspersed about the ECM, together comprising up to 50% of the ECM dry weight (Xu and Shi, 2014). Elastin is a critical component of blood vessels (and of the cardiovascular system as a whole) in the regulation of blood pressure and flow, particularly in the aorta. During systole (ventricular ejection), the aorta dilates to accommodate the

ejected blood column and elastin harnesses this kinetic energy as it distends. In diastole, the recoil of elastin is responsible for the continuation of blood flow and diastolic blood pressure, a process which is crucial for coronary perfusion (Wu *et al.*, 2015).

#### **2.1.2.4 Smooth Muscle Cells**

Vascular smooth muscle cells (SMCs) are the main constitutive stromal cells of the vascular wall (Lacolley *et al.*, 2012). These cells, generally found in situations requiring sustained slow or rhythmic contractions (Lowe and Anderson, 2015), are involuntarily regulated by the autonomic nervous system and serve to regulate both ECM component synthesis and vessel tone. Here we are focused on the latter, i.e., their active role. SMCs, through contraction and relaxation of the elastin-contractile units (Milewicz *et al.*, 2017), regulate blood flow and localized pressure in arteries, a mechanism responsible for the redistribution of blood to target areas within the body (Ovalle and Netter, 2013). SMCs are typically spindle shaped and depending on the site, vary in size from 20  $\mu\text{m}$  to 500  $\mu\text{m}$  (Lowe and Anderson, 2015). Thin filaments (actin), thick filaments (myosin), and intermediate filaments (desmin and vimentin) together with a single nucleus make up the structure of SMCs, where contraction of thin and thick filaments cause the uniform contraction of the entire cell (Chamley-Campbell and Ross, 1979). SMCs may enter a latch state and remain contracted for long periods of time without fatiguing. Furthermore, contraction may occur along the entire muscle producing extrusive movements, or they may contract in a wave like manner producing peristaltic movements (Ross and Pawlina, 2015).

#### **2.1.3 Aortic Wall Layers**

The walls of arteries are composed of three distinct layers known as tunics. Together, from the lumen outward, they make the Tunica Intima, Tunica Media, and Tunica Adventitia. Each layer consists of different types of cells and matrix proteins (Figure 2.3) and serves a specific mechanical or mechanobiological function.

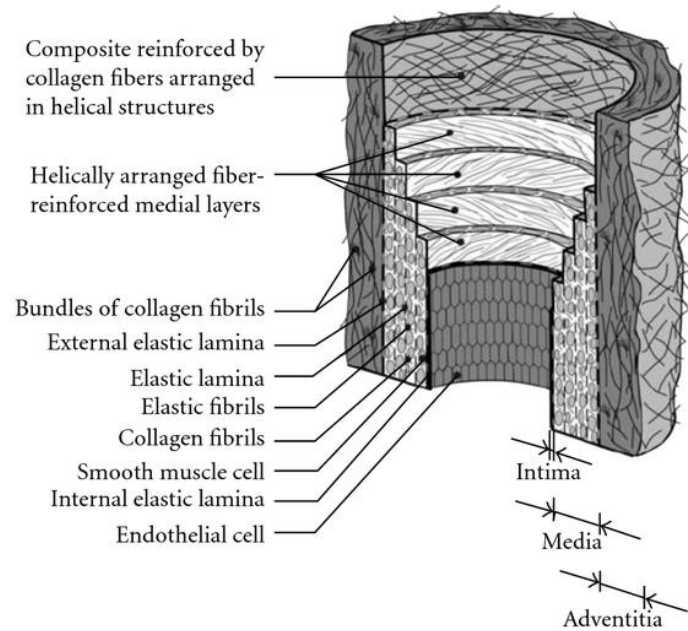


**Figure 2.3: Layers of the Aortic wall (Gasser, Ogden and Holzapfel, 2006). Permission granted by the Journal of Royal Society Interface.**

### **2.1.3.1 Tunica Intima**

The tunica intima is generally referred to as the innermost layer of arteries and can be further split into three sub-segments; (i) the endothelium; (ii) the basal lamina; and (iii) the subendothelial layer (Y.-C. Fung, 1993). The endothelium, or luminal surface, is a monolayer of flattened epithelial cells that are aligned parallel to the direction of flow (Ovalle and Netter, 2013). Each epithelial cell is  $15\ \mu\text{m}$  wide and  $25\text{--}30\ \mu\text{m}$  long providing a smooth wall which is selectively permeability to water, electrolytes, sugars and other substances passing between the blood and the tissues (Chandran and Yoganathan, 2012). These epithelial cells are anchored on the basal lamina; a thin sheet-like membrane of connective tissue including collagen, proteoglycans and glycoproteins (Ross and Pawlina, 2015). The subendothelial layer is usually only present in large elastic arteries such as the aorta, and is comprised of network of interlaced collagen, elastin and SMCs (Lowe and Anderson, 2015). Combined, the adult aorta has an intima that is  $100\text{--}150\ \mu\text{m}$  thick which acts mainly in a sensory manner, and offers a negligible contribution to the mechanical properties of the wall (Chandran and Yoganathan, 2012).

### **2.1.3.2 Tunica Media**

The tunica media is generally the most pronounced layer of the arterial wall ranging from  $0.5\text{--}2\ \text{mm}$  in thickness (Ovalle and Netter, 2013), and that which gives elasticity to the vessel (Pedley, 2003). The inner boundary of tunica media is bounded by the Internal Elastic Lamina (IEL), or a membrane that is not always distinguishable as an individual entity but represents the first layer of the many concentric elastic laminae ( $2\text{--}3\ \mu\text{m}$  wide) in the media of the vessel (Ross and Barnash, 2009). Beginning at the

IEL, concentric layers of elastic sheets radiate outwards which are separated by interlaminar SMCs, collagen, and ground substance (Pedley, 2003; Lowe and Anderson, 2015). In this case SMCs are responsible for both the production of extracellular constituents and the regulation of vessel tone. The medial layer is for the most part, an avascular tissue (Lacolley *et al.*, 2012) and it is the fenestrations in the elastic laminae that allows for the diffusion of nutrients through the wall (Ross and Pawlina, 2015). The external boundary of the tunica media is the outermost elastic layer also known as the External Elastic Lamina (EEL) (Y.-C. Fung, 1993; Ross and Pawlina, 2015).

### **2.1.3.3 Tunica Adventitia**

The outermost portion of the arterial wall, the tunica adventitia is composed of collagenous fibres and ground substance that form a network of loose and disorganised connective tissue. In this regard, it is hypothesized that this layer is not as important mechanically, as the tunica media (Pedley, 2003). Additionally, from a cellular standpoint, fibroblasts and macrophages are dispersed throughout (Ross and Pawlina, 2015). As the lumen supplies the intima and inner media through diffusion of nutrients and other substances, in thick walled vessels small blood vessels can be found in the adventitia known as the vasa vasorum. These vessels supply the outer portions of the arterial wall where radial diffusion is no longer possible due to excessive wall thickness (Ross, Pawlina and Barnash, 2009). An exception to this is the abdominal aorta. Lastly, the tunica adventitia also contain nervi vasorum, or a system of autonomic nerves that control contraction of smooth muscle and hence, tone through constriction and dilation of the vessel. In elastic arteries the adventitia is usually less than half the thickness of the media (Ross and Pawlina, 2015).

### **2.1.4 Aortic Disease**

Aortic disease is among the leading causes of morbidity, mortality, and medical expenses in the United States (Caglayan *et al.*, 2009). A summary of the two primary aortic diseases; aneurysm and dissection, is provided below.

#### **2.1.4.1 Aortic Aneurysm**

An aortic aneurysm (Figure 2.4) is defined as a localized dilation or bulge of the aorta resulting in decreased wall strength and subsequently increased rupture risk (Martufi 2016). Conventionally, an aneurysm is considered a dilation of 50% larger than the original vessel diameter (approximately 30 mm for the aorta), however, aortic aneurysms are known to rupture at various sizes which poses a significant challenge to vascular internationalists worldwide regarding the optimum intervention time (McGloughlin and Doyle, 2010). Currently the threshold for intervention stands at a diameter of 6.5 cm for the descending thoracic aorta and 5.5 cm for the abdominal aorta (Balakhovskiy & Volokh, 2014; Forsell & Gasser, 2013; Martufi & Di Martino, 2014).

This maximum diameter criterion, however, fails to quantify aneurysm rupture risk on a patient-specific basis. Several studies have reported aneurysm rupture below this threshold with one study reporting 24% of aneurysms rupturing below 5.0 cm

(Fillinger & Kennedy, 2002). These indications have been developed according to the point at which aneurysm rupture risk outweighs the risk of the intervention, be it open surgical repair (OSR), endovascular aortic repair (EVAR) or a hybrid approach. It has been well documented, however, that small aortic aneurysms can rupture and large aneurysms can remain stable. Fillinger *et al.*, (2002) and Humphrey and Holzapfel, (2012) report a 24% rupture rate below 5.0 cm and a 57% non-rupture rate over 7.0 cm respectively.

Important factors other than the maximum diameter criterion influence the surgeon's decision to intervene, such as aortic tortuosity, patient age, preoperative renal function, ability to withstand proximal aortic clamping, and involvement of visceral branches (Debakey & Morris, 1956; Orr & Bobadilla, 2014). In patients with aortic aneurysms greater than 5.5 cm, more than 50% of these aneurysms will rupture when surgery is deferred because of such operative risks (Fillinger *et al.*, 2002). With an associated mortality rate following rupture of over 90%, this disease has so been termed the 'Silent Killer' (Elefteriades 2015).

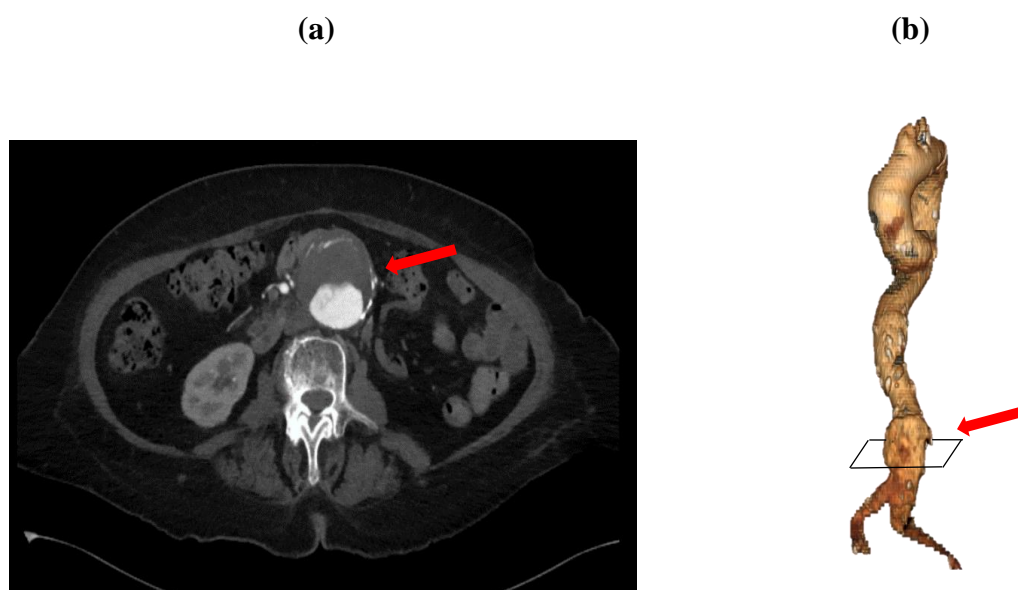


**Figure 2.4: 5.5cm Abdominal Aortic Aneurysm (a) axial CTA (b) 3D Reconstruction using 3Mensio Software (3 Mensio Medical Imaging BV, Netherlands).**

#### ***2.1.4.2 Aortic Dissection***

An aortic dissection occurs when a tear develops in the aortic wall, allowing the entry of blood into a secondary channel within the wall known as the false lumen (Figure 2.5). The intramural haemorrhage leads to propagation or further tearing of the aortic wall, generally away from the heart, in addition to significant aortic dilatation (Fernandez-Moure, 2011). A common complication exists whereby the true lumen becomes compressed by the false lumen, leading to ischaemic complications distally (malperfusion of renal, coeliac, mesenteric and iliac vessels). The International

Registry for Aortic Dissection (IRAD) have identified several risk factors for the development of acute aortic dissection which include; male sex, hypertension and previous medical history of Marfan Syndrome (Evangelista *et al.*, 2016; Beaufort *et al.*, 2017).

Two main classifications exist to describe aortic dissection; the DeBakey Classification and the Stanford Classification. In the DeBakey Classification dissections originating in the ascending aorta consist of those which propagate to the arch (Type I) and those that are confined to the ascending aorta (Type II). Dissections that originate in the descending aorta, regardless of an antegrade or retrograde dissection path are known as Type III tears. The Stanford Classification denotes dissections that involve the ascending aorta as Type A, and the descending aorta as Type B, regardless of the point of origin. The immediate goal in the treatment of patients with an aortic dissection is to reduce blood pressure and lower the likelihood of further propagation and rupture. Emergency or elective interventions can be performed to alleviate complications using an OSR, EVAR, or hybrid approach, however, each with variable results. A 1-2% per hour mortality rate has been associated with acute unoperated Type A aortic dissection (Goldfinger *et al.*, 2014).

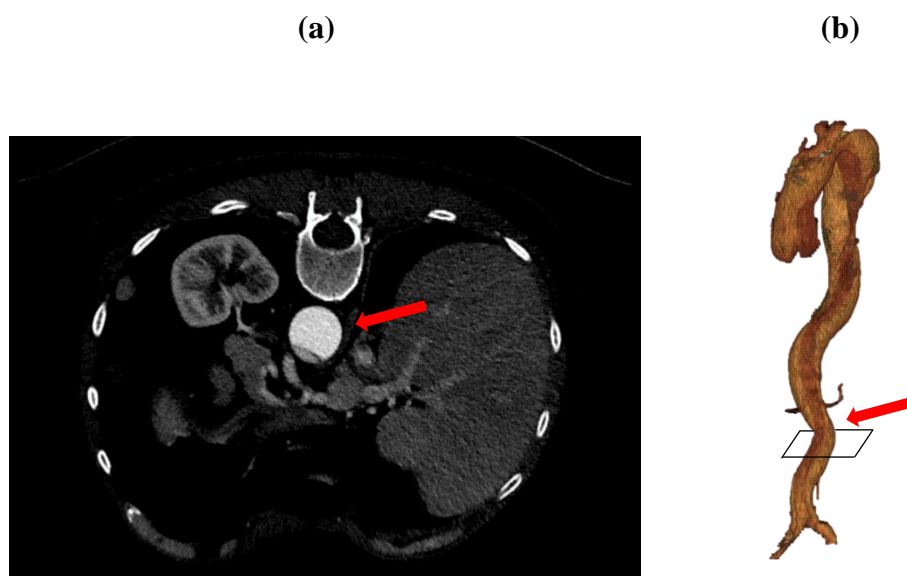


**Figure 2.5: Type B Aortic Dissection with distal propagation (a) true and false lumen on axial CTA and (b) 3D reconstruction using 3Mensio software (3 Mensio Medical Imaging BV, Netherlands).**

### **2.1.5 Aortic Repair**

There are two main treatment options for patients who present with aortic disease which warrants intervention; open surgical repair (OSR) and endovascular aortic repair (EVAR). A brief outline of each treatment method is given below, and a schematic is provided in Figure 2.6.

#### ***2.1.5.1 Open Surgical Repair***

Open surgical repair (OSR) of the aorta is considered one of the most technically challenging and complex procedures performed by vascular surgeons (Rigberg *et al.*, 2006). OSR of the thoracoabdominal aorta involves opening both the chest and abdomen through a long incision beginning at midpoint between the spinal processes and the scapula, down to the umbilicus, and then to the pubis, if the infrarenal aorta requires repair. The upper abdominal aortic segment is exposed via a transperitoneal approach, which allows for direct visualization of the abdominal organs and a comprehensive evaluation of the efficacy of revascularization after completing the aortic repair (Gloviczki, 2002; Chiesa *et al.*, 2012).

The proximal end of the aortic graft is sutured to the descending thoracic aorta using a 2/0 monofilament polypropylene in a running fashion. The clamp is then removed and reapplied onto the distal thoracic aorta above the coeliac axis and the aneurysm is opened. Finally, an end-to-end anastomosis with the distal aorta is performed and the last clamp is then removed (Chiesa *et al.*, 2012). Due to the clamping and excision of the diseased section of the aorta, distal reperfusion is required to offer protection from visceral, lower extremity and spinal cord ischaemia. Conventional OSR of the thoracoabdominal aorta has been the gold standard since its introduction in 1955 (Kheirleisid *et al.*, 2014). Various centres have published mortality rates as high as 48.4% and postoperative spinal cord ischaemia rates up to 8.0% (Rigberg *et al.*, 2006; Greenberg *et al.*, 2008). Modern advances in surgical techniques for OSR including distal reperfusion and hypothermic circulatory arrest have helped reduce complications; however, issues relating to respiratory compromise, brain, spinal cord, cardiac and visceral ischaemia continue to pose significant concern (Riambau *et al.*, 2017).

#### ***2.1.5.2 Endovascular Repair***

The introduction of endovascular aortic repair (EVAR) was fuelled by the need for a less invasive approach to treating aortic disease, which arrived in the early 1990s. The procedure remotely tracks a delivery system to the disease site and deploys a stent-graft to relieve the diseased aortic wall and reduce the risk of rupture. Routine preoperative Computed Tomography Angiography (CTA) with contrast should be performed ensuring to include the aortic arch, chest, abdomen, and pelvis, to fully evaluate the size of the vessels in question along with the degree of aortic angulation, length of landing zones and viability of access vessels. Subsequent measurements of aortic diameter, access vessel diameter, and length of proximal/distal landing zones are essential to determine the feasibility of the procedure and to ensure the selection of appropriately sized aortic endografts (Singh and Makaroun, 2014).

Following definition of the entry side based on preoperative imaging, the ipsilateral Common Femoral Artery (CFA) is generally exposed by standard surgical cut down (Henry et al., 2015) and the stent-graft is introduced through a delivery sheath under fluoroscopic guidance. Strategies for accurate placement are device specific, but the majority of patients benefit from a temporary reduction in mean arterial pressure and short-term cessation of ventilation. Once the delivery system is in position, the outer sheath is retracted, and the self-expanding stent-graft is deployed into the aortic wall. Finally, completion imaging often in the form of Digital Subtraction Angiography (DSA), is used to confirm both accurate endograft placement as well as the absence of endoleaks (Singh and Makaroun, 2014).

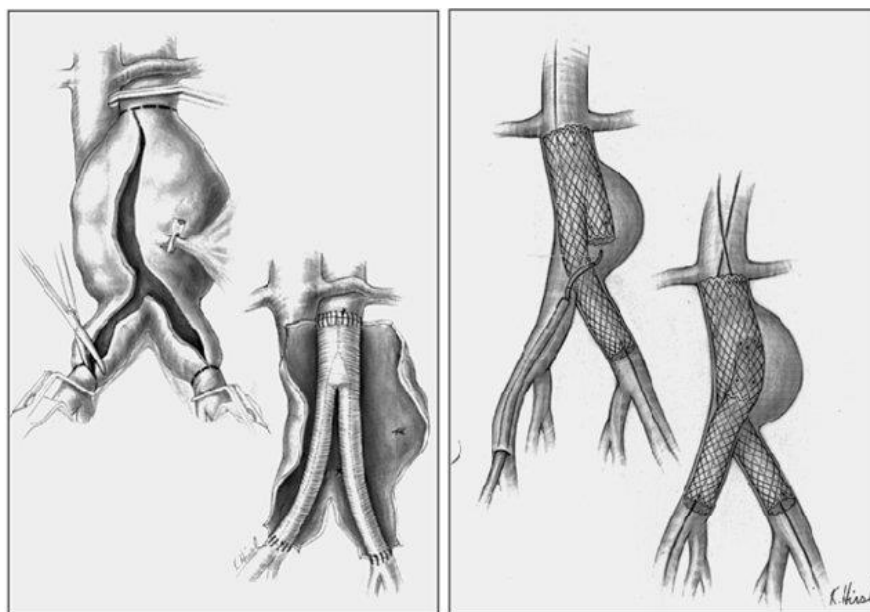


**Figure 2.6: Open surgical (left) versus endovascular (right) repair techniques for abdominal aortic aneurysms (Figuroa and Zarins, 2011). Permission granted by Springer.**

### 2.1.6 Postoperative Complications

Several postoperative complications remain following both OSR and EVAR. Stroke, paraplegia and myocardial infarction remain a concern following OSR, in addition to 30-day mortality rates of up to 48% (Verhoeven *et al.*, 2008). Intensive care unit (ICU) stay, and general recovery is extensive due to the invasive nature of the surgery. The introduction of endovascular aortic repair (EVAR) for the aorta in the early 1990s has had a positive impact on postoperative outcomes such as 30-day mortality (Roselli *et al.*, 2007), however, rates of spinal cord ischaemia, renal failure, and endoleak are still being reported as high as 23.5%, 45.1%, and 44% respectively in certain centres (Rigberg *et al.*, 2006; Clough *et al.*, 2012; Nayeemuddin and Asquith, 2012). Furthermore, up to 36% of patients require a reintervention after endovascular repair, with limb thrombosis (40%) and aneurysm enlargement (40%) necessitating immediate attention (Maleux, & Heye, 2009).

It has not been established whether EVAR or OSR is the superior treatment option for patients with aortic aneurysm or dissection. The endovascular versus open repair of abdominal aortic aneurysms (EVAR 1) trial concluded that EVAR has an early survival benefit but an inferior late survival compared to open repair (Patel *et al.*, 2016), resulting in a lack of consensus regarding the optimal treatment modality throughout the vascular and endovascular surgical community. Furthermore, a meta-analysis of 42 non-randomised studies evaluating EVAR versus OSR for descending thoracic aortic disease reported no significant difference between intervention groups in relation to stroke, reintervention, and mortality beyond 12 months (Cheng *et al.*, 2010).

Several recent studies have shown higher levels of cardiac death post thoracic compared to abdominal aortic stenting, independent of disease type (Martín *et al.*, 2008; Barakat *et al.*, 2015; Bischoff *et al.*, 2016; Atti *et al.*, 2018). A study by Concannon *et al.*, (2017) also found a dependence of stent position on cardiac deaths in a multicentre cohort of 151 patients treated for thoracoabdominal aortic aneurysms with a CoCr stent, where an increased risk of cardiac death was associated with proximal stenting. Recent clinical trials have been initiated to investigate the effects of thoracic-EVAR (TEVAR) on cardiac failure including the CORE trial (Nauta *et al.*, 2016), while van Bakel & Figueroa, (2017) show a 33% increase in left-ventricular mass at 12 months postop following proximal stenting of the aorta (Figure 2.7).

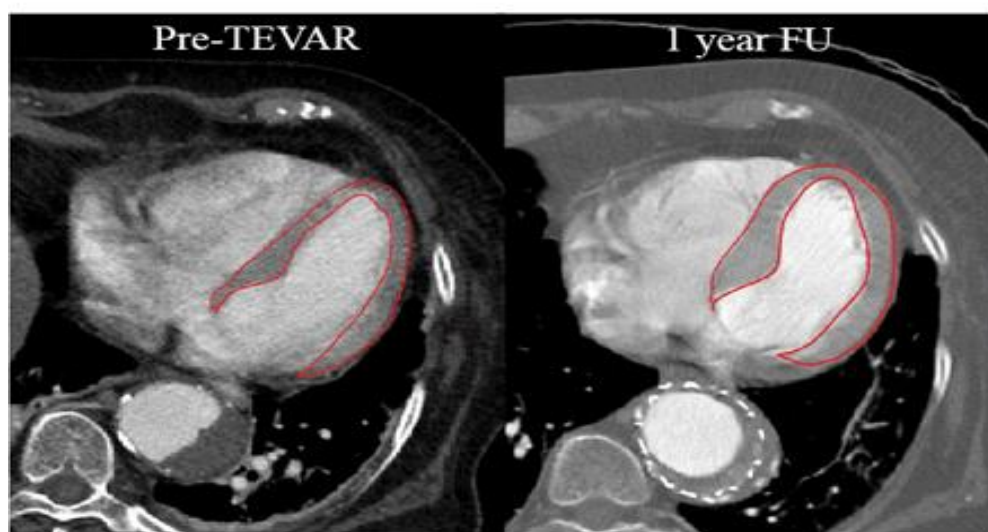


**Figure 2.7:** Outline of left ventricular wall pre-TEVAR (thoracic endovascular aortic repair) (left) versus 1 year follow up (right) (van Bakel, Patel and Figueroa, 2017). Permission granted by Wolters Kluwer.

It is believed that postoperative cardiac complications exist due to the lack of understanding of the spatially varying biomechanics of the aorta, and hence, uncertainty surrounds the regional effects of endovascular repair on the ventriculo-aortic system as a whole. The following sections provide an outline of the work

conducted to date on the regional mechanics of the aorta from both an experimental and computational point of view.

## 2.2 Background and Literature

It has been shown that during embryogenesis the aorta is developed segmentally, each section of which are derived from different regions (Figure 2.8). Specifically, in relation to the thoracic aorta, it does not develop as one-unit or even in a single stage. The descending thoracic aorta is the first segment developed during embryogenesis, followed by the aortic arch, proximal ascending aorta and finally, the aortic root (Sherif, 2014). Additionally, each of these four segments are independently derived from different cell-line ages, be they neural crest or mesodermal in origin. Regional differences in biochemical, phenotypical, protease and cell signalling pathways have also been reported along the length of the aorta (Ruddy et al., 2008).

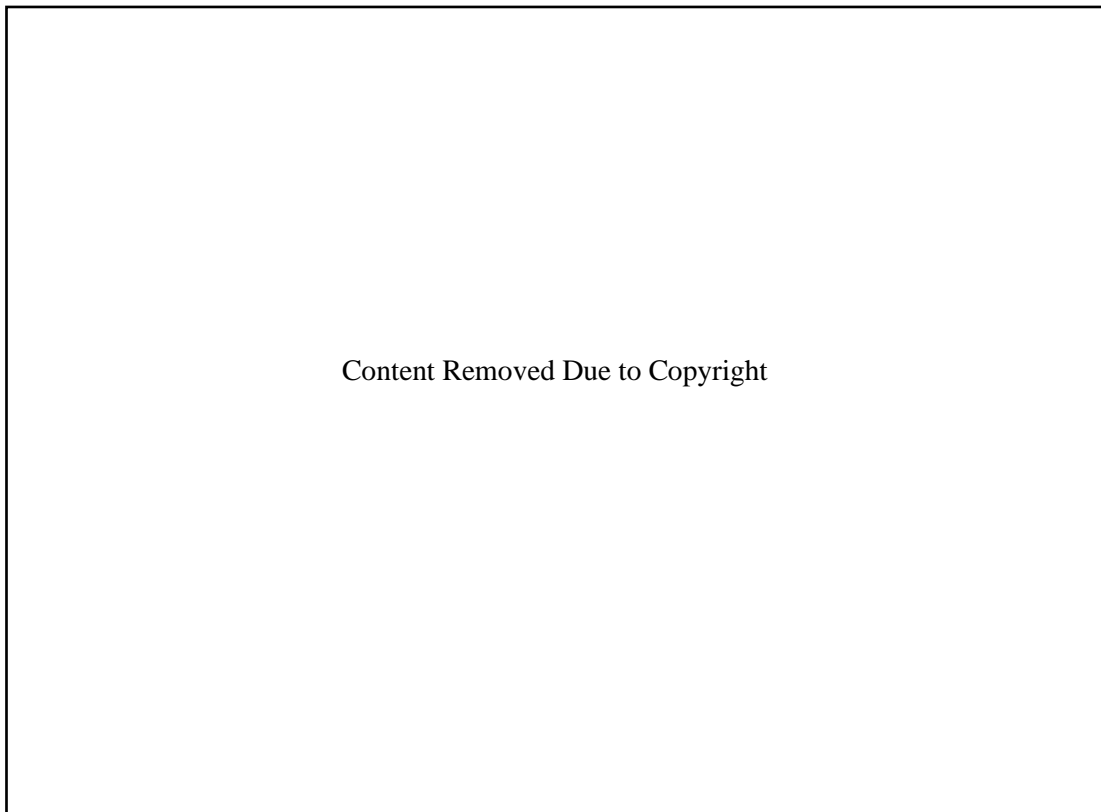


**Figure 2.8: Embryological development of the aorta (Schoenwolf et al., 2009).**

### 2.2.1 Histological analysis of Aortic Tissue

Particular focus has been directed towards the effects of ageing on the microstructure of the aorta (Feldman and Glagov, 1971; Cattell and Hasleton, 1996; Fritze *et al.*, 2012). Hosoda *et al.* (1984) investigated the human thoracic aorta and found that elastin decreased with age, whereas collagen remained the same. Faber and Moller-Hou (2009), also found that elastin decreased with age; however, they found that collagen increased.

Much less emphasis, however, has been placed on the spatial heterogeneity in the microarchitecture of the aorta in health and disease. Due to both the ethics and accessibility of human tissue, the number of animal studies exceeds that of human studies in the literature. Davidson *et al.*, (1985) investigated the regional elastin content in the porcine aorta and found that elastic fibers were reduced in the abdominal compared to thoracic groups, while Saey *et al.*, (2015) report, for an equine population, a greater concentration of collagen in the distal thoracic aorta compared with proximal; however, there were no significant regional differences in elastin content.

Content Removed Due to Copyright

**Figure 2.9: Normal histological features of the aortic wall (a) H&E staining of a rabbit aortic wall with cell nuclei stained dark purple (Xiao *et al.*, 2015). (b) Verhoeff Van Gieson stained murine aortic wall with elastin stained black, and (c) Masson's Trichrome stained murine aortic wall with collagen stained blue (Bersi *et al.*, 2016).**

Others have focused on characterising the orientation of collagen fibers in the aorta in order to provide advance on the anisotropy of aortic tissue. O'Connell *et al.*, (2008), Schriebl *et al.*, (2012), Chow *et al.*, (2014), and Sugita & Matsumoto, (2018) report that a single family of fibres was evident; however, others have reported two (Laksari *et al.*, 2016), three (Schriebl *et al.*, 2012) and even four (Rezakhaniha *et al.*, 2012) families. The vast majority of published studies on the orientation of collagen fibers in the aorta are animal studies, due to ethical and logistical constraints. Although varying numbers of collagen fiber families have been cited, in general, FE models of the aorta to date assume a homogeneous (Roy *et al.*, 2014) and symmetric distribution (Grytsan and Holzapfel, 2015) of fibres in the wall.

Content Removed Due to Copyright

**Figure 2.10: Polarized light micrographs of Picrosirius Red stained tissue samples from (a) intimal, (b) medial, and (c) adventitial layers of the aorta (Schriebl et al., 2012).**

### 2.2.2 Experimental Testing of Aortic Tissue

The vast majority of data that exists in the literature surrounding aortic properties is that of tensile tests performed on excised tissue. Of this data, naturally, all are either diseased or dead. Here we review the body of work performed to date on experimental testing of aortic tissue, with a particular focus on heterogeneity, outlining the key features learned.

Charles Roy stated that ‘ut tensio sic vis’ (as the extension, so the force - Hooke’s Law) does not apply in animal tissues in 1880. It is now well established that the stress-strain curve for the aorta is non-linear. Many others have described the microstructural basis for this stiffening as the progressive straightening and alignment of collagen fibers (Wolinsky and Glagov, 1964)

Significant heterogeneity in terms of the shape of the stress-strain response of aortic tissue to tension has been shown experimentally between young and old aortae. Vande Geest & Vorp, (2004) investigated the age dependency of biaxial mechanical behaviour of the abdominal aorta and found that, specimens from the younger group exhibited far greater extensibility than older groups who exhibited an exponential shape response ( $p < 0.001$ ). The authors go on to model young tissue using a polynomial strain energy function and older groups using a Fung-type exponential strain energy function, highlighting significant age dependency in the mechanical response.

Haskett *et al.*, (2010) subjected samples of human aortic tissue following autopsy to biaxial mechanical testing and found that the abdominal aorta is statistically different from all other aortic regions both in terms of its microstructure and mechanical response. The authors also showed that the abdominal aorta was significantly stiffer than proximal regions. Weisbecker *et al.*, (2012) conducted layer specific experiments on 14 thoracic and 9 abdominal aortic samples with non-atherosclerotic intimal thickening and report a statistically relevant difference between the thoracic and abdominal aorta for several parameter values of the constitutive law used to fit the data in the intima, media and adventitia.

Pierce *et al.*, (2015) was the first to publish on the varying collagen fiber angles and material constitutive law parameters between thoracic aortic aneurysm (TAA) and abdominal aortic aneurysm (AAA) tissues. The authors report a median collagen fiber angle for the TAA samples of  $\Upsilon = 44.81^\circ$ , indicating a nearly isotropic behaviour. In contrast, a median value of  $\Upsilon = 41.91^\circ$  for the AAA samples was found, thus abdominal aneurysmal tissues show a higher stiffness circumferentially (Figure 2.11). The authors also report a statistically significant difference in the parameter  $k_1$  which was larger in the abdominal aorta, indicating that the fibers contribute more to the mechanical response.

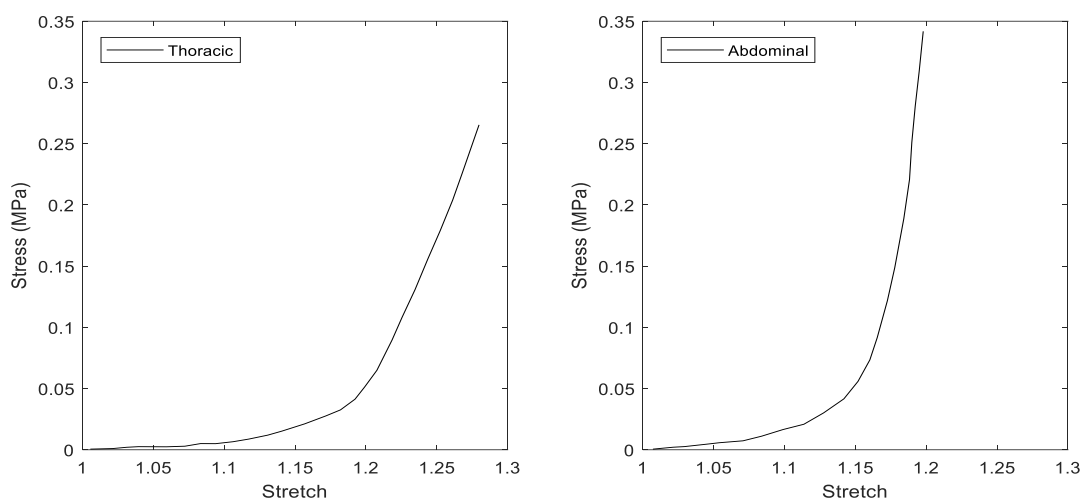


**Figure 2.11: Stress strain plot for human circumferential TAA (thoracic) and AAA (abdominal) tissue samples subjected to uniaxial extension, adapted from (Pierce *et al.*, 2015). The mechanical response of the tissue to loading is notably different between thoracic and abdominal groups.**

The pressure-area relationship of the aorta was first characterised by Roy in 1880, with an experimental setup that consisted of: “*A portion of artery, so arranged that it could be distended by any desired internal pressure, was inclosed in a small vessel, containing olive oil, and the variations of whose contents were recorded by means of a lever, writing on the blackened surface of a cylinder*”. The author showed that the aorta was most extensible at pressures nearing normotension and at higher pressures the extensibility was considerably impaired. The nonlinearity of this pressure-area relationship was subsequently attributed to an increasing number of collagen fibers being drawn taut (Clark and Glagov, 1985).

Hallock & Benson (1937), investigated the effect of various age profiles on the pressure-volume response of aortic tissue and show that in younger groups, the curves are s-shaped exhibiting a high degree of extensibility even at high pressures (Figure 2.12). In older groups this s-shape is lost, and the relationship becomes monotonic, where at high pressures the curve becomes almost a horizontal line.

Content Removed Due to Copyright

**Figure 2.12: Evolution of the aortic pressure-volume relationship with age (Hallock and Benson, 1937). Younger subjects exhibit a more s-shaped curve whereas older subjects exhibit a monotonic relationship.**

Langewouters & Goedhard, (1984) investigated the regional variance in the human aortic pressure-diameter relationship by subjecting segments of thoracic and abdominal tissue to incrementally increasing pressures. Following the experimental protocol, the authors fit an arc-tangent model to the data and observe a similar s-shaped curve in the thoracic segment, however this is less evident distally (Figure 2.13). The authors also report that compliance values at 100 mmHg range from 1.9 to 16.6  $\text{cm}^2/\text{mmHg}^{-1}$  in the thoracic aorta and from 0.6 to 4.4  $\text{cm}^2/\text{mmHg}^{-1}$  in the abdominal aorta.

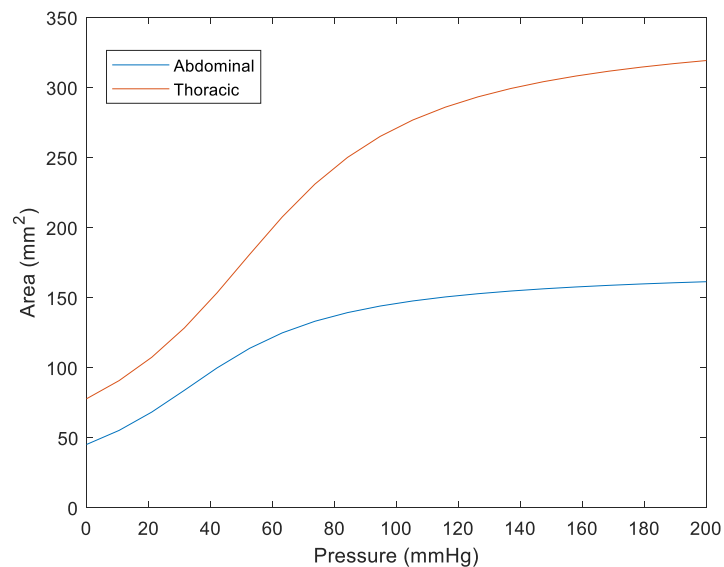


**Figure 2.13: Thoracic versus abdominal pressure-area relation for a 30-year-old subject fitted with the arc-tangent model ( $R^2=0.998$ ,  $R^2=0.999$ ). Adapted from Langewouters & Goedhard, 1984.**

It should be noted at this point that significant work has been published that indicates that even when the aorta is at ‘zero pressure’, that it is not in the ‘zero stress’ state. Bergel stated “*When an artery is split open longitudinally it will unroll itself to a varying degree to the form of a flat ribbon. This surely indicates some degree of stress even when there is no distending pressure*” (Bergel, 1960). Some years later Chuong and Fung, (1983) and Vaishnav and Vossoughi, (1983) independently observed that slicing an artery along the radial dimension results in the springing open of the vessel (by what is now known as the opening angle), implying the existence of circumferential residual strains and therefore stresses. Recently, Sokolis *et al.*, (2017) published the regional heterogeneity in circumferential residual strains (Figure 2.14) along the human aorta, providing further evidence of the significant heterogeneity that exists within the vessel wall.

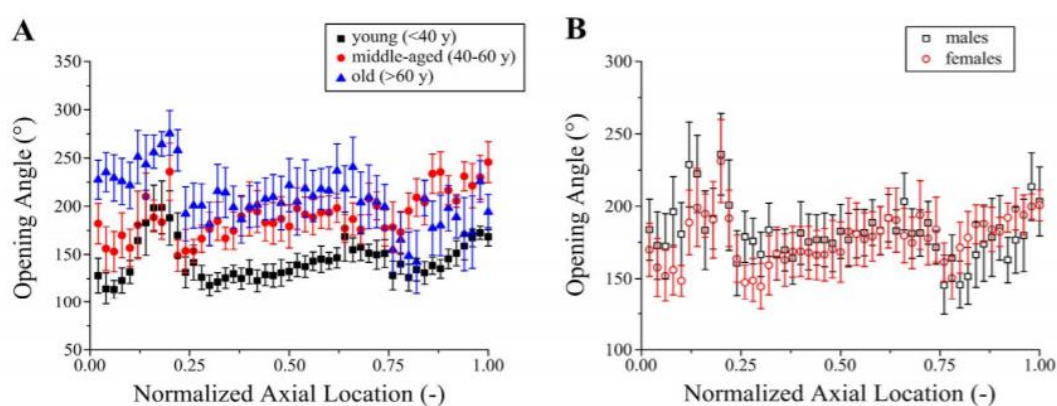


**Figure 2.14:** Regional variation in opening angle along the length of the human aorta for ‘young’, ‘middle’ and ‘old’ age groups, in addition to variation in gender (Sokolis *et al.*, 2017). Permission granted by Springer Nature.

### 2.2.3 4D Flow MRI in the Aorta

Magnetic resonance imaging (MRI) techniques provide non-invasive and non-ionising methods for the highly accurate anatomical depiction of the heart and vessels throughout the cardiac cycle (Markl *et al.*, 2016). In the early 1500s, Leonardo DaVinci proposed that vortices existed in the proximal ascending aorta that would aid in the closure of the aortic valve, today with the use of 4D Flow MRI it is possible to quantify such vortices on a patient-specific basis (Figure 2.15).

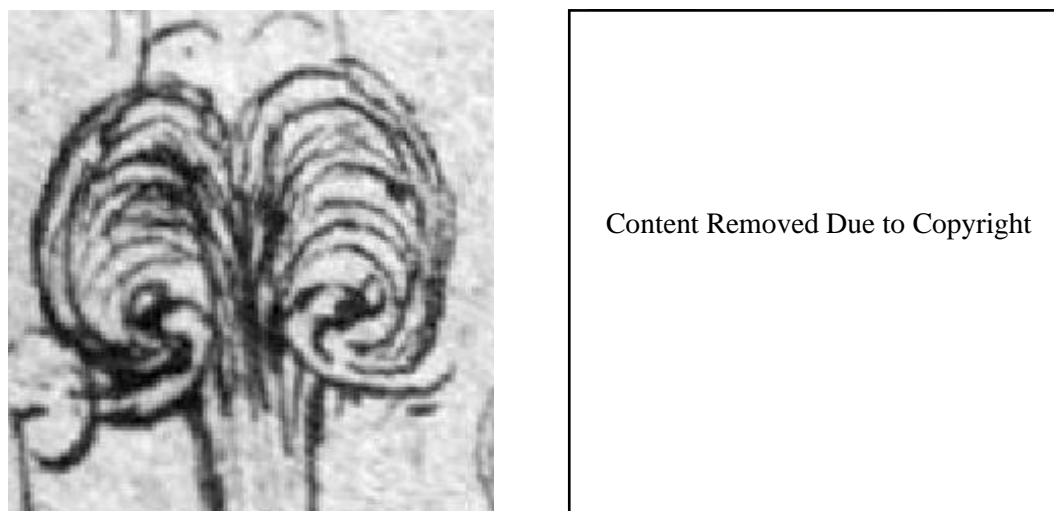


**Figure 2.15:** (left) Sketches of aortic flow patterns in the proximal aorta by Leonardo DaVinci circa. 1512 (Gharib *et al.*, 2002). (right) 4D Flow MRI of ascending aorta illustrating vorticity in the aortic root (Bissell and Choudhury, 2014). Permission granted by Springer Nature.

The majority of 4D Flow MRI studies to date have focused on differences in haemodynamics between control groups and aneurysm (Hope *et al.*, 2007), dissection (François *et al.*, 2013), bicuspid aortic valve (BAV) (van Ooij *et al.*, 2015), and coarctation (Hope *et al.*, 2010). 4D Flow MRI otherwise known as 3D CINE phase contrast (PC) MRI with 3-directional velocity encoding (Dyverfeldt *et al.*, 2015) has several advantages over standard 2D PC MRI including the ability to characterise time-resolved flow in all 3 dimensions, in addition to equivalent accuracy in flow and velocity quantification (Feneis *et al.*, 2018). A further advantage of 4D Flow MRI exists in the ability to retrospectively place planes of analysis at any location within the acquisition volume during post-processing (Dyverfeldt *et al.*, 2015).

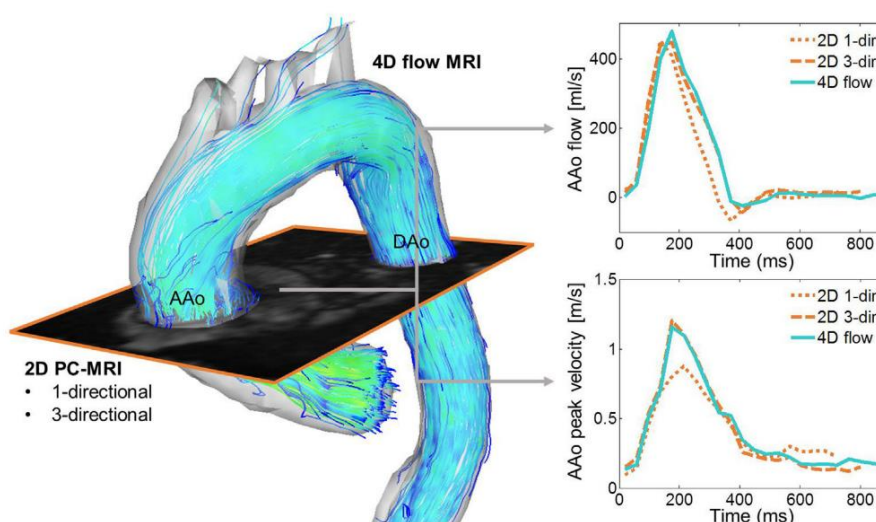


**Figure 2.16:** Comparison of phase contrast MRI techniques (2D 1-dir, 2D 3-dir, 4D Flow) in the calculation of peak velocity and flow within the aorta (Markl *et al.*, 2016). Permission granted by Elsevier.

The “4D flow cardiovascular magnetic resonance consensus statement” published by Dyverfeldt *et al.*, (2015), outlines the acquisition and analysis methods required for a suitable scan. A summary of the main imaging parameters tailored to the human aorta include a spatial resolution of 2.0-2.5 mm, a temporal resolution of 40-50 ms, a velocity encoding coefficient (VENC) of 150-200 cm/s, and a total scan time of 10-20 minutes (Markl *et al.*, 2012). Figure 2.17 below shows the workflow of a typical 4D Flow MRI scan from acquisition to post-processing and data visualization. First, the volume of interest must be chosen to encompass all vessels for which quantification is required. ECG gating is required to synchronise scanning to particular phases within each cardiac cycle, while 3D velocity encoding is used to obtain velocity sensitive phase images along the three principle cartesian axes (antero-posterior, foot-head, and right-left). Data pre-processing consists of correction techniques for noise and velocity aliasing (if required) and the velocity magnitude can be calculated as the root of the squared sum of the individual components ( $V_x$ ,  $V_y$ ,  $V_z$ ). Time resolved flow rates can then be calculated as the integral of the velocity magnitude within the boundary of the fluid domain (Stankovic *et al.*, 2014).

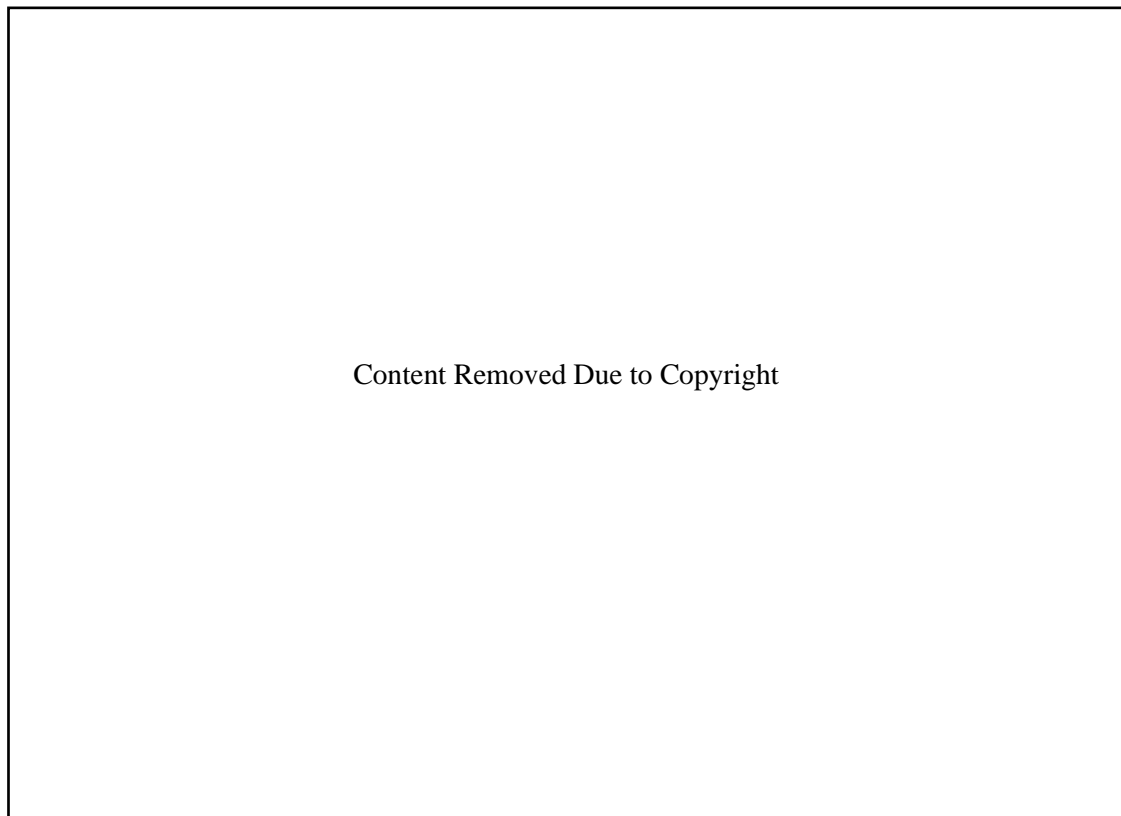


**Figure 2.16: Data acquisition and analysis for 4D flow MRI (Stankovic et al., 2014).**

In a standard 4D Flow acquisition with a single VENC, in order to avoid velocity aliasing, the VENC must be set sufficiently high to capture the highest velocity in systole, a level that is not optimal for measuring low flow. VENC is defined as the velocity that gives a phase shift of  $\pi$  radians, and as phase is a cyclic entity, phase shifts greater than  $\pi$  radians result in velocity aliasing or wrapping, which if uncorrected will result in significant errors in the calculation of flow (Elkins *et al.*, 2003; Markl *et al.*, 2012). Recently, issues regarding the use of a single VENC have been brought to light in that the fluid velocity within the aorta is temporally varying and hence, multi-VENC acquisitions have been proposed to accurately calculate the flow throughout the entire cardiac cycle. As the velocity to noise ratio (VNR) is linearly related to the VENC, the accuracy declines when the true fluid velocity becomes low in comparison to the VENC value assigned (Callaghan *et al.*, 2016). The approach proposed by the authors, resulted in a 31% improvement in spatial and 53% improvement in temporal precision of velocity vector measurements (Figure 2.18) during the mid-late diastolic period when fluid velocity was slow in comparison to a single (mono-) VENC acquisition.

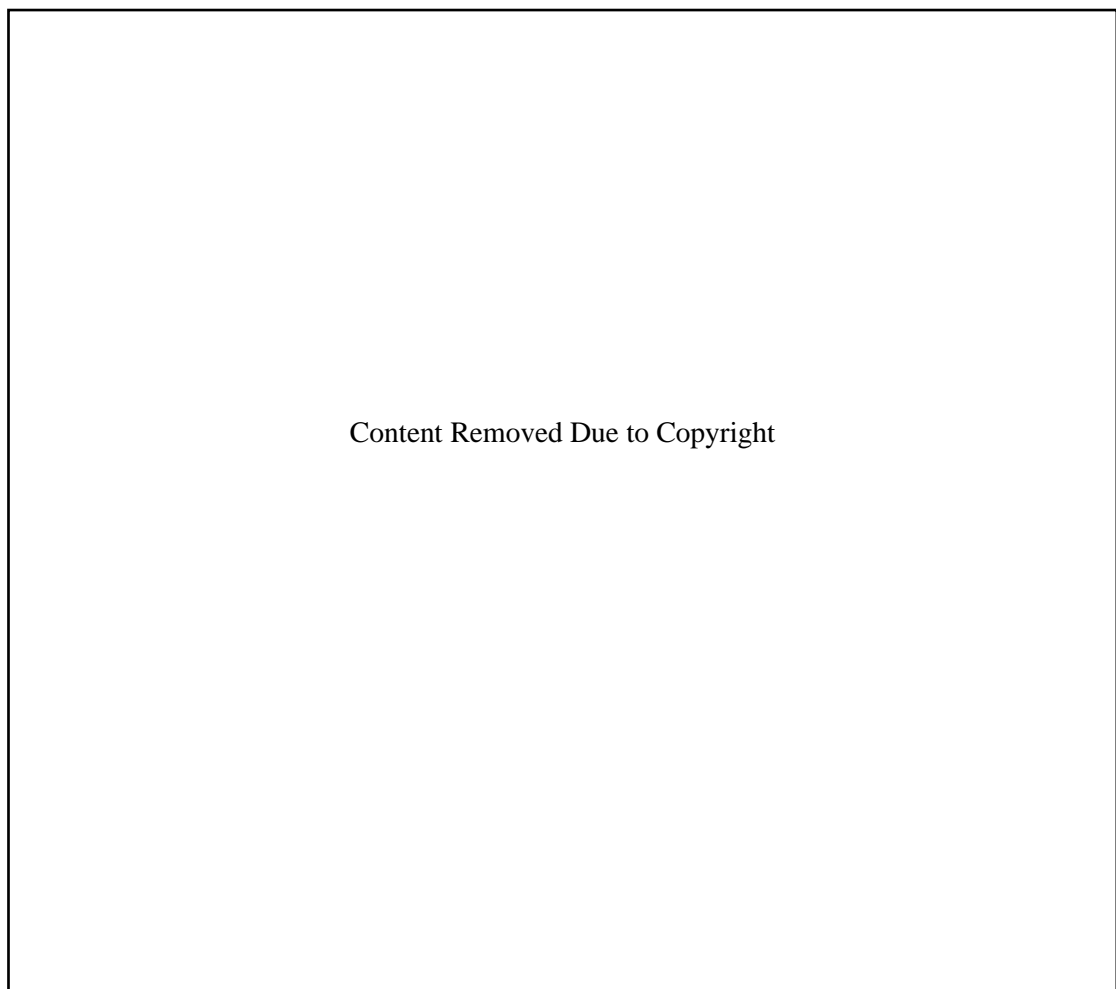


**Figure 2.18: Comparison of mono- versus multi-VENC acquisition by Callaghan et al., (2015). The multi-VENC acquisition resulted in a 31% improvement in spatial and 53% improvement in temporal precision of velocity vector measurements compared to the mono-VENC scan.**

The use of phase/velocity unwrapping techniques, however, must still be accounted for in each scan where the VENC parameter is set below any true velocity. Such techniques add significant time to the post-processing portion of the 4D Flow MRI workflow, in addition to the fact that they are prone to errors, rendering them unpractical for use in most real life applications (Pijewska and Szkulmowski, 2019). An alternative approach is described in the current thesis in Chapter 5, ensuring accurate quantification of flow at each phase of the cardiac cycle and at each plane of interest along the aorta.

#### 2.2.4 Computational Modelling of the Aorta

The integration of computational models in recent years into the field of solid and fluid biomechanics has resulted in significant advance in terms of deepening understanding, generating new insights, and validating experimental investigations. The following section provides a general overview of the current state of the art in computational models of the human aorta, with a more focused literature review available in Chapter 6.

To date, the majority of models assume an idealised ‘candy cane’ geometry (Beller *et al.*, 2004; Fan *et al.*, 2010; Vasava *et al.*, 2012; Ben Ahmed and Figueroa, 2016). This is mostly due to difficulties in; (i) obtaining patient-specific scan data, and (ii) generating a robust FE mesh of such a complex geometry. Plonek *et al.*, (2017), investigated in an idealised aortic geometry the effect of diameter, blood pressure and longitudinal systolic stretching on the stress of the aortic wall, and found that stretching had the greatest effect on the stress distribution. Patient-specificity in terms of geometry, however, will evidently have a significant role in localised stress distribution and so should be taken into account when generating computational models of the aorta.

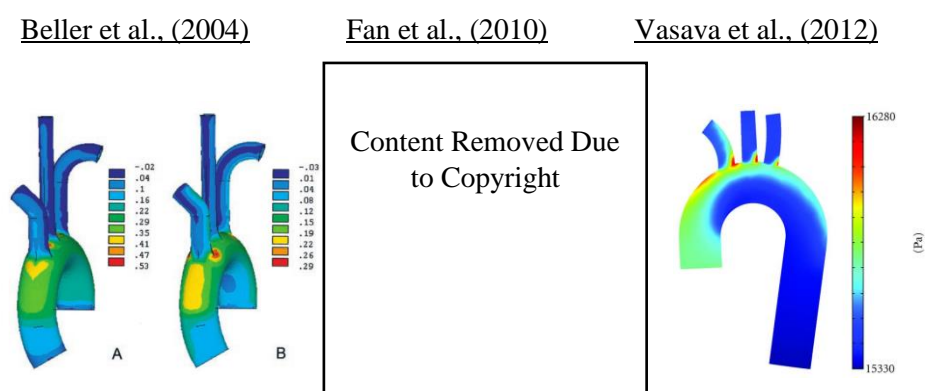


**Figure 2.19: Previously published geometrically idealised models of the aorta. Permission granted by Elsevier and Hindawi.**

Others have published patient-specific models of the human aorta (in a geometrical sense) (Pasta *et al.*, 2013; Martin and Elefteriades, 2015; Martufi *et al.*, 2018; Emerel *et al.*, 2019), although the majority tend to focus on an isolated segment of the aorta such as the ascending thoracic, or an aneurysmal portion. Doyle and McGloughlin, (2007) found that modelling the aorta as an idealised geometry resulted in marked differences in peak wall stress results compared to models with increased geometrical patient-specificity, highlighting the importance of taking into account the true geometry of each patient's vessel.

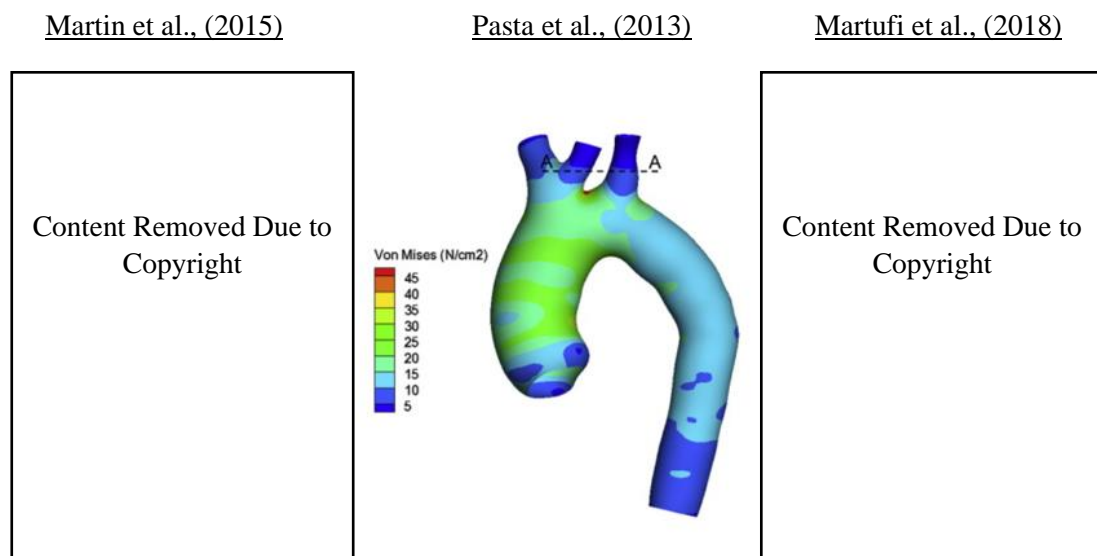


**Figure 2.20: Previously published patient-specific models of the aorta. Permission granted by Elsevier.**

Studies that incorporate heterogeneous material properties along the length of the aorta are few in the literature. The majority of studies assume the aorta to be homogeneous (Kato *et al.*, 2000; Kim *et al.*, 2009; Georgakarakos *et al.*, 2010; Di Achille *et al.*, 2011). Martufi *et al.*, (2015) showed that using homogeneous versus heterogeneous material properties lead to a significantly different ( $p < 0.001$ ) stress response (Figure 2.21) in patient-specific abdominal aortic aneurysm models (Martufi *et al.*, 2015).

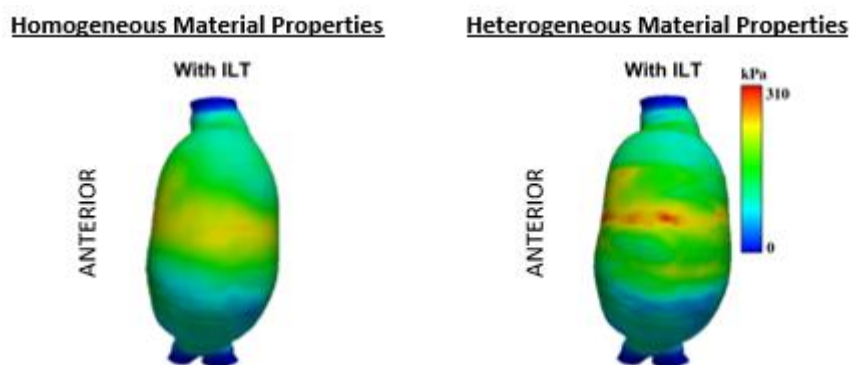


Figure 2.21: Effect of homogeneous versus heterogeneous material properties on the stress distribution in the abdominal aortic aneurysm (Martufi *et al.*, 2015). Permission granted by Springer Nature.

Significant work has been published on the importance of incorporating the unloaded configuration into computational models of arteries (Speelman & Gijzen, 2011). Most FEA models of the aorta are generated from CT/MRI scans at a given cardiac phase, and hence do not correspond to the unloaded geometry. Several techniques have been developed to estimate an unloaded configuration (Bols and Vierendeels, 2013; Riveros *et al.*, 2013), however this is truly never known. Not accounting for the unloaded configuration results in an overestimation the displacement of the AAA wall and an underestimation of peak wall stress by up to 20%. (Raut *et al.*, 2013).

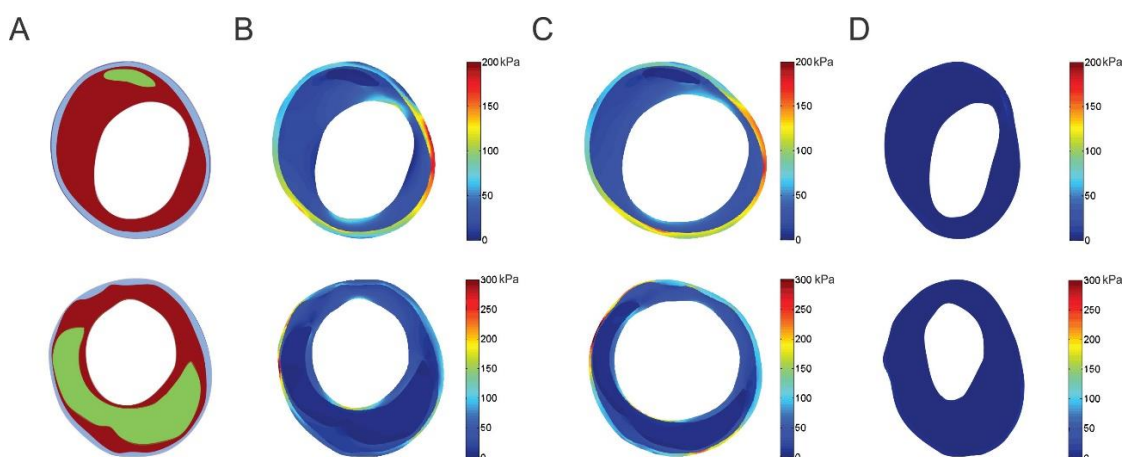


Figure 2.21: Importance of incorporating the zero-pressure geometry (ZPG) on the stress in coronary plaque models. (A) Histological geometries, (B) Systole with ZPG (C) Systole without ZPG, (D) ZPG (Speelman & Gijzen, 2011). Permission granted by Journal of Biomechanics.

A limited number of studies have computationally simulated aortic stent graft deployment in the literature. The majority investigate bending and compression (Demanget et al., 2012a; Demanget et al., 2012b; De Bock, 2013). Demanget *et al.*, compared eight marketed aortic stent-grafts using finite element analysis by simulating 180° bending and pressurization and show that spiral and circular stents provide greater flexibility, as well as lower stress values than Z-stents (Demanget et al., 2013). De Bock *et al.*, details the virtual deployment of a bifurcated stent graft in an Abdominal Aortic Aneurysm model, using the finite element method. The finite element results are validated in vitro with placement of the device in a silicone mock aneurysm, confirming the capability of the finite element method to predict the deformed configuration following device deployment (De Bock et al., 2013). Perrin et al., developed a numerical methodology to predict stent-graft final deployed shapes after surgery in three clinical cases, however these studies neglect the effects of arterial pre-stress (Perrin et al. 2015).



**Figure 2.22: Finite element simulation results for three clinical AAA cases (Perrin et al., 2015). Permission granted by Elsevier.**

### 2.3 Bibliography

- Di Achille, P., Celi, S., Di Puccio, F. and Forte, P. (2011) ‘Anisotropic AAA: Computational comparison between four and two fiber family material models’, *Journal of Biomechanics*, 44(13), pp. 2418–2426. doi: 10.1016/j.jbiomech.2011.06.029.
- Agrawal, V., Kollimada, S. A., Byju, A. G. and Gundiah, N. (2013) ‘Regional variations in the nonlinearity and anisotropy of bovine aortic elastin’, *Biomechanics and Modeling in Mechanobiology*, 12(6), pp. 1181–1194. doi: 10.1007/s10237-013-0474-3.
- Ben Ahmed, S., Dillon-Murphy, D. and Figueroa, C. A. (2016) ‘Computational Study of Anatomical Risk Factors in Idealized Models of Type B Aortic Dissection’, *European Journal of Vascular and Endovascular Surgery*. W.B. Saunders, 52(6), pp. 736–745. doi: 10.1016/J.EJVS.2016.07.025.
- Atti, V., Nalluri, N., Kumar, V., Tabet, R., Yandrapalli, S., Edla, S., Tripathi, A., Patel, N. J., Dave, M., Aronow, W. S., Basir, M. B., Davis, T. P., Drachman, D. E. and Bhatt, D. L. (2018) ‘Frequency of 30-Day Readmission and Its Causes After Endovascular Aneurysm Intervention of Abdominal Aortic Aneurysm (from the Nationwide Readmission Database)’, *The American Journal of Cardiology*. Excerpta Medica. doi: 10.1016/J.AMJCARD.2018.12.006.
- van Bakel, T., Patel, H. J. and Figueroa, C. A. (2017) ‘Echocardiographic and Computational Assessment of Cardiovascular Remodeling Following Thoracic Endovascular Aortic Repair’, *Circulation*, 136, p. A19030.
- Balakhovsky, K., Jabareen, M. and Volokh, K. Y. (2014) ‘Modeling rupture of growing aneurysms.’, *Journal of biomechanics*, 47(3), pp. 653–8. doi: 10.1016/j.jbiomech.2013.11.049.
- Barakat, H. M., Shahin, Y., McCollum, P. T. and Chetter, I. C. (2015) ‘Prediction of organ-specific complications following abdominal aortic aneurysm repair using cardiopulmonary exercise testing’, *Anaesthesia*, 70(6), pp. 679–685. doi: 10.1111/anae.12986.
- Beaufort, H. W. L. de, Trimarchi, S., Korach, A., Eusanio, M. Di, Gilon, D., Montgomery, D. G., Evangelista, A., Braverman, A. C., Chen, E. P., Isselbacher, E. M., Gleason, T. G., Vincentiis, C. De, Sundt, T. M., Patel, H. J. and Eagle, K. A. (2017) ‘Aortic dissection in patients with Marfan syndrome based on the IRAD data’, *Annals of Cardiothoracic Surgery*. AME Publications, 6(6), p. 633. doi: 10.21037/ACS.2017.10.03.
- Beller, C. J., Labrosse, M. R., Thubrikar, M. J. and Robicsek, F. (2004) ‘Role of Aortic Root Motion in the Pathogenesis of Aortic Dissection’, *Circulation*, 109, pp. 763–769. doi: 10.1161/01.CIR.0000112569.27151.F7.
- Bergel, D. H. (1960) ‘The visco-elastic properties of the arterial wall.’ Available at: <https://qmro.qmul.ac.uk/xmlui/handle/123456789/1453> (Accessed: 19 July 2019).

- Bersi, M. R., Bellini, C., Wu, J., Montaniel, K. R. C., Harrison, D. G. and Humphrey, J. D. (2016) 'Excessive adventitial remodeling leads to early aortic maladaptation in angiotensin-induced hypertension', *Hypertension*. Lippincott Williams and Wilkins, 67(5), pp. 890–896. doi: 10.1161/HYPERTENSIONAHA.115.06262.
- Bischoff, M. S., Ante, M., Meisenbacher, K. and Böckler, D. (2016) 'Outcome of thoracic endovascular aortic repair in patients with thoracic and thoracoabdominal aortic aneurysms', *Journal of Vascular Surgery*. Elsevier, 63(5), p. 1170–1181.e1. doi: 10.1016/j.jvs.2015.11.045.
- Bissell, M. M., Dall'Armellina, E. and Choudhury, R. P. (2014) 'Flow vortices in the aortic root: in vivo 4D-MRI confirms predictions of Leonardo da Vinci.', *European heart journal*, 35(20), p. 1344. doi: 10.1093/eurheartj/ehu011.
- Bols, J. and Vierendeels, J. (2013) 'inverse modelling of image-based patient-specific blood vessels: zero-pressure geometry and in vivo stress incorporation', *ESAIM: Mathematical Modelling and Numerical Analysis*.
- Brozovich, F. V, Nicholson, C. J., Degen, C. V, Gao, Y. Z., Aggarwal, M. and Morgan, K. G. (2016) 'Mechanisms of Vascular Smooth Muscle Contraction and the Basis for Pharmacologic Treatment of Smooth Muscle Disorders.', *Pharmacological reviews*. American Society for Pharmacology and Experimental Therapeutics, 68(2), pp. 476–532. doi: 10.1124/pr.115.010652.
- Caglayan, A. O. and Dundar, M. (2009) 'Inherited diseases and syndromes leading to aortic aneurysms and dissections', *European Journal of Cardio-Thoracic Surgery*. Oxford University Press, 35(6), pp. 931–940. doi: 10.1016/j.ejcts.2009.01.006.
- Callaghan, F. M., Kozor, R., Sherrah, A. G., Vallely, M., Celermajer, D., Figtree, G. A. and Grieve, S. M. (2016) 'Use of multi-velocity encoding 4D flow MRI to improve quantification of flow patterns in the aorta', *Journal of Magnetic Resonance Imaging*, 43(2), pp. 352–363. doi: 10.1002/jmri.24991.
- Cattell, M. A., Anderson, J. C. and Hasleton, P. S. (1996) 'Age-related changes in amounts and concentrations of collagen and elastin in normotensive human thoracic aorta', *Clinica Chimica Acta*. Elsevier, 245(1), pp. 73–84. doi: 10.1016/0009-8981(95)06174-6.
- Chamley-Campbell, J., Campbell, G. R. and Ross, R. (1979) 'The smooth muscle cell in culture', *Physiological Reviews*, 59(1), pp. 1–61. doi: 10.1152/physrev.1979.59.1.1.
- Chandran, K. B., Rittgers, S. E. and Yoganathan, A. P. (Ajit P. (2012) *Biofluid mechanics: the human circulation*. CRC Press, Taylor & Francis Group. Available at: <https://www.crcpress.com/Biofluid-Mechanics-The-Human-Circulation-Second-Edition/Chandran-Rittgers-Yoganathan/p/book/9781439845165> (Accessed: 30 May 2018).
- Chiesa, R., Melissano, G., Civilini, E., Bertoglio, L., Rinaldi, E., Marone, E. M. and Tshomba, Y. (2012) 'Video-atlas of open thoracoabdominal aortic aneurysm repair', *Annals of Cardiothoracic Surgery*, 1(3), pp. 398–403. doi: 10.3978/528.
- Chow, M.-J., Turcotte, R., Lin, C. P. and Zhang, Y. (2014) 'Arterial Extracellular Matrix: A Mechanobiological Study of the Contributions and Interactions of

- Elastin and Collagen’, *Biophysical journal*, 106, pp. 2684–2692. doi: 10.1016/j.bpj.2014.05.014.
- Chuong, C. J. and Fung, Y. C. (1983) ‘Three-Dimensional Stress Distribution in Arteries’, *Journal of Biomechanical Engineering*, 105(3), p. 268. doi: 10.1115/1.3138417.
- Clark, J. M. and Glagov, S. (1985) ‘Transmural organization of the arterial media. The lamellar unit revisited.’, *Arteriosclerosis (Dallas, Tex.)*. American Heart Association, Inc., 5(1), pp. 19–34. doi: 10.1161/01.ATV.5.1.19.
- Clough, R. E., Modarai, B., Bell, R. E., Salter, R., Sabharwal, T., Taylor, P. R. and Carrell, T. W. (2012) ‘Total endovascular repair of thoracoabdominal aortic aneurysms.’, *European journal of vascular and endovascular surgery : the official journal of the European Society for Vascular Surgery*, 43(3), pp. 262–7. doi: 10.1016/j.ejvs.2011.11.009.
- Concannon, J., Kavanagh, E. P., Hynes, N., McHugh, P. E., McGarry, J. P. and Sultan, S. (2017) ‘The Streamliner Multilayer Flow Modulator in the treatment of Complex Thoracoabdominal Aortic Aneurysms’, *Vascular*, 25(2), p. suppl.
- Davidson, J. M., Hill, K. E., Mason, M. L. and Giro\$, M. G. (1985) ‘Longitudinal Gradients of Collagen Porcine Aorta\* and Elastin Gene Expression in the’, *THE JOURNAL OF BIOLOGICAL CHEMISTRY*, 260(3), pp. 1301–1908. Available at: <http://www.jbc.org/content/260/3/1901.full.pdf> (Accessed: 7 June 2018).
- Debaeky, M. E., Creech, O. and Morris, G. C. (1956) ‘Aneurysm of thoracoabdominal aorta involving the celiac, superior mesenteric, and renal arteries; report of four cases treated by resection and homograft replacement.’, *Annals of surgery*, 144(4), pp. 549–73. Available at: <http://www.pubmedcentral.nih.gov/articlerender.fcgi?artid=1465510&tool=pmc-entrez&rendertype=abstract> (Accessed: 29 March 2016).
- De Bock, S., Iannaccone, F., De Beule, M., Van Loo, D., Vermassen, F., Verhegghe, B. and Segers, P. (2013) ‘Filling the void: A coalescent numerical and experimental technique to determine aortic stent graft mechanics’, *Journal of Biomechanics*, 46(14), pp. 2477–2482. doi: 10.1016/j.jbiomech.2013.07.010.
- Demanget, N., Avril, S., Badel, P., Orgéas, L., Geindreau, C., Albertini, J. N. and Favre, J. P. (2012) ‘Computational comparison of the bending behavior of aortic stent-grafts’, *Journal of the Mechanical Behavior of Biomedical Materials*, 5(1), pp. 272–282. doi: 10.1016/j.jmbbm.2011.09.006.
- Demanget, N., Latil, P., Orgéas, L., Badel, P., Avril, S., Geindreau, C., Albertini, J.-N. and Favre, J.-P. (2012) ‘Severe Bending of Two Aortic Stent-Grafts: An Experimental and Numerical Mechanical Analysis’, *Annals of Biomedical Engineering*, 40(12), pp. 2674–2686. doi: 10.1007/s10439-012-0618-0.
- Doyle, B. J., Callanan, A. and McGloughlin, T. M. (2007) ‘A comparison of modelling techniques for computing wall stress in abdominal aortic aneurysms.’, *Biomedical engineering online*. BioMed Central, 6, p. 38. doi: 10.1186/1475-925X-6-38.
- Dyverfeldt, P., Bissell, M., Barker, A. J., Bolger, A. F., Carlhäll, C.-J., Ebberts, T., Francios, C. J., Frydrychowicz, A., Geiger, J., Giese, D., Hope, M. D., Kilner, P. J., Kozerke, S., Myerson, S., Neubauer, S., Wieben, O. and Markl, M. (2015) ‘4D

- flow cardiovascular magnetic resonance consensus statement', *Journal of Cardiovascular Magnetic Resonance*. BioMed Central, 17(1), p. 72. doi: 10.1186/s12968-015-0174-5.
- Elefteriades, J. A., Sang, A., Kuzmik, G. and Hornick, M. (2015) 'Guilt by association: paradigm for detecting a silent killer (thoracic aortic aneurysm).', *Open heart*. British Cardiovascular Society, 2(1), p. e000169. doi: 10.1136/openhrt-2014-000169.
- Elkins, C. J., Markl, M., Pelc, N. and Eaton, J. K. (2003) '4D Magnetic resonance velocimetry for mean velocity measurements in complex turbulent flows', *Experiments in Fluids*. Springer Verlag, 34(4), pp. 494–503. doi: 10.1007/s00348-003-0587-z.
- Emerel, L., Thunes, J., Kickliter, T., Billaud, M., Phillippi, J. A., Vorp, D. A., Maiti, S. and Gleason, T. G. (2019) 'Predissection-derived geometric and distensibility indices reveal increased peak longitudinal stress and stiffness in patients sustaining acute type A aortic dissection: Implications for predicting dissection', *The Journal of Thoracic and Cardiovascular Surgery*. Mosby, 158(2), pp. 355–363. doi: 10.1016/J.JTCVS.2018.10.116.
- Evangelista, A., Maldonado, G., Grusso, D., Teixido, G., Rodríguez-Palomares, J. and Eagle, K. (2016) 'Insights from the International Registry of Acute Aortic Dissection.', *Global cardiology science & practice*. Magdi Yacoub Institute, 2016(1), p. e201608. doi: 10.21542/gcsp.2016.8.
- Faber, M. and Moller-Hou, G. (2009) 'THE HUMAN AORTA', *Acta Pathologica Microbiologica Scandinavica*. Wiley/Blackwell (10.1111), 31(3), pp. 377–382. doi: 10.1111/j.1699-0463.1952.tb00205.x.
- Fan, Y., Cheng, S. W.-K., Qing, K.-X. and Chow, K.-W. (2010) 'Endovascular repair of type B aortic dissection: a study by computational fluid dynamics', *Journal of Biomedical Science and Engineering*, 03(09), pp. 900–907. doi: 10.4236/jbise.2010.39120.
- Feldman, S. A. and Glagov, S. (1971) 'Transmedial collagen and elastin gradients in human aortas: Reversal with age', *Atherosclerosis*. Elsevier, 13(3), pp. 385–394. doi: 10.1016/0021-9150(71)90081-5.
- Feneis, J. F., Kyubwa, E., Atianzar, K., Cheng, J. Y., Alley, M. T., Vasanawala, S. S., Demaria, A. N. and Hsiao, A. (2018) '4D flow MRI quantification of mitral and tricuspid regurgitation: Reproducibility and consistency relative to conventional MRI.', *Journal of magnetic resonance imaging : JMRI*, 48(4), pp. 1147–1158. doi: 10.1002/jmri.26040.
- Fernandez-Moure, J. S., Vykoukal, D. and Davies, M. G. (2011) 'Biology Of Aortic Aneurysms And Dissections', *Methodist DeBakey Cardiovascular Journal*. The Methodist Hospital Houston, Texas, 7(3), pp. 2–7. doi: 10.14797/mdcj-7-3-2.
- Figuroa, C. A. and Zarins, C. K. (2011) 'Computational Analysis of Displacement Forces Acting on Endografts Used to Treat Aortic Aneurysms', in *Biomechanics and Mechanobiology of Aneurysms*. Studies in Mechanobiology, Tissue Engineering and Biomaterials, pp. 221–246.

- Fillinger, M. F., Raghavan, M. L., Marra, S. P., Cronenwett, J. L. and Kennedy, F. E. (2002) 'In vivo analysis of mechanical wall stress and abdominal aortic aneurysm rupture risk', *Journal of Vascular Surgery*, 36(3), pp. 589–597. doi: 10.1067/mva.2002.125478.
- Forsell, C., Roy, J. and Gasser, T. C. (2013) 'The Quasi-Static Failure Properties of the Abdominal Aortic Aneurysm Wall Estimated by a Mixed Experimental-Numerical Approach', *Annals of biomedical engineering*.
- François, C. J., Markl, M., Schiebler, M. L., Niespodzany, E., Landgraf, B. R., Schlensak, C. and Frydrychowicz, A. (2013) 'Four-dimensional, flow-sensitive magnetic resonance imaging of blood flow patterns in thoracic aortic dissections', *Journal of Thoracic and Cardiovascular Surgery*, 145(5), pp. 1359–1366. doi: 10.1016/j.jtcvs.2012.07.019.
- Fritze, O., Romero, B., Schleicher, M., Jacob, M. P., Oh, D.-Y., Starcher, B., Schenke-Layland, K., Bujan, J. and Stock, U. A. (2012) 'Age-related changes in the elastic tissue of the human aorta.', *Journal of vascular research*. Karger Publishers, 49(1), pp. 77–86. doi: 10.1159/000331278.
- Fung, Y.-C. (1993) 'Mechanical Properties and Active Remodeling of Blood Vessels', in *Biomechanics*. New York, NY: Springer New York, pp. 321–391. doi: 10.1007/978-1-4757-2257-4\_8.
- Fung, Y. (1993) *Biomechanics: Mechanical Properties of Living Tissues*, Second Edition:, Springer-Verlag Inc. doi: 10.1007/978-1-4757-2257-4.
- Gasser, T. C. (2017) 'Aorta', in *Biomechanics of Living Organs*. Elsevier, pp. 169–191. doi: 10.1016/B978-0-12-804009-6.00008-0.
- Gasser, T. C., Ogden, R. W. and Holzapfel, G. A. (2006) 'Hyperelastic modelling of arterial layers with distributed collagen fibre orientations.', *Journal of the Royal Society, Interface / the Royal Society*, 3(6), pp. 15–35. doi: 10.1098/rsif.2005.0073.
- Geest, J. P. Vande, Sacks, M. S. and Vorp, D. A. (2004) 'Age Dependency of the Biaxial Biomechanical Behavior of Human Abdominal Aorta', *Journal of Biomechanical Engineering*, 126(6), p. 815. doi: 10.1115/1.1824121.
- Georgakarakos, E., Ioannou, C. V., Kamarianakis, Y., Papaharilaou, Y., Kostas, T., Manousaki, E. and Katsamouris, A. N. (2010) 'The Role of Geometric Parameters in the Prediction of Abdominal Aortic Aneurysm Wall Stress', *European Journal of Vascular and Endovascular Surgery*, 39(1), pp. 42–48. doi: 10.1016/j.ejvs.2009.09.026.
- Gharib, M., Kremers, D., Koochesfahani, M. and Kemp, M. (2002) 'Leonardo's vision of flow visualization', *Experiments in Fluids*. Springer Verlag, 33(1), pp. 219–223. doi: 10.1007/s00348-002-0478-8.
- Gloviczki, P. (2002) 'Surgical Repair of Thoracoabdominal Aneurysms: Patient Selection, Techniques and Results', *Vascular*. SAGE Publications, 10(4), pp. 434–441. doi: 10.1177/096721090201000426.
- Goldfinger, J. Z., Halperin, J. L., Marin, M. L., Stewart, A. S., Eagle, K. A. and Fuster, V. (2014) 'Thoracic Aortic Aneurysm and Dissection', *Journal of the American*

- College of Cardiology. *Journal of the American College of Cardiology*, 64(16), pp. 1725–1739. doi: 10.1016/j.jacc.2014.08.025.
- Greenberg, R. K., Lu, Q., Roselli, E. E., Svensson, L. G., Moon, M. C., Hernandez, A. V., Dowdall, J., Cury, M., Francis, C., Pfaff, K., Clair, D. G., Ouriel, K. and Lytle, B. W. (2008) ‘Contemporary analysis of descending thoracic and thoracoabdominal aneurysm repair: a comparison of endovascular and open techniques.’, *Circulation*, 118(8), pp. 808–17. doi: 10.1161/CIRCULATIONAHA.108.769695.
- Grytsan, A., Watton, P. N. and Holzapfel, G. A. (2015) ‘A thick-walled fluid-solid-growth model of abdominal aortic aneurysm evolution: application to a patient-specific geometry.’, *Journal of biomechanical engineering. American Society of Mechanical Engineers*, 137(3), p. 031008. doi: 10.1115/1.4029279.
- Hallock, P. and Benson, I. C. (1937) ‘studies on the elastic properties of human isolated aorta.’, *The Journal of clinical investigation. American Society for Clinical Investigation*, 16(4), pp. 595–602. doi: 10.1172/JCI100886.
- Haskett, D., Johnson, G., Zhou, A., Utzinger, U. and Vande Geest, J. (2010) ‘Microstructural and biomechanical alterations of the human aorta as a function of age and location’, *Biomechanics and Modeling in Mechanobiology*, 9(6), pp. 725–736. doi: 10.1007/s10237-010-0209-7.
- Henry, M., Benjelloun, A. and Henry, I. (2015) ‘The Multilayer Flow Modulator stent for the treatment of arterial aneurysms concept – Indications–contraindications’, *Journal of Indian College of Cardiology*. doi: 10.1016/j.jicc.2015.11.005.
- Hope, M. D., Meadows, A. K., Hope, T. A., Ordovas, K. G., Saloner, D., Reddy, G. P., Alley, M. T. and Higgins, C. B. (2010) ‘Clinical evaluation of aortic coarctation with 4D flow MR imaging’, *Journal of Magnetic Resonance Imaging*, 31(3), pp. 711–718. doi: 10.1002/jmri.22083.
- Hope, T. A., Markl, M., Wigström, L., Alley, M. T., Miller, D. C. and Herfkens, R. J. (2007) ‘Comparison of flow patterns in ascending aortic aneurysms and volunteers using four-dimensional magnetic resonance velocity mapping.’, *Journal of magnetic resonance imaging: JMRI*, 26(6), pp. 1471–9. doi: 10.1002/jmri.21082.
- Hosoda, Y., Kawano, K., Yamasawa, F., Ishii, T., Shibata, T. and Inayama, S. (1984) ‘Age-Dependent Changes of Collagen and Elastin Content in Human Aorta and Pulmonary Artery’, *Angiology. Sage Publications*Sage CA: Thousand Oaks, CA, 35(10), pp. 615–621. doi: 10.1177/000331978403501001.
- Humphrey, J. D. (1995) ‘Mechanics of the arterial wall: Review and directions’, *Critical Reviews in Biomedical Engineering. Begell House Inc Publ*, pp. 1–162. doi: 10.1615/critrevbiomedeng.v23.i1-2.10.
- Humphrey, J. D. and Holzapfel, G. A. (2012) ‘Mechanics, mechanobiology, and modeling of human abdominal aorta and aneurysms.’, *Journal of biomechanics*, 45(5), pp. 805–14. doi: 10.1016/j.jbiomech.2011.11.021.
- Kato, Y., Matsumoto, T., Kumagai, K., Akimoto, H., Tabayashi, K. and Sato, M. (2000) ‘Development of a Simple Method to Construct Finite Element Models of Aortas from MRI Images and Its Application to Thoracic Aortic Aneurysm’,

- JSME international journal. Series C, Mechanical systems, machine elements and manufacturing. The Japan Society of Mechanical Engineers, 43(4), pp. 787–794. Available at: <http://ci.nii.ac.jp/naid/110004155767/en/> (Accessed: 22 May 2016).
- Kheirleiseid, E. A. H., Gardiner, R., Haider, S. N., Martin, Z., Colgan, M. P., O'Neill, S. M. and Madhavan, P. (2014) 'Endovascular repair of thoracoabdominal aortic aneurysm (TAAA): early experience.', *Irish journal of medical science*, 183(2), pp. 153–60. doi: 10.1007/s11845-013-0974-2.
- Kim, H. J., Vignon-Clementel, I. E., Figueroa, C. A., LaDisa, J. F., Jansen, K. E., Feinstein, J. A. and Taylor, C. A. (2009) 'On Coupling a Lumped Parameter Heart Model and a Three-Dimensional Finite Element Aorta Model', *Annals of Biomedical Engineering*. Springer US, 37(11), pp. 2153–2169. doi: 10.1007/s10439-009-9760-8.
- Lacolley, P., Regnault, V., Nicoletti, A., Li, Z. and Michel, J.-B. (2012) 'The vascular smooth muscle cell in arterial pathology: a cell that can take on multiple roles', *Cardiovascular Research*, 95(2), pp. 194–204. doi: 10.1093/cvr/cvs135.
- Laksari, K., Shahmirzadi, D., Acosta, C. J. and Konofagou, E. (2016) 'Energy-based constitutive modelling of local material properties of canine aortas', *Journal of the Royal Society, Interface*, 3(9), p. 160365. doi: 10.1098/rsos.160365.
- Langewouters, G. J., Wesseling, K. H. and Goedhard, W. J. (1984) 'The static elastic properties of 45 human thoracic and 20 abdominal aortas in vitro and the parameters of a new model.', *Journal of biomechanics*, 17(6), pp. 425–35. Available at: <http://www.ncbi.nlm.nih.gov/pubmed/6480618> (Accessed: 16 April 2019).
- Lowe, J. S. and Anderson, P. G. (2015) *Stevens & Lowe's Human Histology*.
- Maleux, G., Koolen, M. and Heye, S. (2009) 'Complications after endovascular aneurysm repair.', *Seminars in interventional radiology*. Thieme Medical Publishers, 26(1), pp. 3–9. doi: 10.1055/s-0029-1208377.
- Markl, M., Frydrychowicz, A., Kozerke, S., Hope, M. and Wieben, O. (2012) '4D flow MRI.', *Journal of magnetic resonance imaging: JMRI*, 36(5), pp. 1015–36. doi: 10.1002/jmri.23632.
- Markl, M., Schnell, S., Wu, C. and Rigsby, C. . (2016) 'Advanced flow MRI: emerging techniques and applications', *Clinical Radiology*.
- Martín, C. E., Forteza, A., Pérez, E., López, M. J., Centeno, J., Blázquez, J. A., de Diego, J., García, D. and Cortina, J. M. (2008) 'Predictors of Mortality and Reoperation in Acute Type-A Aortic Dissection Surgery: 18 Years of Experience', *Revista Española de Cardiología (English Edition)*. Elsevier, 61(10), pp. 1050–1060. doi: 10.1016/S1885-5857(09)60008-6.
- Martin, C., Sun, W. and Elefteriades, J. (2015) 'Patient-specific finite element analysis of ascending aorta aneurysms', *American Journal of Physiology-Heart and Circulatory Physiology*, 308(10), pp. H1306–H1316. doi: 10.1152/ajpheart.00908.2014.
- Martufi, G., Forneris, A., Appoo, J. J. and Di Martino, E. S. (2016) 'Is There a Role for Biomechanical Engineering in Helping to Elucidate the Risk Profile of the

- Thoracic Aorta?', *The Annals of thoracic surgery*, 101(1), pp. 390–8. doi: 10.1016/j.athoracsur.2015.07.028.
- Martufi, G., Forneris, A., Nobakht, S., Rinker, K. D., Moore, R. D. and Di Martino, E. S. (2018) 'Case Study: Intra-Patient Heterogeneity of Aneurysmal Tissue Properties', *Frontiers in Cardiovascular Medicine*. *Frontiers*, 5, p. 82. doi: 10.3389/fcvm.2018.00082.
- Martufi, G., Gasser, T. C., Appoo, J. J. and Di Martino, E. S. (2014) 'Mechano-biology in the thoracic aortic aneurysm: a review and case study.', *Biomechanics and modeling in mechanobiology*, 13(5), pp. 917–28. doi: 10.1007/s10237-014-0557-9.
- Martufi, G., Satriano, A., Moore, R. D., Vorp, D. A. and Di Martino, E. S. (2015) 'Local Quantification of Wall Thickness and Intraluminal Thrombus Offer Insight into the Mechanical Properties of the Aneurysmal Aorta.', *Annals of biomedical engineering*, 43(8), pp. 1759–71. doi: 10.1007/s10439-014-1222-2.
- McGloughlin, T. M. and Doyle, B. J. (2010) 'New approaches to abdominal aortic aneurysm rupture risk assessment: engineering insights with clinical gain.', *Arteriosclerosis, thrombosis, and vascular biology*, 30(9), pp. 1687–94. doi: 10.1161/ATVBAHA.110.204529.
- Milewicz, D. M., Trybus, K. M., Guo, D.-C., Sweeney, H. L., Regalado, E., Kamm, K. and Stull, J. T. (2017) 'Altered Smooth Muscle Cell Force Generation as a Driver of Thoracic Aortic Aneurysms and Dissections.', *Arteriosclerosis, thrombosis, and vascular biology*. American Heart Association, Inc., 37(1), pp. 26–34. doi: 10.1161/ATVBAHA.116.303229.
- Nauta, F. J. H., Kamman, A. V, Ibrahim, E.-S. H., Agarwal, P. P., Yang, B., Kim, K., Williams, D. M., van Herwaarden, J. A., Moll, F. L., Eagle, K. A., Trimarchi, S., Patel, H. J. and Figueroa, C. A. (2016) 'Assessment of Cardiovascular Remodelling following Endovascular aortic repair through imaging and computation: the CORE prospective observational cohort study protocol.', *BMJ open*. BMJ Publishing Group, 6(11), p. e012270. doi: 10.1136/bmjopen-2016-012270.
- Nayeemuddin, M., Pherwani, A. D. and Asquith, J. R. (2012) 'Imaging and management of complications of open surgical repair of abdominal aortic aneurysms', *Clinical Radiology*. W.B. Saunders, 67(8), pp. 802–814. doi: 10.1016/J.CRAD.2011.12.005.
- O'Connell, M. K., Murthy, S., Phan, S., Xu, C., Buchanan, J., Spilker, R., Dalman, R. L., Zarins, C. K., Denk, W. and Taylor, C. A. (2008) 'The three-dimensional micro- and nanostructure of the aortic medial lamellar unit measured using 3D confocal and electron microscopy imaging', *Matrix Biology*. Elsevier, 27(3), pp. 171–181. doi: 10.1016/J.MATBIO.2007.10.008.
- van Ooij, P., Potters, W. V., Collins, J., Carr, M., Carr, J., Malaisrie, S. C., Fedak, P. W. M., McCarthy, P. M., Markl, M. and Barker, A. J. (2015) 'Characterization of Abnormal Wall Shear Stress Using 4D Flow MRI in Human Bicuspid Aortopathy', *Annals of Biomedical Engineering*. Kluwer Academic Publishers, 43(6), pp. 1385–1397. doi: 10.1007/s10439-014-1092-7.

- Orr, N., Minion, D. and Bobadilla, J. L. (2014) ‘Thoracoabdominal aortic aneurysm repair: current endovascular perspectives.’, *Vascular health and risk management*, 10, pp. 493–505. doi: 10.2147/VHRM.S46452.
- Ovalle, W. K., Nahirney, P. C. and Netter, F. H. (Frank H. (2013) *Netter’s essential histology*. Elsevier/Saunders.
- Pasta, S., Cho, J.-S., Dur, O., Pekkan, K. and Vorp, D. A. (2013) ‘Computer modeling for the prediction of thoracic aortic stent graft collapse’, *Journal of Vascular Surgery*. Mosby, 57(5), pp. 1353–1361. doi: 10.1016/J.JVS.2012.09.063.
- Patel, R., Sweeting, M. J., Powell, J. T. and Greenhalgh, R. M. (2016) ‘Endovascular versus open repair of abdominal aortic aneurysm in 15-years’ follow-up of the UK endovascular aneurysm repair trial 1 (EVAR trial 1): a randomised controlled trial’, *The Lancet*. Elsevier, 388(10058), pp. 2366–2374. doi: 10.1016/S0140-6736(16)31135-7.
- Pedley, T. J. (2003) ‘Arterial and Venous Fluid Dynamics’, in *Cardiovascular Fluid Mechanics*. Vienna: Springer Vienna, pp. 1–72. doi: 10.1007/978-3-7091-2542-7\_1.
- Perrin, D. and Avril, S. (2015) ‘Patient-specific numerical simulation of stent-graft deployment: Validation on three clinical cases’, *Journal of Biomechanics*, 48, pp. 1868–1875.
- Pierce, D. M., Maier, F., Weisbecker, H., Viertler, C., Verbrugge, P., Famaey, N., Fourneau, I., Herijgers, P. and Holzapfel, G. A. (2015) ‘Human thoracic and abdominal aortic aneurysmal tissues: Damage experiments, statistical analysis and constitutive modeling’, *Journal of the Mechanical Behavior of Biomedical Materials*, 41, pp. 92–107. doi: 10.1016/j.jmbbm.2014.10.003.
- Pijewska, E., Gorczynska, I. and Szkulmowski, M. (2019) ‘Computationally effective 2D and 3D fast phase unwrapping algorithms and their applications to Doppler optical coherence tomography’, *Biomedical Optics Express*. The Optical Society, 10(3), p. 1365. doi: 10.1364/boe.10.001365.
- Plonek, T., Zak, M., Burzynska, K., Rylski, B., Gozdzik, A., Kustrzycki, W., Beyersdorf, F., Jasinski, M. and Filipiak, J. (2017) ‘The combined impact of mechanical factors on the wall stress of the human ascending aorta – a finite elements study’, *BMC Cardiovascular Disorders*. BioMed Central, 17(1), p. 297. doi: 10.1186/s12872-017-0733-9.
- Raut, S. S., Chandra, S., Shum, J. and Finol, E. A. (2013) ‘The role of geometric and biomechanical factors in abdominal aortic aneurysm rupture risk assessment.’, *Annals of biomedical engineering*, 41(7), pp. 1459–77. doi: 10.1007/s10439-013-0786-6.
- Rezakhaniha, R., Agianniotis, · A, Schrauwen, · J T C, Griffa, · A, Sage, · D, Bouten, · C V C, Van De Vosse, · F N, Unser, · M, Stergiopoulos, · N, Schrauwen, J. T. C., Griffa, A., Sage, D., Bouten, C. V. C. and Agianniotis, A. (2012) ‘Experimental investigation of collagen waviness and orientation in the arterial adventitia using confocal laser scanning microscopy’, *Biomech Model Mechanobiol*, 11, pp. 461–473. doi: 10.1007/s10237-011-0325-z.

- Rhodin, J. A. G. (1980) 'Architecture of the Vessel Wall', in *Comprehensive Physiology*. Hoboken, NJ, USA: John Wiley & Sons, Inc., pp. 1–31. doi: 10.1002/cphy.cp020201.
- Riambau, V., Bockler, D., Brunkwall, J., Cao, P., Chiesa, R., Coppi, G., Czerny, M., Fraedrich, G., Haulon, S., Jacobs, M. J., Lachat, M. L., Moll, F. L., Setacci, C., Taylor, P. R., Thompson, M., Trimarchi, S., Verhagen, H. J., Verhoeven, E. L., Committee, E. G., Kolh, P., de Borst, G. J., Chakf?, N., Debus, E. S., Hinchliffe, R. J., Kakkos, S., Koncar, I., Lindholt, J. S., Vega de Ceniga, M., Vermassen, F., Verzini, F., Reviewers, D., Kolh, P., Black, J. H., Busund, R., Bj?rck, M., Dake, M., Dick, F., Eggebrecht, H., Evangelista, A., Grabenw?ger, M., Milner, R., Naylor, A. R., Ricco, J.-B., Rousseau, H. and Schmidli, J. (2017) 'Management of Descending Thoracic Aorta Diseases: Clinical Practice Guidelines of the European Society for Vascular Surgery (ESVS)', *European Journal of Vascular and Endovascular Surgery*, 53(1), pp. 4–52. doi: 10.1016/j.ejvs.2016.06.005.
- Rigberg, D. A., McGory, M. L., Zingmond, D. S., Maggard, M. A., Agustin, M., Lawrence, P. F. and Ko, C. Y. (2006) 'Thirty-day mortality statistics underestimate the risk of repair of thoracoabdominal aortic aneurysms: a statewide experience.', *Journal of vascular surgery*, 43(2), p. 217–22; discussion 223. doi: 10.1016/j.jvs.2005.10.070.
- Riveros, F., Chandra, S., Finol, E. A., Gasser, T. C. and Rodriguez, J. F. (2013) 'A pull-back algorithm to determine the unloaded vascular geometry in anisotropic hyperelastic AAA passive mechanics.', *Annals of biomedical engineering*, 41(4), pp. 694–708. doi: 10.1007/s10439-012-0712-3.
- Roselli, E. E., Greenberg, R. K., Pfaff, K., Francis, C., Svensson, L. G. and Lytle, B. W. (2007) 'Endovascular treatment of thoracoabdominal aortic aneurysms.', *The Journal of thoracic and cardiovascular surgery*, 133(6), pp. 1474–82. doi: 10.1016/j.jtcvs.2006.09.118.
- Ross, M. H. and Pawlina, W. (2015) *Histology: a text and atlas: with correlated cell and molecular biology*. Wolters Kluwer.
- Ross, M. H., Pawlina, W. and Barnash, T. A. (2009) 'Atlas of Descriptive Histology', *Clinical Anatomy*. Wiley-Blackwell, 23(1), p. NA-NA. doi: 10.1002/ca.20891.
- Ross, R. (1971) 'The smooth muscle cell. II. Growth of smooth muscle in culture and formation of elastic fibers.', *The Journal of cell biology*. The Rockefeller University Press, 50(1), pp. 172–86. Available at: <http://www.ncbi.nlm.nih.gov/pubmed/4327464> (Accessed: 28 May 2018).
- Roy, D., Holzapfel, G. A., Kauffmann, C. and Soulez, G. (2014) 'Finite element analysis of abdominal aortic aneurysms: geometrical and structural reconstruction with application of an anisotropic material model', *IMA Journal of Applied Mathematics*. Oxford University Press, 79(5), pp. 1011–1026. doi: 10.1093/imamat/hxu037.
- Ruddy, J. M., Jones, J. A., Spinale, F. G. and Ikonomidis, J. S. (2008) 'Regional heterogeneity within the aorta: relevance to aneurysm disease.', *The Journal of thoracic and cardiovascular surgery*, 136(5), pp. 1123–30. doi: 10.1016/j.jtcvs.2008.06.027.

- Saey, V., Famaey, N., Smoljkic, M., Claeys, E., Van Loon, G., Ducatelle, R., Ploeg, M., Delesalle, C., Gröne, A., Duchateau, L. and Chiers, K. (2015) 'Biomechanical and biochemical properties of the thoracic aorta in warmblood horses, Friesian horses, and Friesians with aortic rupture', *BMC Veterinary Research*, 11(285). doi: 10.1186/s12917-015-0597-0.
- Schoenwolf, G. C., Bleyl, S. B., Brauer, P. R. and Francis-West, P. H. (2009) *Larsen's Human Embryology*. Fifth.
- Schriefl, A. J., Zeindlinger, G., Pierce, D. M., Regitnig, P. and Holzapfel, G. A. (2012) 'Determination of the layer-specific distributed collagen fibre orientations in human thoracic and abdominal aortas and common iliac arteries.', *Journal of the Royal Society, Interface / the Royal Society*, 9(71), pp. 1275–86. doi: 10.1098/rsif.2011.0727.
- Shadwick, R. E. (1999) 'Mechanical design in arteries', *The Journal of Experimental Biology*, 202, pp. 3305–3313. Available at: <http://jeb.biologists.org/content/jexbio/202/23/3305.full.pdf> (Accessed: 14 June 2018).
- Sherif, H. M. F. (2014) 'Heterogeneity in the Segmental Development of the Aortic Tree: Impact on Management of Genetically Triggered Aortic Aneurysms.', *Aorta (Stamford, Conn.)*. Science International Corporation, 2(5), pp. 186–95. doi: 10.12945/j.aorta.2014.14-032.
- Singh, M. and Makaroun, M. S. (2014) 'Thoracic and Thoracoabdominal Aneurysms', in *Rutherford's Vascular Surgery*, Eighth Edition.
- Sokolis, D. P., Savva, G. D., Papadodima, S. A. and Kourkoulis, S. K. (2017) 'Regional distribution of circumferential residual strains in the human aorta according to age and gender', *Journal of the Mechanical Behavior of Biomedical Materials*, 67, pp. 87–100. doi: 10.1016/j.jmbbm.2016.12.003.
- Speelman, L., Akyildiz, A. C., den Adel, B., Wentzel, J. J., van der Steen, A. F. W., Virmani, R., van der Weerd, L., Jukema, J. W., Poelmann, R. E., van Brummelen, E. H. and Gijzen, F. J. H. (2011) 'Initial stress in biomechanical models of atherosclerotic plaques', *Journal of Biomechanics*, 44(13), pp. 2376–2382. doi: 10.1016/j.jbiomech.2011.07.004.
- Stankovic, Z., Allen, B. D., Garcia, J., Jarvis, K. B. and Markl, M. (2014) '4D flow imaging with MRI.', *Cardiovascular diagnosis and therapy*, 4(2), pp. 173–92. doi: 10.3978/j.issn.2223-3652.2014.01.02.
- Sugita, S. and Matsumoto, · Takeo (2018) 'Local distribution of collagen fibers determines crack initiation site and its propagation direction during aortic rupture', *Biomech Model Mechanobiol*, 17, pp. 577–587. doi: 10.1007/s10237-017-0979-2.
- Trelstad, R. L. (1974) 'Human aorta collagens: Evidence for three distinct species', *Biochemical and Biophysical Research Communications*. Academic Press, 57(3), pp. 717–725. doi: 10.1016/0006-291X(74)90605-6.
- Vaishnav, R. N. and Vossoughi, J. (1983) 'ESTIMATION OF RESIDUAL STRAINS IN AORTIC SEGMENTS', *Biomedical Engineering II*. Pergamon, pp. 330–333. doi: 10.1016/B978-0-08-030145-7.50078-7.

- Vasava, P., Jalali, P., Dabagh, M. and Kolari, P. J. (2012) 'Finite Element Modelling of Pulsatile Blood Flow in Idealized Model of Human Aortic Arch: Study of Hypotension and Hypertension', *Computational and Mathematical Methods in Medicine*. Hindawi, 2012, pp. 1–14. doi: 10.1155/2012/861837.
- Verhoeven, E. L., Kapma, M. R., Groen, H., Tielliu, I. F., Zeebregts, C. J., Bekkema, F. and van den Dungen, J. J. (2008) 'Mortality of ruptured abdominal aortic aneurysm treated with open or endovascular repair', *Journal of Vascular Surgery*. Elsevier, 48(6), pp. 1396–1400. doi: 10.1016/j.jvs.2008.07.054.
- Weisbecker, H., Pierce, D. M., Regitnig, P. and Holzapfel, G. A. (2012) 'Layer-specific damage experiments and modeling of human thoracic and abdominal aortas with non-atherosclerotic intimal thickening.', *Journal of Mechanical Behaviour of Biomedical Materials*.
- Wolinsky, H. and Glagov, S. (1964) 'Structural Basis for the Static Mechanical Properties of the Aortic Media', *Circulation Research*. Lippincott Williams & Wilkins, 14(5), pp. 400–413. doi: 10.1161/01.RES.14.5.400.
- Wu, C.-F., Liu, P.-Y., Wu, T.-J., Hung, Y., Yang, S.-P. and Lin, G.-M. (2015) 'Therapeutic modification of arterial stiffness: An update and comprehensive review.', *World journal of cardiology*. Baishideng Publishing Group Inc, 7(11), pp. 742–53. doi: 10.4330/wjc.v7.i11.742.
- Xiao, W., Jia, Z., Zhang, Q., Wei, C., Wang, H. and Wu, Y. (2015) 'Inflammation and oxidative stress, rather than hypoxia, are predominant factors promoting angiogenesis in the initial phases of atherosclerosis', *Molecular Medicine Reports*. Spandidos Publications, 12(3), pp. 3315–3322. doi: 10.3892/mmr.2015.3800.
- Xu, J. and Shi, G.-P. (2014) 'Vascular wall extracellular matrix proteins and vascular diseases.', *Biochimica et biophysica acta*. NIH Public Access, 1842(11), pp. 2106–2119. doi: 10.1016/j.bbadis.2014.07.008.
- Young, B. (Pathologist), O'Dowd, G. and Woodford, P. (2013) *Wheater's functional histology : a text and colour atlas*.

# CHAPTER 3

## THEORY

### 3.1 Continuum Mechanics

#### 3.1.1 Deformation and motion

The fundamental principles of continuum mechanics that are relevant to this work are presented here. Figure 3.1 shows an arbitrary body in space,  $\Omega_0$ , which undergoes kinematic deformation  $\chi$  to become  $\Omega_c$ . An infinitesimal material “fiber” is described by  $dx$  in the reference configuration and by  $dy$  in the current configuration.

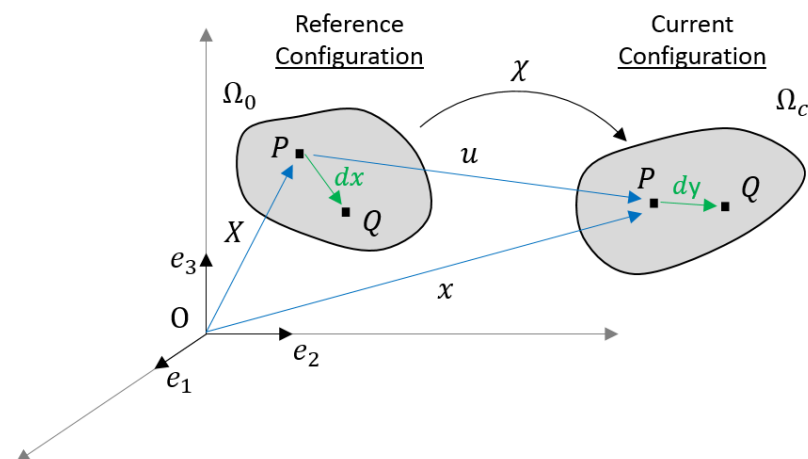


Figure 3.1: Schematic of a body undergoing motion from the reference to current configuration.

The motion of  $\Omega_0$  to  $\Omega_c$  is described by the deformation gradient,  $\mathbf{F}$ , where

$$\mathbf{F} = \frac{\partial \mathbf{y}}{\partial \mathbf{x}} \quad (3.01)$$

where the determinant of the deformation gradient is also known as the Jacobian ( $J$ ), which denotes the ratio of volume change from the reference to the current configuration.

### 3.1.2 Strain and strain rate measures

The Green strain tensor depicts strain with respect to the reference (Lagrangian) configuration and is defined as

$$\mathbf{E} = \frac{1}{2}(\mathbf{F}^T \mathbf{F} - \mathbf{I}) \quad (3.02)$$

where  $\mathbf{F}^T$  is the transpose of  $\mathbf{F}$  and  $\mathbf{I}$  is the identity tensor. The Eulerian strain tensor depicts strain with respect to the current configuration and is defined as

$$\mathbf{e} = \frac{1}{2}(\mathbf{I} - \mathbf{F}^{-T} \mathbf{F}^{-1}) \quad (3.03)$$

The left and right Cauchy-Green deformation tensors  $\mathbf{B}$  and  $\mathbf{C}$  can be obtained from the deformation gradient and are defined according to

$$\mathbf{B} = \mathbf{F} \mathbf{F}^T \quad (3.04)$$

$$\mathbf{C} = \mathbf{F}^T \mathbf{F} \quad (3.05)$$

Decomposition of  $\mathbf{F}$  into an orthogonal rotation tensor  $\mathbf{R}$ , and symmetric left (spatial) and right (material) stretch tensors,  $\mathbf{V}$  and  $\mathbf{U}$ , gives

$$\mathbf{F} = \mathbf{R} \mathbf{U} = \mathbf{V} \mathbf{R} \quad (3.06)$$

which allows stretching followed by rotation ( $\mathbf{F} = \mathbf{V} \mathbf{R}$ ) or vice-versa ( $\mathbf{F} = \mathbf{R} \mathbf{U}$ ) which may be related to the left and right Cauchy-Green tensors via

$$\mathbf{V}^2 = \mathbf{B} \quad (3.07)$$

$$\mathbf{U}^2 = \mathbf{C} \quad (3.08)$$

Defining strain-energy density functions using strain invariants is useful. The first three invariants of  $\mathbf{B}$  and  $\mathbf{C}$ , are equivalent for both of the tensors and are defined as follows

$$I_1 = \text{tr}(\mathbf{C}) = \lambda_1^2 + \lambda_2^2 + \lambda_3^2 \quad (3.09)$$

$$I_2 = \frac{1}{2} [I_1^2 - \text{tr}(\mathbf{C}^2)] = \lambda_1^2 \lambda_2^2 + \lambda_2^2 \lambda_3^2 + \lambda_1^2 \lambda_3^2 \quad (3.10)$$

$$I_3 = \det(\mathbf{C}) = [\det(\mathbf{F})]^2 = \lambda_1^2 \lambda_2^2 \lambda_3^2 \quad (3.11)$$

### 3.1.3 Stress measures

Taking a slice through a body in the current configuration allows definition of a traction tensor  $\mathbf{t}$  and a normal vector to the surface of the slice,  $\tilde{\mathbf{n}}$ . At a point  $P$ , the Cauchy stress  $\boldsymbol{\sigma}$  is a second order symmetric tensor denoting the force per unit surface area  $dS$  given by:

$$\mathbf{t} = \boldsymbol{\sigma} \tilde{\mathbf{n}} \quad (3.12)$$

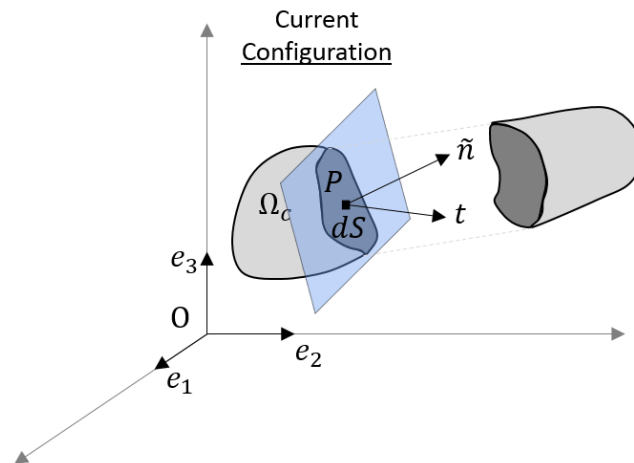


Figure 3.2: Schematic of the traction vector  $\mathbf{t}$  on an internal surface of a body cut by a plane with normal  $\tilde{\mathbf{n}}$  in the current configuration.

The Kirchhoff stress  $\boldsymbol{\tau}$  is defined as:

$$\boldsymbol{\tau} = \mathbf{J} \boldsymbol{\sigma} \quad (3.13)$$

Such that for an incompressible material, the Kirchhoff stress equals the Cauchy stress. The First Piola-Kirchhoff stress  $\mathbf{P}$ , is defined as the force per unit area in the undeformed configuration and is a non-symmetric tensor. Nanson's formula may be used to map the Piola-Kirchhoff stress in the reference configuration to the Cauchy stress in the current configuration

$$\mathbf{P} = \mathbf{J}\boldsymbol{\sigma}\mathbf{F}^{-\mathbf{T}} \quad (3.14)$$

The Second Piola-Kirchhoff stress  $\mathbf{S}$ , is symmetric and can also be expressed in terms of the Cauchy or First Piola-Kirchhoff stress as:

$$\mathbf{S} = \mathbf{J}\mathbf{F}^{-1}\boldsymbol{\sigma}\mathbf{F}^{-\mathbf{T}} \quad ; \quad \mathbf{S} = \mathbf{P}\mathbf{F}^{\mathbf{T}} \quad (3.15a, 3.15b)$$

### 3.1.4 Forms of Strain Energy Density Functions for Soft Tissue

Hyperelasticity refers to a constitutive material response that is derivable from an elastic strain energy potential  $\Psi$ . It is particularly useful for describing materials that undergo large deformation and is hence often used in the realm of soft biological tissue behaviour. In the case of material isotropy, the strain energy during deformation is a function of the first three principal invariants ( $I_1, I_2, I_3$ )

$$\Psi(\mathbf{C}) = \Psi(I_1, I_2, I_3) \quad (3.16)$$

Assuming incompressibility yields the deformation of the system to be purely isochoric and hence there is no volume change, ensuring that  $I_3 \equiv \mathbf{J} \equiv 1$  and so the strain energy becomes a function of  $I_1, I_2$

$$\Psi(\mathbf{C}) = \Psi(I_1, I_2) \quad (3.17)$$

An example of an incompressible isotropic strain energy function is the Ogden model where:

$$\Psi = \sum_{i=1}^N \frac{2\mu_i}{\alpha_i^2} (\bar{\lambda}_1^{\alpha_i} + \bar{\lambda}_2^{\alpha_i} + \bar{\lambda}_3^{\alpha_i} - 3)^i \quad (3.18)$$

For all incompressible hyperelastic materials

$$\boldsymbol{\sigma} = -p\mathbf{I} + 2W_1\mathbf{B} - 2W_2\mathbf{B}^{-1} \quad (3.19)$$

where  $W_1 = \left(\frac{\partial\Psi}{\partial I_1}\right)$ ,  $W_2 = \left(\frac{\partial\Psi}{\partial I_2}\right)$  and  $p$  is the Lagrangian multiplier. However,  $p$  is unknown and can only be determined by imposing equilibrium and boundary conditions. Consider a cube made of isotropic hyperelastic material under uniaxial tension in the  $z$  direction, where the  $x$  and  $y$  faces are free to contract in response to

the load. The stress on such faces must be zero, hence it is trivial to solve for  $p$  the Lagrange multiplier.

Undertaking a simple tension experiment of an incompressible isotropic hyperelastic material ensures, on the faces free of prescribed deformation, that the stretch ( $\lambda_{33} = \lambda_{22} = \lambda_{11}^{-\frac{1}{2}}$ ) and that the boundaries are stress-free, i.e. ( $\sigma_{33} = \sigma_{22} = 0$ ). Imposing equilibrium on these boundaries allows us to calculate the Lagrangian multiplier ( $p$ ) through:

$$\sigma_{33} = \sigma_{22} = -pI + 2W_1\lambda^{-1} - 2W_2\lambda = 0 \quad (3.20)$$

$$p = 2W_1\lambda^{-1} - 2W_2\lambda \quad (3.21)$$

Substituting  $p$  into equation 3.19 gives Cauchy stress along the direction of loading ( $\sigma_{11}$ )

$$\sigma_{11} = -(2W_1\lambda^{-1} - 2W_2\lambda)I + 2W_1\lambda^2 - 2W_2\lambda^{-2} \quad (3.22)$$

Incompressible forms of isotropic strain energy density functions such as the Ogden model have been used extensively in the literature to model soft biological tissues including arteries (Ogden, 2003), skeletal muscle tissue (Bosboom *et al.*, 2001), skin (Groves *et al.*, (2012), and brain tissue (Garcia-Gonzalez *et al.*, 2018). In truth, biological tissue is not fully incompressible (Nolan and McGarry, 2016; Wang and Liu, 2018) and so some form of compressibility is required in order to accurately model the material behaviour. When  $\det(\mathbf{F}) \neq 1$ , the deformation of the system causes a volumetric change and so the strain energy becomes a function of both the shear and the bulk modulus of the material. As materials behave quite differently in bulk and shear it is useful to split the deformation locally into an isochoric and volumetric part. Multiplicative decomposition of the deformation gradient ( $\mathbf{F}$ ) comes in the form

$$\mathbf{F} = J^{\frac{1}{3}}\bar{\mathbf{F}} \quad (3.23)$$

while a decoupled representation of the strain energy function ( $\Psi$ ) and Cauchy stress ( $\boldsymbol{\sigma}$ ) is given by

$$\Psi(\mathbf{C}) = \Psi_{\text{vol}}(J) + \Psi_{\text{iso}}(\bar{\mathbf{C}}) \quad (3.24)$$

$$\boldsymbol{\sigma} = 2J^{-1}\mathbf{b} \frac{\delta\Psi}{\delta\mathbf{b}} = \boldsymbol{\sigma}_{\text{vol}} + \boldsymbol{\sigma}_{\text{iso}} \quad (3.25)$$

where  $\mathbf{b} = \mathbf{F}\mathbf{F}^T$ . The compressible form of the Ogden strain energy function is therefore

$$\Psi = \sum_{i=1}^N \frac{2\mu_i}{\alpha_i^2} (\bar{\lambda}_1^{\alpha_i} + \bar{\lambda}_2^{\alpha_i} + \bar{\lambda}_3^{\alpha_i} - 3)^i + \sum_{i=1}^N \frac{1}{D_i} (J - 1)^{2i} \quad (3.26)$$

The mechanical response of arterial tissue is also directionally variable (anisotropic) due to the presence of collagen fibers (Figure 3.3) and so must be modelled using an appropriate strain energy function that takes material anisotropy into account.

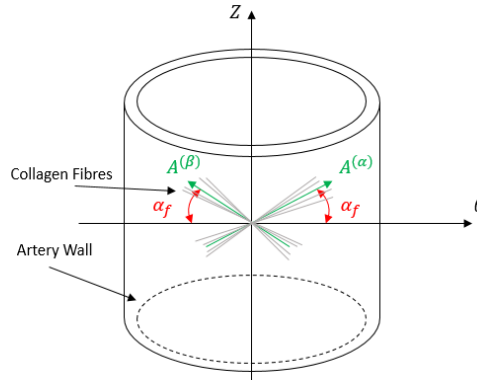


**Figure 3.3:** Schematic of a typical artery with dispersed collagen fibers with mean fiber directions described by  $A^{(\alpha)}$  and  $A^{(\beta)}$ . When fiber symmetry is assumed the mean fiber vector acts at an angle of  $\pm\alpha_f$  to the circumferential direction ( $\theta$ ) of the vessel.

The Holzapfel-Gasser-Ogden (HGO) model proposed in 2000 provides a means of modelling *incompressible* arterial tissue as an anisotropic hyperelastic material, whereby the strain energy is additively split into volumetric, isochoric isotropic and isochoric anisotropic terms

$$\Psi(\mathbf{C}, \mathbf{a}_{04}, \mathbf{a}_{06}) = \Psi_{\text{vol}}(J) + \bar{\Psi}_{\text{iso}}(\bar{\mathbf{C}}) + \bar{\Psi}_{\text{aniso}}(\bar{\mathbf{C}}, \mathbf{a}_{04}, \mathbf{a}_{06}) \quad (3.27)$$

where  $\bar{\mathbf{C}} = J^{-\frac{2}{3}}\mathbf{C}$  is the isochoric right Cauchy-Green deformation tensor. In numerical implementations of the model such as Abaqus, ADINA, etc, the volumetric and isochoric isotropic terms are represented by the Neo-Hookean hyperelastic free energy

$$\Psi_{\text{vol}}(J) = \frac{1}{2} \kappa_0 (J - 1)^2 \quad (3.28)$$

$$\Psi_{\text{iso}}(J) = \frac{1}{2} \mu_0 (\bar{I}_1 - 3) \quad (3.29)$$

Where  $\kappa_0$  and  $\mu_0$  are the bulk and shear moduli respectively. The isochoric anisotropic free-energy term is prescribed as

$$\bar{\Psi}_{\text{aniso}}(\bar{\mathbf{C}}, \mathbf{a}_{04}, \mathbf{a}_{06}) = \frac{k_1}{2k_2} \sum_{i=4,6} \{\exp[k_2(\bar{I}_i - 1)^2] - 1\} \quad (3.30)$$

Where  $k_1$  and  $k_2$  are positive material constants that may be determined from experiments. For the Cauchy stress we also have

$$\boldsymbol{\sigma} = \boldsymbol{\sigma}_{\text{vol}} + \bar{\boldsymbol{\sigma}}_{\text{iso}} + \bar{\boldsymbol{\sigma}}_{\text{aniso}} \quad (3.31)$$

For *compressible* anisotropic hyperelastic tissue, the inbuilt ABAQUS HGO model is often used, whereby the bulk modulus term is used to introduce slight compressibility into the model. The issue pertaining to this however exists in the form that the anisotropic energy described above is isochoric and so with slight compressibility the full representation of the anisotropic contributions to the stress tensor is lost. To overcome this, the Modified Anisotropic (MA) model can be used to model arterial tissue where the total strain energy is a function of the full right Cauchy-Green tensor  $\mathbf{C}$ , the anisotropic strain energy is a function of the full form of  $I_4$  and  $I_6$  invariants and the anisotropic stress component is a function of the total and not isochoric Cauchy stress

$$\Psi(\mathbf{C}, \mathbf{a}_{04}, \mathbf{a}_{06}) = \Psi_{\text{vol}}(J) + \bar{\Psi}_{\text{iso}}(\bar{\mathbf{C}}) + \bar{\Psi}_{\text{aniso}}(\mathbf{C}, \mathbf{a}_{04}, \mathbf{a}_{06}) \quad (3.32)$$

$$\bar{\Psi}_{\text{aniso}}(\bar{\mathbf{C}}, \mathbf{a}_{04}, \mathbf{a}_{06}) = \frac{k_1}{2k_2} \sum_{i=4,6} \{\exp[k_2(I_i - 1)^2] - 1\} \quad (3.33)$$

$$\boldsymbol{\sigma} = \boldsymbol{\sigma}_{\text{vol}} + \bar{\boldsymbol{\sigma}}_{\text{iso}} + \boldsymbol{\sigma}_{\text{aniso}} \quad (3.34)$$

Anisotropic formulations such as the HGO have been used in numerous soft tissue applications including arteries (Roy *et al.*, 2014; Gajewski *et al.*, 2013; Famaey *et al.*, 2012; Tasca *et al.*, 2017), brain tissue (Madouh & Ramesh, 2019), intervertebral disks (Shahraki *et al.*, 2015), cornea (Pandolfi & Holzapfel (2008), skin (Ní Annaidh *et al.*, 2012), ligaments and tendons (Shearer, 2015).

Evidently it is trivial to calculate the stress along the direction of loading for a uniaxial tension experiment as described above in a single representative cube element. The geometries, loads and boundary conditions however used in the following work are far more complex and so we rely upon the Finite Element Method for calculation of the Cauchy stress going forward. For further detail on the principles of continuum

mechanics and hyperelasticity the reader is referred to Holzapfel, (2000), Ogden, (1997), Spencer (2004), Cowin (2013), and Eisenberg & Malvern (1973).

### 3.2 Finite Element Method (FEM)

The numerical solution of continuum mechanics problems in this work is achieved using the FEM, implemented through the commercially available ABAQUS FE platform (DS SIMULUA, USA). In the FEM, the body of interest is divided or discretized into volumes known as *elements* that are connected via points or *nodes*.

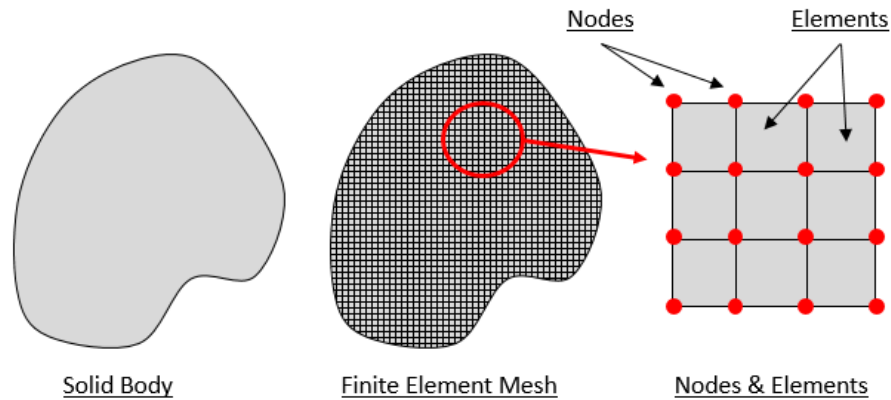


**Figure 3.4:** The finite element method entails discretizing the body into a known number of elements, where each element is connected to its neighbours by nodes.

The application of loads and boundary conditions to the system facilitates the calculation of stress and strain in each element. Energy going into the structure due to deformation is stored in the body in the form of strain energy, due to the principle of conservation of energy. The FEM is built upon the Principle of Virtual Work (PVW) which enforces such conservation through (presented in Voigt notation)

$$\int_V \delta \boldsymbol{\varepsilon}^T \boldsymbol{\sigma} dV = \int_S \delta \mathbf{u}^T \mathbf{t} dS \quad (3.35)$$

Where  $V$  is the reference volume on which equilibrium is enforced, bounded by surface  $S$ ;  $\boldsymbol{\sigma}$  and  $\mathbf{t}$  are the stress and surface traction vectors respectively; and  $\delta \boldsymbol{\varepsilon}$  and  $\delta \mathbf{u}$  are the virtual strain and virtual displacement vectors such that

$$\delta \mathbf{u} = \hat{\mathbf{N}}_e \delta \mathbf{u}_e \quad (3.36)$$

$$\delta \boldsymbol{\varepsilon} = \hat{\mathbf{B}}_e \delta \mathbf{u}_e \quad (3.37)$$

where  $\widehat{\mathbf{N}}_e$  is the global shape function matrix;  $\mathbf{u}_e$  is a vector of the displacement of each node that bounds the element; and  $\widehat{\mathbf{B}}_e$  is the shape function gradient. Substituting these into our equation for PVW gives

$$\sum_e \int_V \delta \mathbf{u}_e^T \widehat{\mathbf{B}}_e^T \boldsymbol{\sigma}(\mathbf{u}_e) dV = \sum_e \int_{S_e} \delta \mathbf{u}_e^T \widehat{\mathbf{N}}_e^T \mathbf{t} dS \quad (3.38)$$

The FEM requires constitutive equations to be calculated for each element which are subsequently assembled to form a system of algebraic equations that describe the behaviour of the body as a whole. Summing over each element in the mesh and removing arbitrary virtual quantities yields the global expression

$$\delta \mathbf{u}^T \left( \int_V \widehat{\mathbf{B}}^T \boldsymbol{\sigma}(\mathbf{u}) dV - \int_S \widehat{\mathbf{N}}^T \mathbf{t} dS \right) = 0 \quad (3.39)$$

$$\int_V \widehat{\mathbf{B}}^T \boldsymbol{\sigma}(\mathbf{u}) dV - \int_S \widehat{\mathbf{N}}^T \mathbf{t} dS = 0 \quad (3.40)$$

The out of balance force vector  $\mathbf{G}$  can be calculated as the difference between internal and external forces acting on the system

$$\mathbf{G}(\mathbf{u}) = \int_V \mathbf{B}^T \boldsymbol{\sigma}(\mathbf{u}) dV - \int_S \mathbf{N}^T \mathbf{t} dS \quad (3.41)$$

Following each increment of displacement, the nonlinear set of equations above must be solved for convergence to ensure an equilibrium stress state in the body, through the residual force vector such that

$$\mathbf{G}(\mathbf{u}) = 0 \quad (3.42)$$

The solution of  $\mathbf{G} = 0$  is usually obtained by incremental methods, whereby an increment in time from  $(t \rightarrow t + \Delta t)$  is solved using either implicit or explicit methods. All simulations in this thesis use the implicit integration scheme.

### 3.2.1 Implicit Integration Scheme

Once the problem being addressed involves non-linearities (material or geometrical), i.e. the stiffness matrix,  $\mathbf{K}$  and/or external loads,  $\mathbf{F}_{\text{ext}}$  are varying, an incremental approach is required to break the system into a series of linear problems in order to achieve a solution. In the following work, quasi-static problems are solved using the Abaqus/Standard Implicit solver. Boundary conditions i.e. force, displacement, pressure etc. are generally applied to the system through the use of a time step where ( $t \in \{0, \dots, 1\}$ ). Consider a state where we have solved for time  $t$  and wish to solve for time  $t + \Delta t$ , we require that

$$\mathbf{G}(\mathbf{u}^{t+\Delta t}) = 0 \quad (3.43)$$

For static structural analysis a form of the Newton-Raphson iterative solution solves for the condition above (Figure 3.5). With each incremental step in time, the algorithm defines the nodal displacements as

$$\mathbf{u}_{n+1}^{t+\Delta t} = \mathbf{u}_n^{t+\Delta t} - \left[ \frac{\partial \mathbf{G}(\mathbf{u}_n^{t+\Delta t})}{\partial \mathbf{u}} \right]^{-1} \cdot \mathbf{G}(\mathbf{u}_n^{t+\Delta t}) \quad (3.44)$$

where  $t$  is the time at the beginning of the increment;  $\Delta t$  represents the value of the time increment in use; and  $n$  is the iteration count. The Newton-Raphson method uses  $\mathbf{u}_n^{t+\Delta t}$  as the initial estimate of the nodal displacement and  $\mathbf{u}_{n+1}^{t+\Delta t}$  is the improved estimate after iteration  $n$ . By reorganising and introducing the *change* in the estimate of nodal displacements  $\delta \mathbf{u}_{n+1}$  in addition to the tangent stiffness matrix,  $\mathbf{K}$  we have

$$\delta \mathbf{u}_{n+1} = \mathbf{u}_{n+1}^{t+\Delta t} - \mathbf{u}_n^{t+\Delta t} = - \left[ \frac{\partial \mathbf{G}(\mathbf{u}_n^{t+\Delta t})}{\partial \mathbf{u}} \right]^{-1} \mathbf{G}(\mathbf{u}_n^{t+\Delta t}) \quad (3.45)$$

$$\partial \mathbf{u}_{n+1} = -\mathbf{K}(\mathbf{u}_n^{t+\Delta t})^{-1} \mathbf{G}(\mathbf{u}_n^{t+\Delta t}) \quad (3.46)$$

$$\mathbf{K}(\mathbf{u}_n^{t+\Delta t}) \partial \mathbf{u}_{n+1} = -\mathbf{G}(\mathbf{u}_n^{t+\Delta t}) \quad (3.47)$$

Finally,  $\mathbf{K}$  may be expressed as

$$\mathbf{K}(\mathbf{u}) = \frac{\partial \mathbf{G}(\mathbf{u})}{\partial \mathbf{u}} = \frac{\partial}{\partial \mathbf{u}} \left( \int_V \mathbf{B}^T \boldsymbol{\sigma}(\mathbf{u}) dV - \mathbf{F}_{\text{ext}} \right) \quad (3.48)$$

$$= \frac{\partial}{\partial \mathbf{u}} \left( \int_V \mathbf{B}^T \boldsymbol{\sigma}(\mathbf{u}) dV \right) \quad (3.49)$$

$$\int_V \mathbf{B}^T \frac{\partial \boldsymbol{\sigma}(\mathbf{u})}{\partial \mathbf{u}} dV = \int_V \mathbf{B}^T \frac{\partial \boldsymbol{\sigma}(\mathbf{u})}{\partial \boldsymbol{\varepsilon}} \frac{\partial \boldsymbol{\varepsilon}}{\delta \mathbf{u}} dV \quad (3.50)$$

$$= \int_V \mathbf{B}^T \frac{\partial \boldsymbol{\sigma}(\mathbf{u})}{\partial \boldsymbol{\varepsilon}} \mathbf{B} dV \quad (3.51)$$

$$\mathbf{K}(\mathbf{u}) = \int_V \mathbf{B}^T \mathbf{D} \mathbf{B} dV \quad (3.52)$$

where  $\mathbf{D}$  is the consistent tangent matrix, equal to the Jacobian of the constitutive law  $\left(\frac{\partial \boldsymbol{\sigma}}{\partial \boldsymbol{\varepsilon}}\right)$ .  $\mathbf{K}$  must be solved for each iteration in the process in order to minimize the out of balance force vector  $\mathbf{G}$ .

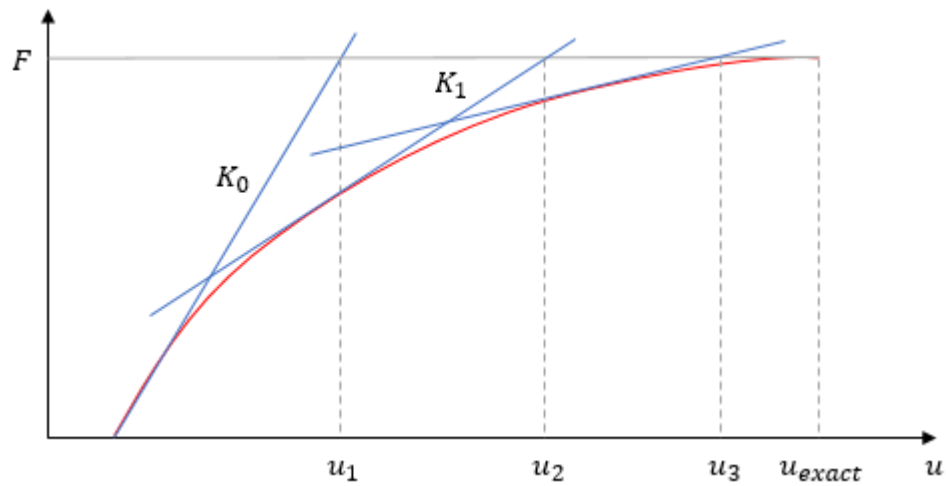


Figure 3.5: Schematic of Newton Raphson integration scheme used by the finite element method.

The implicit integration scheme is unconditionally stable due to this iterative process, whereby equilibrium is enforced upon each successive increment in load and hence is extremely robust and highly accurate in its calculations of field variables such as stress and strain. For further detail on the principles of the finite element method the reader is referred to Fagan (1992) and Bathe (2006).

### 3.2.2 User defined material subroutines

In addition to the in-built library of constitutive laws, Abaqus caters for the use of novel material formulations through user defined material subroutines (UMATs). At each iteration of each time increment, the UMAT is called and the material deformation is passed into the subroutine. The purpose of the UMAT is to calculate the stress and pass it out to the main program. In order to do this, the material Jacobian  $(\partial \Delta \boldsymbol{\sigma} / \partial \Delta \boldsymbol{\varepsilon})$ , defined as the change in stress at the end of a given increment caused by an infinitesimal perturbation of the strain, must be computed. A numerical

approximation of the material Jacobian can be attained through the perturbation method described by Miehe (1996). The aforementioned approach has been used previously in non-linear hyperelastic implementations (Sun *et al.*, 2008, Nolan *et al.*, 2014), and is employed in subsequent chapters of this thesis. The method makes use of a linearised incremental form of the Jaumann rate of the Kirchhoff stress:

$$\Delta \boldsymbol{\tau} - \Delta \mathbf{W} \boldsymbol{\tau} - \boldsymbol{\tau} \Delta \mathbf{W}^T = \mathbb{C}^J : \Delta \mathbf{D} \quad (3.59)$$

where  $\boldsymbol{\tau}$  is the Kirchhoff stress,  $\mathbf{W}$  and  $\mathbf{D}$  are the spin and rate of deformation tensors, and  $\mathbb{C}^J$  is the tangent modulus tensor for the Jaumann rate of the Kirchhoff stress.  $\Delta \mathbf{W}$  and  $\Delta \mathbf{D}$  may be stated in terms of the deformation gradient  $\mathbf{F}$ , such that

$$\Delta \mathbf{W} = \frac{1}{2} (\Delta \mathbf{F} \mathbf{F}^{-1} - (\Delta \mathbf{F} \mathbf{F}^{-1})^T) \quad (3.60)$$

$$\Delta \mathbf{D} = \frac{1}{2} (\Delta \mathbf{F} \mathbf{F}^{-1} + (\Delta \mathbf{F} \mathbf{F}^{-1})^T) \quad (3.61)$$

Through a perturbation of the deformation gradient, the tangent moduli may be approximated by a forward difference scheme. The perturbation is performed on each degree of freedom in an analysis. In a 3D analysis, this requires a perturbation of  $\mathbf{F}$  six times (once for each independent component of  $\Delta \mathbf{D}$ ):

$$\Delta \mathbf{F}^{(ij)} = \frac{\epsilon}{2} (e_i \otimes e_j \mathbf{F} + e_j \otimes e_i \mathbf{F}) \quad (3.62)$$

where  $\epsilon$  is a small perturbation parameter, and  $e_i$  is the basis vector in the spatial description. The total perturbed deformation gradient is given by  $\hat{\mathbf{F}}^{(ij)} = \Delta \mathbf{F}^{(ij)} + \mathbf{F}$ . The Kirchhoff stress is then calculated from this perturbed deformation gradient. Finally, the material Jacobian  $\mathbb{C}$  is approximated with:

$$\mathbb{C}^{(ij)} = \frac{1}{J} \mathbb{C}^{\tau J(ij)} = \frac{1}{J \epsilon} [\boldsymbol{\tau}(\hat{\mathbf{F}}^{(ij)}) - \boldsymbol{\tau}(\mathbf{F})] \quad (3.63)$$

For each perturbation of equation 3.63 above, six independent components of  $\mathbb{C}$  will be attained in a 3D simulation, with six perturbations required to construct the 6x6 tangent matrix.

### 3.3 Optimization Methods

Optimization generally describes the modification of design variables in order to identify the optimum performance of a part. As the derivative ( $f'$ ) describes the slope of a 1D function (whether it increases or decreases in a given direction), in multiple directions or dimensions this is known as the gradient ( $\Delta f$ ). This can be described by the problem outlined in Figure 3.6, below where the goal is; for a given value of  $x$  bound by the parabola  $y = x^2$  what is the minimum value of  $y$ ?

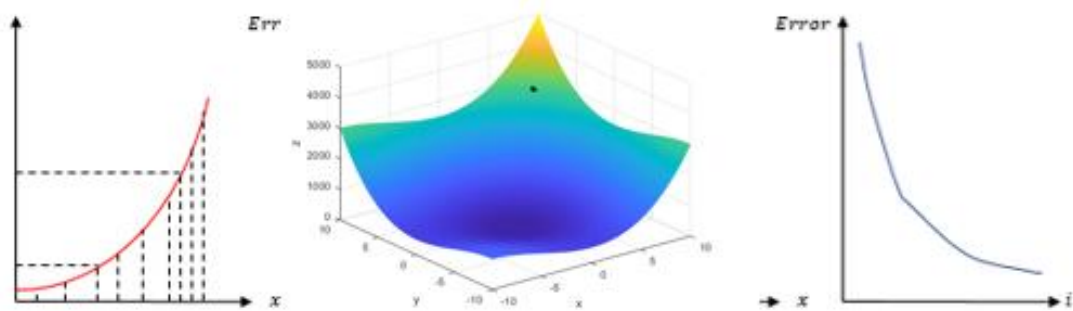


Figure 3.6: Example of optimization problems, whereby the goal is to find the local minimum.

Optimization problems are commonly written in the form

$$\underset{x}{\text{minimise}} \quad f(x) \quad (3.64)$$

where  $f$  is the objective function. Decision variables are the inputs to the problem that the optimizer is allowed to change in order to improve the objective function value. In the above example,  $x$  is the only decision variable. It is of course possible to have a problem with multiple decision variables such that  $x = \{x_1, x_2, \dots, x_n\}$ , which increases the difficulty in solving the optimization problem. The solution of the optimization problem is a set of values of the  $n$ -dimensional vector  $x$  (where  $n$  is the number of design variables) which gives a minimum value of the objective function  $f(x)$  while satisfying a set of constraints  $g(x) < g(u)$

$$g(x) < g(u) \quad ; \quad x_l \geq x \leq x_u \quad (3.65)$$

where  $x_l$  and  $x_u$  are the lower and upper bounds applied to the optimization indicating the constraints inside which values of  $x$  can fluctuate. The optimization approach used in this work, involves determining the optimum material parameters for a given constitutive law that when applied to a continuum model, provide an accurate estimate of experimental data. In order to compute the optimal scalar or vector,  $x$ , it is necessary to minimize a function,  $f(x)$ , by systematically choosing input values from within an allowed boundary set ( $x_i = \{x_l, x_u\}$ ) and computing the value of the function. The two

optimization algorithms used in the following work are the Nelder-Mead and Levenberg-Marquardt algorithms.

### ***Nelder-Mead***

The Nelder-Mead Algorithm (NMA) uses the concept of a *simplex* or *polytope*, consisting of  $n + 1$  vertices in  $n$  dimensions. The initial simplex is constructed by generating  $n + 1$  vertices about the given input guess point ( $x_0$ ). During each iteration, a series of test points bound by the simplex vertices are evaluated with respect to the objective function and are ordered based on accuracy from lowest to highest. The worst point is then replaced by a new vertex defined by the rules of reflection, expansion, contraction and shrinkage. The simplest approach involves replacing the worst point with a point reflected through the centroid of the remaining  $n$  points. The NMA subsequently generates a sequence of simplices which converges to a minimiser. Convergence is achieved when the working simplex is sufficiently small, or the function value is sufficiently close to another.

### ***Levenberg-Marquardt***

The Levenberg-Marquardt Algorithm (LMA) is a composite approach that uses both the Gauss-Newton algorithm when parameters are far from the optimal value and the method of gradient descent when parameters are close to the optimal value. The LMA is iterative and produces (once given an initial starting point) a series of vectors ( $p_1, p_2, \dots, p_n$ ) that converge towards a minimum  $p_*$  that best satisfies the functional relation  $f$ . For a given iteration  $n$ , the goal is to find the next iterate  $x(n + 1)$ , such that the function value is smaller than for iteration  $n$ . To choose  $x(n + 1)$  it is necessary to define a direction from  $x(n)$  and a step size. The LMA computes a linear approximation to  $f$  at  $x(n)$  based on the Jacobian ( $J = \partial f / \partial x$ ) and a step size ( $\delta$ ). The algorithm evaluates the approximating function by taking a step in the prescribed direction and comparing the decrease in the linear approximation to  $f$  with the actual decrease in the function  $f$ .

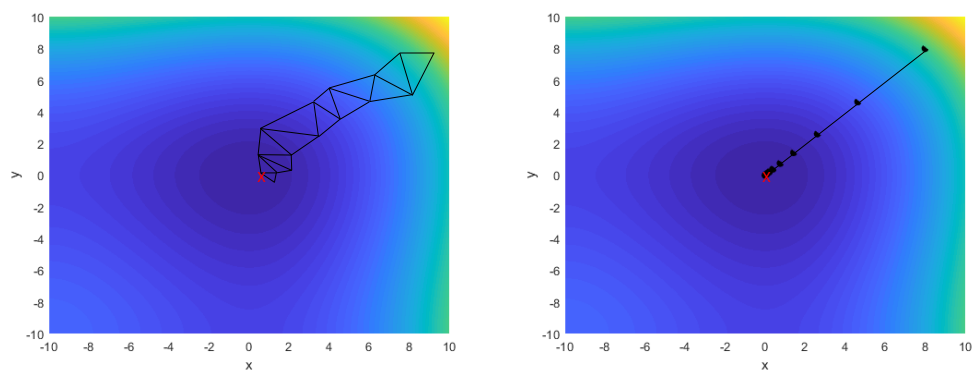


**Figure 3.7:** (a) Nelder Mead: Visualize a small triangle on an elevation map flip-flopping its way down a valley to a local bottom at (0,0). (b) Levenberg-Marquardt: Gradient based approach to determine path to minimum.

To introduce the concept of optimization of parameters for material characterization, a simple example is outlined below. Consider a uniaxial tension experiment Figure 3.8 (a) performed on a sample of excised arterial tissue with the nominal stress vs stretch response denoted by “.EXP” as shown in Figure 3.8 (c). A FE model in the form of a unit cube can be created to simulate the experiment, whereby a vertical displacement ( $u_z$ ) of 0.5mm is applied to the top face while lateral faces are free to contract. By recording the reaction force ( $RF_z$ ) due to  $u_z$ , the nominal stress can be calculated as the force per unit cross sectional area in the reference configuration. The material behaviour of the cube is governed by the incompressible Yeoh model where the strain energy density ( $\Psi$ ) is a function of three parameters, which form the individual components of our decision variables  $x = \{C_{01}, C_{02}, C_{03}\}$ . The  $S_{33}$  component of the stress tensor is output for each strain point and the error function is calculated against the objective function  $f(x)$ , until the tolerance is met.

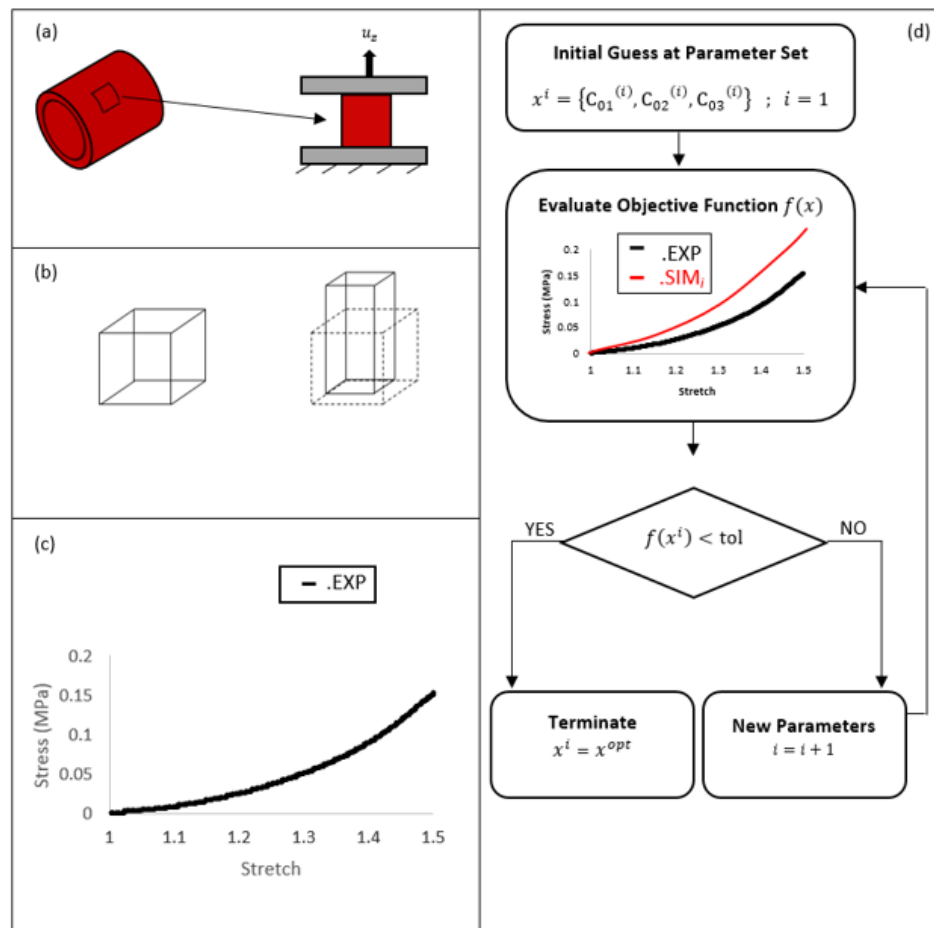


**Figure 3.8: Outline of experimental/computational optimization solution scheme. (a) Isolate tissue from arterial wall and subject tissue to uniaxial tensile test; (b) Schematic of boundary conditions applied to continuum model to replicate uniaxial tension experiment; (c) Stress-Strain relationship for experimental test; (d) Optimization scheme: make initial guess at material parameters, compare experimental vs computational stress strain curves and iterate through parameter variations until tolerance is achieved.**

### 3.4 Magnetic Resonance Imaging

Hydrogen ( $H^1$ ) is the most abundant element in the universe. The human body (in addition to oxygen and carbon) is made up of  $H^1$ , which has an atomic number of 1 and a nucleus that consists of a single proton. The rotating electrical charge causes a magnetic field or moment ( $\vec{\mu}$ ) about which the  $H^1$  proton eternally spins. Outside of an external magnetic field each  $\vec{\mu}$  is randomly aligned and so their sum amounts to zero.

An intrinsic property of  $H^1$  exists where it can only exist in two primary energy states. Once subject to a spatially uniform magnetic field  $\vec{B}_0$ , this property ensures that the element is either in a low ( $\alpha$ ) or high ( $\beta$ ) energy configuration. Suppose we apply a static and spatially uniform magnetic field  $\vec{B}_0$  along the z-direction such that

$$\vec{B}_0 = \begin{bmatrix} 0 \\ 0 \\ B_{z0} \end{bmatrix} = B_{z0} \vec{k}, \quad \text{where } \vec{k} = \begin{bmatrix} 0 \\ 0 \\ 1 \end{bmatrix} \quad (3.66)$$

$\vec{B}_0$  results in *Zeeman splitting*; a process whereby the longitudinal component ( $\mu_z$ ) of  $\vec{\mu}$  is quantized:

$$\mu_z = m_z h \frac{\gamma}{2\pi} \quad ; \quad \mu_z = \pm \frac{1}{2} h \frac{\gamma}{2\pi} \quad (3.67)$$

where  $h$  is Plank's Constant ( $6.62607004 \times 10^{-34}$  m<sup>2</sup> kg / s) and  $\gamma$  is a particle specific constant known as the gyromagnetic ratio that incorporates size, mass and spin (43.58 MHz/Tesla for  $H^1$ ). In the case of  $H^1$  where  $m_z = \pm 1/2$ , we have the two allowed values of energy,  $E$  for a free nucleus with an energy difference  $\Delta E$  of:

$$E(m) = \frac{\gamma B_0 h m}{2\pi} \quad ; \quad \Delta E = \frac{\gamma B_0 h}{2\pi} \quad (3.68a, 3.68b)$$

The number of protons that align parallel (low energy state) or anti-parallel (high energy state) to  $\vec{B}_0$  is governed by a Boltzmann distribution. There are always a larger number of protons aligned parallel to the primary magnetic field. For every 1,000,000 nuclei in the high energy state there are 1,000,006 in the low energy state at  $\vec{B}_0 = 1T$ . At this point, the net longitudinal magnetization is non-zero and the system is in thermodynamic equilibrium. At absolute zero, all nuclei would occupy the lower energy (parallel) state, however, thermal agitation greatly exceeds  $\Delta E$ . The equilibrium ratio of anti-parallel ( $N^-$ ) to parallel ( $N^+$ ) nuclei is governed by:

$$\frac{N^+}{N^-} = e^{\frac{\Delta E}{kT}} \quad (3.69)$$

where  $k$  is the Boltzmann constant ( $1.38 \times 10^{-23}$  J/<sup>o</sup>K) and  $T$  is temperature in degrees Kelvin.

The equilibrium spatial distribution of the magnetization is proportional to the local spin density per unit volume,  $\rho$  of  $H^1$  where  $\vec{M}_0$  denotes the equilibrium magnetization:

$$\vec{M}_0 = \begin{bmatrix} 0 \\ 0 \\ M_z \end{bmatrix} = M_z \vec{k} \quad ; \quad M_z = \rho(h\bar{\gamma})^2 \frac{1}{4kT} B_{z0} \quad (3.70a, 3.70b)$$

In truth the magnetic moment vector ( $\vec{\mu}$ ) of each proton is not directly aligned with the k-axis in the presence of  $\vec{B}_0$  due to thermal agitation and so it must have a transverse component,  $\vec{\mu}_{xy}$ . This transverse component is subject to a torque  $\vec{\tau}$  acting perpendicular to both the field and the direction of angular momentum which causes the proton to precess at a rate of  $\omega_0$  about the direction of the applied field (axis of  $\vec{k}$ ).

$$\vec{\tau} = \vec{\mu}_{xy} \times \vec{B}_0 \quad ; \quad \omega_0 = \gamma B_{z0} \quad (3.71a, 3.71b)$$

This precession in the transverse plane however, is not yet observable because neighbouring spins have random phase about the precessional path and so the net magnetization ( $M$ ) remains along the z-axis as the net magnetization in the transverse plane ( $M_{xy}$ ) is 0.

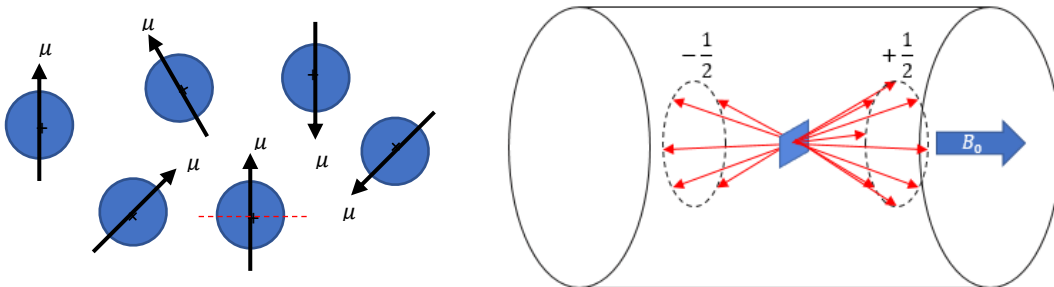


**Figure 3.9:** (a) magnetic moment vectors ( $\vec{\mu}$ ) for hydrogen atoms outside a magnetic field are randomly oriented; (b) Zeeman splitting of energy levels into parallel and anti-parallel.

In order to produce an image, it is necessary to record the net magnetization ( $M$ ) in the receiver coils of the scanner, and as signal is proportional to the length of  $M$  it is desirable to minimise  $M_z$  and maximise  $M_{xy}$ . To send  $M_z$  to zero, energy is transferred into the system in the form of a radiofrequency (RF) pulse  $\vec{B}_1(t)$ . If the frequency or energy of  $\vec{B}_1(t)$  matches the Larmor precession ( $\omega_0$ ), energy can be transferred to the lower energy state protons, which enables them to then occupy the high energy state. Noting that  $\Delta E = hB_0\Gamma = hf_0$ , which is exactly the formula for the energy in the quanta of an electromagnetic field with frequency  $f_0$ , where  $\Gamma = \gamma/2\pi$ , an RF field tuned to  $f_0$  will resonate with protons. If half the difference between parallel and anti-parallel protons can be excited into the higher energy state, the net longitudinal

magnetization will sum to zero. For excitation an RF Field is applied perpendicular to  $\vec{B}_0$ , usually as an amplitude modulated sinusoid:

$$\vec{B}_1(t) = B_1 a_1(t) \begin{bmatrix} +\cos(\omega_0 t + \phi_1) \\ -\sin(\omega_0 t + \phi_1) \\ 0 \end{bmatrix} \quad (3.72)$$

where  $a_1(t)$  is the pulse envelope. If enough energy is transferred into the system, the spins will begin to precess in phase, as they synchronise with the RF pulse frequency and therefore each other. Ultimately, this results in a non-zero  $\vec{M}_{xy}$  which can now be easily detected as signal in the receiver coils where its largest possible magnitude is:

$$|\vec{M}_{xy}| = \vec{M}_z \quad (3.73)$$

Signal acquisition utilises Faraday's Law, whereby a Magnetic Field can be detected as it induces a voltage ( $V$ ) across a conductor by:

$$\xi = -\frac{d\phi}{dt} \quad (3.74)$$

where  $\phi$  is the phase of the net magnetization vector ( $M$ ) in the transverse ( $xy$ ) plane.

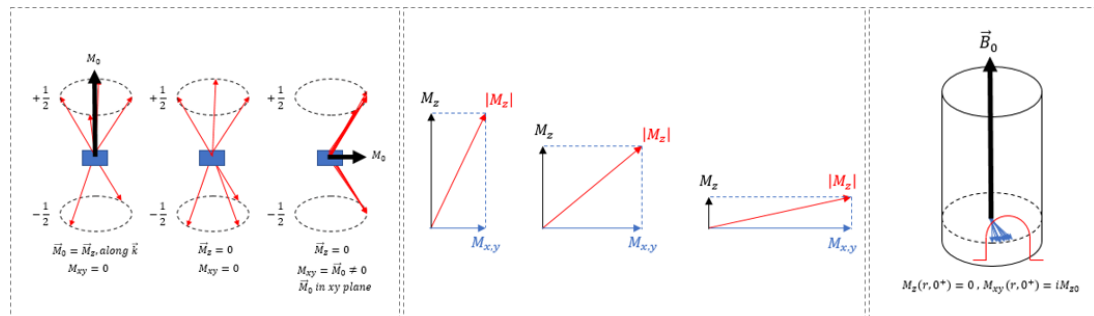


**Figure 3.10: (a) Resonance forcing phase coherence of precession; (b) Flipping of net magnetization vector from longitudinal into transverse plane; (c) Recording rotating magnetization vector as voltage through receiver coil.**

Application of the RF pulse is limited to a short time period, long enough only to tip the net magnetization vector ( $M$ ) into the transverse plane. Once turned off, the system returns towards thermal equilibrium through relaxation. Longitudinal relaxation occurs as previously excited protons return to the lower energy state following removal of the RF energy, thus re-growing the longitudinal magnetization vector ( $\vec{M}_z$ ) as

$$\vec{M}_z(t) = \vec{M}_0 \left(1 - e^{-\frac{t}{T_1}}\right) + \vec{M}_z(0)e^{-\frac{t}{T_1}} \quad (3.75)$$

where  $T_1$  is the *spin-lattice* time constant that governs the exchange of energy between protons and surrounding environment. Transverse relaxation occurs due to the repulsion of positively charged protons that were forced to precess in phase coherence with the energy provided by the RF pulse. Net Transverse magnetization therefore tends towards zero as the spins disperse about the z-axis in the  $xy$  plane

$$\vec{M}_{xy}(t) = |\vec{M}_0| e^{-\frac{t}{T_2}} \quad (3.76)$$

where  $T_2$  is the *spin-spin* time constant that describes the loss of phase coherence due to interactions between spins. The RF signal measured thus reduces in intensity with time following the removal of the RF pulse (known as a free induction decay (FID)) and consists of the superposition of the individual signals from all excited spins.

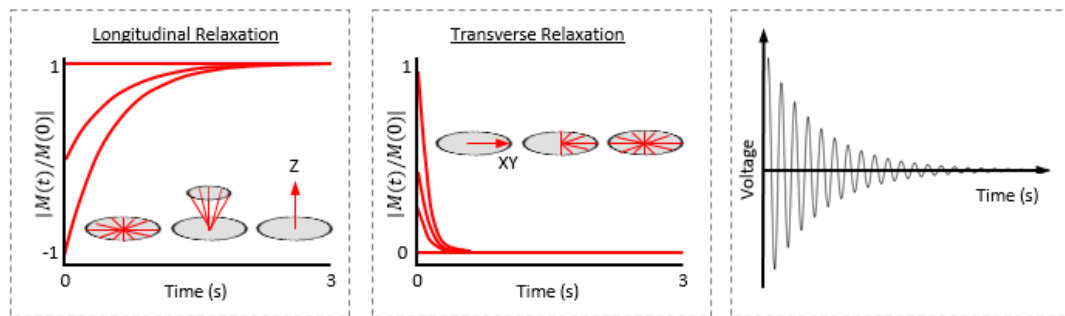


**Figure 3.11:** (a) Longitudinal relaxation due to removal of RF pulse; (b) Transverse relaxation due to positively charged protons repelling against phase coherence of precession once RF energy is removed; (c) Free Induction Decay due to rotating and relaxing net magnetization vector in the transverse plane.

As the energy applied from  $\vec{B}_1$  excites *all* spins precessing at that specific frequency, at this point the signal in the free induction decay is a composite of the total number of  $H^1$  protons in the body and so provides no spatial information regarding the specimen being scanned. To overcome this, excitation of a certain slice of the specimen (e.g. axial) is achieved by applying a gradient magnetic field ( $\vec{G}_z$ ) along the foot-head direction of the patient.

$$\vec{B}(r) = \vec{B}(x, y, z) = \begin{bmatrix} 0 \\ 0 \\ \vec{B}_z + z\vec{G}_z \end{bmatrix} = (\vec{B}_z + z\vec{G}_z) \vec{k} \quad (3.77)$$

In order to excite a single plane, selective excitation techniques are used where the Larmor (precessional) frequency is now spatially variant along the  $z$ -axis. Thus, to excite just the spins in slice  $z_i$ , in principle an RF signal whose spectrum is concentrated at  $f_i$  is applied. Application of an RF Pulse in the presence of a slice

selective gradient magnetic field ( $\vec{G}_z$ ) ensures upon sampling that signal is now confined to protons within the slice  $f_i$ .

$$f_0(r) = f_0(x, y, z) = \bar{\gamma}(\vec{B}_z + z\vec{G}_z) \quad ; \quad f_i = \bar{\gamma}(\vec{B}_z + z_i\vec{G}_z) \quad (3.78a, 3.78b)$$

The next step involves, in-plane signal localisation along the frequency direction (horizontal direction in Figure 3.12 below). Applying a gradient magnetic field from left to right ( $\vec{G}_x$ ) results in spins on the left-hand side precessing slower than spins on the right hand side of the image. By turning on this frequency encoding gradient  $\vec{G}_x$  at the sampling time, protons precess at a range of frequencies along the  $x$  dimension of the image. The FID is a summation of a series of component signals, each of which has a different frequency corresponding to a discrete column in the image matrix.

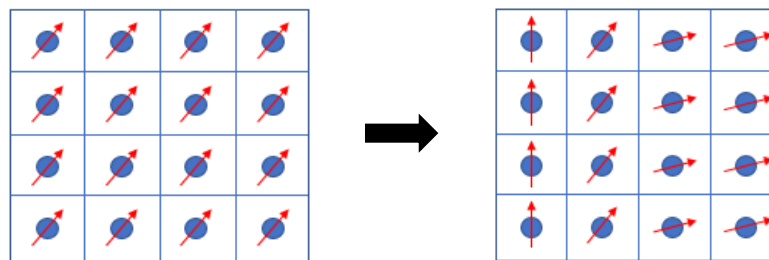


**Figure 3.12:** (a) Slice selection gradient results in each proton precessing with same frequency and phase; (b) Left-Right gradient results in spins on left-hand side to precess slower than those on the right-hand side, hence frequency can be encoded along first in-plane dimension.

Signal is localised by utilizing the Fourier Transform, which is based on the principle that any shape can be replicated by the summation of smaller sine and cosine curves with specific amplitudes and frequencies (Figure 3.13(a)). In MRI the inverse Fourier Transform is used where individual components are determined from the summation. Each component frequency has a specific amplitude that combine together to give the net summation result. Since each frequency is related to the location along  $x$ , it is then trivial to map the frequency to the position according to the frequency encoding gradient ( $\vec{G}_x$ ). A schematic is shown in Figure 3.13(b) representing an axial slice at the knees of a human subject. This image is somewhat representative of the local anatomy with maximal signal intensity visible at two peaks (each knee), however, there is no information regarding the individual components that make up each column in the matrix. The image merely shows that there is signal intensity at the two peaks corresponding to the location of the left and right knee but cannot distinguish between what is bone, muscle or cartilage.

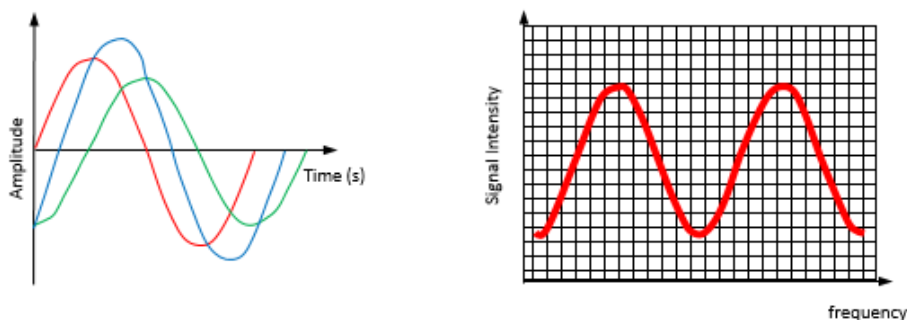


**Figure 3.13:** (a) Example of summation of individual frequency and amplitude data (red and green) results in blue curve; (b) Resultant image of axial slice through human knees, peaks in signal amplitude can be seen at each knee but no information exists regarding the individual components making up signal peaks.

The final step in signal localisation involves a third gradient magnetic field along the  $y$  dimension of the image, in order to detect the individual components of each column in Figure 3.13(b). This gradient is known as the phase encoding gradient ( $\vec{G}_y$ ) which is performed between the slice select gradient ( $\vec{G}_z$ ) and the frequency encoding gradient ( $\vec{G}_x$ ) in the pulse sequence. By applying an RF pulse in the presence of  $\vec{G}_z$  all spins in the slice of interest are excited. Once the RF pulse ends, all spins within the slice precess at the Larmor frequency corresponding to  $\vec{B}_0$ . By turning on  $\vec{G}_y$  at this point a phase shift is induced along the  $y$  dimension. Once this is turned off, all the protons once again precess at the Larmor frequency but there exists a phase shift that is irrecoverable along each column. Finally, sampling of the signal in the presence of  $\vec{G}_x$  encodes spatial information along the  $x$ -dimension. Signal is now generated from each pixel, and a Fourier Transform in multiple directions is employed to obtain final image (Figure 3.14). For further detail on the principles of nuclear magnetic resonance and spin theory, the reader is referred to McRobbie *et al.*, (2006), Ansorge & Graves (2016), and Levitt (2008).

Content Removed Due to Copyright

**Figure 3.14:** Final image following phase encoding gradient allows visualization of individual components of the knee, including bone, muscle and arteries.

### 3.5 Bibliography

- Annaidh, A. N., Karine Bruyère, Destrade, M., Gilchrist, M. D., Maurini, C., Otténio, M. and Saccomandi, G. (2012) ‘Automated estimation of collagen fibre dispersion in the dermis and its contribution to the anisotropic behaviour of skin’, *Annals of Biomedical Engineering*, 40(8), pp. 1666–1678. doi: 10.1007/s10439-012-0542-3.
- Ansorge, R. and Graves, M. (2016) *The physics and mathematics of MRI*, *The Physics and Mathematics of MRI*. Morgan and Claypool Publishers. doi: 10.1088/978-1-6817-4068-3.
- Bathe, K.-J. (2006) *Finite Element Procedures*. 1st edn. Prentice Hall, Pearson Education, Inc. Available at: [http://web.mit.edu/kjb/www/Books/FEP\\_2nd\\_Edition\\_4th\\_Printing.pdf](http://web.mit.edu/kjb/www/Books/FEP_2nd_Edition_4th_Printing.pdf).
- Bosboom, E. M. H., Hesselink, M. K. C., Oomens, C. W. J., Bouten, C. V. C., Drost, M. R. and Baaijens, F. P. T. (2001) ‘Passive transverse mechanical properties of skeletal muscle under in vivo compression’, *Journal of Biomechanics*, 34(10), pp. 1365–1368. doi: 10.1016/S0021-9290(01)00083-5.
- Cowin, S. C. (2013) *Continuum mechanics of anisotropic materials*, *Continuum Mechanics of Anisotropic Materials*. Springer New York. doi: 10.1007/978-1-4614-5025-2.
- Eisenberg, M. A. and Malvern, L. E. (1973) ‘On finite element integration in natural co-ordinates’, *International Journal for Numerical Methods in Engineering*, 7(4), pp. 574–575. doi: 10.1002/nme.1620070421.
- Fagan, M. J. (1992) *Finite element analysis: theory and practice*, Harlow by Longman. Longman Scientific & Technical. Available at: <https://lib.ugent.be/en/catalog/rug01:000288014> (Accessed: 9 October 2019).
- Famaey, N., Sommer, G., Vander Sloten, J. and Holzapfel, G. A. (2012) ‘Arterial clamping: Finite element simulation and in vivo validation’, *Journal of the Mechanical Behavior of Biomedical Materials*, 12, pp. 107–118. doi: 10.1016/j.jmbbm.2012.03.010.
- Gajewski, T., Weisbecker, H., Holzapfel, G. A. and Łodygowski, T. (2013) Implementation of a hyperelastic model for arterial layers considering damage and distributed collagen fiber orientations, *Computer Methods in Mechanics*.
- Garcia-Gonzalez, D., Jérusalem, A., Garzon-Hernandez, S., Zaera, R. and Arias, A. (2018) ‘A continuum mechanics constitutive framework for transverse isotropic soft tissues’, *Journal of the Mechanics and Physics of Solids*. Elsevier Ltd, 112, pp. 209–224. doi: 10.1016/j.jmps.2017.12.001.
- Groves, R. B., Coulman, S. A., Birchall, J. C. and Evans, S. L. (2012) ‘Quantifying the mechanical properties of human skin to optimise future microneedle device design’, *Computer Methods in Biomechanics and Biomedical Engineering*, 15(1), pp. 73–82. doi: 10.1080/10255842.2011.596481.
- Holzapfel, G. A. (2000) *Nonlinear solid mechanics: a continuum approach for engineering*. Wiley.
- Levitt, M. H. (2008) *Spin Dynamics: Basics of Nuclear Magnetic Resonance*. 2nd edn.

- Madouh, F. A. and Ramesh, K. T. (2019) ‘The Influence of Shear Anisotropy in mTBI: A White Matter Constitutive Model’, *Annals of Biomedical Engineering*. Springer New York LLC. doi: 10.1007/s10439-019-02321-1.
- McRobbie, D. W., Moore, E. A., Graves, M. J. and Prince, M. R. (2006) *MRI From Picture to Proton*. Cambridge: Cambridge University Press. doi: 10.1017/CBO9780511545405.
- Miehe, C. (1996) ‘Numerical computation of algorithmic (consistent) tangent moduli in large-strain computational inelasticity’, *Computer Methods in Applied Mechanics and Engineering*. Elsevier, 134(3–4), pp. 223–240. doi: 10.1016/0045-7825(96)01019-5.
- Nolan, D., Ogden, R. W., Destrade, M. and McGarry, J. P. (2014) ‘A robust anisotropic hyperelastic formulation for the modelling of soft tissue’, *Journal of the Mechanical Behaviour of Biomedical Materials*.
- Nolan, D. R. and McGarry, J. P. (2016) ‘On the Compressibility of Arterial Tissue’, *Annals of Biomedical Engineering*. Springer US, 44(4), pp. 993–1007. doi: 10.1007/s10439-015-1417-1.
- Ogden, R. W. (1997) *Non-linear elastic deformations*. Dover Publications.
- Ogden, R. W. (2003) ‘Nonlinear Elasticity, Anisotropy, Material Stability and Residual Stresses in Soft Tissue’, in *Biomechanics of Soft Tissue in Cardiovascular Systems*. Vienna: Springer Vienna, pp. 65–108. doi: 10.1007/978-3-7091-2736-0\_3.
- Pandolfi, A. and Holzapfel, G. A. (2008) ‘Three-dimensional modeling and computational analysis of the human cornea considering distributed collagen fibril orientations.’, *Journal of biomechanical engineering*, 130(6), p. 061006. doi: 10.1115/1.2982251.
- Roy, D., Holzapfel, G. A., Kauffmann, C. and Soulez, G. (2014) ‘Finite element analysis of abdominal aortic aneurysms: geometrical and structural reconstruction with application of an anisotropic material model’, *IMA Journal of Applied Mathematics*. Oxford University Press, 79(5), pp. 1011–1026. doi: 10.1093/imamat/hxu037.
- Shahraki, N. M., Fatemi, A., Goel, V. K. and Agarwal, A. (2015) ‘On the use of biaxial properties in modeling annulus as a Holzapfel-Gasser-Ogden material’, *Frontiers in Bioengineering and Biotechnology*. Frontiers Media S.A., 3(JUN). doi: 10.3389/fbioe.2015.00069.
- Shearer, T. (2015) ‘A new strain energy function for the hyperelastic modelling of ligaments and tendons based on fascicle microstructure’, *Journal of Biomechanics*. Elsevier Ltd, 48(2), pp. 290–297. doi: 10.1016/j.jbiomech.2014.11.031.
- Spencer, A. J. M. (Anthony J. M. (2004) *Continuum mechanics*. Dover Publications.
- Sun, W., Chaikof, E. L. and Levenston, M. E. (2008) ‘Numerical approximation of tangent moduli for finite element implementations of nonlinear hyperelastic material models’, *Journal of Biomechanical Engineering*, 130(6). doi: 10.1115/1.2979872.

- Tasca, G., Selmi, M., Votta, E., Redaelli, P., Sturla, F., Redaelli, A. and Gamba, A. (2017) 'Aortic Root Biomechanics After Sleeve and David Sparing Techniques: A Finite Element Analysis', *Annals of Thoracic Surgery*. Elsevier USA, 103(5), pp. 1451–1459. doi: 10.1016/j.athoracsur.2016.08.003.
- Wang, M. and Liu, F. (2018) 'Compressible Hyperelastic Models for Soft Biological Tissue: A Review', *Journal of Biomaterials and Tissue Engineering*, 8(10), pp. 1375–1389. doi: 10.1166/jbt.2018.1888.

# CHAPTER 4

## QUANTIFICATION OF THE REGIONAL BIOARCHITECTURE IN THE HUMAN AORTA



### **Abstract**

Spatial variance in human aortic bioarchitecture responsible for the elasticity of the vessel is poorly understood. The current study quantifies the elements responsible for aortic compliance, namely elastin, collagen and smooth muscle cells, using histological and stereological techniques on human tissue with a focus on regional heterogeneity. Using donated cadaveric tissue, a series of samples were excised between the proximal ascending aorta and the distal abdominal aorta, for five cadavers, each of which underwent various staining procedures to enhance specific constituents of the wall. Using polarized light microscopy techniques, the orientation of collagen fibers were studied for each location and each tunical layer of the aorta. Significant transmural and longitudinal heterogeneity in collagen fiber orientations is uncovered throughout the vessel. It is shown that a von-Mises mixture model is required to accurately fit the complex collagen fiber distributions that exist along the aorta. Additionally, collagen and smooth muscle cell density is observed to increase with increasing distance from the heart while elastin density decreases. Evidence clearly demonstrates that the aorta is a highly heterogeneous vessel which cannot be simplistically represented by a single compliance value. The quantification and fitting of the spatial aortic bioarchitectural data, although not without its limitations, including mean cohort age of 77.6 years, facilitates the development of next-generation finite element models that can potentially simulate the influence of regional aortic composition and microstructure on vessel biomechanics.

## 4.1 Introduction

Heterogeneity in regional mechanical properties along the aorta is a widely accepted phenomenon. The degree of heterogeneity, however, remains poorly characterised, and the underlying cause remains poorly understood, particularly in humans. In general, a high level of elastic compliance is required in the proximal aorta, so that the kinetic energy expelled during systole can be stored as elastic strain energy in the vessel wall, leading to subsequent augmentation of pressure pulse propagation during diastole due to elastic recoil of the wall. The distal aorta, however, takes an alternative approach to blood transfer with a higher smooth muscle cell (SMC) content and a reduced requirement for elastin. In the absence of a robust study investigating the spatial variance of bioarchitecture of the human aorta using stereological techniques, this study focuses on quantifying the variation in orientations and densities of the main load bearing constituents along the entire vessel length, in an attempt to understand regional heterogeneity observed both *in-vitro* and *in-vivo*.

Significant literature on characterisation of the constituents of arteries to better understand their form and function exists, particularly with reference to the effects of ageing on the microstructural components of the aortic wall (Feldman & Glagov, 1971; Tomaszewski *et al.*, 1976; Cattell & Hasleton, 1996; Fritze *et al.*, 2012; Taghizadeh & Tafazzoli-Shadpour, 2017). Hosoda *et al.*, (1984) investigated the human thoracic aorta and found that elastin decreased with age, while collagen remained the same. Faber *et al.* also found that elastin decreases with age however collagen increases (Faber & Moller-Hou, 2009). Others have focused on pathological states such as hypertension (Berry and Greenwald, 1976), Marfan Syndrome (Halme *et al.*, 1985) dissection (Yamada *et al.*, 2015) and aneurysmal tissue (Baxter *et al.*, 1992; Choudhury & Leask, 2009) and found significant differences compared to control groups. For further detail regarding elastin and collagen microstructure in the human aorta in both ageing and disease, the reader is directed to the comprehensive review paper by Tsamis and colleagues (Tsamis & Vorp, 2013).

Much less emphasis, however, has been placed on the *spatial* heterogeneity in the biomechanics of the aorta in either health or disease. Due to both the ethics and accessibility of human tissue, animal studies surpass human studies. Harkness *et al.* investigated the regional elastin and collagen proportions in dogs and found that in the intrathoracic aorta there was approximately twice as much elastin as collagen in the wall; in all other vessels this relationship was reversed (Harkness & McDonald, 1957). Saey *et al.* report for an equine population, a greater concentration of collagen in the distal thoracic aorta compared to proximal, however there were no significant regional differences in elastin content (Saey *et al.*, 2015). Results by Davidson *et al.* show that elastic fibers were reduced in the abdominal compared to thoracic aorta in a porcine group (Davidson *et al.*, 1985), while Shadwick reported higher compliance proximally than distally in whales (Shadwick, 1999). Despite the wealth of knowledge for animal populations, the spatial variance in biomechanics of the human aorta in terms of bioarchitecture remains relatively unknown.

This work quantifies the orientations of collagen fibers, in addition to the regional density of elastin, collagen and SMCs along the length of the human aorta. Stereological and polarised light microscopy (PLM) techniques provide evidence that a von-Mises mixture model is required to fit the complex axially and transmurally varying fiber distributions of the vessel. Previous finite element models of the aorta assume a homogeneous (Roy *et al.*, 2014) and symmetric (Grytsan and Holzapfel, 2015) orientation of collagen fibers, which cannot capture the true anisotropy of the vessel. The population densities of elastin, collagen and SMCs along the length of the human aorta are quantified using high spatial resolution, intended to further advance the understanding of regional aortic biomechanics. Results are presented for eight sites from the proximal ascending aorta to immediately proximal to the common iliac bifurcation for five cadavers. Histological and stereological techniques reveal significant spatial variations in constituent densities along the aorta, while morphological analyses show marked variation in wall layer thicknesses between intimal, medial and adventitial layers with increasing distance from the heart. Results presented on the spatial heterogeneity of the aorta may aid in the understanding of the underlying causes for the differences in mortality following proximal compared to distal aortic stenting (Martín *et al.*, 2008; Bischoff *et al.*, 2016; Beach *et al.*, 2017; Concannon *et al.*, 2017; Conrad *et al.*, 2017). Additionally, the quantification and fitting of regional aortic microstructural data facilitates the development of next-generation finite element models that can potentially simulate the influence of regional aortic composition and microstructure on vessel biomechanics.

## 4.2 Methodology

In this chapter, the regional aortic microstructure responsible for vessel compliance is quantified using histological and stereological techniques. Localized anterior tissue fractions of elastin, collagen and SMCs are quantified by taking samples at eight sites along the aorta. The dissection procedure is outlined in Section 4.2.1 and illustrated in Figure 4.1(a). Additionally, circumferential distribution of collagen and elastin in the ascending thoracic aorta is quantified, results of which can be found in the supplementary material section. Regional wall layer thicknesses are presented for each cadaver, while SMC content and layer specific collagen fiber orientations (intima, media and adventitia) are also investigated in a single cadaver for each of the eight sample sites. As endothelial cells and SMCs are considered the two major cellular components within the vessel wall which play a role in stiffness (Qi *et al.*, 2011; Kaeberlein & Martin, 2016; Lacolley *et al.*, 2017) and endothelial cells contribute more in a mechanotransductive nature and negligibly to the actual stiffness of the wall themselves (Williams & Wick, 2005; Karšaj & Humphrey, 2012; Gültekin & Holzapfel, 2016) our cellular focus herein concentrates on SMCs.

### 4.2.1 Tissue Harvesting

Aortic samples were harvested from 5 adult human cadavers (age range 67 – 92 years, mean 77.6 years) with no reported history of aortic disease. Table 4.1 outlines the details of the donors. All cadaveric material used was bequeathed to Anatomy, School of Medicine, National University of Ireland Galway in accordance with legislation

governing the practice of Anatomy in the Republic of Ireland (Medical Practitioners Act 2007). Three of the 5 cadavers were female. Cadavers were embalmed using a standard mixture containing formalin, glycerine, phenol, and methanol (12 L water + 2.4 L of a 37–41% formalin solution + 2 L phenol + 6 L glycerine + 6 L methanol).

**Table 4.1: Details of donor cohort.**

Donor	Gender	Age at Death	Reported Cause of Death
1	Female	83 years	Carcinoma of urinary bladder
2	Male	67 years	Carcinoma of sigmoid colon metastatic to liver & lung
3	Male	76 years	Squamous cell carcinoma of parietal scalp with intracranial extension
4	Female	70 years	Heart failure secondary to valvular heart disease
5	Female	92 years	Cerebrovascular accident; ischaemic heart disease

Approximately 1 cm<sup>2</sup> area of the aorta was excised at each of the following levels: (i) ascending thoracic aorta (distal to sinus of Valsalva); (ii) ascending thoracic aorta (proximal to great vessels); (iii) thoracic aorta (distal to great vessels); (iv) thoracic aorta (start of descending); (v) thoracic aorta (mid); (vi) abdominal aorta (proximal to coeliac trunk); (vii) abdominal aorta (distal to superior mesenteric artery), and (viii) abdominal aorta (proximal to common iliac bifurcation). Anterior sample excision sites are illustrated in Figure 4.1(a). Due to anatomical variance between cadavers, including length, curvature and tortuosity, histological results are presented as a function of 8 anatomical sites rather than as a function of physical distance from the aortic root. Following dissection, specimens are dehydrated through a graded series of ethanol (50% - 100%), before being embedded in paraffin wax and sectioned at a thickness of 5 µm in order to maximize collagen to tissue contrast and limit tissue scattering (Yang *et al.*, 2018). For area fraction (AF) analyses, sectioning is performed in the r-c (radial-circumferential) plane to enable investigation through the thickness of the aortic wall, while for fiber orientation (FO) analyses sectioning is performed in the a-c (axial-circumferential) plane on a separate sample obtained from the same site (Figure 4.1(b,c)).

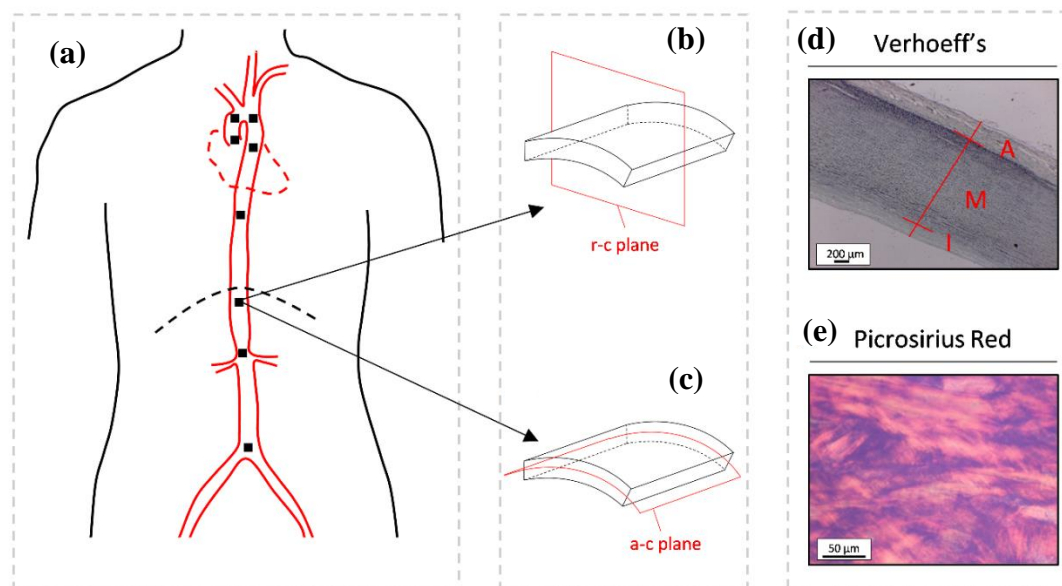


**Figure 4.1:** (a) Excision sites along the aorta (black squares), where the diaphragm is indicated by the dashed black line. (b) Sample orientations for Area fraction (AF) in the r-c (radial-circumferential) plane. (c) Sample orientations for fiber orientation (FO) in the a-c (axial-circumferential) plane. (d) Sections post-staining for AF with Verhoeff's Method. (e) Sections post-staining for FO with Picrosirius Red.

## 4.2.2 Staining Procedures

In each case, the pre-staining procedure involved wax removal from each sample using xylene and sample rehydration through a series of ethanol solutions of decreasing concentrations (100% - 50%). Separate staining procedures are performed on separate slides for quantification of each tissue constituent. For AF analyses, elastin is stained dark blue / black using Verhoeff's method (Zugun and Lacramioara Carmen, 2013); collagen is stained green / blue using Masson's Trichrome (Vorkapic *et al.*, 2016) and nuclei are stained dark blue using Haematoxylin & Eosin (Lo Vasco *et al.*, 2011) protocols. For FO analyses, slides are stained using PicroSirius Red in order to attenuate the birefringence of collagen fibers (Junqueira & Brentani, 1979) which subsequently appear red on a black background. Completion of each staining protocol involves dehydration through alcohols of increasing concentrations followed by xylene clearing and slide mounting with D.P.X.

## 4.2.3 Postprocessing

### 4.2.3.1 Stereological Analysis

Sections were obtained from the tissue blocks of eight regions from the proximal ascending to distal abdominal aorta (as outlined in Section 4.3.1). All AF slides were examined using a Leica DM500 light microscope, with an ICC50 HD camera attachment (Leica Microsystems Limited, Switzerland) and a 40x objective lens. Systematic random sampling procedures were employed and simple point counting methods (using a 12x12 grid generated by MATLAB (R2017b, MathWorks Inc., Natick, MA, USA) were used to estimate the local area fraction of collagen, elastin

and SMCs (Elias & Schwartz, 1971; Mayhew, 1991; Wreford, 1995; Evanko *et al.*, 2018). Given that there are no cells present in the media apart from SMCs (Rhodin, 1980), random sampling during SMC quantification is confined to this layer as Haemotoxylin & Eosin staining provides no specific distinction between cell types. The approach involves calculation of the area fraction ( $V_v$ ) of each tissue component by expressing the proportion of points hitting a tissue component ( $P_c$ ) as a fraction of the total number of points hitting any tissue ( $P_T$ )

$$V_v = \frac{\sum P_c}{\sum P_T} \quad (4.01)$$

The  $V_v$  was calculated for each image in each triplet and the average was recorded for each location. For elastin and collagen, the average  $V_v$  for each location across the 5 cadavers is shown in Figure 4.3 and Figure 4.4 respectively, while SMC content is shown in Figure 4.8.

#### **4.2.3.2 Wall Layer Thickness**

The individual thickness values for each layer of the aortic wall (intima, media, adventitia) are measured at each site for all five cadavers using ImageJ following calibration with the scale bar. The average thickness values are presented in Figure 4.5. The intima/media (IM) border is defined along the Internal Elastic Lamina while the media/adventitia (MA) border is defined by the External Elastic Lamella.

#### **4.2.3.3 Polarized Light Microscopy**

PLM techniques were employed at each location and wall layer for a single donor to investigate both axial and radial heterogeneity in collagen fiber orientations. Each FO slide was reviewed using a Nikon Eclipse E200 transmitted polarised light microscope with an epifluorescence attachment. Images were captured through a Nikon DS-Fi1, 6-megapixel camera equipped with NIS Elements software. The circumferential direction of each tissue sample was oriented along the long axis of the slide to ensure consistency in determining fiber orientations relative to a universal horizontal plane. Each slide was then placed on the rotating stage with the long axis parallel with the polarizer (East/West) and the centre of the sample at the crosshairs of the polarizer and analyzer (filters).

A detailed review of the principles surrounding PLM are outside the scope of this work but can be found in the literature, for example Török *et al.* (1998), Murphy (2002), Chayen (1983), and Carlton (2011). In brief, a birefringent material, such as collagen, changes the polarization state of light, which results in a degree of altered light intensity that depends on the angle between the sample and the filters. Maximum intensity is achieved when fibers are aligned at  $\pm 45^\circ$ .

For each wall layer at each site, such that the full spectrum of fiber orientations is mapped, rotation of the stage and acquisition of  $0^\circ$  and  $45^\circ$  images resulted in the inputs of the composite image (Figure 4.2(a)) (Gaul & Lally, 2017) which was formed

using ImageJ. This image was then analysed using the OrientationJ plugin. Knowledge of the mean fiber thickness ( $\sigma = 24 \mu\text{m}$ ) is required for accurate quantification of fiber orientation, which was obtained from the images via the scale bar. The angle ( $\varphi$ ) is defined relative to the horizontal ( $0^\circ$ ) according to:

$$\varphi = \frac{1}{2} \arctan \left( 2 \frac{\langle f_x, f_y \rangle_w}{\langle f_y, f_y \rangle_w - \langle f_x, f_x \rangle_w} \right) \quad (4.02)$$

where  $f_x$  and  $f_y$  are the spatial partial derivatives of the image function  $f(x, y)$  along the  $x$  and  $y$  directions respectively, angled brackets indicate the inner product, and  $w(x, y)$  is the Gaussian weighting function that specifies the area of interest. Further detail on the theory surrounding OrientationJ can be found in (Rezakhaniha *et al.*, 2012; Püspöki *et al.*, 2016). Figure 4.2(b) shows the result of the input composite image Figure 4.2(a), where horizontal and vertical directions indicate circumferential and axial sample axes respectively. The corresponding probability density histogram is shown in Figure 4.2(c), where MATLAB (R2017b, MathWorks Inc., Natick, MA, USA) based von-Mises mixture models are fit to the individual datasets to estimate the number of fiber families present based on the log-likelihood function (Hung and Yang, 2012; Schymura, 2019). The wavelengths of the individual collagen fibrils observed in (Krasny *et al.*, 2018), which are in the range of 2-3 times the fibril thickness, 60nm (Hansen *et al.*, 2009), are not observed at the magnification used in this study, where the pixel resolution is 500 nm. Therefore, the individual fibril undulations do not affect the von-Mises distributions measured.

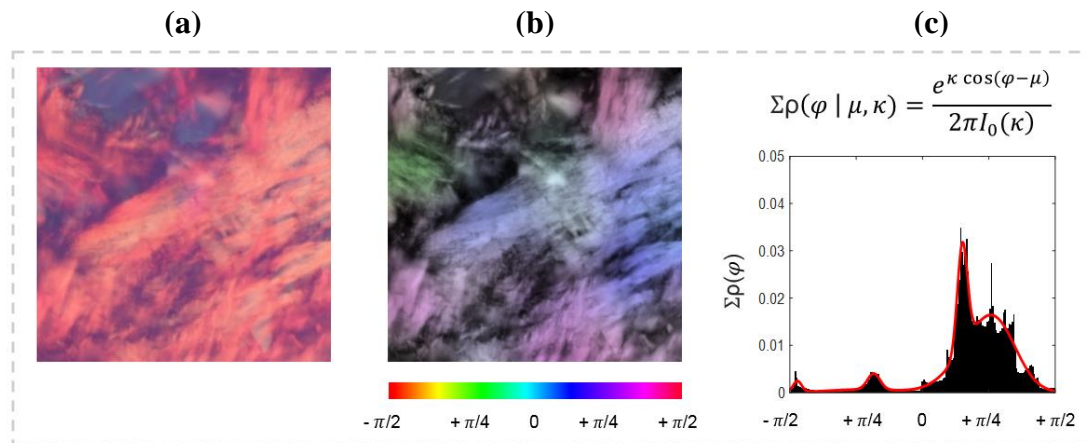


**Figure 4.2:** (a) Raw composite image used as input into Orientation J plugin. (b) Result following input image where  $0^\circ$  indicates the circumferential axis of the sample and  $\pm\pi/2$  indicate the axial axis. (c) Corresponding probability density histogram with fitted von Mises mixture model to raw data in red.

#### **4.2.3.4 Statistical Analysis**

Statistical analysis of this research was performed in MATLAB (R2017b, MathWorks Inc., Natick, MA, USA). After collecting the data, it was entered into a workspace for organisation. Data was analysed and tested using a student's t-test for continuous variables. Statistical significance was accepted with a p-value of less than 0.05.

### **4.3 Results**

We employ histological and stereological techniques to investigate the orientations and densities of aortic wall constituents which contribute to the compliance of the vessel. Stereological analyses allow for quantification of the spatially varying area fractions of elastin, collagen and SMCs within the aortic wall at each location outlined in Section 4.3.1, while PLM techniques allow for the quantification of fiber orientation distributions.

#### **4.3.1 Elastin**

Figure 4.3 shows the spatial change in elastin content from proximal to distal aorta. A downward trend for elastin content is observed with increasing distance from the heart, however statistical significance is not observed when splitting the aorta based on thoracic and abdominal subgroups ( $p=0.07$ ). For example, in the ascending aorta elastin contributes  $27 \pm 4.7\%$  of the area, while in the distal abdominal aorta (immediately proximal to the common iliac bifurcation) the area made up of elastin drops to  $17 \pm 3.9\%$ . Additionally, significant circumferential heterogeneity in elastin content is observed in the ascending thoracic aorta, with the highest area fraction observed on the lateral segment of the wall (see Supplementary Material (Figure S1(a))).

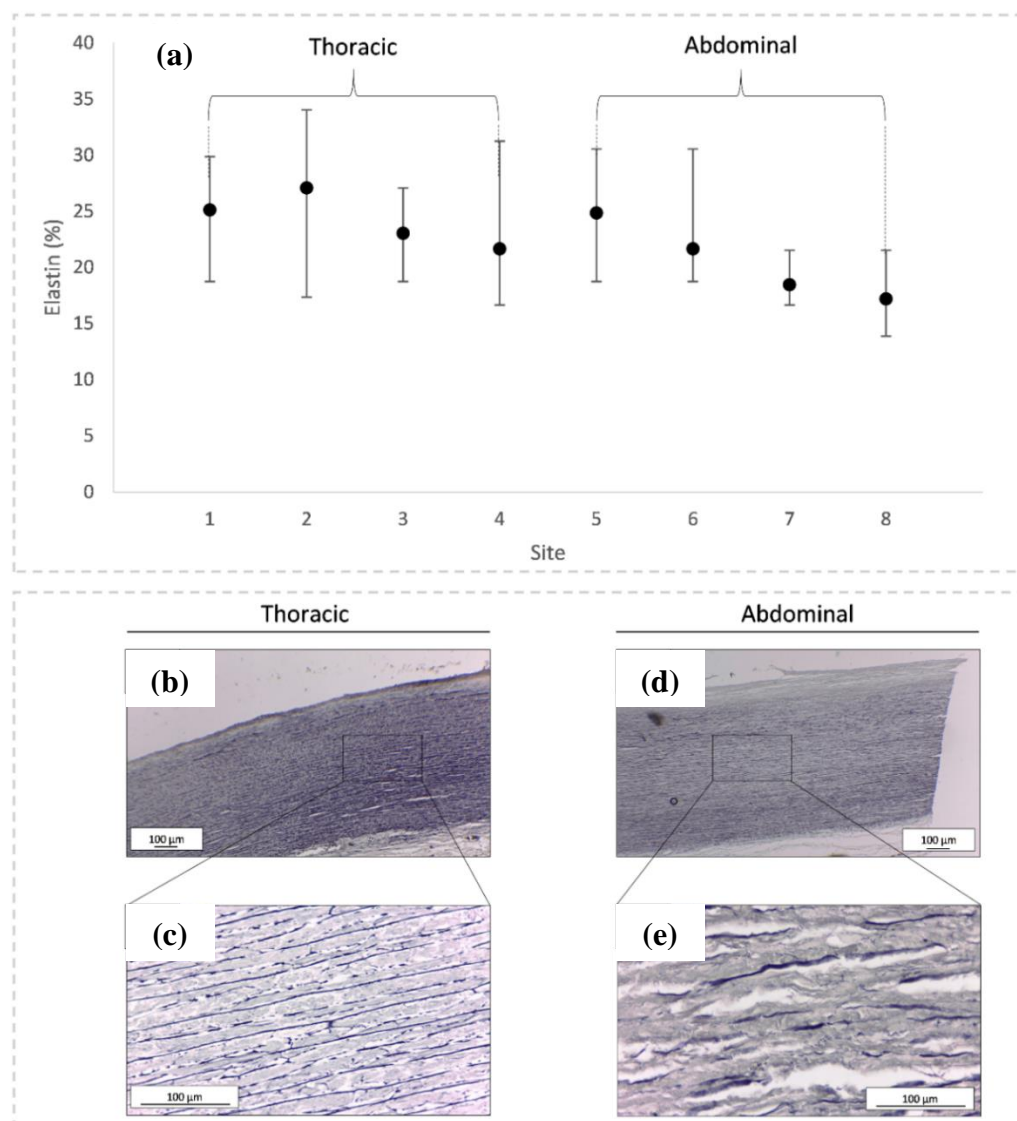


**Figure 4.3: Elastin as a function of location along the aorta; (b,c) thoracic aorta (Sites 1-4), (d,e) abdominal aorta (Sites 5-8). A 36.5% decrease in elastin content is observed between the ascending thoracic and distal abdominal portions of the vessel following staining by Verhoeff's method. Error bars show the range at each site from min to max.**

### 4.3.2 Collagen

Figure 4.4 shows the spatial variance in collagen content along the aorta from proximal to distal. In contrast to elastin, the area fraction of collagen increases with increasing distance from the heart. At the level of the proximal ascending aorta, collagen constitutes  $22 \pm 1.6\%$  of the vessel wall, while in the distal abdominal portion this is markedly increased to  $53 \pm 5.1\%$ . Making use of thoracic and abdominal subgroups, split by the diaphragm, a statistically significant difference in collagen content is observed ( $p=0.006$ ). Additionally, significant circumferential heterogeneity in collagen content is observed in the ascending thoracic aorta, with the highest area fraction observed on the medial segment of the wall (see Supplementary Material (Figure S1(c))).

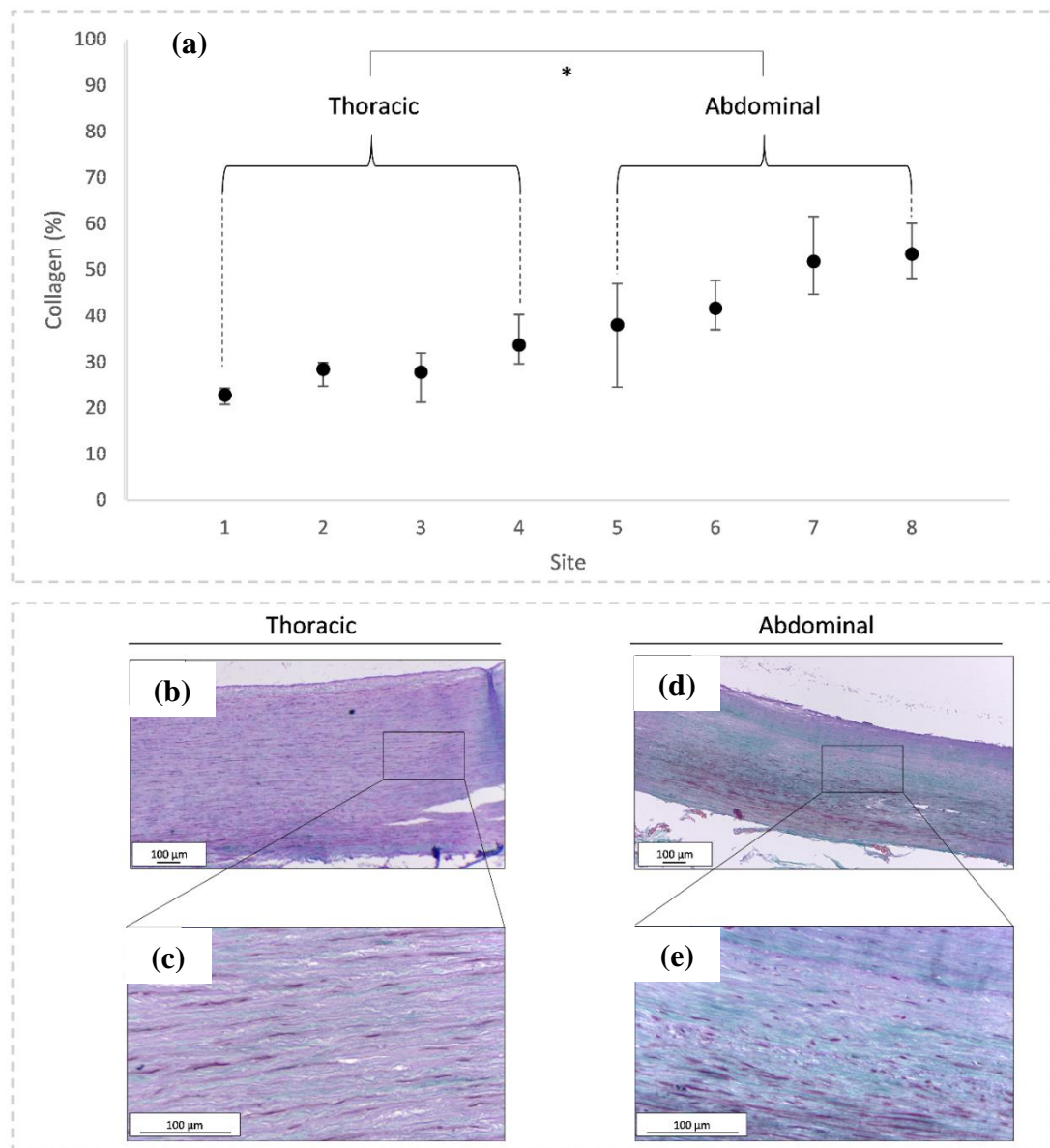


**Figure 4.4:** Collagen as a function of location along the aorta; (b,c) thoracic aorta (Sites 1-4), (d,e) abdominal aorta (Sites 5-8). A 133% increase in collagen content is observed between the ascending thoracic and distal abdominal portions of the vessel following Masson's Trichrome stain. Error bars show the range at each site from min to max, while \* indicates a statistically significant difference between thoracic and abdominal aorta subgroups ( $p < 0.05$ ).

### 4.3.3 Layer Thickness

Individual layer (intima, media and adventitia) thicknesses are presented for each location in Figure 4.5. The intimal thickness (defined by the internal elastic lamina) increases with increasing distance from the heart from  $100 \pm 47 \mu\text{m}$  at the proximal ascending to  $130 \pm 20 \mu\text{m}$  at the distal abdominal aorta. The media, bound by the internal and external elastic laminae markedly decreases from  $877 \pm 123 \mu\text{m}$  proximally to  $369 \pm 33 \mu\text{m}$  distally. Finally, the adventitia defined as outside the external elastic lamina increases from  $221 \pm 71 \mu\text{m}$  nearest the heart to  $323 \pm 12 \mu\text{m}$

immediately proximal to the common iliac bifurcation. Mean layer thickness values for the thoracic and abdominal aorta are presented in Table 4.2.

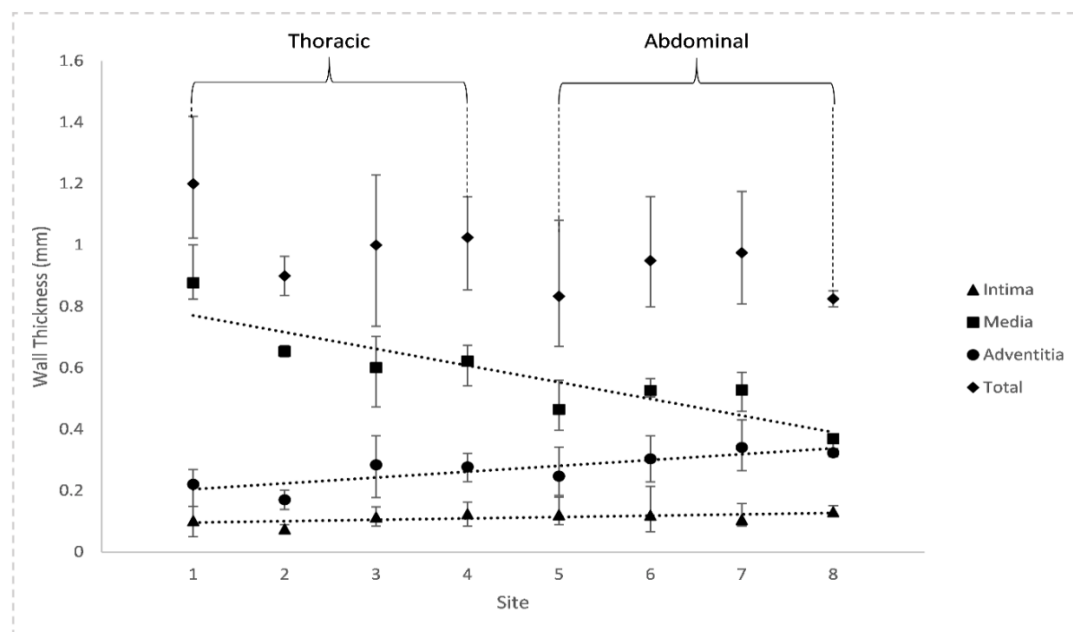


**Figure 4.5:** Intima/Media/Adventitia layer thickness breakdown according to location along the aorta. The overall aortic wall thickness changes from 1.2 mm to 0.83 mm from proximal to distal portions. Error bars show the range at each site from min to max.

**Table 4.2:** Wall layer thickness proportions, where (\*) and (\*\*) indicate  $p < 0.1$  and  $p < 0.05$  respectively.

	<u>Thoracic</u>				<u>Abdominal</u>			
Site	1	2	3	4	5	6	7	8
<b>Intima</b>	0.10	0.08	0.11	0.12	0.12	0.12	0.11	0.13
<b>Mean</b>	0.10				0.12			
<b>Media</b>	0.88	0.65	0.60	0.62	0.46	0.53	0.53	0.37
<b>Mean (**)</b>	0.69				0.47			
<b>Adventitia</b>	0.22	0.17	0.28	0.28	0.25	0.30	0.34	0.32
<b>Mean (*)</b>	0.24				0.30			

#### 4.4.4 Collagen Fiber Orientations

PLM techniques are employed in order to quantify the regional heterogeneity in collagen fiber orientations along both the axial and radial dimensions of the aorta. As outlined in Section 4.3.1, eight samples were analysed along the length of the aorta from proximal ascending to distal abdominal. For each sample, the orientation of the blocks is set to allow sectioning through the thickness of the wall layers, such that samples could be taken from the intima, media and adventitia at each axial location. Figure 4.6 illustrates the probability density histograms (dotted) for each aortic layer for each location along the vessel in ascending order from proximal to distal.

Significant heterogeneity is evident both radially and axially. Von-Mises mixture models (solid) fit to the data allow quantification of the mean and standard deviation (inversely related to Kappa) of each von-Mises ditribution which are taken to represent an individual fiber family. Parameters pertaining to each von-Mises mixture model can be found in Table 4.3.

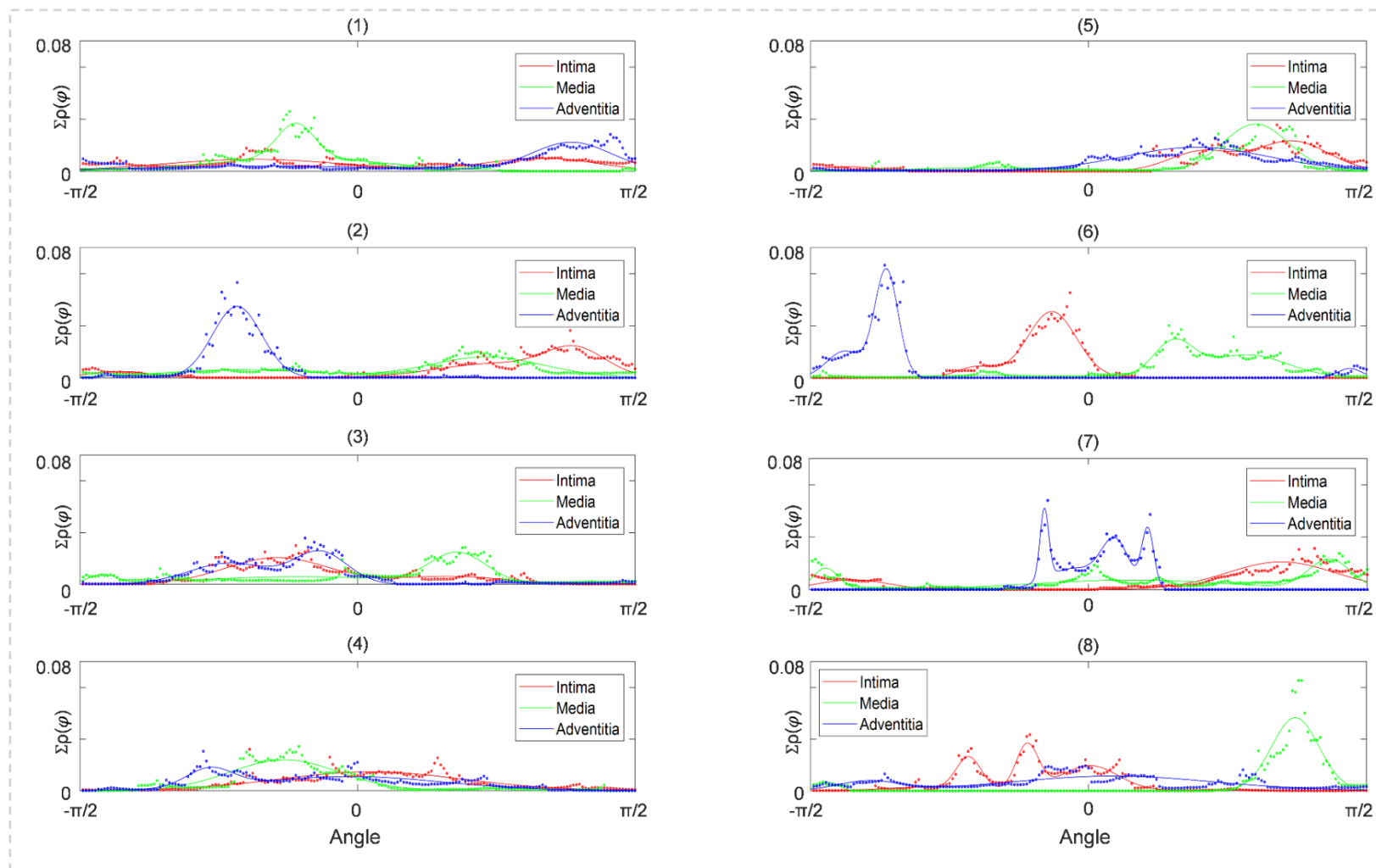


**Figure 4.6: Probability Density Histograms (dotted) for each site along the axial dimension of the aorta, with Von-Mises mixture model fits overlaid (solid). For each location the intima is indicated in red, media in green and adventitia and blue. 0 and  $\pm\pi/2$  represent the circumferential and axial axes of the sample respectively.**

**Table 4.3: Von-Mises mixture model parameters for each site and wall layer.**

<b>Location</b>	<b>n</b>	<b>Mean</b>	<b>Covariance</b>	<b>Proportion</b>
Site1_Intima	2	(-33.7), (59.9)	(3.8), (10.5)	(0.61), (0.39)
Site1_Media	3	(14.9), (-24.8), (-19.7)	(3.5), (5.8), (100.6)	(0.1), (0.57), (0.32)
Site1_Adventitia	2	(-30.5), (69.4)	(2.3), (19.7)	(0.37), (0.63)
Site2_Intima	2	(-77.0), (57.5)	(32.0), (8.5)	(0.11), (0.89)
Site2_Media	2	(-37.9), (42.1)	(5.1), (9.8)	(0.35), (0.65)
Site2_Adventitia	3	(23.2), (-39.0), (-76.5)	(17.9), (51.7), (77.4)	(0.02), (0.96), (0.02)
Site3_Intima	3	(52.8), (-26.6), (26.0)	(565.8), (12.4), (10.3)	(0.02), (0.75), (0.2)
Site3_Media	3	(-80.1), (26.3), (-51.3)	(65.5), (7.3), (11.5)	(0.08), (0.75), (0.17)
Site3_Adventitia	3	(61.7), (-41.5), (-11.9)	(8.9), (19.0), (44.4)	(0.06), (0.48), (0.46)
Site4_Intima	2	(18.9), (-11.9)	(4.2), (5.3)	(0.54), (0.46)
Site4_Media	2	(52.9), (-23.7)	(11.8), (10.7)	(0.06), (0.94)
Site4_Adventitia	2	(-47.9), (-2.2)	(58.2), (3.6)	(0.24), (0.76)
Site5_Intima	2	(-77.9), (55.1)	(37.5), (10.5)	(0.07), (0.93)
Site5_Media	2	(-31.2), (54.1)	(5.0), (29.4)	(0.16), (0.84)
Site5_Adventitia	2	(34.9), (-69.8)	(6.0), (12.0)	(0.97), (0.03)
Site6_Intima	2	(-36.2), (-11.9)	(81.8), (52.3)	(0.12), (0.88)
Site6_Media	3	(-38.9), (26.9), (43.9)	(4.3), (304.9), (11.9)	(0.1), (0.18), (0.71)
Site6_Adventitia	3	(84.6), (-65.4), (-78.9)	(224.8), (231), (97.4)	(0.06), (0.68), (0.26)
Site7_Intima	2	(-75.8), (62.3)	(26.7), (10.8)	(0.18), (0.82)
Site7_Media	3	(-84.7), (77.9), (13.9)	(193.5), (72.3), (3.4)	(0.15), (0.33), (0.52)
Site7_Adventitia	4	(-5.0), (19.3), (-14.1), (8.7)	(0.02), (0.001), (0.0006), (0.0062)	(0.3), (0.19), (0.16), (0.35)
Site8_Intima	5	(-37.4), (0.3), (46.2), (-19.7), (-39.4)	(10.2), (37.8), (11.3), (386.6), (356.2)	(0.2), (0.39), (0.02), (0.23), (0.16)
Site8_Media	2	(-84.4), (66.9)	(279.7), (56.2)	(0.05), (0.95)
Site8_Adventitia	3	(-68.4), (54.1), (-4.6)	(23.4), (11.9), (11.0)	(0.20), (0.23), (0.56)

Figure 4.7 highlights the evolution of fiber peaks along the length of the aorta for each tunical layer. Significant heterogeneity is evident in the mean angle and its standard deviation for each peak. At the majority of sites (intima (6/8 sites); media (5/8 sites); adventitia (6/8 sites)) peaks are observed at both a positive and negative angle to the circumferential axis. However, in general, the magnitude and standard deviation of each of the peaks at a given site are not symmetric about the circumferential axis. In the adventitial layer at sites 4,7 and 8 strong peaks are observed near to the circumferential axis, whereas in the media no strong peak is observed in on the circumferential axis. In the media the mean angle at a site becomes more positive

distally, whereas in the adventitia the mean angle at a site becomes more negative distally.

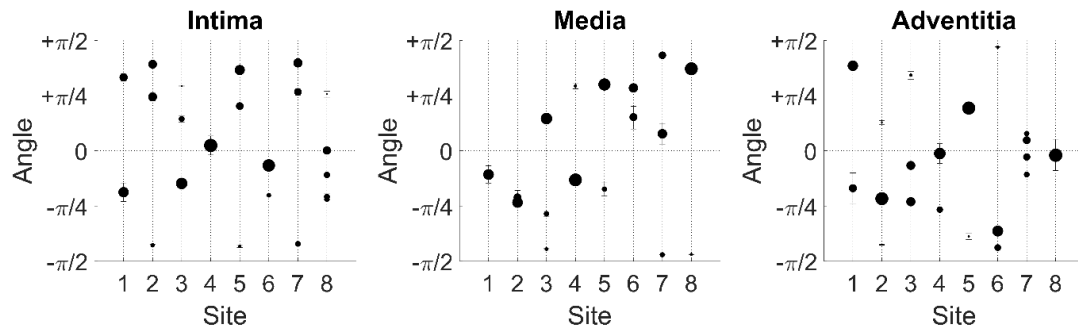


**Figure 4.7: Evolution of fiber peaks along the aorta for each layer (intima, media, adventitia). For each site, from proximal to distal aorta, the size of the filled circle represents the proportion of the von-Mises mixture model captured by the given mean angle and spread of each peak. In each case, the standard deviation about each mean is represented by the solid vertical bars.**

Finally, SMC content is investigated as a function of position along the aorta, results of which are presented in Figure 4.8. The proximal aorta exhibits a lower density of SMCs than the distal abdominal portion with an area fraction of 22.4% vs 27.0% respectively. Categorising the sample sites into thoracic and abdominal subgroups, a statistically significant difference in SMC content (Figure 4.8(a)) is observed between the two groups split by the diaphragm ( $p=0.009$ ). Additionally, a higher number of SMC nuclei/ $\text{mm}^2$  (Figure 4.8(b)) are observed distally compared to proximally.

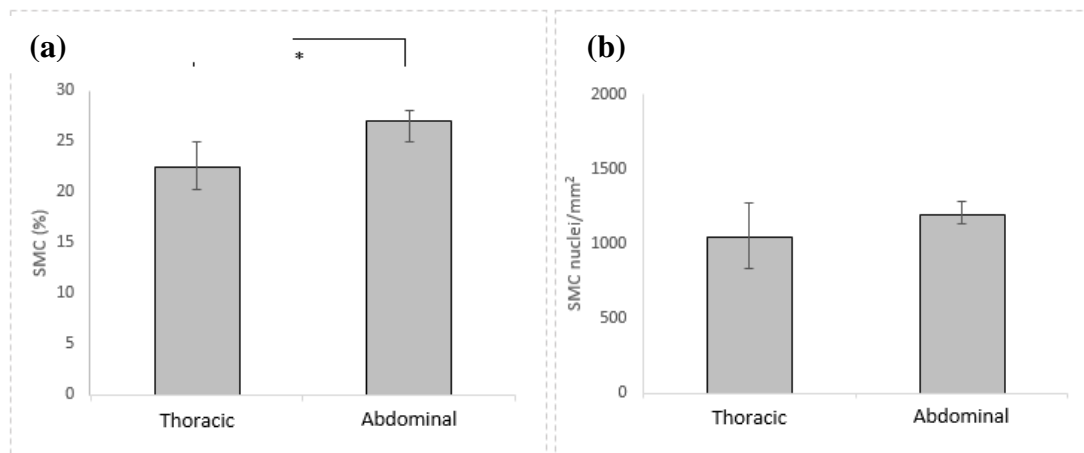


**Figure 4.8: (a) SMC area fraction (%). (b) Number of SMC nuclei/ $\text{mm}^2$ . Error bars show the range at each site from min to max, while \* indicates a statistically significant difference between thoracic (Sites 1-4) and abdominal (Sites 5-8) aorta subgroups ( $p<0.05$ ).**

## 4.4 Discussion

The focus of this chapter is to investigate the regional bioarchitecture of the human aorta, specifically, the constituents which contribute to the compliance of the vessel. The study quantifies the orientation and density of the main load bearing constituents of the wall at a number of discrete points along the aorta from proximal ascending to distal abdominal portions. It is shown that the organisation of collagen fibers is highly complex, while the quantification and fitting of the orientation distributions raises questions regarding the accuracy of models that assume collagen fibers to be homogeneously (Roy *et al.*, 2014) and symmetrically (Grytsan and Holzapfel, 2015) distributed throughout. The quantification of spatial variance in aortic bioarchitecture will provide advance through integration with advanced finite element models, incorporating the true regional microstructure of the aorta to levels of unprecedented detail. To the author's knowledge, no previous study to date has quantified, using histological and stereological methods, the regional variations in elastin, collagen and SMC distributions in human cadaveric aortae.

The regional density of elastin within the aortic wall from the proximal ascending to distal abdominal segments was examined. The high levels of elastin in the proximal ascending aorta ( $27 \pm 4.7\%$ ) render it the dominant protein within the wall proximally. Additionally, significant circumferential heterogeneity in elastin content is observed in the ascending thoracic aorta, with the highest area fraction observed on the lateral segment of the wall (see Supplementary Material (Figure S1(a))). From a biomechanical point of view, high levels of elasticity within the vessel wall proximally are crucial for maintenance of the Windkessel effect, left ventricular function and diastolic flow (Belz, 1995; Davies *et al.*, 2008; João L Cavalcante *et al.*, 2011). Distally, a reduction in elastin concentration of 36.5% is observed at the level immediately proximal to the common iliac bifurcation ( $17 \pm 3.9\%$ ). This is in broad agreement with Halloran *et al.*, (1995) who observed a decrease in elastin concentration using biochemical analysis between the thoracic and abdominal segments. As the Windkessel effect results from the compliance of aortic tissue, a decrease in elastin and increase in collagen and SMCs distally suggests a microstructural mechanism for heterogeneous aortic compliance observed previously *in-vitro*. An inverse relationship between elastin and SMCs exists whereby SMC content is higher distally which dictates vascular tone. Haskett *et al.*, (2010) subjected human aortic tissue samples to biaxial tension and found that the abdominal aorta was significantly stiffer than proximal regions while Kim *et al.*, (2013) observed under bulge inflation tests of thoracic aortic rings, that distal segments were stiffer than proximal segments. Without the implementation of histological and stereological techniques however, the components of aortic tissue contributing to this increased stiffness cannot be determined.

Investigation of the regional density of collagen within the aortic wall provides insight into both its importance at specific anatomical locations and its role in the deformation of the system. In the proximal ascending aorta collagen content is lowest ( $22 \pm$

1.6 %) but becomes far more pronounced with increasing distance from the heart, and distally becomes the dominant protein within the wall ( $53 \pm 5.1$  %). Additionally, significant circumferential heterogeneity in collagen content is observed in the ascending thoracic aorta, with the highest area fraction observed on the medial segment of the wall (see Supplementary Material (Figure S1(c))). The increased density of collagen distally observed here is also in agreement with work published on various species (Grant, 1967) although in Grant, (1967), the authors rely on biochemical methods for the quantification of collagen through hydroxyproline, which is also present in elastin. The inverse relationship between elastin and collagen observed in this study is in agreement with previous work stating that the ratio of elastin to collagen decreases markedly between the aorta and femoral arteries in both porcine and murine populations (Sokolis and Karayannacos, 2008; Basu *et al.*, 2010). With collagen reported to exhibit 5,000 times the tensile stiffness of elastin (João L Cavalcante *et al.*, 2011), results presented here also provide microstructural insight into the increased stiffness seen in the distal aorta both *in-vitro* (Moriwaki *et al.*, 2011a; Krüger *et al.*, 2016) and *in-vivo* (Mohiaddin *et al.*, 1989; Saouti *et al.*, 2012). Moreover, these findings suggest that the common description of aortic compliance by a single coefficient may be inaccurate (Lehmann *et al.*, 1998; Vyas *et al.*, 2007; Lalande *et al.*, 2008a).

Due to the nature of collagen fibers being orders of magnitude stiffer than the other constituents of aortic tissue, the vessel walls behave like a fiber reinforced composite, in that the orientation of the fibers plays a role in the structural anisotropy of the vessel wall. Thus, fiber density alone cannot fully describe the compliance of the vessel, and hence an investigation of the orientation of collagen fibers within the aortic wall at each location was performed as outlined previously. Significant dispersion is evident in each probability density histogram, in addition to notable transmural variation in mean fiber angles between the intima, media and adventitia. Interestingly, the presence of two equally dominant, and symmetric fiber families is absent.

Although two families (peaks in probability density histogram) are frequently apparent in the present data, in each case one constitutes significantly more area fraction than the other. O'Connell *et al.*, (2008), Horny *et al.*, (2010), Schriefl *et al.*, (2012), Chow *et al.*, (2014), Sassani *et al.*, (2015), Weisbecker & Holzapfel, (2015), and Sugita & Matsumoto, (2018) report that a single family of fibers was evident, however others have reported two (Schriefl *et al.*, 2012b; Laksari *et al.*, 2016), three (Schriefl *et al.*, 2012) and even four (R. Rezakhaniha *et al.*, 2012; Schriefl *et al.*, 2012) fiber families, all of which are evident here, further emphasizing aortic microarchitectural heterogeneity at a local level. It is shown that a von Mises mixture model is required to accurately fit the complexity of collagen fiber orientations that exists along the aorta, which suggests that common constitutive laws implemented through finite element analysis (Holzapfel, Gasser and Ogden, 2000; Nolan *et al.*, 2014) may not be capable of fully capturing the full anisotropy of the vessel.

Significant variance in layer thicknesses is observed along the aortic length within the intima, media and adventitia. Results show that intimal thickness increases from the proximal ( $100 \pm 47 \mu\text{m}$ ) to distal aorta ( $130 \pm 20 \mu\text{m}$ ). Similarly, adventitial layer thickness increases from the proximal ( $221 \pm 71 \mu\text{m}$ ) to distal ( $323 \pm 12 \mu\text{m}$ ) aorta. The medial layer however, decreases from the proximal ( $877 \pm 123 \mu\text{m}$ ) to distal ( $369 \pm 33 \mu\text{m}$ ) aorta. The overall wall thickness reduces from  $1200 \pm 430 \mu\text{m}$  to  $825 \pm 192 \mu\text{m}$  with increasing distance from the heart. Results shown here are in agreement with work published by Rhodin, (1980) and Schriefl *et al.*, (2012) where these authors report an increase in both intimal and adventitial thicknesses in addition to a decrease in medial thickness distally.

We also examine SMC content in order to investigate the spatial distribution of active constituents within the aortic wall. Results show that SMC content increases with increasing distance from the heart with 22.4% of the proximal ascending aortic wall comprising of SMCs, while this increases to 27.0% in the distal abdominal aorta. Although the aorta is considered to be, relative to smaller calibre vessels which are termed muscular, an elastic artery (Lacolley *et al.*, 2017), a significant difference is observed regionally between the proximal thoracic and distal abdominal portions that follows the tapering of the aorta with increased SMC density distally. This result is in agreement with reports by Lacolley *et al.*, (2017) and the findings of Arnaud, (2000) where the abdominal aorta exhibited a higher basal requirement for oxygen consumption and mitochondrial activity than its thoracic counterpart in the porcine aorta. The same authors hypothesize that the more passive elastic nature of the proximal aorta overrides the requirement for a dense active component whereas the abdominal aorta may be subject to a more pronounced vasoactive regulation. Future work should investigate the spatial variance in the three-dimensional morphology of SMCs and nuclei, including detailed quantification of aspect ratio and cell volume.

Due to legislative constraints cell content and collagen fiber orientation analyses were only conducted on one of the donors. Further work is warranted here to increase the sample size to gain a better insight into the true variability of such parameters. However, considerable differences are apparent even within each constituent of the cohort studied here, and so care should be taken when averaging values across donors not to lose important inter-sample variances due to age, lifestyle and medical history. Finally, it should be noted that the average age of the donors in this study is 77.6 years which is entirely due to availability, and as such reflects an elderly population. Further scope exists in extending this framework to a younger comparative cohort in order to characterise the effects of ageing on the regional bioarchitecture.

The detailed insights into the spatially varying bioarchitecture of the human aorta revealed in this chapter are critical for the development of a more complete understanding of aortic anatomy and physiology and its complex changes throughout its length. The individual component densities and orientations of elastin, collagen and SMCs, all contribute to the complex local mechanical behaviour of the aorta, ultimately governing the non-linear elasticity and contractility of the vessel. Follow-

on 4D Flow MRI/finite element investigations are being performed to parse the individual contributions of the components of the aortic wall to the spatial heterogeneity in aortic biomechanics. Significant heterogeneity between the thoracic and abdominal aorta in terms of embryology, atherosclerotic plaque deposition, protease profiles and cell signalling pathways has been reported previously (see review by (Ruddy *et al.*, 2008), in addition to heterogeneous changes in mechanical behaviour for porcine tissue, Kim *et al.*, (2013). Results presented in the current study provide new information on the complex distributions of fibres at each section along the aorta, in addition to detailed quantification of the spatial heterogeneity of the aortic microstructure.

All values of wall thickness and fibre orientation reported in this study are for unloaded tissue. Therefore, such data can be directly input to a finite element model in the unloaded reference configuration. Simulation of the artery response to applied physiological loading (e.g. diastolic/systolic lumen pressure profiles) could readily predict heterogeneous changes in wall thickness and fibre orientation during a cardiac cycle. A follow-on study will be performed in which the heterogeneous microstructural and geometric data will be input into a finite element framework. Finally, the data presented can facilitate the generation of the most advanced anisotropic finite element models of the human aorta available to date, highlighting the importance of integrating histological and stereological data with the field of computational science.

#### **4.5 Conclusion**

The spatial variance in bioarchitecture of the human aorta was quantified using histological and stereological techniques. Significant heterogeneity is evident in the orientation of collagen fibers both axially and transmurally within the aortic wall. Heterogeneity in elastin, collagen, and SMC content is also observed along the axial dimension of the aorta. In the proximal ascending portion, elastin is the dominant protein whereas collagen is the dominant protein within the wall distally, rendering this area naturally less compliant. Morphological analyses show the thickness of each tunical layer to also vary significantly with increasing distance from the heart. Finally, the quantification and fitting of regional aortic bioarchitectural data can serve as a direct input into the development of next-generation finite element models, that can potentially simulate the influence of regional aortic composition and microstructure on vessel biomechanics.

#### **4.6 Acknowledgements**

The author would like to thank Mr. Mark Canney, Mr. Ian O' Brien, Mr. Jon Hunt and Mr. Peter Owens for their help throughout this study. The provision, training and supervision of the transmitted polarised light microscopy techniques used during this research were provided by the Geofluids Research Laboratory, Earth and Ocean Sciences, NUI Galway.

## 4.7 Bibliography

- Arnaud, F. (2000) 'Endothelial and Smooth Muscle Changes of the Thoracic and Abdominal Aorta with Various Types of Cryopreservation 1', *Journal of Surgical Research*, 89, pp. 147–154. doi: 10.1006/jsre.2000.5816.
- Basu, P., Sen, U., Tyagi, N. and Tyagi, S. C. (2010) 'Blood flow interplays with elastin: collagen and MMP: TIMP ratios to maintain healthy vascular structure and function.', *Vascular health and risk management*. Dove Press, 6, pp. 215–28. Available at: <http://www.ncbi.nlm.nih.gov/pubmed/20407629> (Accessed: 12 March 2019).
- Baxter, B. T., McGee, G. S., Shively, V. P., Drummond, I. A. S., Dixit, S. N., Yamauchi, M. and Pearce, W. H. (1992) 'Elastin content, cross-links, and mRNA in normal and aneurysmal human aorta', *Journal of Vascular Surgery*. Elsevier, 16(2), pp. 192–200. doi: 10.1016/0741-5214(92)90107-J.
- Beach, J. M., Kuramochi, Y., Brier, C., Roselli, E. E. and Eagleton, M. J. (2017) 'Durable outcomes of thoracic endovascular aortic repair with Zenith TX1 and TX2 devices.', *Journal of vascular surgery*. Elsevier, 65(5), pp. 1287–1296. doi: 10.1016/j.jvs.2016.11.029.
- Belz, G. G. (1995) 'Elastic Properties and of the Human Aorta Windkessel Function', *Cardiovascular Drugs and Therapy*, 9, pp. 73–83. Available at: <https://link.springer.com/content/pdf/10.1007%2F00877747.pdf> (Accessed: 19 September 2018).
- Berry, C. L. and Greenwald, S. E. (1976) 'Effects of hypertension on the static mechanical properties and chemical composition of the rat aorta', *Cardiovascular Research*. Oxford University Press, 10(4), pp. 437–451. doi: 10.1093/cvr/10.4.437.
- Bischoff, M. S., Ante, M., Meisenbacher, K. and Böckler, D. (2016) 'Outcome of thoracic endovascular aortic repair in patients with thoracic and thoracoabdominal aortic aneurysms', *Journal of Vascular Surgery*. Elsevier, 63(5), p. 1170–1181.e1. doi: 10.1016/j.jvs.2015.11.045.
- Carlton, R. A. (2011) 'Polarized Light Microscopy', in *Pharmaceutical Microscopy*. New York, NY: Springer New York, pp. 7–64. doi: 10.1007/978-1-4419-8831-7\_2.
- Cattell, M. A., Anderson, J. C. and Hasleton, P. S. (1996) 'Age-related changes in amounts and concentrations of collagen and elastin in normotensive human thoracic aorta', *Clinica Chimica Acta*. Elsevier, 245(1), pp. 73–84. doi: 10.1016/0009-8981(95)06174-6.
- Cavalcante, J. L., Lima, J. A. C., Redheuil, A. and Al-Mallah, M. H. (2011) 'Aortic Stiffness Current Understanding and Future Directions', *JAC*, 57, pp. 1511–1522. doi: 10.1016/j.jacc.2010.12.017.
- Chayen, J. (1983) 'Polarised light microscopy: principles and practice for the rheumatologist', *Ann Rheum Dis*, 42, p. p64. Available at: <https://www.ncbi.nlm.nih.gov/pmc/articles/PMC1035042/pdf/annrheumd00249-0071.pdf> (Accessed: 18 September 2018).

- Choudhury, N. and Leask, R. L. (2009) 'Local mechanical and structural properties of healthy and diseased human ascending aorta tissue', *Cardiovascular Pathology*, 18(2), pp. 83–91. doi: 10.1016/j.carpath.2008.01.001.
- Chow, M.-J., Turcotte, R., Lin, C. P. and Zhang, Y. (2014) 'Arterial Extracellular Matrix: A Mechanobiological Study of the Contributions and Interactions of Elastin and Collagen', *Biophysical journal*, 106, pp. 2684–2692. doi: 10.1016/j.bpj.2014.05.014.
- Concannon, J., Kavanagh, E. P., Hynes, N., McHugh, P. E., McGarry, J. P. and Sultan, S. (2017) 'The Streamliner Multilayer Flow Modulator in the treatment of Complex Thoracoabdominal Aortic Aneurysms', *Vascular*, 25(2), p. suppl.
- Conrad, M. F., Tucek, J., Freezor, R., Bavaria, J., White, R. and Fairman, R. (2017) 'Results of the VALOR II trial of the Medtronic Valiant Thoracic Stent Graft', *Journal of Vascular Surgery*. Mosby, 66(2), pp. 335–342. doi: 10.1016/J.JVS.2016.12.136.
- Davidson, J. M., Hill, K. E., Mason, M. L. and Giro\$, M. G. (1985) 'Longitudinal Gradients of Collagen Porcine Aorta\* and Elastin Gene Expression in the', *THE JOURNAL OF BIOLOGICAL CHEMISTRY*, 260(3), pp. 1301–1908. Available at: <http://www.jbc.org/content/260/3/1901.full.pdf> (Accessed: 7 June 2018).
- Davies, J. E., Parker, K. H., Francis, D. P., Hughes, A. D., Mayet, J. and Davies, J. (2008) 'What is the role of the aorta in directing coronary blood flow?', *Heart*, (144808). doi: 10.1136/hrt.2008.144808.
- Elias, H., Hennig, A. and Schwartz, D. E. (1971) 'Stereology: Applications to Biomedical Research', *Physiological Reviews*, 51(1). Available at: [www.physiology.org/journal/physrev](http://www.physiology.org/journal/physrev) (Accessed: 18 September 2018).
- Evanko, S. P., Chan, C. K., Johnson, P. Y., Frevert, C. W. and Wight, T. N. (2018) 'The biochemistry and immunohistochemistry of versican', *Methods in Cell Biology*. Academic Press, 143, pp. 261–279. doi: 10.1016/BS.MCB.2017.08.015.
- Faber, M. and Moller-Hou, G. (2009) 'The human aorta', *Acta Pathologica Microbiologica Scandinavica*. Wiley/Blackwell (10.1111), 31(3), pp. 377–382. doi: 10.1111/j.1699-0463.1952.tb00205.x.
- Feldman, S. A. and Glagov, S. (1971) 'Transmedial collagen and elastin gradients in human aortas: Reversal with age', *Atherosclerosis*. Elsevier, 13(3), pp. 385–394. doi: 10.1016/0021-9150(71)90081-5.
- Fritze, O., Romero, B., Schleicher, M., Jacob, M. P., Oh, D.-Y., Starcher, B., Schenke-Layland, K., Bujan, J. and Stock, U. A. (2012) 'Age-related changes in the elastic tissue of the human aorta.', *Journal of vascular research*. Karger Publishers, 49(1), pp. 77–86. doi: 10.1159/000331278.
- Gaul, R. T., Nolan, D. R. and Lally, C. (2017) 'Collagen fibre characterisation in arterial tissue under load using SALS', *Journal of the Mechanical Behavior of Biomedical Materials*. Elsevier, 75, pp. 359–368. doi: 10.1016/J.JMBBM.2017.07.036.
- Grant, R. A. (1967) 'Content and distribution of aortic collagen, elastin and carbohydrate in different species', *Journal of Atherosclerosis Research*. Elsevier, 7(4), pp. 463–472. doi: 10.1016/S0368-1319(67)80024-3.

- Grytsan, A., Watton, P. N. and Holzapfel, G. A. (2015) ‘A thick-walled fluid-solid-growth model of abdominal aortic aneurysm evolution: application to a patient-specific geometry.’, *Journal of biomechanical engineering*. American Society of Mechanical Engineers, 137(3), p. 031008. doi: 10.1115/1.4029279.
- Gültekin, O., Dal, H. and Holzapfel, G. A. (2016) ‘A phase-field approach to model fracture of arterial walls: Theory and finite element analysis’, *Computer Methods in Applied Mechanics and Engineering*, 312, pp. 542–566. doi: 10.1016/j.cma.2016.04.007.
- Halloran, B. G., Davis, V. A., McManus, B. M., Lynch, T. G. and Baxter, B. T. (1995) ‘Localization of Aortic Disease Is Associated with Intrinsic Differences in Aortic Structure’, *Journal of Surgical Research*. Academic Press, 59(1), pp. 17–22. doi: 10.1006/jsre.1995.1126.
- Halme, T., Savunen, T., Aho, H., Vihersaari, T. and Penttinen, R. (1985) ‘Elastin and collagen in the aortic wall: Changes in the Marfan syndrome and annuloaortic ectasia’, *Experimental and Molecular Pathology*. Academic Press, 43(1), pp. 1–12. doi: 10.1016/0014-4800(85)90050-4.
- Hansen, M., Kongsgaard, M., Holm, L., Skovgaard, D., Magnusson, S. P., Qvortrup, K., Larsen, J. O., Aagaard, P., Dahl, M., Serup, A., Frystyk, J., Flyvbjerg, A., Langberg, H. and Kjaer, M. (2009) ‘Effect of estrogen on tendon collagen synthesis, tendon structural characteristics, and biomechanical properties in postmenopausal women’, *Journal of Applied Physiology*. American Physiological Society, 106(4), pp. 1385–1393. doi: 10.1152/jappphysiol.90935.2008.
- Harkness, M. L., Harkness, R. D. and McDonald, D. A. (1957) ‘The collagen and elastin content of the arterial wall in the dog.’, *Proceedings of the Royal Society of London. Series B, Biological sciences*, 146(925), pp. 541–51. Available at: <http://www.ncbi.nlm.nih.gov/pubmed/13441679> (Accessed: 31 May 2018).
- Haskett, D., Johnson, G., Zhou, A., Utzinger, U. and Vande Geest, J. (2010) ‘Microstructural and biomechanical alterations of the human aorta as a function of age and location’, *Biomechanics and Modeling in Mechanobiology*. Springer-Verlag, 9(6), pp. 725–736. doi: 10.1007/s10237-010-0209-7.
- Holzapfel, G. A., Gasser, T. C. and Ogden, R. W. (2000) ‘A New Constitutive Framework for Arterial Wall Mechanics and a Comparative Study of Material Models’, *Journal of elasticity and the physical science of solids*. Kluwer Academic Publishers, 61(1–3), pp. 1–48. doi: 10.1023/A:1010835316564.
- Horny, L., Kronek, J., Chlup, H., Zitny, R., Vesely, J. and Hulam, M. (2010) ‘Orientations of collagen fibers in aortic histological section’, *BULLETIN OF APPLIED MECHANICS*, 6(22), pp. 25–29. Available at: <http://users.fs.cvut.cz/~hornyluk/files/Horny-L-2010-Orientations-of-collagen-fibers-in-aortic-histological-section.pdf> (Accessed: 20 September 2018).
- Hosoda, Y., Kawano, K., Yamasawa, F., Ishii, T., Shibata, T. and Inayama, S. (1984) ‘Age-Dependent Changes of Collagen and Elastin Content in Human Aorta and Pulmonary Artery’, *Angiology*. Sage PublicationsSage CA: Thousand Oaks, CA, 35(10), pp. 615–621. doi: 10.1177/000331978403501001.

- Hung, W.-L., Chang-Chien, S.-J. and Yang, M.-S. (2012) 'Self-updating clustering algorithm for estimating the parameters in mixtures of von Mises distributions', *Journal of Applied Statistics*. Taylor & Francis, 39(10), pp. 2259–2274. doi: 10.1080/02664763.2012.706268.
- Junqueira, L. C. U., Bignolas, G. and Brentani, R. R. (1979) 'Picrosirius staining plus polarization microscopy, a specific method for collagen detection in tissue sections', *The Histochemical Journal*. Kluwer Academic Publishers, 11(4), pp. 447–455. doi: 10.1007/BF01002772.
- Kaerberlein, M. and Martin, G. M. (2016) *Handbook of the biology of aging*. 8th edn. Edited by N. Musi and P. Hornsby. Academic Press.
- Karšaj, I. and Humphrey, J. D. (2012) 'A multilayered wall model of arterial growth and remodeling', *Mechanics of Materials*, 44, pp. 110–119. doi: 10.1016/j.mechmat.2011.05.006.
- Kim, J., Hong, J.-W. and Baek, S. (2013) 'Longitudinal differences in the mechanical properties of the thoracic aorta depend on circumferential regions.', *Journal of biomedical materials research. Part A*, 101(5), pp. 1525–9. doi: 10.1002/jbm.a.34445.
- Krasny, W., Magoariec, H., Morin, C. and Avril, S. (2018) 'Kinematics of collagen fibers in carotid arteries under tension-inflation loading', *Journal of the Mechanical Behavior of Biomedical Materials*. Elsevier, 77, pp. 718–726. doi: 10.1016/J.JMBBM.2017.08.014.
- Krüger, T., Veseli, K., Lausberg, H., Vöhringer, L., Schneider, W. and Schlensak, C. (2016) 'Regional and directional compliance of the healthy aorta: an ex vivo study in a porcine model', *Interactive CardioVascular and Thoracic Surgery*, 23(1), pp. 104–111. doi: 10.1093/icvts/ivw053.
- Lacolley, P., Regnault, V., Segers, P. and Laurent, S. (2017) 'Vascular Smooth Muscle Cells and Arterial Stiffening: Relevance in Development, Aging, and Disease', *Physiol Rev*, 97, pp. 1555–1617. doi: 10.1152/physrev.00003.2017.
- Laksari, K., Shahmirzadi, D., Acosta, C. J. and Konofagou, E. (2016) 'Energy-based constitutive modelling of local material properties of canine aortas', *Journal of the Royal Society, Interface*, 3(9), p. 160365. doi: 10.1098/rsos.160365.
- Lalande, A., Khau Van Kien, P., Walker, P. M., Zhu, L., Legrand, L., Claustres, M., Jeunemaître, X., Brunotte, F. and Wolf, J. E. (2008) 'Compliance and pulse wave velocity assessed by MRI detect early aortic impairment in young patients with mutation of the smooth muscle myosin heavy chain', *Journal of Magnetic Resonance Imaging*. Wiley Subscription Services, Inc., A Wiley Company, 28(5), pp. 1180–1187. doi: 10.1002/jmri.21565.
- Lehmann, E. D., Hopkins, K. D., Rawesh, A., Joseph, R. C., Kongola, K., Coppack, S. W. and Gosling, R. G. (1998) 'Relation between number of cardiovascular risk factors/events and noninvasive Doppler ultrasound assessments of aortic compliance.', *Hypertension (Dallas, Tex. : 1979)*. American Heart Association, Inc., 32(3), pp. 565–9. doi: 10.1161/01.HYP.32.3.565.
- Martín, C. E., Forteza, A., Pérez, E., López, M. J., Centeno, J., Blázquez, J. A., de Diego, J., García, D. and Cortina, J. M. (2008) 'Predictors of Mortality and

- Reoperation in Acute Type-A Aortic Dissection Surgery: 18 Years of Experience', *Revista Española de Cardiología (English Edition)*. Elsevier, 61(10), pp. 1050–1060. doi: 10.1016/S1885-5857(09)60008-6.
- Maurel, E., Shuttleworth, C. A. and Bouissou, H. (1987) 'Interstitial collagens and ageing in human aorta.', *Virchows Archiv. A, Pathological anatomy and histopathology*, 410(5), pp. 383–90. Available at: <http://www.ncbi.nlm.nih.gov/pubmed/3103320> (Accessed: 19 September 2018).
- Mayhew, T. (1991) 'The new stereological methods for interpreting functional morphology from slices of cells and organs', *Experimental Physiology*. Wiley/Blackwell (10.1111), 76(5), pp. 639–665. doi: 10.1113/expphysiol.1991.sp003533.
- Mohiaddin, R. H., Underwood, S. R., Bogren, H. G., Firmin, D. N., Klipstein, R. H. and Longmore, D. B. (1989) 'Regional aortic compliance studied by magnetic resonance imaging: the effects of age, training, and coronary artery disease', *Br Heart J*, 62, pp. 90–6. Available at: <http://heart.bmj.com/content/heartjnl/62/2/90.full.pdf> (Accessed: 2 March 2018).
- Moriwaki, T., Oie, T., Takamizawa, K., Murayama, Y., Fukuda, T., Omata, S., Kanda, K. and Nakayama, Y. (2011) 'Variations in local elastic modulus along the length of the aorta as observed by use of a scanning haptic microscope (SHM)', *Journal of Artificial Organs*. Springer Japan, 14(4), pp. 276–283. doi: 10.1007/s10047-011-0596-2.
- Murphy, D. B. (2002) *Fundamentals of Light Microscopy and Electronic Imaging*. 2nd edn. John Wiley & Sons, Ltd.
- Nolan, D. ., Ogden, R. W., Destrade, M. and McGarry, J. P. (2014) 'A robust anisotropic hyperelastic formulation for the modelling of soft tissue', *Journal of the Mechanical Behaviour of Biomedical Materials*.
- O'Connell, M. K., Murthy, S., Phan, S., Xu, C., Buchanan, J., Spilker, R., Dalman, R. L., Zarins, C. K., Denk, W. and Taylor, C. A. (2008) 'The three-dimensional micro- and nanostructure of the aortic medial lamellar unit measured using 3D confocal and electron microscopy imaging', *Matrix Biology*. Elsevier, 27(3), pp. 171–181. doi: 10.1016/J.MATBIO.2007.10.008.
- Püspöki, Z., Storath, M., Sage, D. and Unser, M. (2016) 'Transforms and Operators for Directional Bioimage Analysis: A Survey', *Advances in Anatomy, Embryology and Cell Biology*, 219, pp. 63–93. doi: 10.1007/978-3-319-28549-8\_3.
- Qi, Y.-X., Jiang, J., Jiang, X.-H., Wang, X.-D., Ji, S.-Y., Han, Y., Long, D.-K., Shen, B.-R., Yan, Z.-Q., Chien, S. and Jiang, Z.-L. (2011) 'PDGF-BB and TGF- $\beta$ 1 on cross-talk between endothelial and smooth muscle cells in vascular remodeling induced by low shear stress.', *Proceedings of the National Academy of Sciences of the United States of America*. National Academy of Sciences, 108(5), pp. 1908–13. doi: 10.1073/pnas.1019219108.
- Rezakhaniha, R., Agianniotis, A., Schrauwen, J. T. C., Griffa, A., Sage, D., Bouten, C. V. C., van de Vosse, F. N., Unser, M. and Stergiopoulos, N. (2012) 'Experimental investigation of collagen waviness and orientation in the arterial

- adventitia using confocal laser scanning microscopy’, *Biomechanics and Modeling in Mechanobiology*. Springer-Verlag, 11(3–4), pp. 461–473. doi: 10.1007/s10237-011-0325-z.
- Rhodin, J. A. G. (1980) ‘Architecture of the Vessel Wall’, in *Comprehensive Physiology*. Hoboken, NJ, USA: John Wiley & Sons, Inc., pp. 1–31. doi: 10.1002/cphy.cp020201.
- Roy, D., Holzapfel, G. A., Kauffmann, C. and Soulez, G. (2014) ‘Finite element analysis of abdominal aortic aneurysms: geometrical and structural reconstruction with application of an anisotropic material model’, *IMA Journal of Applied Mathematics*. Oxford University Press, 79(5), pp. 1011–1026. doi: 10.1093/imamat/hxu037.
- Ruddy, J. M., Jones, J. A., Spinale, F. G. and Ikonomidis, J. S. (2008) ‘Regional heterogeneity within the aorta: relevance to aneurysm disease.’, *The Journal of thoracic and cardiovascular surgery*, 136(5), pp. 1123–30. doi: 10.1016/j.jtcvs.2008.06.027.
- Saey, V., Famaey, N., Smoljkic, M., Claeys, E., Van Loon, G., Ducatelle, R., Ploeg, M., Delesalle, C., Gröne, A., Duchateau, L. and Chiers, K. (2015) ‘Biomechanical and biochemical properties of the thoracic aorta in warmblood horses, Friesian horses, and Friesians with aortic rupture’, *BMC Veterinary Research*, 11(285). doi: 10.1186/s12917-015-0597-0.
- Saouti, N., Marcus, J. T., Noordegraaf, A. V. and Westerhof, N. (2012) ‘Aortic function quantified: the heart’s essential cushion’, *Journal of Applied Physiology*, 113(8), pp. 1285–1291. doi: 10.1152/jappphysiol.00432.2012.
- Sassani, S. G., Kakisis, J., Tsangaris, S. and Sokolis, D. P. (2015) ‘Layer-dependent wall properties of abdominal aortic aneurysms: Experimental study and material characterization’, *Journal of the Mechanical Behavior of Biomedical Materials*. Elsevier, 49, pp. 141–161. doi: 10.1016/J.JMBBM.2015.04.027.
- Schrieffl, A. J., Zeindlinger, G., Pierce, D. M., Regitnig, P. and Holzapfel, G. A. (2012) ‘Determination of the layer-specific distributed collagen fibre orientations in human thoracic and abdominal aortas and common iliac arteries.’, *Journal of the Royal Society, Interface / the Royal Society*, 9(71), pp. 1275–86. doi: 10.1098/rsif.2011.0727.
- Schymura, C. (2019) ‘Matlab package for mixtures of von Mises distributions’. doi: 10.5281/ZENODO.2602907.
- Shadwick, R. E. (1999) ‘Mechanical design in arteries’, *The Journal of Experimental Biology*, 202, pp. 3305–3313. Available at: <http://jeb.biologists.org/content/jexbio/202/23/3305.full.pdf> (Accessed: 14 June 2018).
- Sokolis, D. P., Boudoulas, H. and Karayannacos, P. E. (2008) ‘Segmental differences of aortic function and composition: clinical implications.’, *Hellenic journal of cardiology: HJC = Hellenike kardiologike epitheorese*, 49(3), pp. 145–54. Available at: <http://www.ncbi.nlm.nih.gov/pubmed/18543643> (Accessed: 12 March 2019).

- Sugita, S. and Matsumoto, · Takeo (2018) ‘Local distribution of collagen fibers determines crack initiation site and its propagation direction during aortic rupture’, *Biomech Model Mechanobiol*, 17, pp. 577–587. doi: 10.1007/s10237-017-0979-2.
- Taghizadeh, H. and Tafazzoli-Shadpour, M. (2017) ‘Characterization of mechanical properties of lamellar structure of the aortic wall: Effect of aging’, *Journal of the Mechanical Behavior of Biomedical Materials*, 65, pp. 20–28. doi: 10.1016/j.jmbbm.2016.08.011.
- Tomaszewski, J., Hanzlik, J., Grzywa, M., Zawisłak, H. and Stepień, A. (1976) ‘[Studies on the chemical composition of the vascular wall. Collagen and elastin in the walls of human aorta in the course of physiological aging].’, *Polskie Archiwum Medycyny Wewnętrznej*, 55(6), pp. 557–66. Available at: <http://www.ncbi.nlm.nih.gov/pubmed/951214> (Accessed: 14 June 2018).
- Török, P., Higdon, P. D. and Wilson, T. (1998) ‘On the general properties of polarised light conventional and confocal microscopes’, *Optics Communications*. North-Holland, 148(4–6), pp. 300–315. doi: 10.1016/S0030-4018(97)00576-2.
- Tsamis, A., Krawiec, J. T. and Vorp, D. A. (2013) ‘Elastin and collagen fibre microstructure of the human aorta in ageing and disease: a review.’, *Journal of the Royal Society, Interface / the Royal Society*, 10(83), p. 20121004. doi: 10.1098/rsif.2012.1004.
- Lo Vasco, V. R., Salmaso, R., Zanardo, V., Businaro, R., Visentin, S., Trevisanuto, D. and Cosmi, E. (2011) ‘Fetal aorta wall inflammation in ultrasound-detected aortic intima/media thickness and growth retardation’, *Journal of Reproductive Immunology*. Elsevier, 91(1–2), pp. 103–107. doi: 10.1016/J.JRI.2011.03.010.
- Vorkapic, E., Dugic, E., Vikingsson, S., Roy, J., M, M. I., Eriksson, P. and Wågs, D. (2016) ‘Imatinib treatment attenuates growth and inflammation of angiotensin II induced abdominal aortic aneurysm’. doi: 10.1016/j.atherosclerosis.2016.04.006.
- Vyas, M., Izzojr, J., Lacourciere, Y., Arnold, J., Dunlap, M., Amato, J., Pfeffer, M. and Mitchell, G. (2007) ‘Augmentation Index and Central Aortic Stiffness in Middle-Aged to Elderly Individuals’, *American Journal of Hypertension*. Oxford University Press, 20(6), pp. 642–647. doi: 10.1016/j.amjhyper.2007.01.008.
- Weisbecker, H., Unterberger, M. J. and Holzapfel, G. A. (2015) ‘Constitutive modelling of arteries considering fibre recruitment and three-dimensional fibre distribution.’, *Journal of the Royal Society, Interface*. The Royal Society, 12(105), p. 20150111. doi: 10.1098/rsif.2015.0111.
- Williams, C. and Wick, T. M. (2005) ‘Endothelial cell-smooth muscle cell co-culture in a perfusion bioreactor system.’, *Annals of biomedical engineering*, 33(7), pp. 920–8. Available at: <http://www.ncbi.nlm.nih.gov/pubmed/16060532> (Accessed: 21 September 2018).
- Wreford, N. G. (1995) ‘Theory and practice of stereological techniques applied to the estimation of cell number and nuclear volume in the testis’, *Microscopy Research and Technique*. Wiley-Blackwell, 32(5), pp. 423–436. doi: 10.1002/jemt.1070320505.

- Yamada, H., Sakata, N., Wada, H., Tashiro, T. and Tayama, E. (2015) ‘Age-related distensibility and histology of the ascending aorta in elderly patients with acute aortic dissection’, *Journal of Biomechanics*, 48(12), pp. 3267–3273. doi: 10.1016/j.jbiomech.2015.06.025.
- Yang, B., Brazile, B., Jan, N.-J., Hua, Y., Wei, J. and Sigal, I. A. (2018) ‘Structured polarized light microscopy for collagen fiber structure and orientation quantification in thick ocular tissues’, *Journal of Biomedical Optics*. International Society for Optics and Photonics, 23(10), p. 1. doi: 10.1117/1.JBO.23.10.106001.
- Zugun, F., Folescu, R. and Lacramioara Carmen, Z. (2013) Morphometric study of aortic wall parameters evolution in newborn and child experimental model of endometriosis View project Cell sources for cartilage regeneration View project. Available at: <https://www.researchgate.net/publication/239525195> (Accessed: 22 March 2019).

# CHAPTER 5

## A DUAL-VENC 4D FLOW MRI FRAMEWORK TO UNCOVER SPATIOTEMPORAL COMPLIANCE AND PULSE WAVE VELOCITY IN THE HUMAN AORTA



### **Abstract**

Accurate measurement of the highly heterogeneous compliance and pulse wave velocity throughout the entire aorta and cardiac cycle presents a considerable challenge. This study focuses on the development of a dual-VENC 4D Flow MRI protocol to capture the spatial variation in the biomechanics of the entire human aorta. The generation of a composite dataset ensures accurate quantification of unsteady non-uniform blood flow throughout the entire vessel and cardiac cycle, in addition to measurement of the dynamically changing geometry of the aortic wall. The protocol provides high sensitivity to all blood flow velocities throughout the entire cardiac cycle, overcoming the challenge of accurately measuring the highly unsteady non-uniform flow field in the aorta. Cross sectional area change, volumetric flow rate, and compliance are observed to decrease with distance from the heart, while pulse wave velocity is observed to increase. A non-linear aortic lumen pressure-area relationship is observed throughout the aorta, such that a high vessel compliance occurs at low pressures, and a low vessel compliance occurs at high pressures. This clearly demonstrates that vessel compliance during a cardiac cycle cannot be simplistically represented by a single value. The biomechanical behaviour of the aorta is highly dependent on the time-point of the cardiac cycle and on the spatial location relative to the heart. This dual-VENC methodology potentially provides a framework for pre-operative evaluation of stent positioning on ventriculo-aortic mechanics, for post-operative surveillance, and for design of next-generation patient-specific endografts.

## 5.1 Introduction

Of the 97,000 km of blood vessels in the human body, the near-metre long segment connecting the left ventricle to the periphery, known as the aorta, is the most important. Diseases affecting the aorta such as aneurysm and dissection have long been documented, but still today remain difficult to treat. According to the Centre for Disease Control and Prevention, an average of 47,000 deaths each year in the United States are attributed to diseases of the aorta and its branches (excluding carotid and coronary disease). This exceeds the number of annual deaths due to breast cancer, pancreatic cancer, colon cancer and prostate cancer (Svensson and Rodriguez, 2005). Patients undergoing surgery of the aorta have two main treatment options: open surgical repair (OSR); or endovascular aortic repair (EVAR). The introduction of EVAR in the early 1990s was fuelled by the need for a less invasive treatment option for co-morbid patients and poor outcomes following OSR. In the quarter-century since its introduction, EVAR has shown superiority over OSR in the short-term, where studies continue to report mortality rates from 14% to 45% in the first 30 days post-OSR (Hicks *et al.*, 2015; IMPROVE Trial Investigators, 2014), but no significant benefits are apparent for EVAR patients in the long-term (Patel *et al.*, 2016).

As the first thoracic endovascular aortic repair (TEVAR) graft only received FDA approval in 2005 (Bhamidipati *et al.*, 2011), long-term results are only now coming to light. A number of studies have reported high levels of cardiac complications following TEVAR, where Conrad *et al.* (2017) reports 34% mortality due to cardiac events in thoracic aortic aneurysms (TAA), while a study by Bischoff *et al.* (2016) reports 30% cardiac mortality for a larger TAA cohort. A recent study by Concannon *et al.* (2017) reports that, from a cohort of 151 patients with thoracoabdominal aortic aneurysms (TAAA), 39% of total deaths were due to cardiac failure. Notably, all deaths due to new onset cardiac complications were in patients who underwent stenting of the supradiaphragmatic aorta. Altogether, these results suggest a dependence of post-operative cardiac outcomes on the location of stent deployment in the aorta.

A detailed biomechanical investigation of the influence of stent deployment on aortic deformation, haemodynamics, and pulse wave velocity (PWV) is required to uncover the mechanisms that cause cardiac complications post-TEVAR. As an important first step in this process, we propose a non-invasive 4D Flow MRI protocol to accurately characterise spatial variations in biomechanical behaviour throughout the entire aorta, in addition to dynamic variations throughout a cardiac cycle. The ability to characterise spatially dependent vessel geometry and deformation, blood flow patterns, and PWV will potentially guide the selection of stent-graft design and position in EVAR procedures in order to minimise the risk of cardiac complications post-intervention. An increased PWV has been established as a strong risk factor for cardiac events, independent of traditional risk factors such as smoking, hypertension and diabetes mellitus (Ben-Shlomo *et al.*, 2014). The ability to accurately determine the spatially non-uniform PWV throughout the entire aorta, both pre- and post-intervention, could potentially provide new insights.

The increase in clinical acceptance of EVAR has resulted in a reduction in the number of primary OSR cases (Dua *et al.*, 2014), and a consequent reduction in the availability of tissue samples for *in-vitro* biomechanical testing. Moreover, surgically excised tissue often consists of a small portion (approximately 1 cm<sup>2</sup>) of the aorta, presenting significant challenges in terms of bi-axial mechanical testing (Nolan and McGarry, 2016). Therefore, *in-vitro* testing of excised tissue does not present a viable methodology to accurately determine the detailed spatial variations in compliance and PVW in a patient-specific aorta. Alternative approaches of combined medical imaging and computational analysis (finite element (FE) and computational fluid dynamics (CFD) modelling) to determine biomechanical properties non-invasively are highly promising, particularly in light of recent advances in medical imaging technology and computational capability.

Of the few studies that attempt to investigate the biomechanics of the aorta, its heterogeneity has been reasonably well established in animals through *ex-vivo* testing of the excised vessel (Moriwaki *et al.*, 2011b; Krüger *et al.*, 2016). Previous *in-vivo* analyses of the human aorta have focused on limited isolated segments, such as the thoracic (Mohiaddin *et al.*, 1989) or abdominal aorta (Länne *et al.*, 1992), which fail to provide the necessary anatomical coverage to capture the true heterogeneity and therefore cannot be taken to represent the entire vessel. Due to the lack of reliable and detailed information on the heterogeneity of the aorta, computational models have typically assumed that the wall stiffness is spatially uniform throughout the vessel (Kim *et al.* 2009; Morbiducci *et al.* 2013; Crosetto *et al.* 2011; Gohean and Zhang 2009). An improved robust methodology to non-invasively characterise patient-specific spatial variation in aortic PWV and compliance throughout the cardiac cycle has the potential to provide accurate heterogeneous material properties for computational models, leading to significant improvements in EVAR device design, and subsequently, postoperative outcomes.

The current study presents a framework using 4D Flow MRI to characterise the biomechanics of the entire human aorta. A dual-VENC protocol is developed to achieve accurate measurement of the dynamically changing flow velocity field and lumen area throughout the entire cardiac cycle. This methodology uncovers highly detailed measurements on the deformation of the aorta during the cardiac cycle. For the first time, a nonlinear relationship between lumen area and pressure is uncovered *in-vivo* over the duration of a cardiac cycle throughout the entire aorta, providing key evidence that aortic biomechanics cannot be characterised by a single value compliance coefficient, as commonly assumed (Tierney and McGloughlin 2011; Lalande *et al.*, 2008; Musa *et al.*, 2016). Furthermore, our detailed *in-vivo* measurements reveal that the lumen pressure-area relationship, and PWV are highly heterogeneous throughout the aorta. The capability of the proposed dual-VENC protocol to generate high spatial and temporal resolution measurements of the entire aorta throughout an entire cardiac cycle has the potential to significantly improve disease diagnosis (e.g. dissection, coarctation or aneurysm rupture risk) and provide

guidance for patient specific intervention (e.g. choice of stent design and effect of stent position).

## 5.2 Methodology

In this chapter a protocol is proposed to evaluate patient-specific haemodynamics and lumen deformation along the entire human aorta, and throughout the entire cardiac cycle, using phase-contrast magnetic resonance (PC-MRI) principles (specifically, 4D Flow MRI). Further details of the applications and potential uses of 4D Flow MRI can be found in: Cibis *et al.*, (2014), Potters *et al.*, (2014), Markl *et al.* (2012), Stankovic *et al.* (2014), Markl *et al.* (2016), and Ha *et al.* (2016). Generally, with the aim of assessing anatomical structures, it is the magnitude of the local spin magnetization vector that is used in the creation of typical MR images. However, important information regarding the movement of hydrogen protons is encoded in the phase of this vector. In the field of PC-MRI, such information is exploited to determine the flow velocity of targeted protons. A brief summary of the theoretical background to PC-MRI is presented in Section 5.2.1 to motivate the protocol proposed in this chapter.

### 5.2.1 Theoretical Background

In this section we provide a brief overview of the key theory and equations that motivate the dual-VENC protocol proposed in Section 5.2.2. The theoretical physics underlying MRI is extensively outlined in literature, e.g. (Ridgway 2010; Biglands and Ridgway 2012; Bernstein and Zhou 2004). In summary, MRI is a phase-sensitive modality that encodes information regarding the velocity of the targeted protons into the detected signal. The velocity is proportional to the phase of the local transverse magnetization vector. In the remainder of this chapter the term *spins* is used to refer to a finite group of protons within a given volume.

The phase of spins is governed by the local Larmor or precessional frequency  $\omega_L$ :

$$\omega_L(\vec{r}, t) = \gamma B(\vec{r}, t) \quad (5.01)$$

$$\omega_L(\vec{r}, t) = \gamma B_0 + \gamma \Delta B_0 + \gamma \vec{G}(t) \vec{r}(t) \quad (5.02)$$

where  $\gamma$  is the gyromagnetic ratio;  $B_0$  is the primary magnetic field;  $\Delta B_0$  relates to field imperfections or inhomogeneity;  $\vec{G}$  is the magnetic field gradient; and  $\vec{r}$  is the location of the spins. If spin acceleration is constant between  $t_0$  and the time at which we sample our signal or echo time ( $t$ ), then  $\vec{r}(t)$  can be represented by a 1<sup>st</sup> order displacement, expressed through a Taylor expansion (Bernstein and Zhou 2004)

$$\vec{r}(t) = \vec{r}_0 + \vec{v}_0(t - t_0) + \frac{1}{2} \vec{a}_0(t - t_0)^2 + \dots \quad (5.03)$$

where  $\vec{r}_0$  is the initial position,  $\vec{v}_0$  is the velocity,  $t_0$  is the initial time, and  $\vec{a}_0$  is the acceleration. Substituting (5.03) into (5.02) and neglecting higher order terms gives:

$$\omega_L(\vec{r}, t) = \gamma B_0 + \gamma \Delta B_0 + \gamma \vec{G}(t) \vec{r}_0 + \gamma \vec{G}(t) \vec{v}_0 t \quad (5.04)$$

Making use of the rotating frame of reference sets the first term on the left-hand side in equation 5.04 to zero, and integration of the frequency  $\omega_L$  with respect to time,  $t$ , yields the phase shift,  $\Phi$ , of the fluid, such that

$$\Phi(\vec{r}, t) = \gamma \int_{T_0}^{T_0+\Delta T} \Delta B_0 dt + \gamma \int_{T_0}^{T_0+\Delta T} \vec{G}(t) (\vec{r}_0 + \vec{v}_0 t) dt \quad (5.05)$$

Decomposing our equation for phase shift into a moment expansion yields:

$$\Phi_0 = \gamma \Delta B_0 (\Delta T) \quad (5.06)$$

Defining the  $n^{\text{th}}$  gradient moment as

$$M_n(t) = \int_{T_0}^{T_0+\Delta T} \vec{G}(t) t^n dt, \quad (5.07)$$

the phase shift (Bernstein and Zhou 2004) is then expressed as

$$\Phi(\vec{r}, t) = \Phi_0 + \gamma M_0(t) \vec{r}_0 + \gamma M_1(t) \vec{v}_0 \quad (5.08)$$

In order to extract information regarding the velocity of spins, all other components contributing to the phase of the precessing magnetization vector must be eliminated, i.e. the first term on the right-hand side of equation 5.08 (due to inhomogeneities) and the second term on the right-hand side of equation 5.08 (due to static protons). Employing a Bipolar Gradient ( $\vec{G}$ ) removes phase accrual due to static spins. Turning on a magnetic field gradient augments  $B_0$  to a degree that is related to position in space. Spins at the isocentre ( $I$ ) of the scanner precess at the Larmor frequency and adjacent spins precess either faster or slower depending on their position relative to  $I$ . Therefore, at a certain spin position relative to  $I$ , turning on  $\vec{G}$  for a given increment in time will invoke a phase shift of a *static proton* of  $\Delta\Phi$ . By inverting the polarization of  $\vec{G}$  and leaving it on for the same period of time, this same spin packet will recover its original phase. By removing phase accrual due to static spins, the total phase is now only made up of contributions from background (inhomogeneities) and velocity terms

$$\phi(\vec{r}, t) = \phi_0 + \gamma \vec{v} M_1 \quad (5.09)$$

Phase offset due to background is constant so toggling the order by which  $\vec{G}$  is employed yields:

$$\phi_a(\vec{r}, t) = \phi_0 + \gamma \vec{v} M_{1,a} \quad ; \quad \phi_b(\vec{r}, t) = \phi_0 + \gamma \vec{v} M_{1,b} \quad (5.10)$$

Subtraction of the above terms removes phase accumulation due to background, giving  $\Delta\phi$ , which is now only dependent on  $\vec{v}$  and  $\Delta M_1$  (the shape of the bipolar gradient):

$$\Delta\phi = \phi_a - \phi_b = \gamma \vec{v} \Delta M_1 \quad (5.11)$$

Fluid velocity along the direction of  $\vec{G}$  can therefore be determined through:

$$\vec{v} = \frac{\Delta\phi}{\gamma \Delta M_1} \quad (5.12)$$

Changing  $\Delta M_1$  determines the velocity encoding sensitivity (VENC), defined as the velocity that causes a phase shift of  $\pi$ , such that

$$\gamma \Delta M_1 = \frac{\pi}{VENC} \quad (5.13)$$

giving the local fluid velocity  $\vec{v}$  (Bernstein and Zhou 2004) as

$$\vec{v} = \frac{\Delta\phi}{\pi} VENC \quad (5.14)$$

By performing this procedure along the three orthogonal directions a scanner can be sensitized to calculate, of each voxel, the component of the velocity vector in the foot-head (FH), antero-posterior (AP) and right-left (RL) directions (Figure 5.1). Combined with a CINE acquisition, time provides the fourth dimension for a so called 4D Flow MRI or formally “3D CINE Phase Contrast CMR with 3-directional velocity encoding” sequence.

In Figure 5.1, cranial flow (in the positive z-direction) is indicated in red on the FH image in the ascending thoracic aorta. The flow direction is in the negative z-direction in the descending aorta, as indicated by blue in the FH image. In the AP image, posterior flow can be seen traversing the apex of the aortic arch while anterior flow is indicated by blue as blood leaves the left ventricle into the ascending thoracic aorta. Similarly, flow sensitization is seen with the RL image although velocity encoding is less obvious in the RL direction upon viewing a sagittal plane.

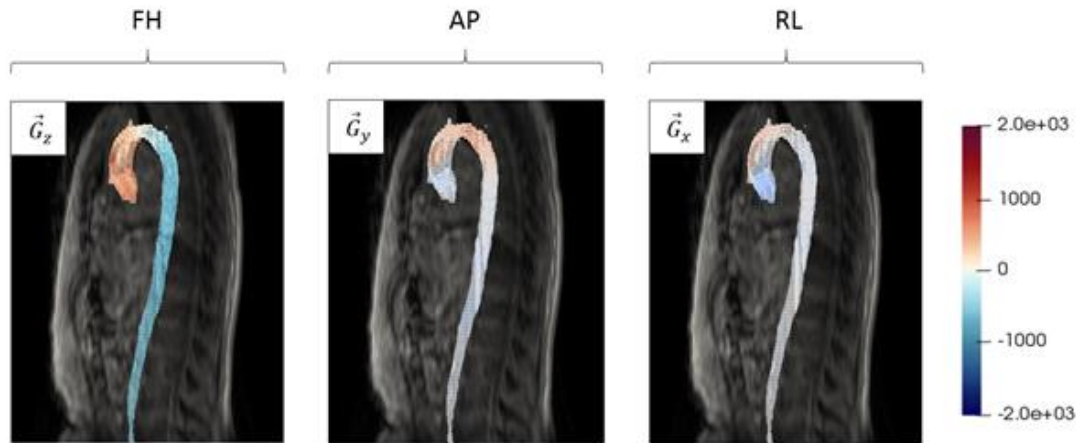


**Figure 5.1:** Sensitization along the three principle orthogonal directions, where FH, AP and RL indicate Foot-Head, Antero-Posterior and Right-Left, respectively (also referred to as the z, y, and x components of a Cartesian coordinate system).

Due to the orthogonality of the chosen velocity encoding directions, the velocity magnitude of a given voxel is simply given as:

$$|\vec{v}| = \sqrt{\vec{v}_x^2 + \vec{v}_y^2 + \vec{v}_z^2} \quad (5.15)$$

Defining  $\Delta T$  as the period for which  $\vec{G}$  is switched on, regardless of its polarization, the first moment  $M_1$  of the bipolar gradient can be calculated directly as:

$$M_1 = \int_{T_0}^{T_0+\Delta T} +\vec{G}_i t \, dt + \int_{T_1}^{T_1+\Delta T} -\vec{G}_i t \, dt = \vec{G}_i T_1 \Delta T \quad (5.16)$$

Recognising that  $\vec{G}_i \Delta T$  is equal to the area of an individual gradient lobe  $A$  and  $T$  is the time from  $T_0$  to the time at the beginning of the second gradient lobe  $T_1$ , an instantaneous flip of the polarization of  $\vec{G}$  (Bernstein and Zhou 2004) gives:

$$M_1 = AT = \vec{G}_i T^2 \quad ; \quad \Delta M_1 = 2\vec{G}_i T^2 \quad (5.17)$$

The velocity sensitization is therefore dependent upon the strength of  $\vec{G}$  and the time  $T$  over which it is active, such that

$$\vec{v} = \frac{\Delta\phi}{2\gamma\vec{G}_i T^2} \quad (5.18)$$

Equation 5.17 dictates how the scanner can sensitize to specific fluid velocities. For example, reducing the velocity sensitization from  $VENC = 200$  cm/s to  $VENC = 50$  cm/s requires a four-fold increase in the strength of  $\vec{G}$ , or an increase in the time over which it is activated. Thus, it is preferable that the strength of the magnetic field gradient be increased to achieve a reduction in velocity sensitization, instead of increasing T necessitating unfeasibly long scan times.

### 5.2.2 Proposed dual-VENC protocol for complete characterisation of aortic flow

Maximal sensitivity is obtained for spins moving at a velocity equal to the specified VENC value. This presents a particular challenge for determination of blood flow patterns in the aorta where flow is highly unsteady (temporally varying) and non-uniform (spatially varying). For example, a VENC of 200 cm/s, may provide a suitable level of sensitivity to determine the high velocity blood flow patterns in the aortic arch during systole. However, such a VENC value is not suitable during the diastolic phase, where the fluid velocity is considerably lower. In fact, in using a VENC of 200 cm/s, low velocity blood flow during diastole cannot be distinguished from static tissue and the lumen of the aorta cannot be reliably identified. A reduced VENC is required to achieve sufficient resolution of the flow field during diastole.

Of course, such a low VENC is not suitable for systolic flow velocities; any fluid velocity greater than VENC will be misrepresented and aliased, as described elsewhere (Su and Chen, 2004; Tan *et al.*, 2008; Loecher *et al.*, 2016). In an attempt to overcome this issue, previous studies have proposed phase unwrapping algorithms to estimate velocities higher than VENC. However, significant errors have been reported for such techniques, in addition to increased post-processing time (Cusack and Papadakis, 2002; Bioucas-Dias and Valadao, 2007; Cheng *et al.*, 2018).

The dual-VENC protocol proposed in this study generates a composite dataset, with a high-VENC of 200 cm/s targeted to systole and a low-VENC of 50 cm/s targeted to diastole. As the only difference between our two datasets is the velocity sensitization, accurate velocity field measurement and lumen boundary isolation can be performed for each phase and plane throughout the entire cardiac cycle, all the while keeping acquisition parameters within the bounds specified in the most recent *4D Flow MRI expert consensus statement* (Dyverfeldt *et al.*, 2015). If the velocity of any pixel in an arbitrary plane of interest is greater than our low-VENC value (50 cm/s) we use the high-VENC matrix to calculate the cross-sectional-area and volumetric flow rate; otherwise, we use the corresponding low-VENC matrix. This approach negates the need for phase unwrapping techniques and provides greater accuracy in flow quantification in areas where the fluid velocity is low than single high-VENC acquisitions.

### 5.2.3 Imaging Parameters

The current study was approved by the institutional review board (Research Assessment Group (RAGp), Galway Clinic) and was conducted on a healthy 25-year-old male with a normotensive blood pressure measurement of 117/73 mmHg and a heart rate of 60 bpm. The subject was placed in a Philips Ingenia 3T MRI scanner

(Philips Medical Systems, Best, Netherlands) and a 4-lead ECG system was placed on the chest with retrospective synchronization to the scanner to image according to specific phases of the subjects' cardiac cycle. A non-contrast RF-Spoiled Gradient Echo pulse sequence was employed in order to capture a sufficient number of heart phases under free-breathing conditions. The field of view was set to encompass the entire aorta. The longitudinal (FH) boundaries spanned from above the level of the aortic arch to distal to the common iliac bifurcation, while the lateral (AP) and (RL) bounds enclosed the breadth and width of the subject respectively. The frequency encoding direction was set to AP to reduce artefact from respiratory motion. Important scan parameters are as follows: repetition time (TR) = 3.1 ms, echo time (TE) = 1.9 ms, Flip Angle =  $8^\circ$ , cardiac phases = 20, temporal resolution = 50 ms, isotropic in-plane resolution = 1 mm, slice thickness = 4 mm, VENC = 200 cm/s and 50 cm/s. VENC scouts were ran to obtain the minimum high-VENC value to prevent aliasing and optimize Signal to Noise Ratio (SNR), while a 4 mm slice thickness was used to limit scanning time. The scan time for a VENC of 200 cm/s was 4 minutes, and 8 minutes for a VENC of 50 cm/s. In the case of the latter, the TR was increased to 10 ms to allow sufficient down-time for the gradient coils to prevent excessive overheating. A balanced four-point encoding scheme was used, further details of which can be found in (Pelc *et al.*, 1991).

#### 5.2.4 Postprocessing

All data was processed using in-house developed C++, Python and MATLAB code. Data processing was performed on an Intel Core i7 CPU with 16GB DDR3 RAM. Post-processing time for the dual-VENC dataset was approximately 20 minutes. Raw MRI data files were sorted according to their encoding direction using RadiAnt DICOM Viewer (v4.2.1, Medixant, Poznan, Poland) and subsequently organised according to the time-point in the cardiac cycle using a custom Image J plugin (Figure 5.2(a)). ParaView (5.4.1, [www.paraview.org](http://www.paraview.org)) visualisation software served as the platform for reading the image data for each encoding direction, developing voxel associativity and subsequent calculation of local velocity magnitudes  $|\vec{v}|(x, y, z, t)$  as illustrated in Figure 5.2(b). It is necessary to ensure that observational planes are orthogonal to the mean direction of blood flow when attempting to characterize lumen deformations and volumetric flow rates due to the onset of a pressure pulse. A centreline detection algorithm was developed to ensure such requirements were fulfilled as shown in Figure 5.2(c), where the centreline is defined as the centroid of the aortic flow domain.

Analyses were performed at 10 planes along the aorta (Figure 5.2(d)), ranging from Plane 1 distal to the sinus of Valsalva to Plane 10 immediately proximal to the common iliac bifurcation, with an average section spacing along the centreline of 50 mm. Each time-point for each plane in both VENC datasets was then exported for all further postprocessing in MATLAB (R2013b, MathWorks Inc., Natick, MA, USA). A bicubic interpolation algorithm is employed in order to attain further clarity for aortic lumen edge detection. A series of cubic splines were fit to the intensity values of individual pixels along both the x and y dimensions in a given plane (Figure 5.2(e))

and the grid density was increased to 0.5 x 0.5 mm in-plane spatial resolution. Figure 5.2(f) (i) and (ii) highlight in-plane pixel data pre- and post-interpolation.

At this point, each velocity magnitude image is masked by the square of the corresponding magnitude (anatomical) image (Figure 5.2(f) (iii)) in order to create a PC-MRA matrix according to methods described in (Bustamante *et al.*, 2017). Using each PC-MRA image, an ellipse is fit to the boundary of the fluid domain for each plane and phase of interest to determine the lumen area as a function of space and time based on a custom-built segmentation algorithm. Using the high-VENC velocity matrix, if the velocity of any pixel is greater than the low-VENC value (50 cm/s) we use this matrix to calculate the cross-sectional-area and volumetric flow rate. Otherwise, the corresponding low-VENC matrix is used. The composite data set generated by the dual-VENC protocol eliminates the need for any phase unwrapping techniques.

For each of the 10 planes analysed, the percentage cross-sectional-area change ( $\Delta\hat{A}$ ) is defined according to  $(A_{sys} - A_{dia})/A_{dia}$ , where subscripts 'sys' and 'dia' represent systole and diastole respectively. After isolating the aortic lumen from surrounding structures, streamlines and flow vectors can be plotted as shown in Figure 5.2(g). The integral of the velocity within the boundary of the aortic lumen provides the instantaneous volumetric flow rate (Q) as shown in Figure 5.2(h). Finally, the local PWV at each plane is calculated according to the QA method described in (Vulli  moz and Meuli 2002) and shown in Figure 5.2(i), where PWV is defined as the coefficient of proportionality between Q (blue) and CSA (red) bound by the systolic upstroke of the cardiac cycle. Additionally, spatial variance in PWV is calculated using the time-to-peak (TTP) method described in (Wentland and Wieben 2014), where in this case the wave speed is defined as  $\Delta z/\Delta t$ , where  $\Delta z$  is the distance along the vessel centreline between regions of interest and  $\Delta t$  is the time lag between flow peaks for the thoracic and abdominal aortic segments in this case.

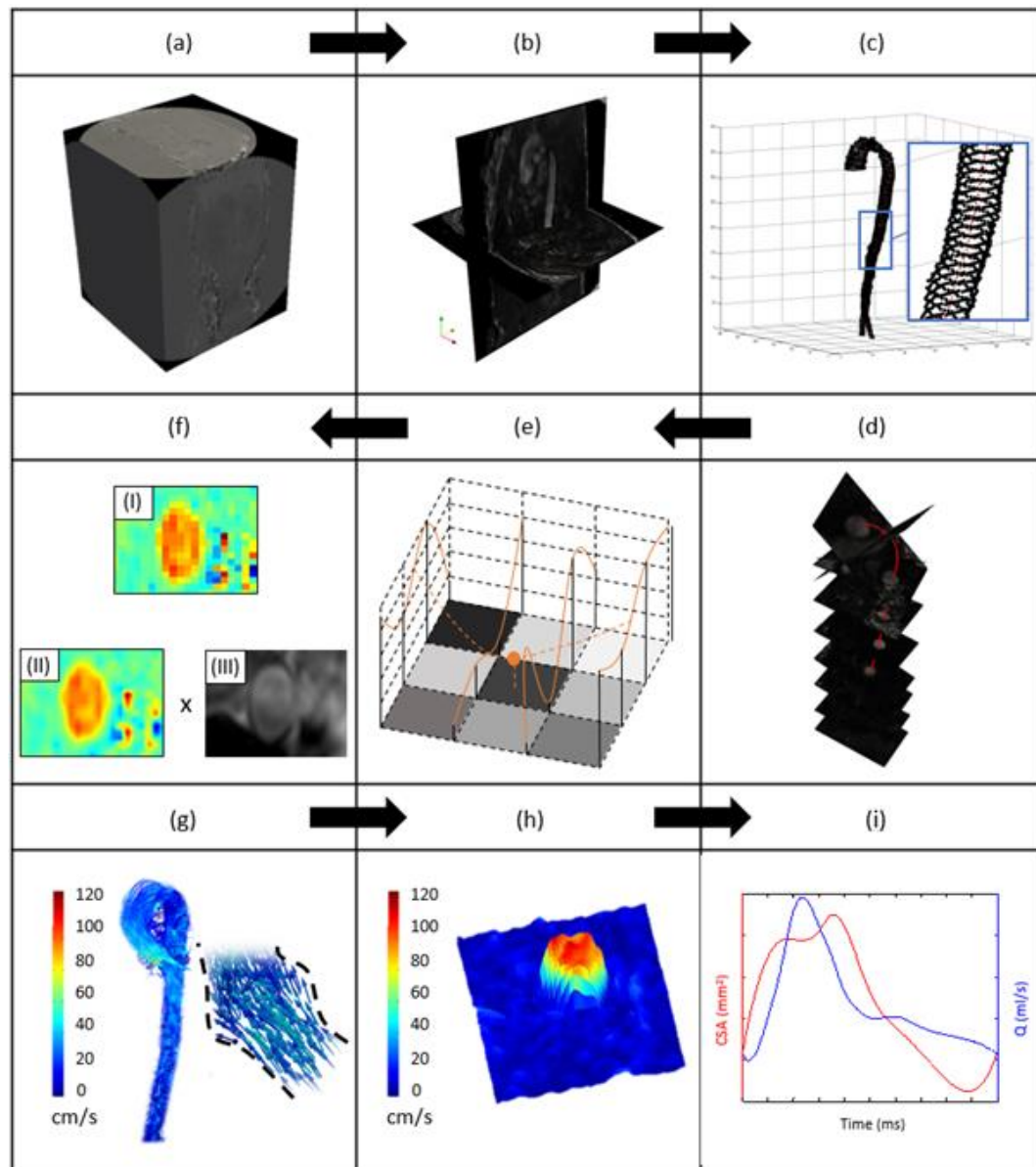


**Figure 5.2:** Basic overview of postprocessing steps. (a) Raw MRI volume of interest (b) velocity magnitude calculation using equation (14) from each encoding direction. (c) Centreline detection algorithm and (d) centreline highlighted in red with 10 orthogonal observational planes created normal to the mean direction of flow along entire aorta. (e) Bicubic interpolation process to increase in-plane spatial resolution. (f) Pre- (I) and Post- (II) interpolation, final matrix is multiplied by magnitude data (III) to form a PC-MRA image. (g) Streamlines plotted at 200ms into cardiac cycle. (h) Volumetric flow rate through an observational plane in the descending thoracic aorta during the systolic upstroke. (i) Flow (blue) and CSA (red) as a function of time in cardiac cycle, where the constant of proportionality can be used to calculate pulse wave velocity.

### 5.2.5 Compliance

To estimate local vessel compliance, the pressure must be estimated throughout the cardiac cycle at the location in question. The clinical definition of vessel compliance is typically given as  $\Delta CSA/\Delta P$  during a cardiac cycle. Typically, vessel compliance is reported as a single value (Lalande *et al.*, 2008b; João L. Cavalcante *et al.*, 2011; Musa *et al.*, 2016) as only the systolic (SBP) and diastolic pressures (DBP) are recorded. However, it is trivial to demonstrate that, even for the simplistic thin-walled linear-elastic cylindrical vessel undergoing infinitesimal deformation, a linear relationship does not exist between  $\Delta P$  and  $\Delta CSA$  and therefore a single value of local compliance cannot be identified. Moreover, the well-established non-linear material behaviour of arterial tissue, e.g. (Zhou and Fung, 1997; Ogden, 2003; Agrawal *et al.*, 2013), further invalidates the concept of a single value of compliance. By considering the entire blood pressure waveform, we investigate the time-dependence in local compliance along the length of the aorta.

As local variations in pressure are not directly measured, we consider three methodologies for estimation of time-dependent blood pressure throughout the aorta: Firstly, a generic central aortic blood pressure curve was scaled to the subject's cardiac cycle time, SBP and DBP (Figure 5.3(a)). This pressure-time relationship is applied to each plane in the aorta.

Secondly, setting the central aortic blood pressure waveform to Plane 5, we employ the unsteady Bernoulli equation to calculate the blood pressure waveform at discrete proximal and distal planes (Figure 5.3(b)). Beginning with the Navier-Stokes equation;

$$\rho \left[ \frac{\partial \vec{v}}{\partial t} + (\vec{v} \cdot \nabla) \vec{v} \right] = -\nabla P + \rho \vec{g} + \mu \nabla^2 \vec{v} \quad (5.19)$$

and assuming viscous effects contribute little to pressure differential compared to transient and convective terms as shown by (Lamata *et al.*, 2014), the last term in equation 5.19 goes to zero and we obtain the Euler equation. Multiplying by an infinitesimal increment  $dz$  along a streamline, such that  $dz$  is parallel to the mean velocity direction  $\vec{v}$  gives

$$\rho \left[ \frac{\partial \vec{v}}{\partial t} + (\vec{v} \cdot \nabla) \vec{v} \right] \cdot dz = -\nabla P \cdot dz + \rho \vec{g} \cdot dz \quad (5.20)$$

Integrating between two arbitrary points (*Point 1* and *Point 2*) along a streamline yields

$$\int_1^2 \rho \frac{\partial \vec{v}}{\partial t} dz + \frac{1}{2} \rho (v_2^2 - v_1^2) = -(P_2 - P_1) - \rho \vec{g} \cdot (z_2 - z_1) \quad (5.21)$$

where the first term on the left in equation 5.21 contains the integral of the local acceleration of a fluid particle along a streamline between *Point 1* and *Point 2*.  $\rho$  is the fluid density,  $P$  is the pressure, and  $\vec{v}$  is the fluid velocity. We neglect the last term on the right-hand side as the subject is in the supine position in the scanner and hence the change in elevation along the vessel  $\Delta z$  can be taken as zero.

Thirdly, we investigate a piecewise approach of determining the aortic blood pressure waveform from PC-MRI data and non-invasive brachial blood pressure measurements (Figure 5.3(c)). The approach is described in detail in Vennin *et al.*, (2015). Briefly, the method makes use of the water hammer equation for the systolic upstroke phase of the cardiac cycle according to:

$$\Delta P = \rho \cdot PWV \cdot \Delta v \quad (5.22)$$

where  $P$  is pressure,  $\rho$  is density and  $v$  is blood velocity. A diastolic decay function driven by time constant  $\tau$  is utilized for the phase between aortic valve closure and re-opening where:

$$P(t) = P_0 \cdot e^{-\frac{t}{\tau}} \quad (5.23)$$

Finally, the systolic peak is approximated by a second-order polynomial which satisfies continuity and produces the prescribed mean arterial pressure (MAP). The corresponding area versus pressure graphs are shown for each method in Figure 5.9(a), Figure 5.9(b) and Figure 5.9(c) respectively.

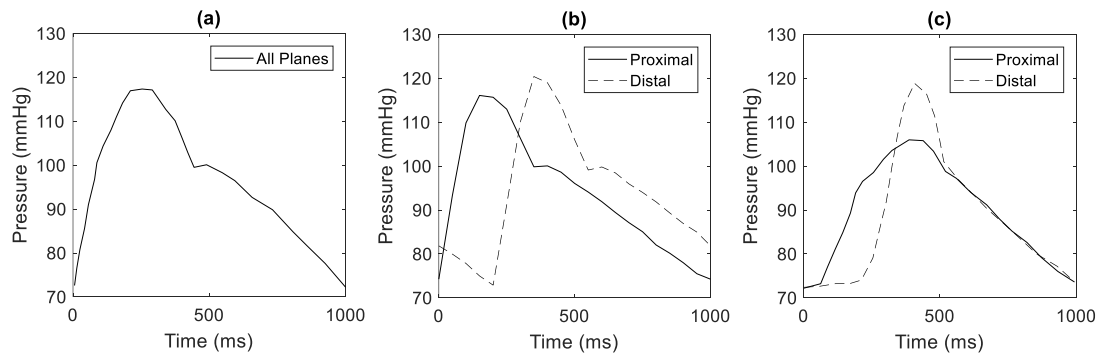


**Figure 5.3: Pressure boundary conditions applied to calculate local aortic compliance. (a) Uniform; (b) Unsteady Bernoulli; (c) Piecewise.**

## 5.3 Results

### 5.3.1 Dual-VENC protocol for complete characterisation of aortic flow

We employ PC-MRI principles to capture both the deformation and haemodynamics of the entire aorta. The proposed dual-VENC protocol provides high sensitivity to all blood flow velocities throughout the entire cardiac cycle, overcoming the challenge of accurately measuring the highly unsteady non-uniform flow field in the aorta. A single high-VENC approach, while providing accurate measurements of high velocities during systole, was found to have insufficient resolution at low velocities to differentiate blood flow during diastole from the surrounding static tissue; this observation has been previously reported (Callaghan *et al.*, 2016; Nett *et al.*, 2012; Markl *et al.*, 2016). Consequently, the lumen geometry cannot be accurately determined in any region of the aorta during diastole, as clearly illustrated in Figure 5.4(a) (only the high velocity flow in thoracic aorta at a time-point of 200 ms (systole) is accurately measured). An inability to accurately determine the lumen geometry and velocity field in the entire aorta for the entire cardiac cycle prohibits the determination of clinically relevant quantities such as cross-sectional-area, aortic compliance, volumetric flow rate and PWV. As discussed in Section 5.2.2, a single acquisition low-VENC will not provide accurate measurement of high velocities during systole due to phase wrapping. This is evident in Figure 5.4(a), where the high velocities at 200 ms are significantly under-predicted by the low-VENC acquisition, compared to the high-VENC that is specifically sensitized for accurate measurement during systole. However, flow velocities and the flow domain are accurately determined at all other time-points (0, 500, 700 and 900 ms) using a low-VENC, in contrast to the high-VENC measurements where flow is indistinguishable from the noise associated with surrounding static tissue. Figure 5.4(b), further highlights this motivation for a dual-VENC approach. At 200 ms (top row), high-VENC accurately represents the fluid domain for the thoracic plane (indicated in red), whereas velocity aliasing is evident in low-VENC. In fact, some velocity vectors over 50 cm/s are misrepresented as negative velocities travelling towards the heart for low-VENC at this thoracic plane during systole. At 900 ms (bottom row), high-VENC is incapable of distinguishing the fluid domain from static tissue in the abdominal plane (indicated in blue), while the low-VENC accurately represents the flow field and aortic lumen boundary.

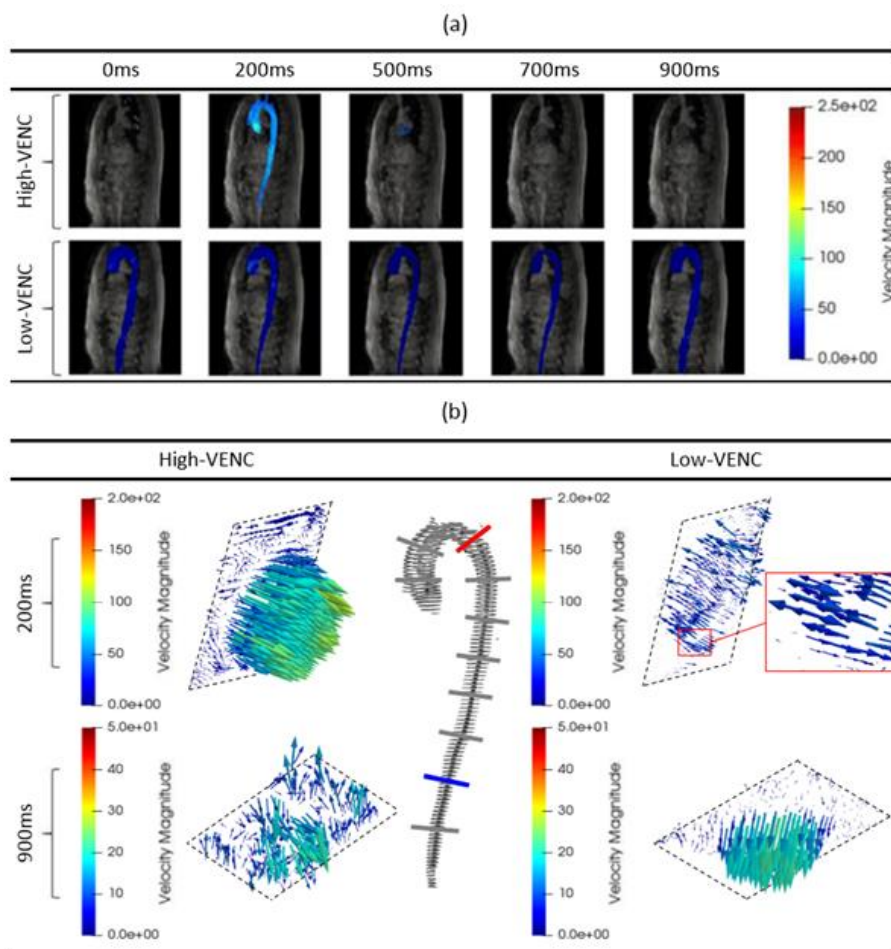


**Figure 5.4:** (a) Sagittal view of velocity magnitude vectors. The high-VENC (top row) captures systole, as shown at the 200 ms time-point. However, during diastole, low-velocity blood flow is not distinguishable from surrounding static tissue. The low-VENC provides accurate data on the region of blood-flow (and thus the lumen boundary) throughout the entire cardiac cycle. However, velocity aliasing is evident in low-VENC during systole. (b) Further emphasis of the requirement for dual-VENC approach, where top row indicates systole (200ms) in the thoracic plane (red), where high-VENC accurately illustrates the flow profile but velocity aliasing is evident in low-VENC (vectors above 50 cm/s travelling towards the heart). The bottom row illustrates how high-VENC cannot distinguish low velocity vectors from static tissue clearly in the abdominal plane (blue), while low-VENC can. By combining both data-sets in our dual-VENC approach, we obtain accurate measurements of the region of flow (and thus the lumen boundary) in addition to accurate measurement of the velocity vectors throughout the entire R-R interval in the entire aorta.

### 5.3.2 Spatial Deformation

Figure 5.5 shows the spatial and temporal change in lumen cross-sectional-area throughout a cardiac cycle. Clearly the lumen cross-section-area (CSA) decreases with increasing distance from the heart at any given time-point in the cardiac cycle. For example, at time  $t=250$  ms, the CSA at Plane 2 in the ascending aorta is  $644 \text{ mm}^2$ , compared to  $295 \text{ mm}^2$  at Plane 5 and  $158 \text{ mm}^2$  at Plane 10.

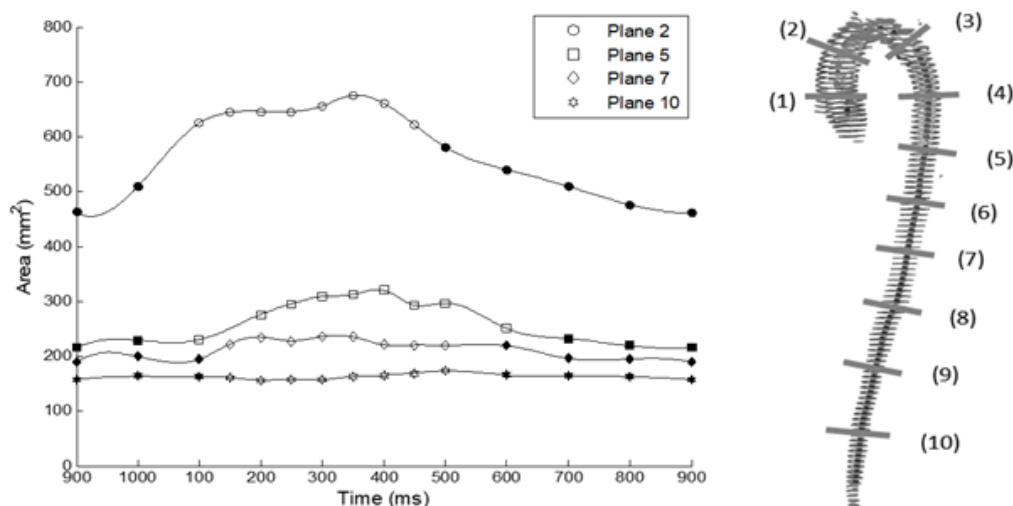


**Figure 5.5:** Area as a function of cardiac cycle time for a series of discrete planes along the vessel from proximal to distal aorta. Filled markers indicate phases where low-VENC data were used and unfilled markers indicate where high-VENC were used.

Figure 5.6(a) shows the lumen area at the end of diastole,  $A_{dia}$ , for all 10 planes. The well-known tapering of the aorta is also evident, with a decrease in  $A_{dia}$  with increasing distance from the heart. The percentage change in cross-sectional-area,  $\Delta\hat{A}$ , due to the onset of the pressure pulse is presented for each plane in Figure 5.6(b), where  $\Delta\hat{A} = (A_{sys} - A_{dia})/A_{dia}$ . Firstly, it should be noted that  $\Delta\hat{A}$  ranges from 15% for Plane 10 up to 65% for Plane 1, providing an indication of the extremely large deformation of the aortic wall during a cardiac cycle. Indeed, it should be noted that the circumferential strains in the aortic tissue will be significantly larger than the values of  $\Delta\hat{A}$  reported, given that the undeformed reference area (at zero pressure) is significantly lower than  $A_{dia}$  (clearly the true undeformed reference area cannot be determined in a “live” aorta, so the measure  $\Delta\hat{A}$  is instead presented here to demonstrate the high aortic deformations during a cardiac cycle). Categorising the planes into two subgroups, namely ‘*thoracic*’ and ‘*abdominal*’, a statistically significant difference in  $\Delta\hat{A}$  is observed between the two groups ( $p < 0.005$ ).

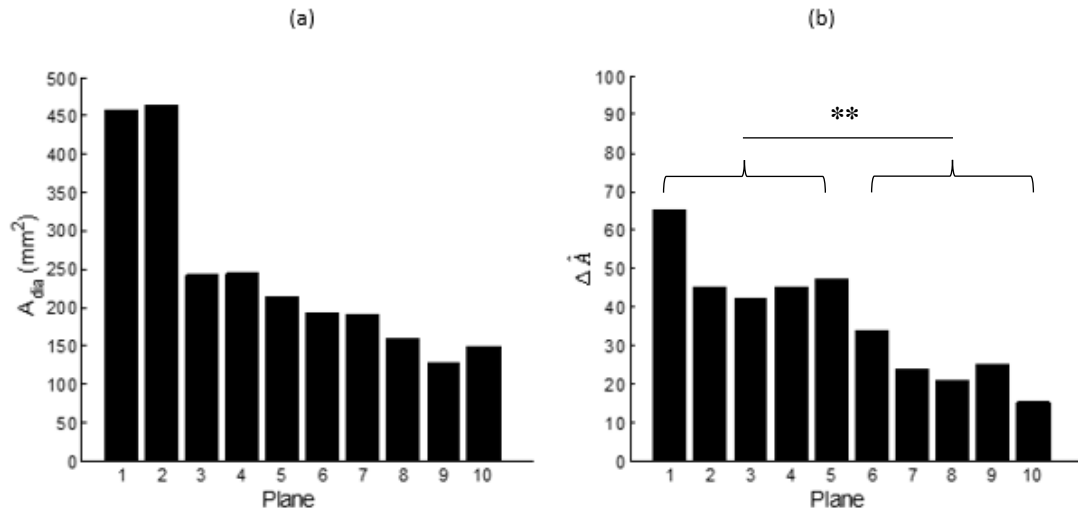
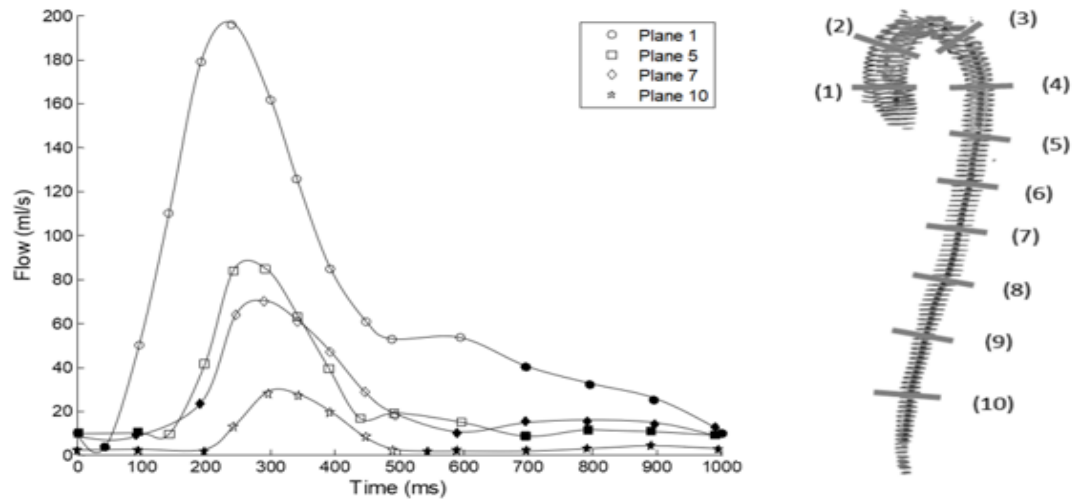


Figure 5.6: (a) Diastolic cross-sectional-area for each plane, highlighting the tapering of the aorta distally. (b) Cross-sectional-area change for each plane along the aorta. \*\* indicates a statistically significant difference between thoracic and abdominal aorta subgroups ( $p < 0.005$ ).

### 5.3.3 Spatial Haemodynamics

The integral of the velocity matrix within the boundary of the fluid domain yields the volumetric flow rate,  $Q$  (Figure 5.7). The reduction of  $Q$  with increasing distance from the heart can be attributed, in part, to out-flow to visceral arteries including the supra-aortic, mesenteric and renal vessels. For example, the large drop in flow between Plane 1 and Plane 5 is associated with out-flow to the innominate, left common carotid, and left subclavian arteries supplying the head, neck, and upper body with a large volumetric blood flow. The opening of the aortic valve occurs at approximately 50 ms and closes at 500 ms, while the time lag between the flow peaks of each plane is related to the speed of the ejected pulse wave propagating through the aortic tree. Peak systolic blood flow ranges from 196 ml/s at Plane 1 in the ascending aorta to 28 ml/s at Plane 10 in the abdominal aorta, while diastolic flow at timepoint 600 ms ranges from 53 ml/s at Plane 1 to 2 ml/s in Plane 10. The non-zero flow during diastole, illustrates the well-known Windkessel effect. The measurements presented here demonstrate that the diastolic flow due to the Windkessel effect is highest in the ascending aorta and reduces with increasing distance from the heart.



**Figure 5.7:** Aortic volumetric flow rate,  $Q$  throughout the cardiac cycle for a series of discrete planes along the vessel from proximal to distal aorta. Filled markers indicate phases where low-VENC was used and clear markers where high-VENC was used.

The coefficient of proportionality between  $Q$  and  $CSA$  provides the wave propagation speed (i.e. the speed of a blood column as it travels through the aorta following ventricular ejection), formally known as the pulse wave velocity (PWV). Figure 5.8(a) shows a higher wave velocity in the distal aorta than in the proximal aorta. Again, categorising the planes into two subgroups, *thoracic* and *abdominal*, a statistically significant difference in PWV between the two groups is found ( $p < 0.005$ ). The implementation of the TTP method to determine the PWV also provides a similar result, as shown in Figure 5.8(b); the PWV in the abdominal aorta (8.2 m/s) is found to be approximately 28% higher than in the thoracic aorta (6.4 m/s). The increased PWV in the abdominal aorta is due, in part, to the tapered geometry, as shown in Figure 5.6(a). However, spatial changes in vessel compliance also contribute to the observed increase in PWV.

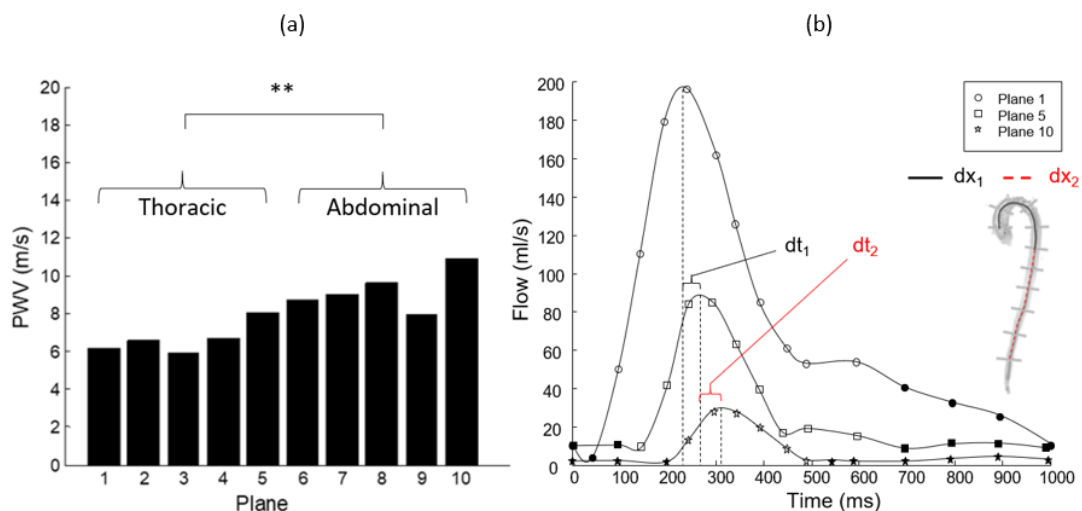


**Figure 5.8:** (a) PWV determined using the QA method. A gradient in wave speed is evident, increasing with distance from the heart. (b) PWV determined using the TTP method from Plane 1 to Plane 5 (thoracic) and Plane 5 to Plane 10 (abdominal). Thoracic and abdominal aortic segments exhibit a wave velocity of 6.36 m/s and 8.21 m/s respectively.

### 5.3.4 Spatial and Temporal Compliance

Spatial and temporal changes in vessel compliance are next investigated using the three blood pressure waveforms ((i) uniform brachial pressure wave, (ii) spatially varying pressure wave computed using the unsteady Bernoulli approach, (iii) spatially varying pressure wave determined using the piecewise approach) determined in Section 5.2.5. In Figure 5.9, the instantaneous lumen cross-sectional-area is plotted as a function of blood pressure. Results are presented for the three aforementioned pressure waveforms at the proximal ascending aorta and the distal abdominal aorta. The instantaneous compliance at a given lumen pressure is given by the slope of the pressure-area graph. In all cases two distinct linear regions are observed, such that a high vessel compliance occurs at low pressures, and a low vessel compliance occurs at high pressures. This clearly demonstrates that vessel compliance during a cardiac cycle cannot be simplistically represented by a single value. The decrease in compliance at higher lumen pressures is due to strain stiffening constitutive behaviour of the aortic wall.

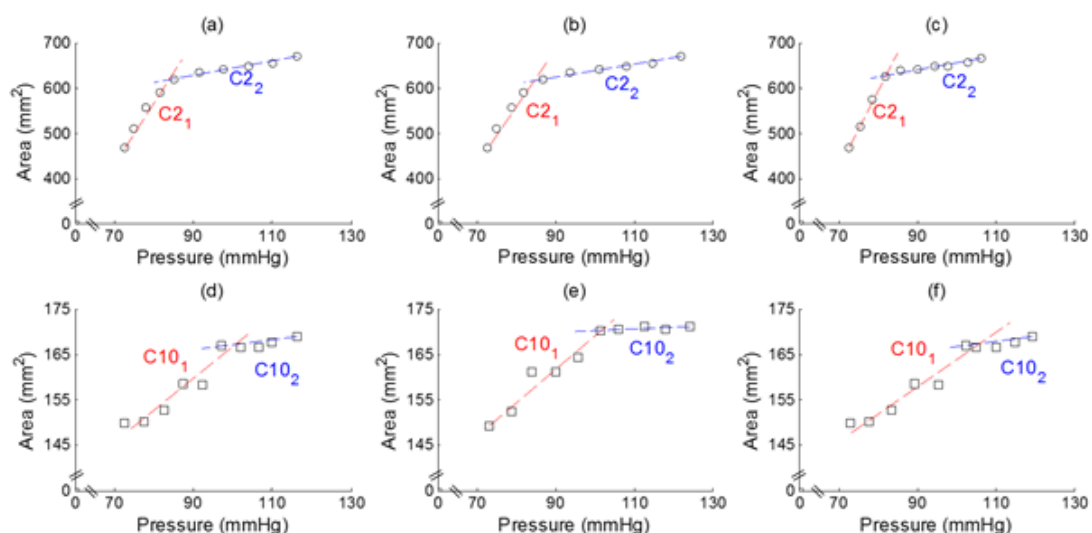


**Figure 5.9:** Area versus Pressure for the three pressure waveforms: (a,d) uniform brachial pressure wave; (b,e) spatially varying pressure wave computed using unsteady Bernoulli approach; (c,f) spatially varying pressure wave determined using piecewise approach. Circular markers represent Plane 2 (proximal ascending thoracic aorta) and square markers represent Plane 10 (distal infrarenal abdominal aorta). Two-distinctive linear compliance regimes are evident in each case. The values of the bi-linear compliance are determined from the slope of the best-fit lines. High compliance regimes labelled with red lines and subscript “1”, and low compliance regimes labelled with blue lines and subscripts “2”; e.g. C10<sub>2</sub> indicates the low compliance regime of plane 10. Results highlight a strong dependence of compliance on transient lumen pressure and on spatial location.

For each case presented in Figure 5.9, the value of compliance is determined using linear regression fits for the two distinct regions (red and blue) of the pressure-area graphs (values are presented in Table 5.1). Clear evidence of strain stiffening is visible in each subplot of Figure 5.9, where significantly higher aortic dilation for a given change in pressure are observed in the high compliance (red) regime, compared to the low compliance (blue) regime. As an example, for Plane 2 (Figure 5.9a (uniform blood pressure waveform)) the compliance at low pressure ( $C2_1 = 11.94 \text{ mm}^2/\text{mmHg}$ ) is over eight times higher than the compliance at high pressure ( $C2_2 = 1.48 \text{ mm}^2/\text{mmHg}$ ). For Plane 2 the high compliance regime occurs for pressures below 85 mmHg. While a broadly similar bi-linear behaviour is also observed at Plane 10 (abdominal aorta), compliance values are an order of magnitude lower than those at Plane 2 (ascending aorta). As an example, for Plane 10 (Figure 5.9d (uniform blood pressure waveform)) a high compliance value of  $C10_1 = 0.67 \text{ mm}^2/\text{mmHg}$  is determined, with a low compliance value of  $C10_2 = 0.11 \text{ mm}^2/\text{mmHg}$ . Furthermore, at Plane 10 the change in compliance regime is observed to occur at a pressure of  $\sim 100 \text{ mmHg}$  (compared to  $\sim 85 \text{ mmHg}$  at Plane 2). These results highlight the dramatic differences in *in-vivo* material behaviour between the thoracic and abdominal aorta. Despite the fact that higher material strains occur in the thoracic aorta, as evident from Figure 5.6, the instantaneous material stiffness is significantly higher in the abdominal aorta. The higher stiffness of the abdominal aorta explains, in part, the higher PWV in this region, as observed in Figure 5.8.

**Table 5.1: Compliance values based on linear regression best-fits to the low and high compliance regime data presented in Figure 5.9. C2 represents Plane 2 and C10 Plane 10 with subscripts 1 and 2 representing high and low compliance regimes, respectively.**

	Uniform		Bernoulli		Piecewise	
	Compliance (mm <sup>2</sup> /mmHg)	(R <sup>2</sup> )	Compliance (mm <sup>2</sup> /mmHg)	(R <sup>2</sup> )	Compliance (mm <sup>2</sup> /mmHg)	(R <sup>2</sup> )
C2 <sub>1</sub>	11.94	(0.973)	10.64	(0.961)	17.1	(0.998)
C2 <sub>2</sub>	1.48	(0.974)	1.32	(0.976)	1.40	(0.944)
C10 <sub>1</sub>	0.67	(0.892)	0.70	(0.933)	0.56	(0.919)
C10 <sub>2</sub>	0.11	(0.619)	0.04	(0.523)	0.12	(0.649)

## 5.4 Discussion

The focus of this chapter is to employ 4D Flow MRI techniques to investigate, non-invasively, the spatiotemporal heterogeneity of the entire human aorta. The study aims to create a framework capable of developing a map of the aorta with respect to cross-sectional-area change, volumetric flow rate, pulse wave velocity and compliance throughout both the spatial and temporal domain. Novel contributions include: (i) implementation of a dual-VENC composite dataset approach to imaging the entire aorta, which ensures accuracy in both area and flow quantification throughout the unsteady velocity profile of the cardiac cycle, providing an alternative approach to phase unwrapping; (ii) quantification of local PWV along the entire aorta, and demonstration that PWV increases with increasing distance from the heart; (iii) quantification of local compliance throughout the cardiac cycle, and demonstration that aortic compliance is characterised by a bi-linear relationship, with significantly higher compliance values at low pressures.

To the author's knowledge, this study presents the most comprehensive dataset of patient-specific aortic measurements to date, highlighting several key points that have the potential to guide clinical practice and aortic device design. The motivation for the work stems from the scarcity of data published on the regional variance of biomechanical properties of the aorta and the persistence of post-operative cardiac complications following TEVAR.

### 5.4.1 Spatial Deformation

We examine the deformation of the human aorta during the entire cardiac cycle at 10 planes, ranging from the sinus of Valsalva to immediately proximal to the common iliac bifurcation. The high levels of cross-sectional-area change,  $\Delta\hat{A}$  during a cardiac cycle, ranging from 15% in the abdominal aorta to 65% in the ascending aorta, highlight the extremely large deformations of the aortic wall. Accurate characterisation of such large deformations requires detailed imaging of the entire aorta throughout the entire cardiac cycle. While the observed trend that dilation reduces with distance from the heart is in broad agreement with previous non-invasive

imaging studies by Mohiaddin *et al.*, (1989) and Saouti *et al.*, (2012), the current study provides further insights by measuring dilation on a large number of planes spanning the entire aorta. A number of *ex-vivo* studies also suggest that compliance decreases with distance from the heart (Moriwaki *et al.*, 2011b; Krüger *et al.*, 2016). A study by Tsamis and Vorp (2013) reports that the ascending thoracic aorta contains 80 elastin lamellar units while the infra-renal abdominal aorta contains 32. The decrease in elastin and increase in collagen observed in Chapter 4 of this thesis (in addition to the tapering of the aorta and the spatially dependent strain at which collagen fibers become taught (Zeinali-Davarani *et al.*, 2015)) provides a microstructural explanation for the decrease in compliance observed here with distance from the heart. Moreover, Tsamis and Vorp (2013) also report a 50% decrease in elastin units between the descending thoracic and supra-celiac aorta, possibly providing an explanation for locally varying cross-sectional-area change observed in the current study. A review paper by Sherif (2014) reports that the aorta, from a developmental point of view, is not a homogeneous structure nor one contiguous anatomical entity. Rather, it is suggested that the vessel can be split into discrete segments, each of which develops and differentiates under a distinct set of genetic and transcriptional factors. It is hypothesized that the regional differences in biomechanical behaviour may be due to the development of the ascending thoracic from neural crest cells and descending thoracic aorta from the mesoderm. With distinct connections or “weld points” between such segments, this may be the cause for local differences in cross-sectional-area change and PWV measured between adjacent planes in the current study.

#### **5.4.2 Spatial Haemodynamics**

A notable outcome of this study is the spatial variance in PWV along the aorta. Results show that the PWV increases with increasing distance from the heart. This finding is reinforced using the TTP method, uncovering a 28% increase in PWV between the thoracic and abdominal aorta (6.4 m/s versus 8.2 m/s). Generally, PWV is defined in the literature as a single value for the aorta (Wilson *et al.*, 1998; Blacher *et al.*, 1999; McEniery *et al.*, 2005; Ben-Shlomo *et al.*, 2014; McDonnell *et al.*, 2017). The assumption of a uniform single valued PVW is primarily due to the method of clinical measurement, where the pressure pulse between two distinct sites, most commonly the carotid and femoral arteries (cfPWV) is recorded. The Reference Values for Arterial Stiffness' Collaboration (2010), report a mean PWV value of 6.2 m/s for a cohort of 1455 normal subjects < 30 year of age. However, the pathway over which cfPWV is defined does not include the highly compliant ascending aorta. The utilization of MRI techniques to quantify aortic PWV has the ability to quantify changes at a local level, producing an accurate patient-specific spatial map of PVW. A study by Quinaglia *et al.* (2018) reported PWV readings targeted to the ascending aorta and found velocities of between 4 and 5.8 m/s, while Boardman *et al.* (2017) investigated the brachio-femoral pathway in 152 young adults and found mean PWV values of 8.7 m/s. Such measurements are comparable with the data presented in the current study for the thoracic and abdominal aorta respectively.

### 5.4.3 Spatial and Temporal Compliance

Compliance is generally presented as a single value, by taking the difference in area between diastole and systole and dividing this by patient's change in blood pressure. Aortic tissue is not a simple linear elastic material. Rather it exhibits a significant increase in stiffness when it is stretched to a high level of deformation (Nolan and McGarry, 2016). Such mechanical behaviour occurs due to the structural contribution of collagen fibres. At low arterial strains collagen fibres are wavy, and an incremental increase in applied force will result in a significant increase in the length of the fibre, i.e. the fibre exhibits a low structural stiffness at low levels of deformation. A further incremental increase in force applied to a straightened collagen fibre will not result in a large increase in the length of the fibre. This is because the straightening of the fibre at high levels of deformation results in an increase of the structural stiffness (Holzapfel, Gasser and Ogden, 2000).

The structural contribution of collagen results in the well-established non-linear stress-strain relationship for arterial tissue, whereby the material exhibits low stiffness at low strains and high stiffness at high strains. The transition from the low stiffness regime to the high stiffness regime is commonly modelled using exponential strain stiffening material laws (Holzapfel, Gasser and Ogden, 2000; Nolan *et al.*, 2014). To date such models have been motivated and calibrated using *in-vitro* tests of excised arterial tissue. Our study provides evidence, for the first time, that significant strain stiffening of the aorta occurs *in-vivo* over the deformation range of a cardiac cycle. Our results suggest that clinical compliance (defined as a change in lumen area with respect to a change in pressure) should not be characterised by a single value. Rather, a high compliance regime is observed for low pressures during diastole, followed by a transition to a low compliance regime for high pressures during systole. This *in-vivo* observation is consistent with strain stiffening observed in *in-vitro* testing, and it calls into question the accuracy of the common assumption that *in-vivo* lumen area increases linearly with lumen pressure during a cardiac cycle (inherent in the description of compliance by a single coefficient, e.g. Lehmann *et al.* 1998; Bogren *et al.* 1989; Mitéran *et al.* 2018; van Herwaarden *et al.* 2006; Ioannou *et al.* 2009; Lalande *et al.* 2008; Vyas *et al.* 2007). Furthermore, our study quantifies the values of high and low compliance during a cardiac cycle, and demonstrates that these values, and the associated transition pressures, are spatially heterogeneous. Such detailed insights into vessel compliance are critical for development of an enhanced understanding of the relationship between pressure, blood flow, and PWV in the aorta, and will potentially lead to improved interventional procedures and device designs.

### 5.4.4 Limitations

A number of limitations should be noted for the current study, providing motivation for follow-on studies. The purpose of this study was to develop a dual-VENC imaging protocol to generate high resolution subject-specific data on heterogeneous non-linear aortic compliance and pulse wave velocity in a clinically feasible timeframe. While the data generated in the current study is limited to a single subject, the demonstration

of this capability of our methodology provides a platform for extensive high-resolution characterisation of aortic biomechanics for populations of healthy and diseased subjects. It should be noted that increased temporal resolution, spatial resolution, coverage and signal to noise ratio all incur the cost of higher scan time and gradient coil capabilities in every MRI system. Hence, in order to maintain clinical feasibility temporal resolution was sacrificed in this study. In the ideal situation each phase would span a segment shorter than 50 ms, which may lead to greater accuracy in the quantification of area, flow and hence PWV, and so, more work may be justified in this area to see if any further optimization of parameters is possible for imaging the aorta in its entirety, while maintaining a short scan time.

In terms of determining aortic compliance, a challenge remains to accurately measure a continuous location-specific blood pressure waveform throughout the aorta without resorting to an invasive catheterization procedure. In the absence of a clearly defined best strategy to compute a continuous pressure waveform noninvasively (Dyverfeldt *et al.*, 2015; Adji and O'Rourke, 2017), we implemented three separate waveform generation methods, namely; 'Uniform', 'Unsteady Bernoulli' and 'Piecewise'. In any case, the current study demonstrates that the bi-linearity of the measured compliance is not strongly affected by the method of approximating the lumen pressure waveform.

#### **5.4.5 Implications**

The results of this study have a number of potential implications for the fields of aortic biomechanics and cardiovascular surgery. The study presents a protocol that can provide accurate spatial and temporal measurements of compliance and PWV in the aorta. This may provide an incremental step in understanding why cardiac events occur post-TEVAR, through a better understanding of the relationship between PWV, aortic stiffness and cardiac function. Stenting may have a spatially varying effect on the biomechanics of the aorta by inducing a cascade analogous to "*accelerated arteriosclerosis*" on the system. This in turn effects cardiac function, as documented elsewhere for arteriosclerosis developed during the ageing process (Tsamis and Vorp 2013; Kohn and Reinhart-King 2015; Wohlfahrt *et al.* 2015). During EVAR however, a significant reduction in compliance may occur instantaneously due to stent deployment, in contrast to arteriosclerosis, where compliance gradually reduces over a period of decades. The current study shows that aortic compliance cannot be captured by a single value, and that the vessel is significantly less compliant in systole than diastole. Incorporating such detailed information into the design of EVAR devices with the aim of replicating the natural non-linear compliance of the vessel may reduce the prevalence of the aforementioned complications.

## **5.5 Conclusions**

A dual-VENC 4D Flow MRI protocol is developed and implemented in a commercial scanner for characterising the biomechanics of the entire human aorta. A composite dataset approach is employed to maximally attenuate fluid contrast throughout the unsteady velocity profile of the cardiac cycle, providing an alternative method to phase unwrapping techniques. Pulse wave velocity increases from proximal to distal aorta, while cross-sectional-area change, volumetric flow rate and compliance all reduce with distance from the heart. Finally, compliance is shown to alter significantly during the cardiac cycle, with significantly higher compliance being observed during periods of low blood pressure.

## **5.6 Acknowledgements**

The author would like to acknowledge Mr. Torben Shneider and Mr. Matthew Clemence of Philips (Philips Medical Systems, Best, Netherlands) and Evelyn Smith and Marie McMullen (Department of Radiology, Galway Clinic) for their support and guidance during this study.

## 5.7 Bibliography

- Adji, A. and O'Rourke, M. F. (2017) 'Central aortic pressure calibration', *Journal of Hypertension*, 35(4), pp. 893–894. doi: 10.1097/HJH.0000000000001246.
- Agrawal, V., Kollimada, S. A., Byju, A. G. and Gundiah, N. (2013) 'Regional variations in the nonlinearity and anisotropy of bovine aortic elastin', *Biomechanics and Modeling in Mechanobiology*, 12(6), pp. 1181–1194. doi: 10.1007/s10237-013-0474-3.
- Ben-Shlomo, Y., Spears, M., Boustred, C., May, M., Anderson, S. G., Benjamin, E. J., Boutouyrie, P., Cameron, J., Chen, C.-H., Cruickshank, J. K., Hwang, S.-J., Lakatta, E. G., Laurent, S., Maldonado, J., Mitchell, G. F., Najjar, S. S., Newman, A. B., Ohishi, M., Pannier, B., Pereira, T., Vasani, R. S., Shokawa, T., Sutton-Tyrell, K., Verbeke, F., Wang, K.-L., Webb, D. J., Willum Hansen, T., Zoungas, S., McEniery, C. M., Cockcroft, J. R. and Wilkinson, I. B. (2014) 'Aortic Pulse Wave Velocity Improves Cardiovascular Event Prediction', *Journal of the American College of Cardiology*. *Journal of the American College of Cardiology*, 63(7), pp. 636–646. doi: 10.1016/j.jacc.2013.09.063.
- Bernstein, M. A., King, K. F. and Zhou, X. J. (2004) *Handbook of MRI pulse sequences*. Academic Press.
- Bhamidipati, C. M., LaPar, D. J., Mehta, G. S., Kern, J. A., Kron, I. L., Upchurch, G. R., Ailawadi, G. and Ailawadi, G. (2011) 'Have thoracic endografting outcomes improved since US Food and Drug Administration approval?', *The Annals of thoracic surgery*. *NIH Public Access*, 91(5), p. 1314–22; discussion 1322. doi: 10.1016/j.athoracsur.2011.01.037.
- Biglands, J. D., Radjenovic, A. and Ridgway, J. P. (2012) 'Cardiovascular magnetic resonance physics for clinicians: part II', *Journal of Cardiovascular Magnetic Resonance*. *BioMed Central*, 14(1), p. 66. doi: 10.1186/1532-429X-14-66.
- Bioucas-Dias, J. M. and Valadao, G. (2007) 'Phase Unwrapping via Graph Cuts', *IEEE Transactions on Image Processing*, 16(3), pp. 698–709. doi: 10.1109/TIP.2006.888351.
- Bischoff, M. S., Ante, M., Meisenbacher, K. and Böckler, D. (2016) 'Outcome of thoracic endovascular aortic repair in patients with thoracic and thoracoabdominal aortic aneurysms', *Journal of Vascular Surgery*. *Elsevier*, 63(5), p. 1170–1181.e1. doi: 10.1016/j.jvs.2015.11.045.
- Blacher, J., Asmar, R., Djane, S., London, G. M. and Safar, M. E. (1999) 'Aortic pulse wave velocity as a marker of cardiovascular risk in hypertensive patients.', *Hypertension (Dallas, Tex. : 1979)*. *American Heart Association, Inc.*, 33(5), pp. 1111–7. doi: 10.1161/01.HYP.33.5.1111.
- Boardman, H., Lewandowski, A. J., Lazdam, M., Kenworthy, Y., Whitworth, P., Zwager, C. L., Francis, J. M., Aye, C. Y. L., Williamson, W., Neubauer, S. and Leeson, P. (2017) 'Aortic stiffness and blood pressure variability in young people', *Journal of Hypertension*, 35(3), pp. 513–522. doi: 10.1097/HJH.0000000000001192.

- Bogren, H. G., Mohiaddin, R. H., Klipstein, R. K., Firmin, D. N., Underwood, R. S., Rees, S. R. and Longmore, D. B. (1989) 'The function of the aorta in ischemic heart disease: A magnetic resonance and angiographic study of aortic compliance and blood flow patterns', *American Heart Journal*. Mosby, 118(2), pp. 234–247. doi: 10.1016/0002-8703(89)90181-6.
- Bustamante, M., Gupta, V., Carlhäll, C.-J. and Ebbers, T. (2017) 'Improving visualization of 4D flow cardiovascular magnetic resonance with four-dimensional angiographic data: generation of a 4D phase-contrast magnetic resonance CardioAngiography (4D PC-MRCA)', *Journal of Cardiovascular Magnetic Resonance*. BioMed Central, 19(1), p. 47. doi: 10.1186/s12968-017-0360-8.
- Callaghan, F. M., Kozor, R., Sherrah, A. G., Valley, M., Celermajer, D., Figtree, G. A. and Grieve, S. M. (2016) 'Use of multi-velocity encoding 4D flow MRI to improve quantification of flow patterns in the aorta', *Journal of Magnetic Resonance Imaging*, 43(2), pp. 352–363. doi: 10.1002/jmri.24991.
- Cavalcante, J. L., Lima, J. A. C., Redheuil, A. and Al-Mallah, M. H. (2011) 'Aortic Stiffness', *Journal of the American College of Cardiology*. *Journal of the American College of Cardiology*, 57(14), pp. 1511–1522. doi: 10.1016/j.jacc.2010.12.017.
- Cheng, J., Mei, Y., Liu, B., Guan, J., Liu, X., Wu, E. X., Feng, Q., Chen, W. and Feng, Y. (2018) 'A novel phase-unwrapping method based on pixel clustering and local surface fitting with application to Dixon water-fat MRI', *Magnetic Resonance in Medicine*, 79(1), pp. 515–528. doi: 10.1002/mrm.26647.
- Cibis, M., Potters, W. V., Gijssen, F. J. H., Marquering, H., vanBavel, E., van der Steen, A. F. W., Nederveen, A. J. and Wentzel, J. J. (2014) 'Wall shear stress calculations based on 3D cine phase contrast MRI and computational fluid dynamics: A comparison study in healthy carotid arteries', *NMR in Biomedicine*. John Wiley and Sons Ltd, 27(7), pp. 826–834. doi: 10.1002/nbm.3126.
- Concannon, J., Kavanagh, E. P., Hynes, N., McHugh, P. E., McGarry, J. P. and Sultan, S. (2017) 'The Streamliner Multilayer Flow Modulator in the treatment of Complex Thoracoabdominal Aortic Aneurysms', *Vascular*. *Vascular*, 25(2\_suppl).
- Conrad, M. F., Tucek, J., Freezor, R., Bavaria, J., White, R. and Fairman, R. (2017) 'Results of the VALOR II trial of the Medtronic Valiant Thoracic Stent Graft', *Journal of Vascular Surgery*. Mosby, 66(2), pp. 335–342. doi: 10.1016/J.JVS.2016.12.136.
- Crosetto, P., Reymond, P., Deparis, S., Kontaxakis, D., Stergiopoulos, N. and Quarteroni, A. (2011) 'Fluid–structure interaction simulation of aortic blood flow', *Computers & Fluids*. Pergamon, 43(1), pp. 46–57. doi: 10.1016/J.COMPFLUID.2010.11.032.
- Cusack, R. and Papadakis, N. (2002) 'New Robust 3-D Phase Unwrapping Algorithms: Application to Magnetic Field Mapping and Undistorting Echoplanar Images', *NeuroImage*. Academic Press, 16(3), pp. 754–764. doi: 10.1006/NIMG.2002.1092.

- Dua, A., Kuy, S., Lee, C. J., Upchurch, G. R. and Desai, S. S. (2014) 'Epidemiology of aortic aneurysm repair in the United States from 2000 to 2010', *Journal of Vascular Surgery*, 59(6), pp. 1512–1517. doi: 10.1016/j.jvs.2014.01.007.
- Dyverfeldt, P., Bissell, M., Barker, A. J., Bolger, A. F., Carlhäll, C.-J., Ebbers, T., Francios, C. J., Frydrychowicz, A., Geiger, J., Giese, D., Hope, M. D., Kilner, P. J., Kozerke, S., Myerson, S., Neubauer, S., Wieben, O. and Markl, M. (2015) '4D flow cardiovascular magnetic resonance consensus statement', *Journal of Cardiovascular Magnetic Resonance*. BioMed Central, 17(1), p. 72. doi: 10.1186/s12968-015-0174-5.
- Gohean, J. R., Moser, R. D. and Zhang, Y. (2009) 'Patient-specific isogeometric fluid–structure interaction analysis of thoracic aortic blood flow due to implantation of the Jarvik 2000 left ventricular assist device', *Computer Methods in Applied Mechanics and Engineering*. North-Holland, 198(45–46), pp. 3534–3550. doi: 10.1016/J.CMA.2009.04.015.
- Ha, H., Kim, G. B., Kweon, J., Lee, S. J., Kim, Y.-H., Lee, D. H., Yang, D. H. and Kim, N. (2016) 'Hemodynamic Measurement Using Four-Dimensional Phase-Contrast MRI: Quantification of Hemodynamic Parameters and Clinical Applications', *Korean Journal of Radiology*, 17(4), p. 445. doi: 10.3348/kjr.2016.17.4.445.
- van Herwaarden, J. A., Muhs, B. E., Vincken, K. L., van Prehn, J., Teutelink, A., Bartels, L. W., Moll, F. L. and Verhagen, H. J. M. (2006) 'Aortic Compliance Following EVAR and the Influence of Different Endografts: Determination Using Dynamic MRA', *Journal of Endovascular Therapy*. SAGE PublicationsSage CA: Los Angeles, CA, 13(3), pp. 406–414. doi: 10.1583/06-1848.1.
- Hicks, C. W., Wick, E. C., Canner, J. K., Black, J. H., Arhuidese, I., Qazi, U., Obeid, T., Freischlag, J. A. and Malas, M. B. (2015) 'Hospital-Level Factors Associated With Mortality After Endovascular and Open Abdominal Aortic Aneurysm Repair', *JAMA Surgery*. American Medical Association, 150(7), p. 632. doi: 10.1001/jamasurg.2014.3871.
- Holzapfel, G. A., Gasser, T. C. and Ogden, R. W. (2000) 'A New Constitutive Framework for Arterial Wall Mechanics and a Comparative Study of Material Models', *Journal of elasticity and the physical science of solids*. Kluwer Academic Publishers, 61(1–3), pp. 1–48. doi: 10.1023/A:1010835316564.
- IMPROVE Trial Investigators, I. trial, Powell, J. T., Sweeting, M. J., Thompson, M. M., Ashleigh, R., Bell, R., Gomes, M., Greenhalgh, R. M., Grieve, R., Heatley, F., Hinchliffe, R. J., Thompson, S. G. and Ulug, P. (2014) 'Endovascular or open repair strategy for ruptured abdominal aortic aneurysm: 30 day outcomes from IMPROVE randomised trial.', *BMJ (Clinical research ed.)*. British Medical Journal Publishing Group, 348, p. f7661. doi: 10.1136/BMJ.F7661.
- Ioannou, C. V., Morel, D. R., Katsamouris, A. N., Katranitsa, S., Startchik, I., Kalangos, A., Westerhof, N. and Stergiopoulos, N. (2009) 'Left ventricular hypertrophy induced by reduced aortic compliance.', *Journal of vascular research*. Karger Publishers, 46(5), pp. 417–25. doi: 10.1159/000194272.

- Kim, H. J., Vignon-Clementel, I. E., Figueroa, C. A., LaDisa, J. F., Jansen, K. E., Feinstein, J. A. and Taylor, C. A. (2009) 'On Coupling a Lumped Parameter Heart Model and a Three-Dimensional Finite Element Aorta Model', *Annals of Biomedical Engineering*. Springer US, 37(11), pp. 2153–2169. doi: 10.1007/s10439-009-9760-8.
- Kohn, J. C., Lampi, M. C. and Reinhart-King, C. A. (2015) 'Age-related vascular stiffening: causes and consequences.', *Frontiers in genetics*, 6, p. 112. doi: 10.3389/fgene.2015.00112.
- Krüger, T., Veseli, K., Lausberg, H., Vöhringer, L., Schneider, W. and Schlensak, C. (2016) 'Regional and directional compliance of the healthy aorta: an ex vivo study in a porcine model', *Interactive CardioVascular and Thoracic Surgery*, 23(1), pp. 104–111. doi: 10.1093/icvts/ivw053.
- Lalande, A., Khau Van Kien, P., Walker, P. M., Zhu, L., Legrand, L., Claustres, M., Jeunemaître, X., Brunotte, F. and Wolf, J. E. (2008a) 'Compliance and pulse wave velocity assessed by MRI detect early aortic impairment in young patients with mutation of the smooth muscle myosin heavy chain', *Journal of Magnetic Resonance Imaging*. Wiley-Blackwell, 28(5), pp. 1180–1187. doi: 10.1002/jmri.21565.
- Lalande, A., Khau Van Kien, P., Walker, P. M., Zhu, L., Legrand, L., Claustres, M., Jeunemaître, X., Brunotte, F. and Wolf, J. E. (2008b) 'Compliance and pulse wave velocity assessed by MRI detect early aortic impairment in young patients with mutation of the smooth muscle myosin heavy chain', *Journal of Magnetic Resonance Imaging*. Wiley Subscription Services, Inc., A Wiley Company, 28(5), pp. 1180–1187. doi: 10.1002/jmri.21565.
- Lamata, P., Pitcher, A., Krittian, S., Nordsletten, D., Bissell, M. M., Cassar, T., Barker, A. J., Markl, M., Neubauer, S. and Smith, N. P. (2014) 'Aortic relative pressure components derived from four-dimensional flow cardiovascular magnetic resonance', *Magnetic Resonance in Medicine*, 72(4), pp. 1162–1169. doi: 10.1002/mrm.25015.
- Länne, T., Sonesson, B., Bergqvist, D., Bengtsson, H. and Gustafsson, D. (1992) 'Diameter and compliance in the male human abdominal aorta: Influence of age and aortic aneurysm', *European Journal of Vascular Surgery*. W.B. Saunders, 6(2), pp. 178–184. doi: 10.1016/S0950-821X(05)80237-3.
- Lehmann, E. D., Hopkins, K. D., Rawesh, A., Joseph, R. C., Kongola, K., Coppack, S. W. and Gosling, R. G. (1998) 'Relation between number of cardiovascular risk factors/events and noninvasive Doppler ultrasound assessments of aortic compliance.', *Hypertension* (Dallas, Tex. : 1979). American Heart Association, Inc., 32(3), pp. 565–9. doi: 10.1161/01.HYP.32.3.565.
- Loecher, M., Schrauben, E., Johnson, K. M. and Wieben, O. (2016) 'Phase unwrapping in 4D MR flow with a 4D single-step laplacian algorithm', *Journal of Magnetic Resonance Imaging*, 43(4), pp. 833–842. doi: 10.1002/jmri.25045.
- Markl, M., Frydrychowicz, A., Kozerke, S., Hope, M. and Wieben, O. (2012) '4D flow MRI.', *Journal of magnetic resonance imaging : JMRI*, 36(5), pp. 1015–36. doi: 10.1002/jmri.23632.

- Markl, M., Schnell, S., Wu, C., Bollache, E., Jarvis, K., Barker, A. J., Robinson, J. D. and Rigsby, C. K. (2016) 'Advanced flow MRI: emerging techniques and applications', *Clinical Radiology*. W.B. Saunders, 71(8), pp. 779–795. doi: 10.1016/J.CRAD.2016.01.011.
- Markl, M., Schnell, S., Wu, C. and Rigsby, C. . (2016) 'Advanced flow MRI: emerging techniques and applications', *Clinical Radiology*.
- McDonnell, B. J., Yasmin, Butcher, L., Cockcroft, J. R., Wilkinson, I. B., Erusalimsky, J. D. and McEniery, C. M. (2017) 'The age-dependent association between aortic pulse wave velocity and telomere length', *The Journal of Physiology*. Wiley/Blackwell (10.1111), 595(5), pp. 1627–1635. doi: 10.1113/JP273689.
- McEniery, C. M., Yasmin, Hall, I. R., Qasem, A., Wilkinson, I. B. and Cockcroft, J. R. (2005) 'Normal Vascular Aging: Differential Effects on Wave Reflection and Aortic Pulse Wave Velocity: The Anglo-Cardiff Collaborative Trial (ACCT)', *Journal of the American College of Cardiology*. Elsevier, 46(9), pp. 1753–1760. doi: 10.1016/J.JACC.2005.07.037.
- Mitéran, J., Bouchot, O., Cochet, A. and Lalande, A. (2018) 'Automatic determination of aortic compliance based on MRI and adapted curvilinear detector', *Biomedical Signal Processing and Control*. Elsevier, 40, pp. 295–311. doi: 10.1016/J.BSPC.2017.09.002.
- Mohiaddin, R. H., Underwood, S. R., Bogren, H. G., Firmin, D. N., Klipstein, R. H. and Longmore, D. B. (1989) 'Regional aortic compliance studied by magnetic resonance imaging: the effects of age, training, and coronary artery disease', *Br Heart J*, 62, pp. 90–6. Available at: <http://heart.bmj.com/content/heartjnl/62/2/90.full.pdf> (Accessed: 2 March 2018).
- Morbiducci, U., Ponzini, R., Gallo, D., Bignardi, C. and Rizzo, G. (2013) 'Inflow boundary conditions for image-based computational hemodynamics: impact of idealized versus measured velocity profiles in the human aorta.', *Journal of biomechanics*. Elsevier, 46(1), pp. 102–9. doi: 10.1016/j.jbiomech.2012.10.012.
- Moriwaki, T., Oie, T., Takamizawa, K., Murayama, Y., Fukuda, T., Omata, S., Kanda, K. and Nakayama, Y. (2011) 'Variations in local elastic modulus along the length of the aorta as observed by use of a scanning haptic microscope (SHM)', *Journal of Artificial Organs*. Springer Japan, 14(4), pp. 276–283. doi: 10.1007/s10047-011-0596-2.
- Musa, T. Al, Uddin, A., Fairbairn, T. A., Dobson, L. E., Sourbron, S. P., Steadman, C. D., Motwani, M., Kidambi, A., Ripley, D. P., Swoboda, P. P., McDiarmid, A. K., Erhayiem, B., Oliver, J. J., Blackman, D. J., Plein, S., McCann, G. P. and Greenwood, J. P. (2016) 'Assessment of aortic stiffness by cardiovascular magnetic resonance following the treatment of severe aortic stenosis by TAVI and surgical AVR', *Journal of Cardiovascular Magnetic Resonance*. BioMed Central, 18(1), p. 37. doi: 10.1186/s12968-016-0256-z.
- Nett, E. J., Johnson, K. M., Frydrychowicz, A., Del Rio, A. M., Schrauben, E., Francois, C. J. and Wieben, O. (2012) 'Four-dimensional phase contrast MRI with accelerated dual velocity encoding', *Journal of Magnetic Resonance Imaging*.

- Wiley Subscription Services, Inc., A Wiley Company, 35(6), pp. 1462–1471. doi: 10.1002/jmri.23588.
- Nolan, D. ., Ogden, R. W., Destrade, M. and McGarry, J. P. (2014) ‘A robust anisotropic hyperelastic formulation for the modelling of soft tissue’, *Journal of the Mechanical Behaviour of Biomedical Materials*.
- Nolan, D. R. and McGarry, J. P. (2016) ‘On the Compressibility of Arterial Tissue’, *Annals of Biomedical Engineering*. Springer US, 44(4), pp. 993–1007. doi: 10.1007/s10439-015-1417-1.
- Nolan, D. R. and McGarry, J. P. (2016) ‘On the correct interpretation of measured force and calculation of material stress in biaxial tests’, *Journal of the Mechanical Behavior of Biomedical Materials*. Elsevier, 53, pp. 187–199. doi: 10.1016/J.JMBBM.2015.08.019.
- Ogden, R. W. (2003) ‘Nonlinear Elasticity, Anisotropy, Material Stability and Residual Stresses in Soft Tissue’, in *Biomechanics of Soft Tissue in Cardiovascular Systems*. Vienna: Springer Vienna, pp. 65–108. doi: 10.1007/978-3-7091-2736-0\_3.
- Patel, R., Sweeting, M. J., Powell, J. T. and Greenhalgh, R. M. (2016) ‘Endovascular versus open repair of abdominal aortic aneurysm in 15-years’ follow-up of the UK endovascular aneurysm repair trial 1 (EVAR trial 1): a randomised controlled trial’, *The Lancet*. Elsevier, 388(10058), pp. 2366–2374. doi: 10.1016/S0140-6736(16)31135-7.
- Pelc, N. J., Bernstein, M. A., Shimakawa, A. and Glover, G. H. (1991) ‘Encoding strategies for three-direction phase-contrast MR imaging of flow.’, *Journal of magnetic resonance imaging: JMRI*, 1(4), pp. 405–13. Available at: <http://www.ncbi.nlm.nih.gov/pubmed/1790362> (Accessed: 2 March 2018).
- Potters, W. V, Cibis, M., Marquering, H. A., vanBavel, E., Gijzen, F., Wentzel, J. J. and Nederveen, A. J. (2014) ‘4D MRI-based wall shear stress quantification in the carotid bifurcation: a validation study in volunteers using computational fluid dynamics’, *Journal of Cardiovascular Magnetic Resonance*. Springer Nature, 16(S1). doi: 10.1186/1532-429x-16-s1-p162.
- Quinaglia, T., Bensalah, M. Z., Bollache, E., Kachenoura, N., Soulat, G., Boutouyrie, P., Laurent, S. and Mousseaux, E. (2018) ‘Differential impact of local and regional aortic stiffness on left ventricular remodeling’, *Journal of Hypertension*, 36(3), pp. 552–559. doi: 10.1097/HJH.0000000000001597.
- Reference Values for Arterial Stiffness’ Collaboration (2010) ‘Determinants of pulse wave velocity in healthy people and in the presence of cardiovascular risk factors: “establishing normal and reference values”’, *European Heart Journal*, 31(19), pp. 2338–2350. doi: 10.1093/eurheartj/ehq165.
- Ridgway, J. P. (2010) ‘Cardiovascular magnetic resonance physics for clinicians: part I’, *Journal of Cardiovascular Magnetic Resonance*. BioMed Central, 12(1), p. 71. doi: 10.1186/1532-429X-12-71.
- Saouti, N., Marcus, J. T., Noordegraaf, A. V. and Westerhof, N. (2012) ‘Aortic function quantified: the heart’s essential cushion’, *Journal of Applied Physiology*, 113(8), pp. 1285–1291. doi: 10.1152/jappphysiol.00432.2012.

- Sherif, H. M. F. (2014) 'Heterogeneity in the Segmental Development of the Aortic Tree: Impact on Management of Genetically Triggered Aortic Aneurysms.', *Aorta* (Stamford, Conn.). Science International Corporation, 2(5), pp. 186–95. doi: 10.12945/j.aorta.2014.14-032.
- Stankovic, Z., Allen, B. D., Garcia, J., Jarvis, K. B. and Markl, M. (2014) '4D flow imaging with MRI.', *Cardiovascular diagnosis and therapy*, 4(2), pp. 173–92. doi: 10.3978/j.issn.2223-3652.2014.01.02.
- Su, X. and Chen, W. (2004) 'Reliability-guided phase unwrapping algorithm: a review', *Optics and Lasers in Engineering*. Elsevier, 42(3), pp. 245–261. doi: 10.1016/J.OPTLASENG.2003.11.002.
- Svensson, L. G. and Rodriguez, E. R. (2005) 'Aortic organ disease epidemic, and why do balloons pop?', *Circulation*. American Heart Association, Inc., 112(8), pp. 1082–4. doi: 10.1161/CIRCULATIONAHA.105.564682.
- Tan, K. C., Kim, T. H., Chun, S. I., Shin, W. J. and Mun, C. W. (2008) 'A Simple, Fast, and Robust Phase Unwrapping Method to Unwrap MR Phase Images', in *4th Kuala Lumpur International Conference on Biomedical Engineering 2008*. Berlin, Heidelberg: Springer Berlin Heidelberg, pp. 487–490. doi: 10.1007/978-3-540-69139-6\_123.
- Tierney, Á. P., Callanan, A. and McGloughlin, T. M. (2011) 'In vivo feasibility case study for evaluating abdominal aortic aneurysm tissue properties and rupture potential using acoustic radiation force impulse imaging', *Journal of the Mechanical Behavior of Biomedical Materials*. Elsevier, 4(3), pp. 507–513. doi: 10.1016/J.JMBBM.2010.12.017.
- Tsamis, A., Krawiec, J. T. and Vorp, D. A. (2013) 'Elastin and collagen fibre microstructure of the human aorta in ageing and disease: a review.', *Journal of the Royal Society, Interface / the Royal Society*, 10(83), p. 20121004. doi: 10.1098/rsif.2012.1004.
- Vennin, S., Mayer, A., Li, Y., Fok, H., Clapp, B., Alastruey, J. and Chowienczyk, P. (2015) 'Non-invasive calculation of the aortic blood pressure waveform from the flow velocity waveform: a proof of concept', *American Journal of Physiology - Heart and Circulatory Physiology*, p. ajpheart.00152.2015. doi: 10.1152/ajpheart.00152.2015.
- Vulliémoz, S., Stergiopoulos, N. and Meuli, R. (2002) 'Estimation of local aortic elastic properties with MRI', *Magnetic Resonance in Medicine*. Wiley Subscription Services, Inc., A Wiley Company, 47(4), pp. 649–654. doi: 10.1002/mrm.10100.
- Vyas, M., Izzojr, J., Lacourciere, Y., Arnold, J., Dunlap, M., Amato, J., Pfeffer, M. and Mitchell, G. (2007) 'Augmentation Index and Central Aortic Stiffness in Middle-Aged to Elderly Individuals', *American Journal of Hypertension*. Oxford University Press, 20(6), pp. 642–647. doi: 10.1016/j.amjhyper.2007.01.008.
- Wentland, A. L., Grist, T. M. and Wieben, O. (2014) 'Review of MRI-based measurements of pulse wave velocity: a biomarker of arterial stiffness.', *Cardiovascular diagnosis and therapy*. AME Publications, 4(2), pp. 193–206. doi: 10.3978/j.issn.2223-3652.2014.03.04.

- Wilson, P. W., D'Agostino, R. B., Levy, D., Belanger, A. M., Silbershatz, H., Kannel, W. B. and Jeppesen, J. (1998) 'Prediction of coronary heart disease using risk factor categories.', *Circulation*. American Heart Association, Inc., 97(18), pp. 1837–47. doi: 10.1161/01.cir.97.18.1837.
- Wohlfahrt, P., Redfield, M. M., Melenovsky, V., Lopez-Jimenez, F., Rodeheffer, R. J. and Borlaug, B. A. (2015) 'Impact of chronic changes in arterial compliance and resistance on left ventricular ageing in humans.', *European journal of heart failure*. NIH Public Access, 17(1), pp. 27–34. doi: 10.1002/ejhf.190.
- Xu, J., Shiota, T., Omoto, R., Zhou, X., Kyo, S., Ishii, M., Rice, M. J. and Sahn, D. J. (1997) 'Intravascular ultrasound assessment of regional aortic wall stiffness, distensibility, and compliance in patients with coarctation of the aorta', *American Heart Journal*. Mosby, 134(1), pp. 93–98. doi: 10.1016/S0002-8703(97)70111-X.
- Zeinali-Davarani, S., Wang, Y., Chow, M.-J., El Turcotte, R. € and Zhang, Y. (2015) 'Contribution of Collagen Fiber Undulation to Regional Biomechanical Properties Along Porcine Thoracic Aorta', *Journal of Biomechanical Engineering*, 137. doi: 10.1115/1.4029637.
- Zhou, J. and Fung, Y. C. (1997) 'The degree of nonlinearity and anisotropy of blood vessel elasticity', *Proceedings of the National Academy of Sciences*, 94(26).

# CHAPTER 6

## CHARACTERIZATION OF THE IN-VIVO BIOMECHANICS OF THE HUMAN AORTA

---

### **Abstract**

This chapter develops a novel subject-specific finite element modelling approach based on the dual-VENC 4D Flow MRI measurements presented in Chapter 5. Simulations reveal that internal vessel contractility, due to pre-stretched elastin fibres and actively generated smooth muscle stress, must be incorporated into the artery constitutive law, along with collagen strain stiffening, in order to accurately predict the non-linear pressure-area relationship uncovered by our MRI investigation. Modelling of elastin and smooth muscle contractility allows for the identification of the reference vessel configuration at zero-lumen pressure, in addition to accurately predicting high- and low-compliance regimes under a physiological range of pressures. This modelling approach is also shown to capture the key features of elastin and SMC knockout experiments. A subject-specific FE model is generated directly from the MRI data presented in Chapter 5, and the volume fractions of the constituent components of the aortic material model (i.e. non-linear elastic collagen, pre-stretched elastin, and contractile smooth muscle cells) were computed so that the *in-silico* pressure-area curves accurately predict the corresponding MRI data at each location. This leads to the prediction that collagen and smooth muscle volume fractions increase distally, while elastin volume fraction decreases distally. This finding is supported by the histological analyses presented in Chapter 4. Furthermore, the strain at which collagen transitions from low to high stiffness is lower in the abdominal aorta, again supporting the histological finding that collagen waviness is lower in this distally. The analyses presented in this chapter provides new insights into the heterogeneous structure-function relationship that underlies aortic biomechanics. This novel subject-specific MRI/FEA methodology provides a foundation for personalised *in-silico* clinical analysis and tailored aortic device development.

## 6.1 Introduction

Regional heterogeneity in the biomechanics of the aorta is a key feature that ensures optimal function of the cardiovascular system. In general, a high level of elastic compliance is required in the proximal aorta, so that the kinetic energy expelled during systole can be stored as elastic strain energy in the vessel, leading to subsequent augmentation of pressure pulse propagation during diastole due to elastic recoil of the wall. The distal aorta, however, takes an alternative approach to blood transfer with a higher smooth muscle cell (SMC) content and a reduced requirement for elastin.

A significant body of literature exists on the experimental testing of aortic tissue, in particular material characterization through uniaxial and biaxial tensile tests (Vande Geest, & Vorp, 2006; Matsumoto *et al.*, 2009; Forsell & Gasser, 2013; Gundiah & Pruitt, 2013; Reeps *et al.*, 2013; Weisbecker *et al.*, 2013; Pierce *et al.*, 2015; Teng *et al.*, 2015; Laksari *et al.*, 2016). Due to both the ethical and logistical constraints surrounding the destructive testing of human tissue, animal data exceeds that of humans in the literature. The majority of material characterization of the human aorta is performed on surgically excised samples, for example during the open surgical repair of an abdominal or thoracic aortic aneurysm (Vande Geest & Vorp, 2006; Choudhury *et al.*, 2009; Iliopoulos *et al.*, 2009; Pasta *et al.*, 2015; Sassani & Sokolis, 2015). The tissue obtained is in this case however, is (i) too localised to capture the spatially varying biomechanics of the aorta, and (ii) diseased. An alternative approach exists in the testing of aortic tissue post-autopsy; however, further ethical and logistical difficulties exist here, and as such, few studies with this design exist in the literature (Mohan and Melvin, 1982; Vande Geest & Vorp, 2004; Raghavan *et al.*, 2011). The limitation of this approach is that the tissue is dead, raising concerns about the applicability of such results which ultimately cannot be compared to unknown ‘live’ tissue properties.

In characterizing the mechanical properties of the aorta experimentally, particular focus has been directed towards the effects of ageing. Hallock and Benson, (1937) found that young aortic tissue exhibits a high degree of extensibility through a bi-concave s-shaped pressure-volume relationship, while in older tissue the total increase in volume is lower and at high pressures the slope of the pressure-volume relationship tends towards a straight horizontal line. Additionally, Vande Geest, & Vorp, (2004) found that an older cohort exhibited a much stiffer exponential shaped stress-strain response compared to the younger cohort, with such a notable difference that different forms of strain energy functions were used for younger and older cohorts (polynomial and exponential forms, respectively). Investigation of aortic heterogeneity has typically relied on *ex-vivo* testing of excised porcine/canine tissue (Moriwaki *et al.*, 2011; Krüger *et al.*, 2016). A biomechanical study of excised canine aortae by Tanaka and Fung, (1974), reports that proximal samples exhibit a higher compliance than distal samples. A study on the equibiaxial tension behaviour of human aortic samples following autopsy by Haskett *et al.*, (2010) report that the overall compliance decreases with distance from the heart in a cohort less than 30 years of age.

Investigation of the volume fractions of individual wall constituents can provide insight into the local behaviour of the arterial tissue (He & Roach, 1994; Laksari *et al.*, 2016). Harkness *et al.*, (1957) report that the volume fraction of elastin is approximately twice as high as that of collagen in intrathoracic canine aorta. In all other arteries the volume fraction of collagen was found to exceed that of elastin. Saey *et al.*, (2015) report a greater concentration of collagen in the distal thoracic equine aorta than in proximal sections. Davidson *et al.* (1985) report lower concentrations of elastin fibres in the abdominal regions of porcine aorta than in thoracic regions. Recently, Concannon *et al.*, (2019) found that elastin volume fraction decreases, and collagen increases with distance from the heart in the human aorta.

Despite extensive *in-vitro* mechanical testing and histological analysis of excised tissue, few studies to date have attempted to characterise the *in-vivo* biomechanical behaviour of the aorta using non-invasive methodologies. Previous *in-vivo* MRI analyses of the human aorta have focused on limited isolated segments, such as the thoracic (Mohiaddin *et al.*, 1989) or abdominal aorta (Länne *et al.*, 1992). Such a focus on a single region does not provide insight into the significant spatial variation in aortic biomechanical behaviour. This limitation is addressed in Chapter 5, whereby a dual-VENC 4D Flow MRI sequence is developed and implemented in a commercial scanner, providing high resolution measurements of aortic deformation at all locations throughout the entire cardiac cycle.

This chapter develops a subject-specific MRI/FEA framework to uncover the biomechanisms underlying the spatially varying non-linear aortic compliance measured *in-vivo* in Chapter 5. A constitutive law is developed to incorporate the biomechanical contributions of pre-stretched elastin, contractile SMCs, and strain stiffening collagen. Firstly, the role of pre-stretched elastin is investigated. In particular, analyses are performed to identify an equilibrium vessel configuration at zero applied lumen pressure, which is observed to be critical step required in order to predict the key features of the pressure-area relationship observed *in-vivo*. The role of elastin pre-stretch on the lumen pressure at which the aorta transitions from a high compliance to a low compliance regime due to collagen strain stiffening, is also investigated. A subject-specific FE model is generated directly from the MRI data presented in Chapter 5 and the *in-vivo* pressure-area curves are fit using the constitutive law. Finally, the volume fractions of the constituent components of the aortic wall (elastin, collagen and SMCs) are computed throughout the subject-specific aortic FE model and excellent agreement is found with the histological analyses presented in Chapter 4.

## 6.2 Methodology

In this chapter, the biomechanical properties of the entire human aorta are characterized *in-vivo*, using an MRI/FEA framework. A novel anisotropic hyperelastic constitutive law is presented, that accounts for the individual contributions of elastin, collagen and SMCs within the arterial wall, while making use of a constrained mixture-based approach. Additionally, a framework for generating subject-specific FE models directly from MRI/CT scans is presented. The pressure-area relationship (derived in Chapter 5) throughout the entire cardiac cycle is captured at 10 planes from the proximal ascending to distal abdominal aorta using the novel constitutive law.

### 6.2.1 Novel Constitutive Law

In this section we outline the key equations that describe of the stress response of the material to deformation. The constitutive model is decomposed into isotropic and anisotropic parts; the isotropic portion is used to model the arterial groundmatrix, while the anisotropic part is further divided into separate stress components that describe elastin, collagen and SMCs. Additionally, we model the aortic wall as compressible (D. R. Nolan and McGarry, 2016).

We employ a rule of mixtures approach where each component of the wall undergoes the same strain, but the stresses are additive, and the sum of constituent densities ( $V_\alpha^f$ ) equals unity, which yields

$$\boldsymbol{\sigma} = \boldsymbol{\sigma}_{\text{col}} + \boldsymbol{\sigma}_{\text{ela}} + \boldsymbol{\sigma}_{\text{smc}} + \boldsymbol{\sigma}_{\text{mat}} \quad (6.01)$$

$$\sum V_\alpha^f = 1 \quad (6.02)$$

We employ a bilinear strain energy function to capture the strain stiffening behaviour of fibrillar collagen under tension

$$\boldsymbol{\sigma}_{\text{col}} = V_{\text{col}}^f * \begin{cases} 0 & \rightarrow 0 > \varepsilon \\ (k_1 \varepsilon) * (\mathbf{a}_{\text{col}} \otimes \mathbf{a}_{\text{col}}) & \rightarrow 0 < \varepsilon < \varepsilon_t \\ (k_1 \varepsilon + k_2 (\varepsilon - \varepsilon_t)) * (\mathbf{a}_{\text{col}} \otimes \mathbf{a}_{\text{col}}) & \rightarrow 0 < \varepsilon > \varepsilon_t \end{cases} \quad (6.03)$$

where the strain,  $\varepsilon = (\sqrt{I_{4c}} - 1)$ ,  $V_{\text{col}}^f$  is the volume fraction of collagen in the wall,  $k_1$  is the initial stiffness of collagen,  $k_2$  is the secondary stiffness of collagen,  $\varepsilon_t$  is the transition strain and  $\mathbf{a}_{\text{col}}$  denotes the direction of collagen fibres in the reference configuration with respect to the circumferential axis of the artery.

Elastin fibres may also contribute to the anisotropy of the vessel with a mean directionality defined by  $\mathbf{a}_{\text{ela}}$ . The elastin fibres also exhibit a constant pre-stretch and stiffness and to allow contraction of the vessel such that the stress is

$$\boldsymbol{\sigma}_{\text{ela}} = V_{\text{ela}}^f * \left( (\sqrt{I_{4e}} - 1 + \lambda_e) * k_e \right) * (\mathbf{a}_{\text{ela}} \otimes \mathbf{a}_{\text{ela}}). \quad (6.4)$$

The model parameter  $\lambda_e$  is the pre-stretch of the elastin component in the initial undeformed configuration.  $V_{ela}^f$  is the volume fraction of elastin in the wall, and  $k_e$  is the stiffness of elastin.

We also incorporate the active component of the wall as represented by  $\sigma_{smc}$ . The contractile stress generated by a single SMC ( $\sigma_{act}$ ) is held constant at 25kPa (McGarry *et al.*, 2009). SMCs also contribute to the anisotropy of the vessel through  $\mathbf{a}_{smc}$

$$\boldsymbol{\sigma}_{smc} = V_{smc}^f * (\sigma_{act} * (\mathbf{a}_{smc} \otimes \mathbf{a}_{smc})) \quad (6.5)$$

where  $V_{smc}^f$  is the volume fraction of SMCs in the wall,  $\sigma_{act}$  is the active stress of an individual SMC and  $\mathbf{a}_{smc}$  denotes the direction of SMCs in the reference configuration.

Finally, the stress in the isotropic groundmatrix can be defined as

$$\boldsymbol{\sigma}_{mat} = V_{mat}^f * \left( \frac{\mu_0}{J^{\frac{2}{3}}} \left( \bar{\mathbf{B}} - \frac{1}{3} \bar{I}_1 \mathbf{I} \right) + \frac{2J}{D_1} (J - 1) \right) \quad (6.6)$$

Where  $V_{mat}^f$  is the volume fraction of matrix in the wall,  $\mu_0$  is the shear modulus and  $D_1$  is related to the bulk modulus of the groundmatrix.

### 6.2.2 Experimental/clinical motivation for constitutive model

The following three experimental/clinical observations are used to motivate the bespoke arterial constitutive law presented in the previous section:

As illustrated in the schematic in Figure 6.1, our MRI measurements presented in Chapter 5 reveal a bi-linear pressure-area curve in the physiological pressure range (PPR), with a high compliance regime (HCR) transitioning to a low compliance regime (LCR) at an identifiable transition pressure and area ( $P_t$ ,  $A_t$ ).

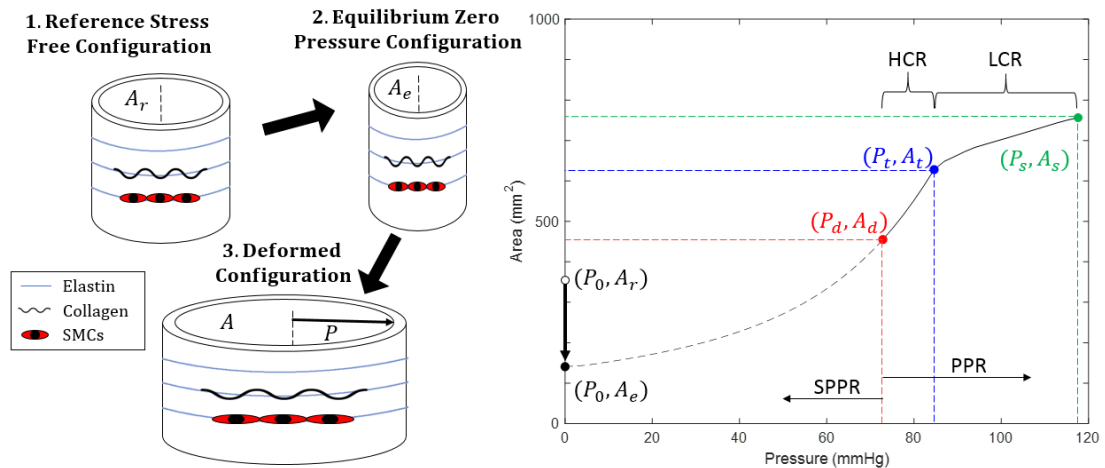


**Figure 6.1:** Schematic of modelling framework for simulation of in-vivo aorta behaviour. 1. A reference stress-free configuration is constructed with an area  $A_r$ . 2. An equilibrium zero-pressure configuration is computed, whereby the cross-sectional area of the vessel reduces to  $A_e$ , such that the internal tensile circumferential stress due to elastin pre-stretch and SMC contractility is in equilibrium with the compressive circumferential stress generated in the matrix. 3.) The lumen pressure is increased from zero up to the end systolic value (117 mmHg). The pressure increases through a sub-physiological pressure regime (SPPR). At the start-diastolic pressure,  $P_d$ , (73 mmHg) the computed lumen area is denoted  $A_d$ . The pressure is then increased through the physiological pressure range (PPR) up to the end-systolic value,  $P_s$  (117 mmHg), at which point the computed area is denoted  $A_s$ . As illustrated in the pressure-area curve above, based on the MRI measurements of Chapter 5, the PPR is characterised by a high compliance regime (HCR) up to a transition pressure,  $P_t$ , followed by a low compliance regime (LCR) up to the end of systole.

Furthermore, a study by Swanson and Clark, (1974) reveals that the aortic lumen area at zero pressure ( $A_r$ ) is  $\sim 30\%$  lower than the end-diastolic lumen area ( $A_d$ ). A computational model must predict the deformation from the zero-pressure aortic configuration ( $A_r$ ) up to the maximum systolic pressure configuration ( $A_s$ ), including the transition from HCR to LCR in the PPR. To consider the ability of purely elastic models to capture such behaviour, we simulate the expansion of an idealised cylindrical artery with undeformed lumen area  $A_r$  with the lumen pressure increasing from zero to 120 mmHg. Firstly, we consider a standard Yeoh hyperelastic model. As shown in Figure 6.2(a) a good fit for the expected pressure-area curve is obtained. However, the required sigmoidal shape of the associated stress-strain curve (Figure 6.2(b)) is not representative of the expected bi-linear strain stiffening that has been widely reported for the aorta. In Figure 6.2(c) we consider the behaviour of our bi-linear collagen and Neo-Hookean matrix model (equations 6.03 and 6.06) without the inclusion of elastin or SMCs. A reasonable fit is achieved for the pressure-area curve only if an extremely high transition strain ( $\varepsilon_t > 60\%$ ) is specified for the collagen model. As shown in Figure 6.2(d), this requires the specification of a stress-strain relationship that is not representative of the aorta. In summary, Figures 6.2(a-d) demonstrate that non-contractile elastic models can only predict the pressure-area behaviour of the aorta if an incorrect stress-strain relationship is used. We next

consider aortic contractility through the addition of pre-stretched elastin to the model (equation 6.04). In this case, we choose a starting reference lumen area  $A_r = 485 \text{ mm}^2$ . A preliminary analysis step is implemented in which the artery contracts until the tensile stress of the pre-stretched elastin is in equilibrium with the compressive stress of the groundmatrix (collagen fibres shorten in such a deformation and therefore do not contribute to the stress state at this point of the analysis). Elastin and matrix properties ( $\lambda_e$ ,  $k_e$  and  $\mu$ ) are chosen so that this equilibrium lumen area is close to the expected zero-pressure area ( $A_e \approx A_0$ ). Next, starting from this equilibrium configuration ( $A_e$ ), the lumen pressure is then increased from zero to 120 mmHg and the resultant pressure-area curve is computed (Figure 6.2(e)). This model provides an accurate representation of clinical/experimental pressure-area data while the corresponding stress-strain behaviour is in the experimentally reported range. The contractility due to the elastin results in a collagen induced stiffness increase at a nominal strain of  $\sim 0.4$ , as reported in the literature. Finally, inclusion of the SMC contribution (equation 6.05) adds further internal contractility. Again, an accurate representation of the pressure-area curve is achieved (Figure 6.2(g)) while the corresponding stress-strain curve is within the expected experimental range (Figure 6.2(h)).

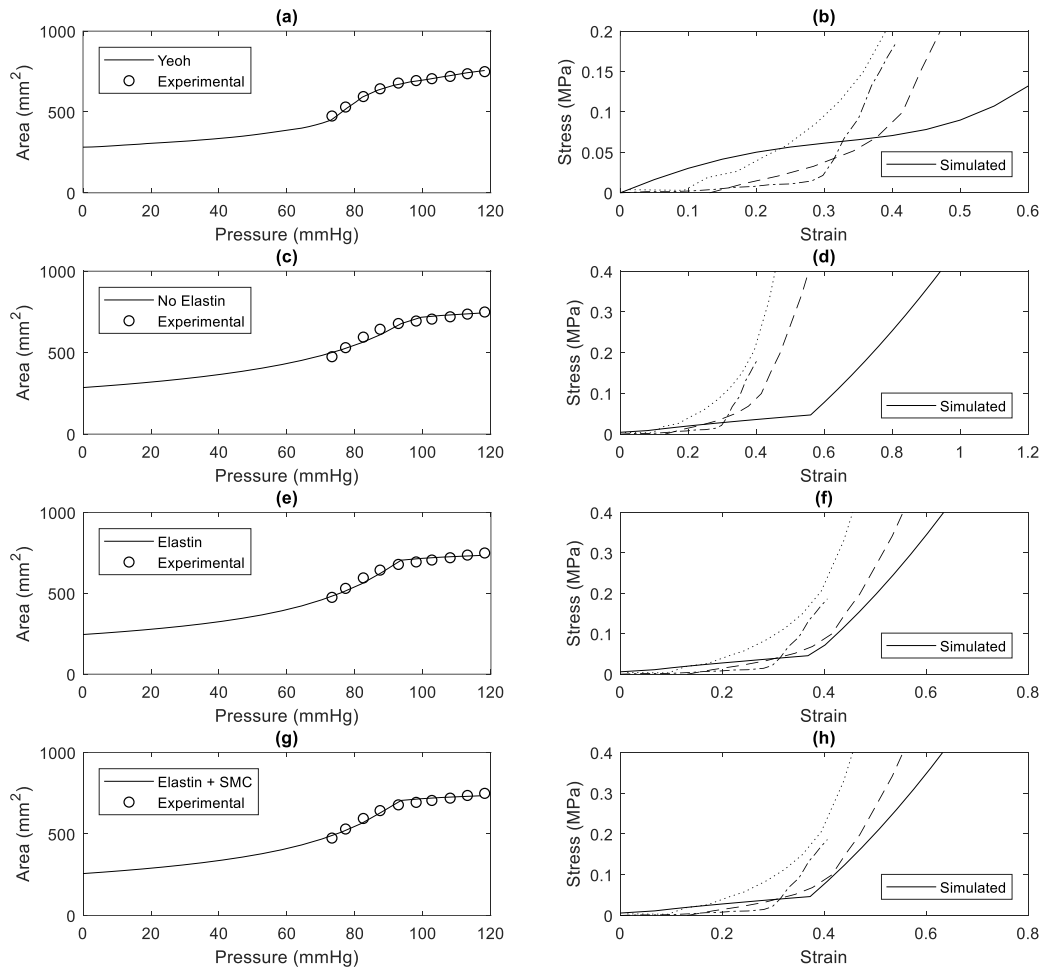


**Figure 6.2:** Assessment of modelling strategies to simulate the bi-linear pressure-area curve measured in the PPR *in-vivo* using dual-VENC 4D Flow MRI framework (Chapter 5). (a) Internal contractility is ignored, and the vessel is simply inflated from the reference stress free configuration ( $A_r$ ). A sigmoidal shaped bi-concave Yeoh hyperelastic material model can be used to fit the pressure-area curve. However, as shown in (b), the tensile stress-strain relationship of this model does not resemble reported experimental data for arterial tissue (dashed=(Kochova *et al.*, 2008); dotted=(Khanafar *et al.*, 2013); dashed/dotted=(Azadani *et al.*, 2013)). (c) shows the pressure-area curve computed using the bi-linear collagen (equation 6.3) and Neo-Hookean matrix (equation 6.6) components of the proposed model *without* the inclusion of internal contractility due to elastin or smooth muscle. A reasonable fit can be achieved for the pressure-area curve. However, as shown in (d), an extremely high transition strain ( $\epsilon_t > 60\%$ ) must be specified for the collagen model, and as such, the corresponding stress-strain relationship is not representative of reported experimental data. (e) Internal contractility is next implemented by addition of elastin pre-stretch (equation 6.4) to the model. A reasonable prediction for the pressure-area curve is obtained, and, as shown in (f), the corresponding tensile stress-strain relationship is now within the experimentally reported range. (g & h) show that similarly accurate and physiologically relevant predictions can also be achieved by the further addition of SMC contractility (equation 6.5) to the model.

Further evidence of the importance of the elastin pre-stretch component of our model is provided by the recent experiments of Gabriela-Espinosa *et al.*, (2018) (Figure 6.3(a)) whereby pressure-diameter curves for excised rat arteries are measured. The contribution of elastin is then removed by treatment with elastase, which results in an increase in the zero-pressure diameter from 379 $\mu\text{m}$  to 473 $\mu\text{m}$ , and an increase in compliance across the range of applied lumen pressures. Others have also observed

this phenomenon in both canine (Dobrin & Gley, 1984), and murine arteries (Faury *et al.*, 2003; Bellini *et al.*, 2017). As shown in Figure 6.3(b), our computational model accurately predicts the experimentally observed alteration in the pressure-diameter curve upon the removal of the pre-stretched elastin contribution from the model. This demonstrates that the proposed mechanism of elastin generated internal tension, and its relative contribution to observed non-linear arterial compliance, is physiologically appropriate. Regarding the influence of SMC contractility on aortic biomechanics, Figure 6.3(c) reproduces the results of an experimental study performed on canine aortae by Barra *et al.*, (1993). The measured circumferential stress-strain relationship for untreated excised tissue is compared to the stress-strain relationship following SMC activation by phenylephrine. SMC activation results in a ~25-40% increase in stress over the applied strain range. Similar trends have also been reported for middle cerebral arteries of rats (Coulson *et al.*, 2004). As shown in Figure 6.3(d), our model replicates the experimentally observed contribution of SMC active contractility and suggests that the value of  $\sigma_{act}$  in the range from 25-50 kPa (McGarry *et al.*, 2009) is physiologically appropriate for aortic tissue.

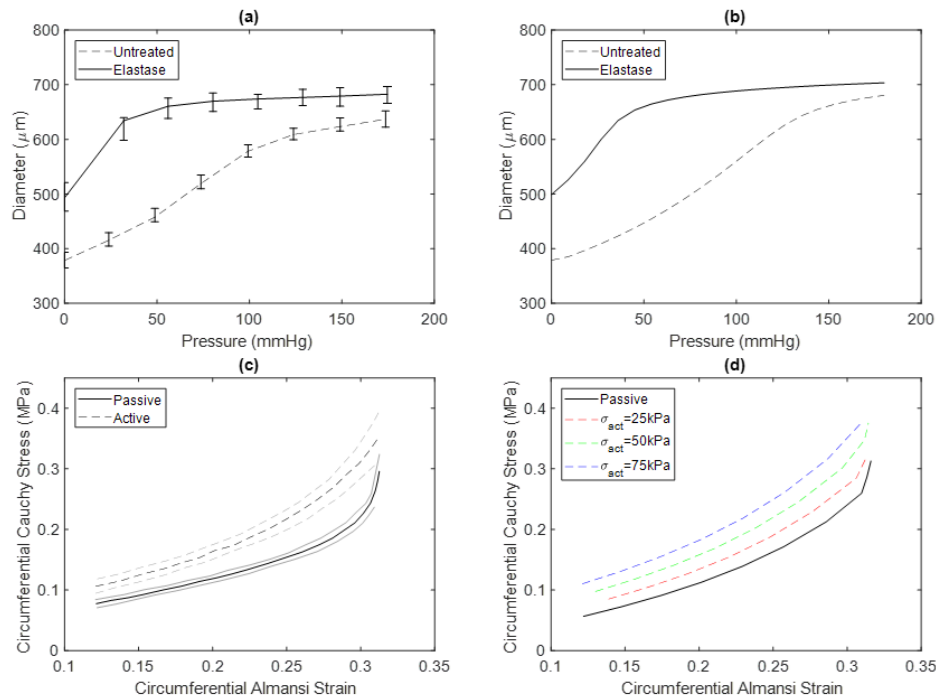


**Figure 6.3:** (a) Experimental data reported by Gabriela-Espinosa *et al.*, (2018) are reproduced, demonstrating that the digestion of elastin from excised aortae (using elastase treatment) leads to an increase in the observed diameter at zero pressure. Subsequent increases in lumen pressure demonstrate a significant difference between the pressure-area curve between untreated aortae and elastase treated aortae. (b) Computational prediction of the experimental data of Gabriela-Espinosa *et al.* (2018) using our novel constitutive law (equations 6.1-6.6). Here we simulate elastase treatment by removing the contribution of the pre-stretched elastin (equation 6.4). (c) Experimental data reported by Barra *et al.*, (1993) are reproduced, demonstrating that activation of SMCs in excised aortae (using phenylephrine) leads to a ~25-40% increase in stress over the applied strain range. (d) Computational prediction of the experimental data of Barra *et al.* (1993) using our novel constitutive law (equations 6.1-6.6). An active SMC stress of  $\sigma_{act}=25\text{-}50\text{ kPa}$  provides a reasonably accurate prediction of the experimental data.

### 6.2.3 Model Parameter Sensitivity Study

As outlined in the previous section, our model is physically based, with each component motivated by physiological observations of artery pressure-area and stress-strain curves. This allows for a physiologically based calibration of the model, rather than a black-box fitting of model parameters. For example, the increased collagen stiffness parameter ( $k_2$ ) is determined through observation of the LCR region of the pressure-area curve (see Figure 6.1), whereas the equilibrium zero-pressure lumen area,  $A_e$  is governed by the values of elastin stiffness ( $k_e$ ) and pre-stretch ( $\lambda_e$ ) relative to the value of the matrix stiffness ( $\mu$ ). Notwithstanding the physiological interpretation of each model parameter, it is useful to consider the sensitivity of the artery pressure-area curve to each parameter, as presented in Figure 6.4. In terms of collagen parameters,  $k_1$  and  $k_2$  influence the HCR and LCR region, respectively, as expected, while  $\varepsilon_t$  strongly influences the transition pressure from HCR to LCR. Collagen parameters do not influence the behaviour in the sub-physiological pressure range (SPPR), as in its highly wavy shortened state the mechanical contribution of collagen is assumed to be negligible (Holzapfel, Gasser and Ogden, 2000). The elastin parameters,  $k_e$  and  $\lambda_e$ , and the matrix stiffness,  $\mu$ , influence the pressure-area curve in the SPPR and in the HCR (with the collagen contribution dominating the slope of the pressure-area curve in the LCR).  $\lambda_e$  and  $\mu$  strongly influences the zero-pressure equilibrium area  $A_e$ . The bulk modulus of the matrix is assumed to be slightly compressible (D. R. Nolan and McGarry, 2016) and does not strongly influence the pressure-area curve. Finally, as expected, an increase in SMC contractility ( $\sigma_{act}$ ) results in a reduction in the zero-pressure equilibrium area  $A_e$  and an increase in the transition area  $P_t$ .

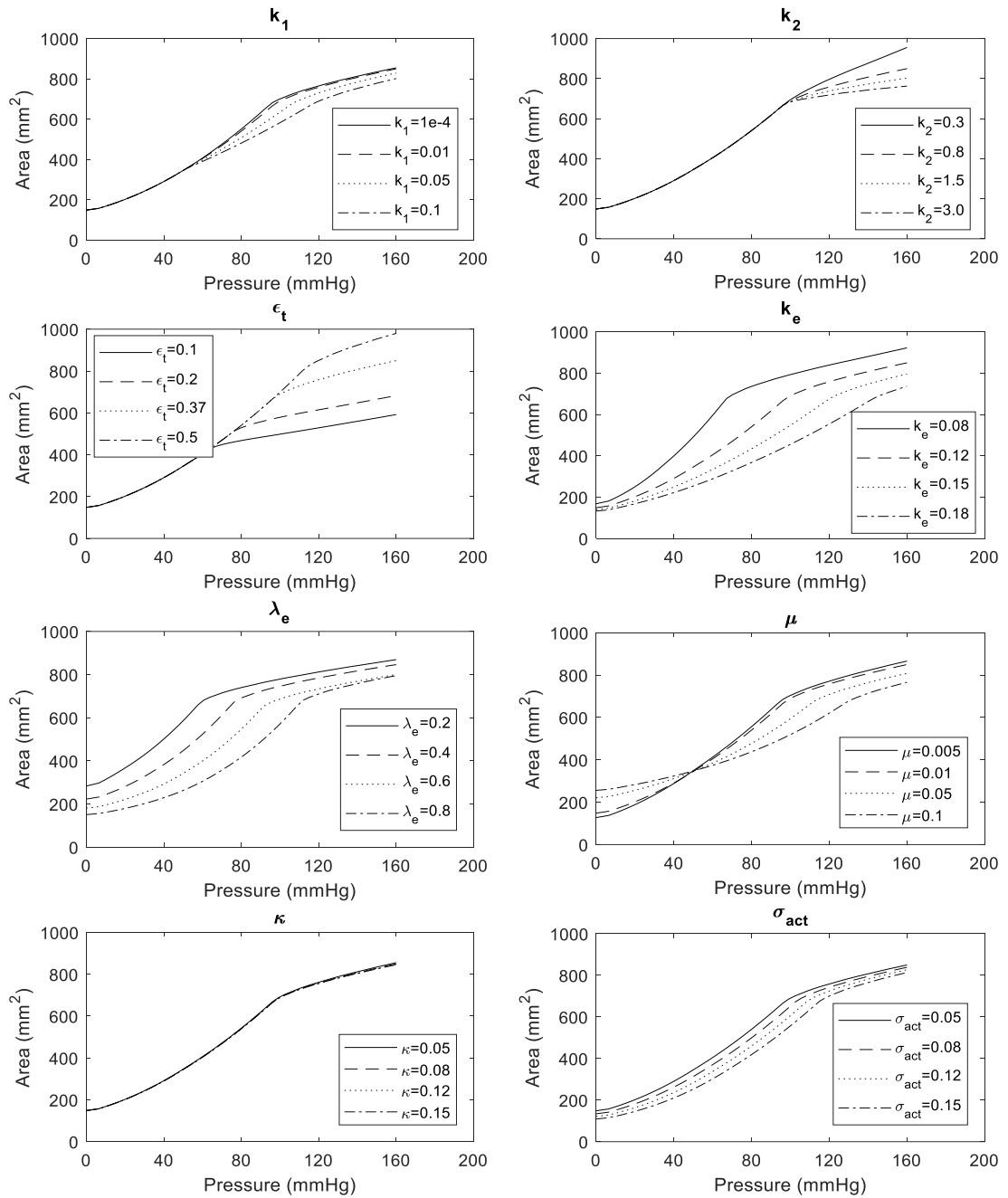


**Figure 6.4: Parametric study to investigate the sensitivity of the computed pressure-area curve to model parameters. Unless otherwise indicated, the following baseline parameter values are used: (Collagen component)  $k_1 = 0.01$  MPa,  $k_2 = 0.8$  MPa,  $\epsilon_t = 0.37$ ; (Elastin component)  $k_e = 0.12$  MPa,  $\lambda_e = 0.4$ ; (Matrix component)  $\mu = 0.01$  MPa,  $\kappa = 0.08$  MPa; (SMC component)  $\sigma_{act} = 0$  kPa .**

We dedicate the remainder of this chapter to the analysis of the subject-specific MRI dataset uncovered in Chapter 5. In keeping with the physiological motivation and interpretation of our model, we assume that fundamental material properties that describe collagen ( $k_1, k_2$ ) and elastin ( $k_e, \lambda_e$ ) do not change as a function of location in the aorta. Rather, we assume that volume fractions of collagen ( $V_{col}^f$ ), elastin ( $V_{ela}^f$ ), smooth muscle ( $V_{smc}^f$ ) and matrix ( $V_{mat}^f$ ) may spatially vary (Harkness & McDonald, 1957; Davidson *et al.*, 1985; Concannon *et al.*, 2019). Therefore, the subject-specific model is primarily calibrated by altering  $V_{col}^f$ ,  $V_{ela}^f$  and  $V_{smc}^f$ .

In Figure 6.5 we illustrate the sensitivity of the pressure-area curve to changes in artery composition. As expected, an increase in  $V_{col}^f$  increases the stiffness of the aorta in the LCR but does not affect the stiffness in the HCR, as the collagen here is crimped. An increase in  $V_{col}^f$  also results in a decrease in the  $A_e$  through the volume conservation relationship described in equation 6.02 (as  $V_{col}^f$  increases,  $V_{mat}^f$  must decrease and the elastin contraction leads to a greater matrix compression. Note: collagen does not contribute mechanically in compression). An increase in  $V_{ela}^f$  also results in a decrease in  $A_e$ , due to a greater volume of contractile elastin compressing within a lesser volume of matrix. Increasing  $V_{ela}^f$  alters the stiffness of the aorta in both the SPPR and the HCR but has no effect on the stiffness in the LCR as once  $\varepsilon_t$  is exceeded the secondary collagen stiffness dominates the behaviour of the material. Increasing the  $V_{smc}^f$  does not influence the stiffness in either the HCR or the LCR, as effectively the same material behaviour is achieved as decreasing the matrix stiffness ( $\mu$ ), (see Figure 6.4). As a result, an increase in  $V_{smc}^f$ , results in a decrease in  $A_e$ , and an increase in  $P_t$ .

In addition to spatial variation in volume fractions of the constituent components, we also consider spatial variation in the collagen transition strain ( $\varepsilon_t$ ). This assumption is based on the reported histological observations that the waviness of collagen in the aorta decreases distally (Zeinali-Davarani *et al.*, 2015). The waviness of collagen fibers directly effects the strain at which increased stiffness occurs. We also consider spatial variations in the stiffness of the matrix based on reported data that the makeup of GAGs in the aorta differs proximally versus distally (Humphrey, 2012).

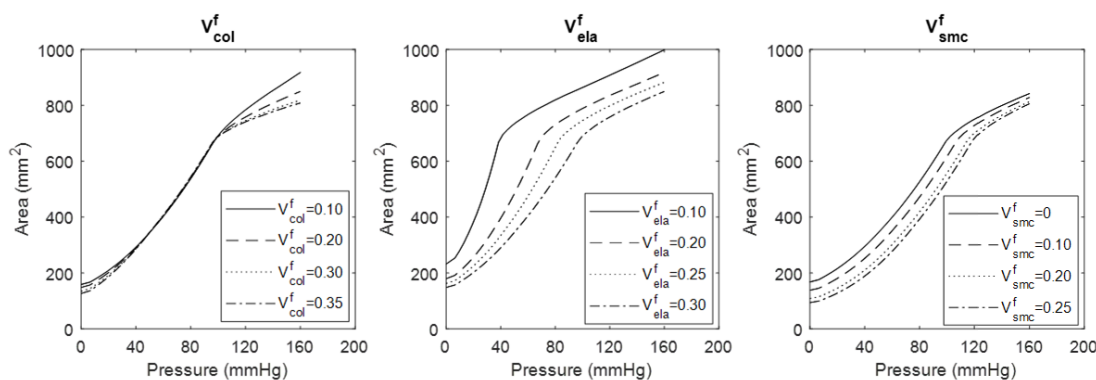


**Figure 6.5:** Parametric study to investigate the sensitivity of computed PA curves to the volume fractions of collagen ( $V_{col}^f$ ), elastin ( $V_{ela}^f$ ), and smooth muscle cells ( $V_{smc}^f$ ).

### 6.2.4 Construction of Subject-Specific finite element model

The following section describes the methodology surrounding the generation of a subject-specific FE model, directly from the MRI data obtained in Chapter 5 using a custom-built MATLAB framework.

Firstly, the aortic centreline (Figure 6.6(a)) and the lumen boundary points corresponding to the diastolic timepoint in the cardiac cycle, for each of the 10 planes analysed (Figure 6.6(b)), were used to sweep a surface mesh along the main trunk of the aorta. All major branch vessels were added to the main trunk including the innominate artery, left common carotid artery, left subclavian artery, coeliac artery, superior and inferior mesenteric arteries, left and right renal arteries and left and right common iliac arteries, to form the full aortic internal and external surface models (Figure 6.6(c)). Cadaveric aortic wall thickness data from Concannon *et al.*, (2019) is highlighted as a function of aortic location in Figure 6.6(d), which can be used to specify the element specific offset distance from the internal surface elements (green) to the external surface elements (red) in Figure 6.6(e). Finally, the transformation of both sets of surface elements into 3D continuum elements, yields the final aortic model shown in Figure 6.6(f).

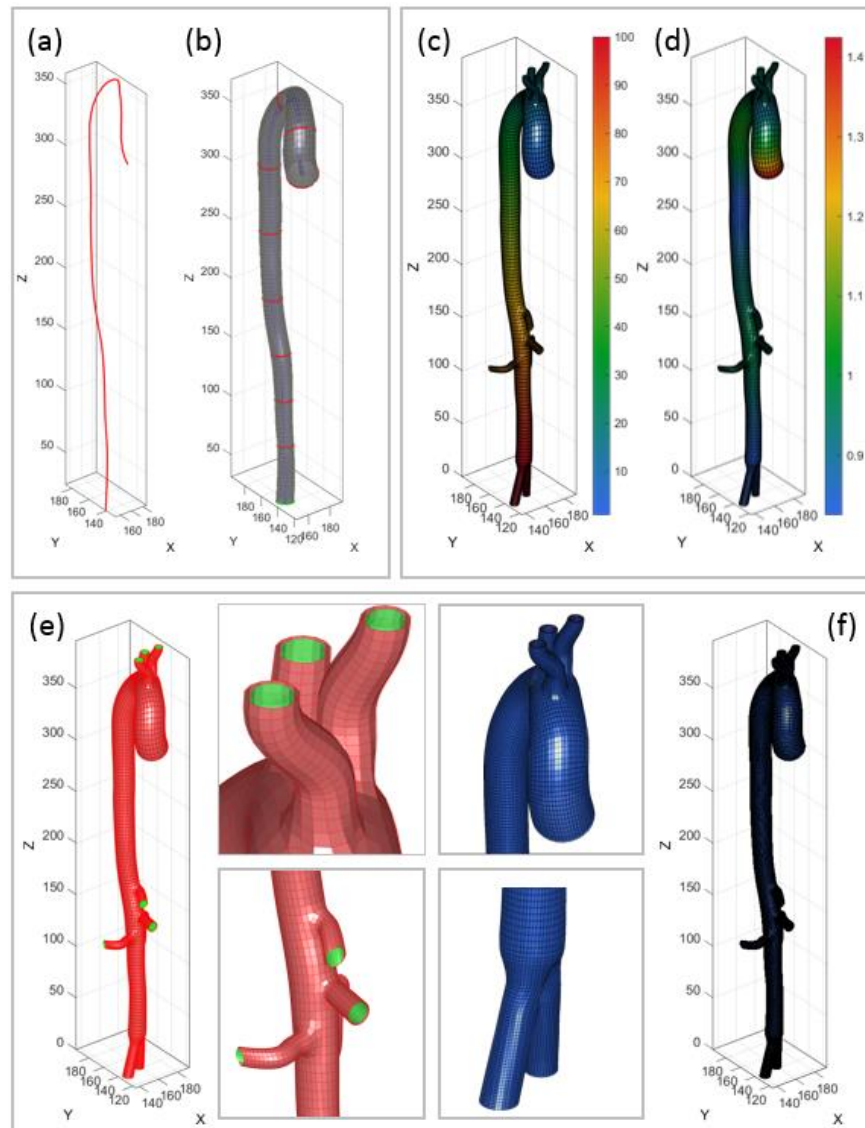


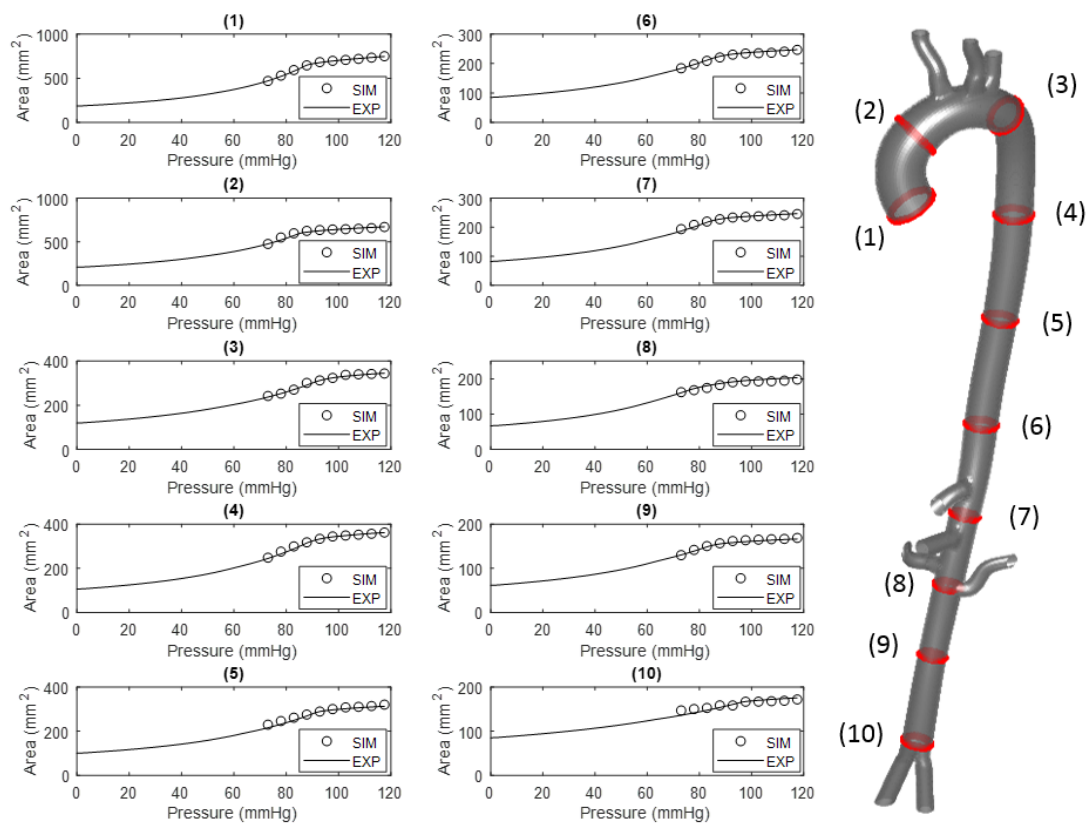
**Figure 6.6:** Finite element mesh generation. (a) aortic centreline and (b) plane profiles used for sweeping the internal surface mesh, (c) major branching vessels along the aorta (d), spatially varying aortic wall thickness, (e) offset of internal surface elements by the wall thickness to generate the external surface mesh (red), and (f) hexahedral splitting to generate C3D8 continuum elements.

### 6.2.5 Simulation of subject specific aorta biomechanical behaviour

A discrete fiber orientation based on the aortic centreline and internal lumen surface of the aorta was prescribed to ensure the circumferential orientation of each element was defined. The pre-stretched elastin is incorporated in the subject-specific FE model in the same manner described previously, through an initial contraction step resulting in a new equilibrium configuration, in this case for the entire aorta. The subject-specific diastolic pressure load of 73 mmHg was then applied to the internal lumen surface, followed by a tabular pulse pressure wave along the length of the aorta based on the measurements outlined in Chapter 5. A linear interpolation of material parameters is assumed between each of the 10 calibrated sections. The final simulated versus experimental pressure-area curve fits are shown in Figure 6.7.

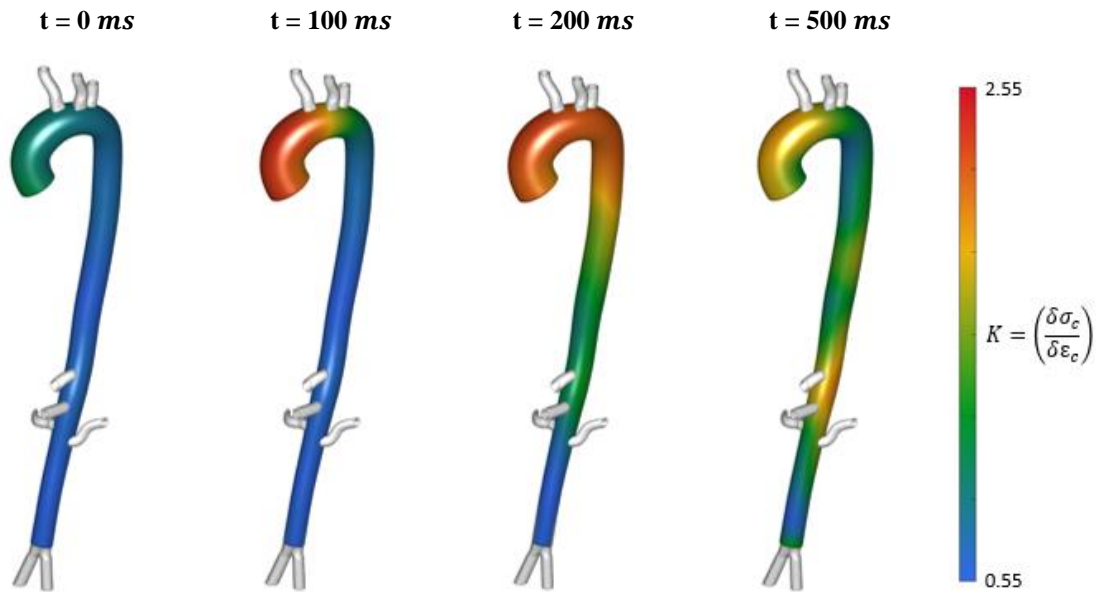
### 6.3 Results

Figure 7 shows the computed pressure-area curves at the 10 planes along the length of the subject-specific aorta. At each section, the volume fractions of collagen ( $V_{col}^f$ ), elastin ( $V_{ela}^f$ ), and SMCs ( $V_{smc}^f$ ) within the wall, in addition to the isotropic groundmatrix shear modulus ( $\mu$ ) and the transition strain ( $\varepsilon_t$ ) are adjusted so that the MRI measured data at each section is accurately predicted. Furthermore, at each plane, the contraction of the aorta due to the pre-stretch of elastin results in a 31-49% reduction from the reference configuration to the new equilibrated configuration, accurately reflecting the range reported by the experiments of Gabriela-Espinosa *et al.*, (2018), Bellini *et al.*, (2017), and Dobrin *et al.*, (1984).



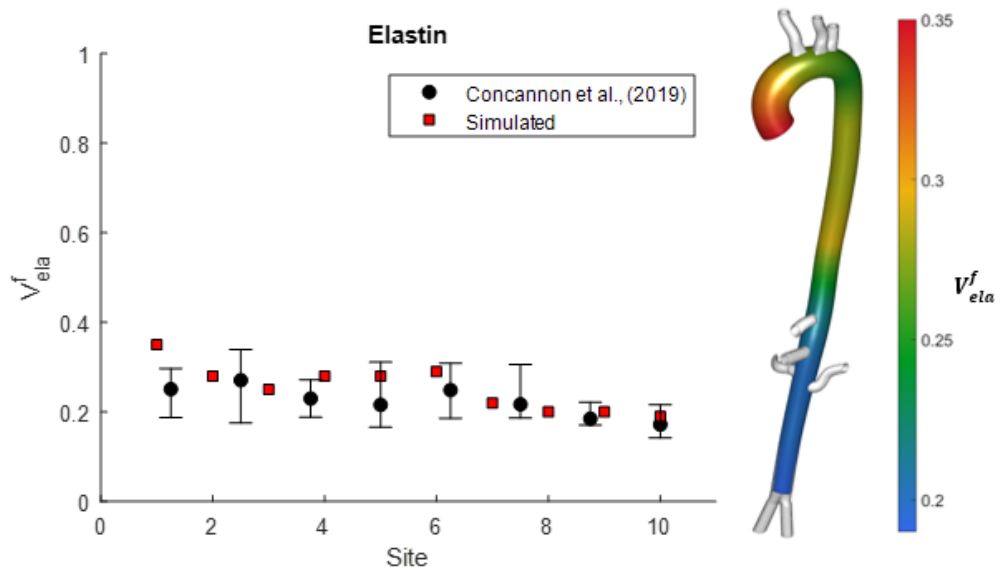
**Figure 6.7:** Comparison of computed pressure-area curves (SIM) with MRI measurements at 10 planes along the length of the aorta. Computed data in the SPPR (including the contracted area  $A_e$  at zero pressure) is shown, in addition to the bi-linear pressure-area predictions in the PPR. The model is shown to accurately capture the spatially varying MRI data simply by calibrating the spatially varying volume fractions of the constituent phases ( $V_{col}^f$ ,  $V_{ela}^f$ ,  $V_{smc}^f$ ), the transition strain of the collagen (reflecting the waviness of the collagen), and the matrix shear modulus (reflecting spatially varying GAG content). All other model parameters are uniform throughout the aorta.

The time dependence in circumferential tangent stiffness ( $\delta\sigma_c/\delta\varepsilon_c$ ) due to the pressure wave of a single cardiac cycle is shown in Figure 6.8 and reflects the high and low compliance regimes in the pressure-area relationship along the entire aorta.



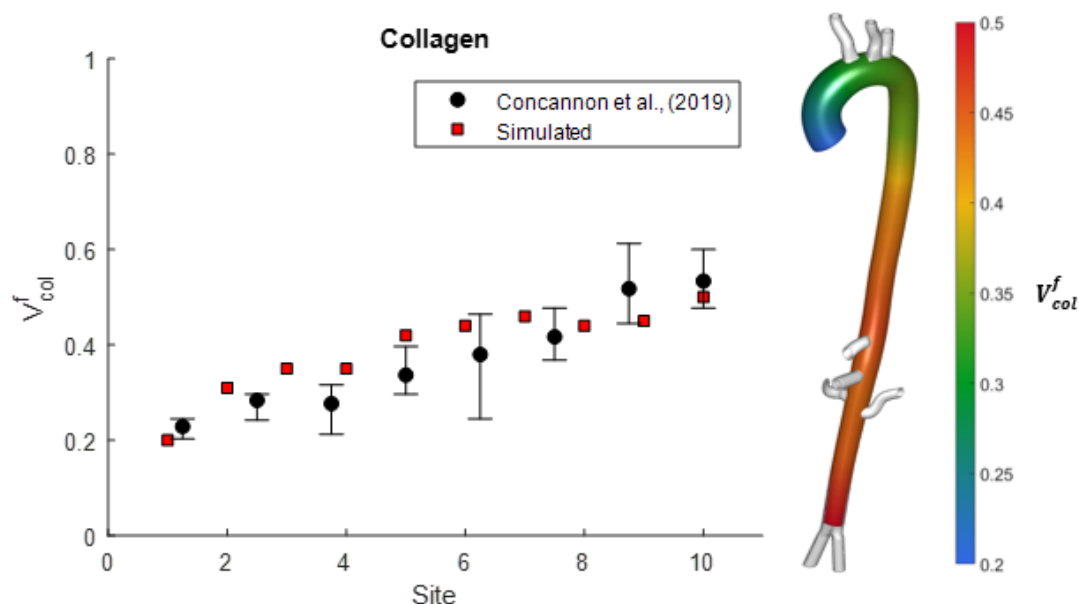
**Figure 6.8:** Computed effective circumferential tangent stiffness,  $K$  (MPa) throughout the aorta at four different time-points during the cardiac cycle ( $t=0 \text{ ms}$ ,  $t=100 \text{ ms}$ ,  $t=200 \text{ ms}$ , and  $t=500 \text{ ms}$ ). The complex spatial and temporal changes in effective material tangent stiffness are clearly illustrated.

Figure 6.9 shows the FE model predictions of elastin volume fraction ( $V_{ela}^f$ ) along the length of the aorta. The model predicts that  $V_{ela}^f$  decreases from a maximum value of 35% at Plane 1 (proximal aorta) to a minimum value of 19% at Plane 10 (distal aorta). This finding is strongly supported by the histological data uncovered in Chapter 4 and superimposed in Figure 6.9 for comparison.



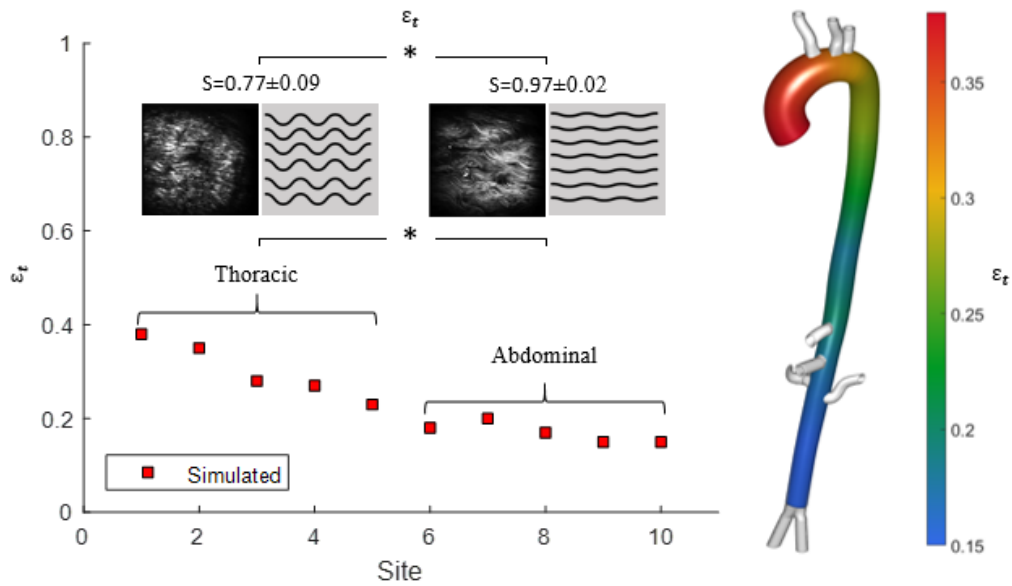
**Figure 6.9:** Computed elastin volume fractions ( $V_{ela}^f$ ) as a function of position (anatomical site – see Figure 5.5) in the aortic wall (red squares). Corresponding elastin content measured in the experimental histology study (Chapter 4, (Concannon et al., 2019)) are superimposed for comparison (black circles).

Figure 6.10 shows the FE model predictions of collagen volume fraction ( $V_{col}^f$ ) along the length of the aorta. The model predicts that  $V_{col}^f$  increases from a minimum value of 20% at Plane 1 (proximal aorta) to a maximum value of 50% at Plane 10 (distal aorta). This finding is strongly supported by the histological data uncovered in Chapter 4 and superimposed in Figure 6.10 for comparison.



**Figure 6.10:** Computed collagen volume fractions ( $V_{col}^f$ ) as a function of position (anatomical site – see Figure 5.5) in the aortic wall (red squares). Corresponding collagen content measured in the experimental histology study (Chapter 4, (Concannon et al., 2019)) are superimposed for comparison (black circles).

The transition strain is plotted as a function of aortic location in Figure 6.11. It is observed that in order to fit the regional *in-vivo* pressure-area curves that the transition strain decreases from 0.38 in the proximal ascending aorta to 0.15 in the distal abdominal segment. This result is in agreement with the *in-vitro* work of Zeinali-Davarani *et al.*, (2015) who found that the degree of collagen undulation observed under multi-photon microscopy also decreased between the proximal and distal aorta in pigs. The waviness ( $S$ ) is defined as the direct distance between the end points of a fiber ( $L$ ) divided by the actual length of fiber ( $l$ ) (i.e.  $S=1$  for a perfectly straight fiber, whereas  $S<1$  for a wavy fibre). A statistically significant difference was found in the waviness of collagen fibers between the thoracic ( $S=0.77\pm 0.09$ ) and abdominal ( $S=0.37\pm 0.02$ ) aorta.



**Figure 6.11:** Computed collagen transition strain ( $\varepsilon_t$ ) as a function of position (anatomical site – see Figure 5.5) in the aortic wall (red squares). The parameter  $\varepsilon_t$  represents the waviness of the collagen, with a high transition strain indicating a high level of waviness. Experimental histological measurements of collagen waviness (characterised by the waviness factor  $S$ ) in thoracic and abdominal porcine aortas are shown for comparison. The statistically significant difference ( $p < 0.05$ ) between the two experimental groups is also evident in our computational results.

Finally, in Figure 6.12 we show the FE model predictions of SMC volume fraction ( $V_{smc}^f$ ) along the length of the aorta. The model predicts that  $V_{smc}^f$  increases from a minimum value of 20% at Plane 1 (proximal aorta) to a maximum value of 27% at Plane 10 (distal aorta). This finding is strongly supported by the histological data uncovered in Chapter 4 and superimposed in Figure 6.12 for comparison.

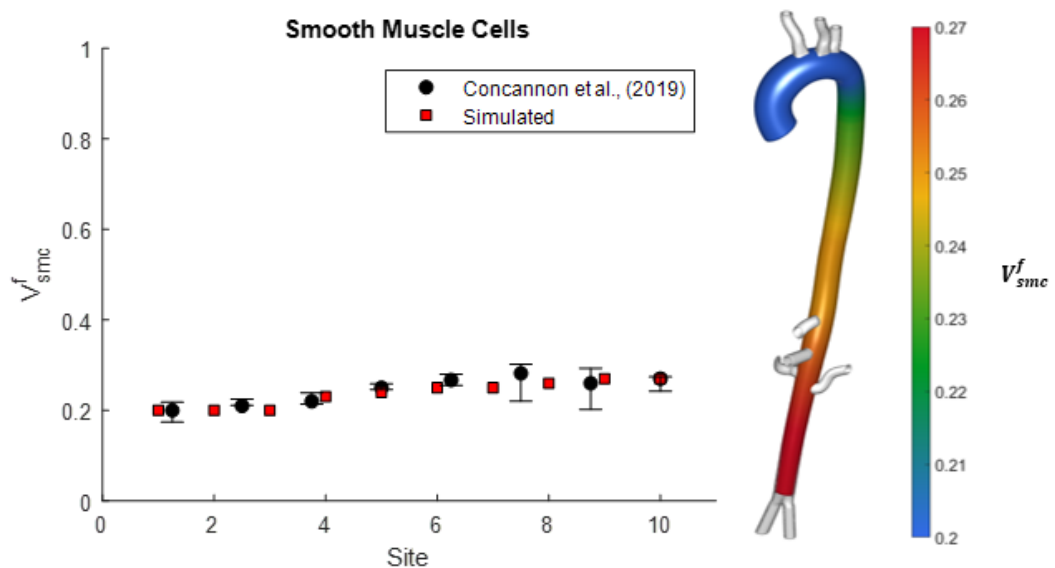


**Figure 6.12:** Computed SMC volume fractions ( $V_{smc}^f$ ) as a function of position (anatomical site – see Figure 5.5) in the aortic wall (red squares). Corresponding SMC content measured in the experimental histology study (Chapter 4, (Concannon et al., 2019)) are superimposed for comparison (black circles).

## 6.4 Discussion

This chapter develops a subject-specific MRI/FEA framework to uncover the biomechanisms underlying the spatially varying non-linear aortic compliance measured *in-vivo* in Chapter 5. Several key findings emerge from the work:

- (i) Internal vessel contractility, due to pre-stretched elastin fibres and actively generated smooth muscle cell stress, must be incorporated into the arterial constitutive law, along with collagen strain stiffening, in order to accurately predict the non-linear pressure-area relationship uncovered by our MRI investigation.
- (ii) Modelling of elastin and smooth muscle contractility allows for the identification of the reference vessel configuration at zero-lumen pressure. This modelling approach is also shown to capture the key features of elastin and SMC knockout experiments.
- (iii) Incorporation of elastin and SMC contractility is critical for the accurate prediction of the physiological lumen pressure at which the aorta transitions from a high-compliance regime to a low-compliance regime due to collagen strain stiffening.
- (iv) Volume fractions of the constituent components of the aortic material model (i.e. non-linear elastic collagen, pre-stretched elastin, and contractile smooth muscle cells) were computed throughout the subject-specific aortic FE model so that the *in-silico* pressure-area curves accurately predict the corresponding MRI data at 10 separate anatomical locations. This leads to the prediction that collagen and smooth muscle volume fractions increase distally, while elastin volume fraction decreases distally. This finding is supported by the histological analyses presented in Chapter 4.
- (v) The model parameter that sets the strain at which collagen transitions from low- to high-stiffness is computed to be lower in the abdominal aorta. This model prediction supports the histological finding that collagen waviness is lower in this region.

It has been shown that the digestion of elastin significantly increases the zero-pressure vessel diameter and alters the pressure-area relationship in arteries over a range of applied physiological lumen pressures (Bellini *et al.*, 2017; Gabriela Espinosa *et al.*, 2018). The inclusion of a pre-stretched linear elastic elastin component in our model accurately replicates the experimental observations of Gabriela Espinosa *et al.*, (2018). In our modelling approach the artery configuration at zero-pressure is computed whereby the pre-strained elastin reduces the vessel diameter until the elastin tensile stress is in equilibrium with the compressive stresses in the groundmatrix. The subsequent application of a lumen pressure within the physiological range leads to the accurate prediction of the experimentally measured pressure-area curve. Our model also includes active contractility of SMCs component. The active SMC stress ( $\sigma_{act} = 25 \text{ kPa}$ ) determined by McGarry *et al.* (2009) for single SMCs seeded on arrays of micro-pillars leads to a reasonable prediction of the experimentally observed increase in aortic wall stress due to phenylephrine induced SMC contractility (Barra *et al.*, 1993; Coulson *et al.*, 2004). Future developments of the SMC component of the model should include descriptions of the active contractility of SMCs in the aortic wall could

include Hill-type tension-strain rate formulations and kinetic formulations for dynamic intra-cellular remodelling of stress fibres (McEvoy *et al.*, (2019), Reynolds *et al.*, (2014), Reynolds *et al.*, (2015)).

The computation of the contracted zero-pressure artery configuration with a lumen area that is ~30-50% lower than the undeformed stress-free configuration due to elastin pre-strain and SMC active contractility is a key component of our subject-specific modelling strategy. This approach is physiologically based on experimental observations of lumen area change following the digestion of elastin using elastase and measured stress changes following SMC activation (Gabriela-Espinosa *et al.*, (2018); Bellini *et al.*, (2017); Dobrin *et al.*, (1984); Barra *et al.*, 1993; Coulson *et al.*, 2004). We demonstrate that the identification of the contracted configuration prior to the application of the lumen pressure (up to a physiological loading range) is a critical step in order to accurately predict MRI measurements of *in-vivo* non-linear pressure-area relationship (presented in Chapter 5). If elastin and SMC contractility are ignored and the vessel is merely loaded from a ‘*stress-free*’ reference state, a non-physiological stress-strain relationship (e.g. a bi-concave sigmoidal Yeoh hyperelastic formulation, or a non-physiological collagen model that does not strain stiffen until 60% tensile strain) must be used for the artery wall. In contrast, if elastin and SMC contractility are included, the *in-vivo* pressure-area relationship is accurately predicted using a physiologically realistic stress-strain relationship, with collagen strain stiffening at 30-35% tensile strain (Kochova *et al.*, 2008; Azadani *et al.*, 2013; Khanafer & Berguer, 2013). A previous artery modelling strategy by Bols *et al.*, (2013), ignores the key contribution of vessel contractility and assumes a polynomial hyperelastic material law. An iterative numerical backwards displacement algorithm was used to estimate zero-pressure stress-free configuration and lumen pressure was directly applied without considering the contracted configuration. A similar approach was implemented by Krishnan *et al.*, (2015), with the added simplification of linear elastic material behaviour. Indeed it should be noted that the majority of patient-specific aortic FE models in the literature incorrectly assume that the observed geometry (from MRI or CT imaging) represents a zero-stress state configuration (Martin *et al.*, (2015), Martufi *et al.*, (2018), Pasta *et al.*, (2013), Erhart *et al.*, (2014), Finotello *et al.*, (2017), Dumenil *et al.*, (2013), Stevens *et al.*, (2017), Burkhardt *et al.*, (2018), and Emerel *et al.*, (2019)), despite the significant applied lumen pressure loading of the vessel during *in-vivo* imaging.

The incorporation of a bi-linear strain-stiffening collagen constitutive law enables accurate fitting to both the bi-linear *in-vivo* pressure-area data, while providing physiologically realistic uniaxial tension stress-strain behaviour. Within the SPPR and HCR, collagen is crimped, and its mechanical contribution is lower than that of the elastin and groundmatrix. This physical interpretation is validated by the experimental study of Schriebl *et al.* (2015) in which the effects of elastase and collagenase on the mechanical response of aortic tissue is investigated. Elastin is demonstrated to contribute primarily to the effective material stiffness in the low stiffness regime. The removal of elastin using elastase is shown to significantly reduce the material stiffness

in the low strain regime. However, removal of elastin does not significantly alter the tangent modulus in the high strain regime, with pronounced (and similar) strain stiffening observed for both treated and untreated samples. However, pronounced strain stiffening is still observed following elastin removal, and the tangent modulus in the high-stiffness regime at high strains is not strongly influenced by elastin removal. Removal of collagen using collagenase does not strongly influence the material stiffness in the low strain regime. However, collagen removal dramatically alters material behaviour in the high strain regime, with strain stiffening being completely eliminated. Our strain stiffening collagen model is supported by reported experimental imaging of collagen deformation in arteries under physiological loading conditions. Collagen fibres are observed to reach a straightened (uncripped) configuration at an applied lumen pressure of 100mmHg (Bloksgaard *et al.*, 2017), and at an applied strain of 0.4 (Chow *et al.*, 2014; Mattson & Zhang, 2017). These data strongly support the range of values of transition strains ( $\varepsilon_t = 0.18 - 0.35$ ) and resultant transition pressures ( $P_t = 83 - 93\text{mmHg}$ ) determined by our MRI/FEA framework.

In order to simulate the spatially varying heterogeneous pressure-area relationships uncovered at 10 aortic planes in the *in-vivo* MRI study in Chapter 5, our modelling framework predicts that the volume fraction of collagen increases with distance from the heart (from 20% in the most proximal Plane 1 to 50% in the most distal Plane 10). We also compute that the volume fraction of elastin decreases with distance from the heart (35% proximally to 19% distally), and the SMC volume fraction increases with distance from the heart (20% proximally to 27% distally). These computed spatial variations in collagen, elastin and SMC are strongly supported by histological data. In Chapter 4 (Concannon *et al.*, 2019) histological analyses of excised cadaveric aorta samples reveals that the area fraction of collagen increased from  $22 \pm 1.6\%$  to  $53 \pm 5.1\%$ , elastin decreased from  $27 \pm 4.7\%$  to  $17 \pm 3.9\%$ , and SMC density increased from  $22 \pm 2.2\%$  to  $27 \pm 1.0\%$ . Other studies have also observed that collagen (Saey *et al.*, 2015; Zhang *et al.*, 2016a) and SMC concentrations increase distally, while elastin concentration decreases distally (Davidson *et al.*, 1985; Zhang *et al.*, 2016b) in horses, pigs and monkeys. Our modelling framework also computes that the transition strain ( $\varepsilon_t$ ) decreases from 0.38 in the proximal aorta to 0.15 in the abdominal aorta. This finding is supported by the experimental study of Zeinali-Davarani *et al.*, (2015) who report that collagen in the proximal aorta was more crimped than collagen in the distal aorta in pigs. Furthermore, the experimental biaxial mechanical test data reported Kamenskiy *et al.*, (2014) and Peña *et al.*, (2018) demonstrate that the transition strain is lower in samples extracted from the distal aorta compared to samples from the proximal aorta.

Several computational studies have used the simplifying assumption that the aorta exhibits a single spatially uniform stiffness (Isnard *et al.*, 1989; Blacher *et al.*, 1999; Vyas *et al.*, 2007; Lalande *et al.*, 2008b; Ioannou *et al.*, 2009; Duprey *et al.*, 2010; Behkam *et al.*, 2017; Schäfer *et al.*, 2018). Using our novel MRI/FEA framework, we highlight the inaccuracy of this assumption, and our constitutive law provides a new

insight into the link between spatially varying tissue composition and resultant biomechanical function. Furthermore, our framework provides a detailed characterisation of a high compliance regime at low physiological lumen pressures and a low compliance regime at high physiological pressures within a single cardiac cycle. This finding is supported by several *ex-vivo* studies that demonstrate a non-linear compliance over the physiological pressure regime in whales (Lillie *et al.*, 2013), octopus (Shadwick and Gosline, 1985), pigs (Vychytil *et al.*, 2010) and humans (Langewouters & Goedhard, 1984; Wang *et al.*, 2006).

The generation of a framework for building subject-specific FE models directly from medical imaging data is of significant value to the field of computational biomechanics. Typically, FE meshes are generated through manual segmentation techniques in commercially available software packages such as Mimics (Materialise, Belgium). Such approaches, however, require significant post-processing time, hindering their feasibility as real-time clinical diagnostic tools. Robust alternative approaches to *in-vivo* geometry construction include IVUS and Multislice CT (Gijssen *et al.*, 2007, Gijssen *et al.*, 2014) as well as pyFormex software (<http://www.pyformex.org>) (Bols *et al.*, 2013). The custom-built framework developed in this study is open source (now freely available on the MATLAB GIBBON toolbox) and can serve as an *in-silico* test-bed for the testing of novel synthetic materials and stent designs.

This study did not consider the effect of non-circumferentially aligned elastin, collagen and SMCs. O'Connell *et al.*, (2008) showed in rats that all three primary medial constituents (elastic lamina, collagen bundles, and smooth muscle cells) have a predominately circumferential orientation. However, collagen fibers have been reported to align at  $+27.75^\circ$  and  $-27.19^\circ$  to the circumferential direction (Schriebl *et al.*, 2012b), and in non-symmetric complex distributions which require a von Mises mixture model to capture (Concannon *et al.*, (2019)). Elastin fibers have been reported to align at  $-40^\circ$  (Bostan *et al.*, 2016) and  $+75^\circ$  (Yu & Zhang, 2018) to the circumferential axis, while SMCs have been reported to align between  $-50^\circ$  and  $-20^\circ$  (Horny *et al.*, 2010) with respect to the circumferential axis. The constitutive law implemented in the current study can readily be extended to include non-circumferential fibre alignments and non-uniform fibre dispersion distributions. The bi-linear form used in this study to describe the strain stiffening collagen contribution can also readily be extended to include a smooth transition region between the low- and high-stiffness regimes. However, the results of the current study demonstrate that such an additional feature is not required to simulate the distinctly bi-linear shape of the pressure-area curves measured *in-vivo* using our dual-VENC protocol in Chapter 5. Future implementations could also consider the simulation of collagen strain stiffening using exponential strain stiffening hyperelastic formulations (Holzapfel, Gasser and Ogden, (2000), Nolan *et al.*, (2014), Mansouri & Darijani, (2014)). Additionally, our study did not consider the effect of anatomical constraints on aortic deformation, such as the spinal column or lungs. Such additional features can readily be identified from MRI images and incorporated into future model implementations.

In summary, this computational investigation provides new insights into the spatially varying non-linear compliance of the aorta, uncovering the key role of pre-stretched elastin, contractile SMCs and strain stiffening collagen on in vivo biomechanical behaviour. We demonstrate that our subject-specific MRI/FEA framework can predict the spatial variation of collagen, elastin and SMC throughout the aorta and can accurately predict the complex spatially varying pressure-area relationship under physiological loading. The subject-specific MRI/FEA framework can potentially be used to guide preoperative planning of aortic surgery, e.g. endovascular or open surgical repair, and aid in the design of next generation patient-specific aortic devices.

## 6.5 Bibliography

- Azadani, A. N., Chitsaz, S., Mannion, A., Mookhoek, A., Wisneski, A., Guccione, J. M., Hope, M. D., Ge, L. and Tseng, E. E. (2013) 'Biomechanical Properties of Human Ascending Thoracic Aortic Aneurysms', *The Annals of Thoracic Surgery*, 96, pp. 50–58. doi: 10.1016/j.athoracsur.2013.03.094.
- Barra, J. G., Armentano, R. L., Levenson, J., Fischer, E. I. C., Pichel, R. H. and Simon, A. (1993) 'Assessment of smooth muscle contribution to descending thoracic aortic elastic mechanics in conscious dogs', *Circulation Research*, 73(6), pp. 1040–1050. doi: 10.1161/01.RES.73.6.1040.
- Behkam, R., Roberts, K. E., Bierhals, A. J., Jacobs, M. E., Edgar, J. D., Paniello, R. C., Woodson, G., Vande Geest, J. P. and Barkmeier-Kraemer, J. M. (2017) 'Aortic arch compliance and idiopathic unilateral vocal fold paralysis', *Journal of Applied Physiology*. American Physiological Society, 123(2), pp. 303–309. doi: 10.1152/jappphysiol.00239.2017.
- Bellini, C., Bersi, M. R., Caulk, A. W., Ferruzzi, J., Milewicz, D. M., Ramirez, F., Rifkin, D. B., Tellides, G., Yanagisawa, H. and Humphrey, J. D. (2017a) 'Comparison of 10 murine models reveals a distinct biomechanical phenotype in thoracic aortic aneurysms', *Journal of the Royal Society Interface*. Royal Society, 14(130). doi: 10.1098/rsif.2016.1036.
- Blacher, J., Asmar, R., Djane, S., London, G. M. and Safar, M. E. (1999) 'Aortic pulse wave velocity as a marker of cardiovascular risk in hypertensive patients.', *Hypertension (Dallas, Tex. : 1979)*. American Heart Association, Inc., 33(5), pp. 1111–7. doi: 10.1161/01.HYP.33.5.1111.
- Bloksgaard, M., Leurgans, T. M., Spronck, B., Heusinkveld, M. H. G., Thorsted, B., Rosenstand, K., Nissen, I., Hansen, U. M., Brewer, J. R., Bagatolli, L. A., Rasmussen, L. M., Irmukhamedov, A., Reesink, K. D. and De Mey, J. G. R. (2017) 'Imaging and modeling of acute pressure-induced changes of collagen and elastin microarchitectures in pig and human resistance arteries', *American Journal of Physiology-Heart and Circulatory Physiology*, 313(1), pp. H164–H178. doi: 10.1152/ajpheart.00110.2017.
- Bols, J. and Vierendeels, J. (2013) 'inverse modelling of image-based patient-specific blood vessels: zero-pressure geometry and in vivo stress incorporation', *esaim: Mathematical Modelling and Numerical Analysis*.
- Bostan, L., Noble, C. and Smulders, N. (2016) 'Measurement of friction-induced changes in pig aorta fibre organization by non-invasive imaging as a model for detecting the tissue response to endovascular catheters', *Biotribology*. doi: 10.1016/j.biotri.2017.02.003.
- Burkhardt, B. E., Byrne, N., Velasco Forte, M. N., Iannaccone, F., De Beule, M., Morgan, G. J. and Hussain, T. (2018) 'Evaluation of a modified Cheatham-Platinum stent for the treatment of aortic coarctation by finite element modelling', *JRSM Cardiovascular Disease*. SAGE Publications, 7, p. 204800401877395. doi: 10.1177/2048004018773958.

- Choudhury, N., Bouchot, O., Rouleau, L., Tremblay, D., Cartier, R., Butany, J., Mongrain, R. and Leask, R. L. (2009) 'Local mechanical and structural properties of healthy and diseased human ascending aorta tissue', *Cardiovascular Pathology*, 18, pp. 83–91. doi: 10.1016/j.carpath.2008.01.001.
- Chow, M.-J., Turcotte, R., Lin, C. P. and Zhang, Y. (2014) 'Arterial Extracellular Matrix: A Mechanobiological Study of the Contributions and Interactions of Elastin and Collagen', *Biophysj*, 106, pp. 2684–2692. doi: 10.1016/j.bpj.2014.05.014.
- Concannon, J., Dockery, P., Black, A., Sultan, S., Hynes, N., McHugh, P. E., Moerman, K. M. and McGarry, J. P. (2019) 'Quantification of the regional bioarchitecture in the human aorta', *Journal of Anatomy*, p. joa.13076. doi: 10.1111/joa.13076.
- Coulson, R. J., Cipolla, M. J., Vitullo, L. and Chesler, N. C. (2004) 'Mechanical properties of rat middle cerebral arteries with and without myogenic tone.', *Journal of biomechanical engineering*, 126(1), pp. 76–81. doi: 10.1115/1.1645525.
- Davidson, J. M., Hill, K. E., Mason, M. L. and Giro\$, M. G. (1985) 'Longitudinal Gradients of Collagen Porcine Aorta\* and Elastin Gene Expression in the', *The journal of biological chemistry*, 260(3), pp. 1301–1908. Available at: <http://www.jbc.org/content/260/3/1901.full.pdf> (Accessed: 7 June 2018).
- Dobrin, P. B., Baker, W. H. and Gley, W. C. (1984) 'Elastolytic and Collagenolytic Studies of Arteries: Implications for the Mechanical Properties of Aneurysms', *Archives of Surgery*, 119(4), pp. 405–409. doi: 10.1001/archsurg.1984.01390160041009.
- Dobrin, P. B., Baker, W. H. and Gley, W. C. (1984) 'Elastolytic and collagenolytic studies of arteries.', *JAMA*, 119(4), pp. 405–409.
- Doyle, B. J., Callanan, A. and McGloughlin, T. M. (2007) 'A comparison of modelling techniques for computing wall stress in abdominal aortic aneurysms.', *Biomedical engineering online*, 6, p. 38. doi: 10.1186/1475-925X-6-38.
- Dumenil, A., Kaladji, A., Castro, M., Esneault, S., Lucas, A., Rochette, M., Goksu, C. and Haigron, P. (2013) 'Finite-element-based matching of pre-and intraoperative data for image-guided endovascular aneurysm repair', *IEEE Transactions on Biomedical Engineering*, 60(5), pp. 1353–1362. doi: 10.1109/TBME.2012.2235440.
- Duprey, A., Khanafer, K., Schlicht, M., Avril, S., Williams, D. and Berguer, R. (2010) 'In Vitro Characterisation of Physiological and Maximum Elastic Modulus of Ascending Thoracic Aortic Aneurysms Using Uniaxial Tensile Testing', *European Journal of Vascular and Endovascular Surgery*. W.B. Saunders Ltd, 39(6), pp. 700–707. doi: 10.1016/j.ejvs.2010.02.015.
- Emerel, L., Thunes, J., Kickliter, T., Billaud, M., Phillippi, J. A., Vorp, D. A., Maiti, S. and Gleason, T. G. (2019) 'Predissection-derived geometric and distensibility indices reveal increased peak longitudinal stress and stiffness in patients sustaining acute type A aortic dissection: Implications for predicting dissection',

- The Journal of Thoracic and Cardiovascular Surgery. Mosby, 158(2), pp. 355–363. doi: 10.1016/J.JTCVS.2018.10.116.
- Erhart, P., Grond-Ginsbach, C., Hakimi, M., Lasitschka, F., Dihlmann, S., Böckler, D. and Hyhlik-Dürr, A. (2014) ‘Finite element analysis of abdominal aortic aneurysms: predicted rupture risk correlates with aortic wall histology in individual patients.’, *Journal of endovascular therapy : an official journal of the International Society of Endovascular Specialists*, 21(4), pp. 556–64. doi: 10.1583/14-4695.1.
- Finotello, A., Morganti, S. and Auricchio, F. (2017) ‘Finite element analysis of TAVI: Impact of native aortic root computational modeling strategies on simulation outcomes’, *Medical Engineering and Physics*. Elsevier Ltd, 47, pp. 2–12. doi: 10.1016/j.medengphy.2017.06.045.
- Faury, G., Pezet, M., Knutsen, R. H., Boyle, W. A., Heximer, S. P., McLean, S. E., Minkes, R. K., Blumer, K. J., Kovacs, A., Kelly, D. P., Li, D. Y., Starcher, B. and Mecham, R. P. (2003) ‘Developmental adaptation of the mouse cardiovascular system to elastin haploinsufficiency.’, *The Journal of clinical investigation*, 112(9), pp. 1419–28. doi: 10.1172/JCI19028.
- Forsell, C., Roy, J. and Gasser, T. C. (2013) ‘The Quasi-Static Failure Properties of the Abdominal Aortic Aneurysm Wall Estimated by a Mixed Experimental-Numerical Approach’, *Annals of biomedical engineering*.
- Gabriela Espinosa, M., Catalin Staiculescu, M., Kim, J., Marin, E. and Wagenseil, J. E. (2018a) ‘Elastic Fibers and Large Artery Mechanics in Animal Models of Development and Disease.’, *Journal of biomechanical engineering*, 140(2). doi: 10.1115/1.4038704.
- Geest, J. P. Vande, Sacks, M. S. and Vorp, D. A. (2004) ‘Age Dependency of the Biaxial Biomechanical Behavior of Human Abdominal Aorta’, *Journal of Biomechanical Engineering*, 126(6), p. 815. doi: 10.1115/1.1824121.
- Gijsen, F. J. H., Wentzel, J. J., Thury, A., Lamers, B., Schuurbijs, J. C. H., Serruys, P. W. and van der Steen, A. F. (2007) ‘A new imaging technique to study 3-D plaque and shear stress distribution in human coronary artery bifurcations in vivo’, *Journal of Biomechanics*, 40(11), pp. 2349–2357. doi: 10.1016/j.jbiomech.2006.12.007.
- Gijsen, F. J. H., Schuurbijs, J. C. H., van de Giessen, A. G., Schaap, M., van der Steen, A. F. W. and Wentzel, J. J. (2014) ‘3D reconstruction techniques of human coronary bifurcations for shear stress computations’, *Journal of Biomechanics*, 47(1), pp. 39–43. doi: 10.1016/j.jbiomech.2013.10.021.
- Vande Geest, J. P., Sacks, M. S. and Vorp, D. A. (2006) ‘The effects of aneurysm on the biaxial mechanical behavior of human abdominal aorta.’, *Journal of biomechanics*, 39(7), pp. 1324–34. doi: 10.1016/j.jbiomech.2005.03.003.
- Vande Geest, J. P., Schmidt, D. E., Sacks, M. S. and Vorp, D. A. (2008) ‘The effects of anisotropy on the stress analyses of patient-specific abdominal aortic aneurysms.’, *Annals of biomedical engineering*, 36(6), pp. 921–32. doi: 10.1007/s10439-008-9490-3.

- Gundiah, N., Babu, A. R. and Pruitt, L. A. (2013) 'Effects of elastase and collagenase on the nonlinearity and anisotropy of porcine aorta', *Physiological Measurement*. IOP Publishing, 34(12), pp. 1657–1673. doi: 10.1088/0967-3334/34/12/1657.
- Hallock, P. and Benson, I. C. (1937) 'Studies on the elastic properties of human isolated aorta.', *The Journal of clinical investigation*. American Society for Clinical Investigation, 16(4), pp. 595–602. doi: 10.1172/JCI100886.
- Harkness, M. L., Harkness, R. D. and McDonald, D. A. (1957) 'The collagen and elastin content of the arterial wall in the dog.', *Proceedings of the Royal Society of London. Series B, Biological sciences*, 146(925), pp. 541–51. Available at: <http://www.ncbi.nlm.nih.gov/pubmed/13441679> (Accessed: 31 May 2018).
- Haskett, D., Johnson, G., Zhou, A., Utzinger, U. and Vande Geest, J. (2010) 'Microstructural and biomechanical alterations of the human aorta as a function of age and location', *Biomechanics and Modeling in Mechanobiology*, 9(6), pp. 725–736. doi: 10.1007/s10237-010-0209-7.
- He, C. M. and Roach, M. R. (1994) 'The composition and mechanical properties of abdominal aortic aneurysms', *Journal of Vascular Surgery*. Elsevier, 20(1), pp. 6–13. doi: 10.1016/0741-5214(94)90169-4.
- Holzapfel, G. A., Gasser, T. C. and Ogden, R. W. (2000) 'A New Constitutive Framework for Arterial Wall Mechanics and a Comparative Study of Material Models', *Journal of elasticity and the physical science of solids*. Kluwer Academic Publishers, 61(1–3), pp. 1–48. doi: 10.1023/A:1010835316564.
- Horny, L., Kronek, J., Chlup, H., Zitny, R., Vesely, J. and Hulam, M. (2010) 'Orientations of collagen fibers in aortic histological section', *Bulletin of applied mechanics*, 6(22), pp. 25–29. Available at: <http://users.fs.cvut.cz/~hornyluk/files/Horny-L-2010-Orientations-of-collagen-fibers-in-aortic-histological-section.pdf> (Accessed: 20 September 2018).
- Humphrey, J. D. (2012) 'Possible mechanical roles of glycosaminoglycans in thoracic aortic dissection and associations with dysregulated transforming growth factor- $\beta$ ', *Journal of Vascular Research*, pp. 1–10. doi: 10.1159/000342436.
- Iliopoulos, D. C., Deveja, R. P., Kritharis, E. P., Perrea, D., Sionis, G. D., Toutouzas, K., Stefanadis, C. and Sokolis, D. P. (2009) 'Regional and directional variations in the mechanical properties of ascending thoracic aortic aneurysms', *Medical Engineering & Physics*, 31(1), pp. 1–9. doi: 10.1016/j.medengphy.2008.03.002.
- Ioannou, C. V., Morel, D. R., Katsamouris, A. N., Katranitsa, S., Startchik, I., Kalangos, A., Westerhof, N. and Stergiopulos, N. (2009) 'Left ventricular hypertrophy induced by reduced aortic compliance.', *Journal of vascular research*. Karger Publishers, 46(5), pp. 417–25. doi: 10.1159/000194272.
- Isnard, R. N., Pannier, B. M., Laurent, S., London, G. M., Diebold, B. and Safar, M. E. (1989) 'Pulsatile diameter and elastic modulus of the aortic arch in essential hypertension: A noninvasive study', *Journal of the American College of Cardiology*, 13(2), pp. 399–405. doi: 10.1016/0735-1097(89)90518-4.
- Kamenskiy, A. V., Dzenis, Y. A., Kazmi, S. A. J., Pemberton, M. A., Pipinos, I. I., Phillips, N. Y., Herber, K., Woodford, T., Bowen, R. E., Lomneth, C. S. and MacTaggart, J. N. (2014) 'Biaxial mechanical properties of the human thoracic

- and abdominal aorta, common carotid, subclavian, renal and common iliac arteries', *Biomechanics and Modeling in Mechanobiology*. Springer Verlag, 13(6), pp. 1341–1359. doi: 10.1007/s10237-014-0576-6.
- Khanafer, K., Schlicht, M. S. and Berguer, R. (2013) 'How should we measure and report elasticity in aortic tissue?', *European Journal of Vascular and Endovascular Surgery*, 45(4), pp. 332–339. doi: 10.1016/j.ejvs.2012.12.015.
- Kochova, P., Tonar, Z., Matejka, V. M., Svirglerova, J., Stengl, M. and Kuncova, J. (2008) 'Morphology and mechanical properties of the subrenal aorta in normotensive and hypertensive rats.', *Biomedical papers of the Medical Faculty of the University Palacký, Olomouc, Czechoslovakia*, 152(2), pp. 239–245. doi: 10.5507/bp.2008.037.
- Krishnan, K., Ge, L. and Tseng, E. E. (2014) 'Ascending thoracic aortic aneurysm wall stress analysis using patient-specific finite element modeling of in vivo magnetic resonance imaging', *Interactive CardioVascular and Thoracic Surgery*.
- Krüger, T., Veseli, K., Lausberg, H., Vöhringer, L., Schneider, W. and Schlensak, C. (2016) 'Regional and directional compliance of the healthy aorta: an ex vivo study in a porcine model', *Interactive CardioVascular and Thoracic Surgery*, 23(1), pp. 104–111. doi: 10.1093/icvts/ivw053.
- Laksari, K., Shahmirzadi, D., Acosta, C. J. and Konofagou, E. (2016) 'Energy-based constitutive modelling of local material properties of canine aortas', *Journal of the Royal Society, Interface*, 3(9), p. 160365. doi: 10.1098/rsos.160365.
- Lalande, A., Khau Van Kien, P., Walker, P. M., Zhu, L., Legrand, L., Claustres, M., Jeunemaître, X., Brunotte, F. and Wolf, J. E. (2008) 'Compliance and pulse wave velocity assessed by MRI detect early aortic impairment in young patients with mutation of the smooth muscle myosin heavy chain', *Journal of Magnetic Resonance Imaging*. Wiley-Blackwell, 28(5), pp. 1180–1187. doi: 10.1002/jmri.21565.
- Langewouters, G. J., Wesseling, K. H. and Goedhard, W. J. (1984) 'The static elastic properties of 45 human thoracic and 20 abdominal aortas in vitro and the parameters of a new model.', *Journal of biomechanics*, 17(6), pp. 425–35. Available at: <http://www.ncbi.nlm.nih.gov/pubmed/6480618> (Accessed: 16 April 2019).
- Länne, T., Sonesson, B., Bergqvist, D., Bengtsson, H. and Gustafsson, D. (1992) 'Diameter and compliance in the male human abdominal aorta: Influence of age and aortic aneurysm', *European Journal of Vascular Surgery*. W.B. Saunders, 6(2), pp. 178–184. doi: 10.1016/S0950-821X(05)80237-3.
- Lillie, M. A., Piscitelli, M. A., Vogl, A. W., Gosline, J. M. and Shadwick, R. E. (2013) 'Cardiovascular design in fin whales: High-stiffness arteries protect against adverse pressure gradients at depth', *Journal of Experimental Biology*, 216(14), pp. 2548–2563. doi: 10.1242/jeb.081802.
- Mansouri, M. R. and Darijani, H. (2014) 'Constitutive modeling of isotropic hyperelastic materials in an exponential framework using a self-contained approach', *International Journal of Solids and Structures*. Elsevier Ltd, 51(25–26), pp. 4316–4326. doi: 10.1016/j.ijsolstr.2014.08.018.

- Martin, C., Sun, W. and Elefteriades, J. (2015) 'Patient-specific finite element analysis of ascending aorta aneurysms', *American Journal of Physiology-Heart and Circulatory Physiology*, 308(10), pp. H1306–H1316. doi: 10.1152/ajpheart.00908.2014.
- Martufi, G., Forneris, A., Nobakht, S., Rinker, K. D., Moore, R. D. and Di Martino, E. S. (2018) 'Case Study: Intra-Patient Heterogeneity of Aneurysmal Tissue Properties', *Frontiers in Cardiovascular Medicine*. *Frontiers*, 5, p. 82. doi: 10.3389/fcvm.2018.00082.
- Matsumoto, T., Fukui, T., Tanaka, T., Ikuta, N., Ohashi, T., Kumagai, K., Akimoto, H., Tabayashi, K. and Sato, M. (2009) 'Biaxial Tensile Properties of Thoracic Aortic Aneurysm Tissues', *Journal of Biomechanical Science and Engineering*, 4(4). doi: 10.1299/jbse.4.518.
- Mattson, J. M. and Zhang, Y. (2017) 'Structural and Functional Differences Between Porcine Aorta and Vena Cava.', *Journal of biomechanical engineering*. *American Society of Mechanical Engineers*, 139(7), p. 0710071. doi: 10.1115/1.4036261.
- McEvoy, E., Deshpande, V. S. and McGarry, P. (2019) 'Transient active force generation and stress fibre remodelling in cells under cyclic loading', *Biomechanics and Modeling in Mechanobiology*. Springer Verlag, 18(4), pp. 921–937. doi: 10.1007/s10237-019-01121-9.
- McGarry, J. P., Fu, J., Yang, M. T., Chen, C. S., McMeeking, R. M., Evans, A. G. and Deshpande, V. S. (2009) 'Simulation of the contractile response of cells on an array of micro-posts', *Philosophical Transactions of the Royal Society A: Mathematical, Physical and Engineering Sciences*. The Royal Society Publishing, 367(1902), pp. 3477–3497. doi: 10.1098/rsta.2009.0097.
- Merkx, M. A. G., van 't Veer, M., Speelman, L., Breeuwer, M., Buth, J. and van de Vosse, F. N. (2009) 'Importance of initial stress for abdominal aortic aneurysm wall motion: dynamic MRI validated finite element analysis.', *Journal of biomechanics*, 42(14), pp. 2369–73. doi: 10.1016/j.jbiomech.2009.06.053.
- Mohan, D. and Melvin, J. W. (1982) Failure properties of passive human aortic tissue. i-uniaxial tension tests. Available at: <https://deepblue.lib.umich.edu/bitstream/handle/2027.42/24140/0000397.pdf;jsessionid=2E1FC73B828B5C831937E31ADD93B083?sequence=1> (Accessed: 18 July 2019).
- Mohiaddin, R. H., Underwood, S. R., Bogren, H. G., Firmin, D. N., Klipstein, R. H. and Longmore, D. B. (1989) 'Regional aortic compliance studied by magnetic resonance imaging: the effects of age, training, and coronary artery disease', *Br Heart J*, 62, pp. 90–6. Available at: <http://heart.bmj.com/content/heartjnl/62/2/90.full.pdf> (Accessed: 2 March 2018).
- Moriwaki, T., Oie, T., Takamizawa, K., Murayama, Y., Fukuda, T., Omata, S., Kanda, K. and Nakayama, Y. (2011) 'Variations in local elastic modulus along the length of the aorta as observed by use of a scanning haptic microscope (SHM)', *Journal of Artificial Organs*. Springer Japan, 14(4), pp. 276–283. doi: 10.1007/s10047-011-0596-2.

- Nolan, D., Ogden, R. W., Destrade, M. and McGarry, J. P. (2014) ‘A robust anisotropic hyperelastic formulation for the modelling of soft tissue’, *Journal of the Mechanical Behaviour of Biomedical Materials*.
- Nolan, D. R. and McGarry, J. P. (2016) ‘On the Compressibility of Arterial Tissue’, *Annals of Biomedical Engineering*. Springer US, 44(4), pp. 993–1007. doi: 10.1007/s10439-015-1417-1.
- O’Connell, M. K., Murthy, S., Phan, S., Xu, C., Buchanan, J., Spilker, R., Dalman, R. L., Zarins, C. K., Denk, W. and Taylor, C. A. (2008) ‘The three-dimensional micro- and nanostructure of the aortic medial lamellar unit measured using 3D confocal and electron microscopy imaging’, *Matrix Biology*. Elsevier, 27(3), pp. 171–181. doi: 10.1016/J.MATBIO.2007.10.008.
- Pasta, S., Cho, J.-S., Dur, O., Pekkan, K. and Vorp, D. A. (2013) ‘Computer modeling for the prediction of thoracic aortic stent graft collapse’, *Journal of Vascular Surgery*. Mosby, 57(5), pp. 1353–1361. doi: 10.1016/J.JVS.2012.09.063.
- Pasta, S., Phillippi, J. A., Tsamis, A., D’Amore, A., Raffa, G. M., Pilato, M., Scardulla, C., Watkins, S. C., Wagner, W. R., Gleason, T. G. and Vorp, D. A. (2015) ‘Constitutive modeling of ascending thoracic aortic aneurysms using microstructural parameters.’, *Medical engineering & physics*. doi: 10.1016/j.medengphy.2015.11.001.
- Peña, J. A., Corral, V., Martínez, M. A. and Peña, E. (2018) ‘Over length quantification of the multiaxial mechanical properties of the ascending, descending and abdominal aorta using Digital Image Correlation’, *Journal of the Mechanical Behavior of Biomedical Materials*. Elsevier, 77, pp. 434–445. doi: 10.1016/J.JMBBM.2017.10.007.
- Pierce, D. M., Maier, F., Weisbecker, H., Viertler, C., Verbrugge, P., Famaey, N., Fourneau, I., Herijgers, P. and Holzapfel, G. A. (2015) ‘Human thoracic and abdominal aortic aneurysmal tissues: Damage experiments, statistical analysis and constitutive modeling’, *Journal of the Mechanical Behavior of Biomedical Materials*, 41, pp. 92–107. doi: 10.1016/j.jmbbm.2014.10.003.
- Raghavan, M. L., Ma, B. and Fillinger, M. F. (2006) ‘Non-Invasive Determination of Zero-Pressure Geometry of Arterial Aneurysms’, *Annals of Biomedical Engineering*. Springer US, 34(9), pp. 1414–1419. doi: 10.1007/s10439-006-9115-7.
- Raghavan, M. L., Hanaoka, M. M., Kratzberg, J. A., Higuchi, M. de L. and da Silva, E. S. (2011) ‘Biomechanical failure properties and microstructural content of ruptured and unruptured abdominal aortic aneurysms’, *Journal of Biomechanics*, 44(13), pp. 2501–2507. doi: 10.1016/j.jbiomech.2011.06.004.
- Reeps, C., Maier, A., Pelisek, J., Härtl, F., Grabher-Meier, V., Wall, W. A., Essler, M., Eckstein, H.-H. and Gee, M. W. (2013) ‘Measuring and modeling patient-specific distributions of material properties in abdominal aortic aneurysm wall’, *Biomechanics and Modeling in Mechanobiology*. Springer-Verlag, 12(4), pp. 717–733. doi: 10.1007/s10237-012-0436-1.

- Reynolds, N. H. and McGarry, J. P. (2015) ‘Single cell active force generation under dynamic loading - Part II: Active modelling insights’, *Acta Biomaterialia*. Elsevier Ltd, 27, pp. 251–263. doi: 10.1016/j.actbio.2015.09.004.
- Reynolds, N. H., Ronan, W., Dowling, E. P., Owens, P., McMeeking, R. M. and McGarry, J. P. (2014) ‘On the role of the actin cytoskeleton and nucleus in the biomechanical response of spread cells’, *Biomaterials*, 35(13), pp. 4015–4025. doi: 10.1016/j.biomaterials.2014.01.056.
- Saey, V., Famaey, N., Smoljkic, M., Claeys, E., Van Loon, G., Ducatelle, R., Ploeg, M., Delesalle, C., Gröne, A., Duchateau, L. and Chiers, K. (2015) ‘Biomechanical and biochemical properties of the thoracic aorta in warmblood horses, Friesian horses, and Friesians with aortic rupture’, *BMC Veterinary Research*, 11(285). doi: 10.1186/s12917-015-0597-0.
- Sassani, S. G., Tsangaris, S. and Sokolis, D. P. (2015) ‘Layer- and region-specific material characterization of ascending thoracic aortic aneurysms by microstructure-based models’, *Journal of Biomechanics*, 48(14), pp. 3757–3765. doi: 10.1016/j.jbiomech.2015.08.028.
- Schäfer, M., Browne, L. P., Morgan, G. J., Barker, A. J., Fonseca, B., Ivy, D. D. and Mitchell, M. B. (2018) ‘Reduced proximal aortic compliance and elevated wall shear stress after early repair of tetralogy of Fallot’, *Journal of Thoracic and Cardiovascular Surgery*. Mosby Inc., 156(6), pp. 2239–2249. doi: 10.1016/j.jtcvs.2018.08.081.
- Schriefl, A. J., Schmidt, T., Balzani, D., Sommer, G. and Holzapfel, G. A. (2015) ‘Selective enzymatic removal of elastin and collagen from human abdominal aortas: Uniaxial mechanical response and constitutive modeling’, *Acta Biomaterialia*, 17, pp. 125–136. doi: 10.1016/j.actbio.2015.01.003.
- Schriefl, A. J., Zeindlinger, G., Pierce, D. M., Regitnig, P. and Holzapfel, G. A. (2012) ‘Determination of the layer-specific distributed collagen fibre orientations in human thoracic and abdominal aortas and common iliac arteries.’, *Journal of the Royal Society, Interface / the Royal Society*, 9(71), pp. 1275–86. doi: 10.1098/rsif.2011.0727.
- Shadwick, R. and Gosline, J. M. (1985) Mechanical properties of the octopus aorta, *J. exp. Biol.*
- Stevens, R. R. F., Grytsan, A., Biasetti, J., Roy, J., Liljeqvist, M. L. and Christian Gasser, T. (2017) ‘Biomechanical changes during abdominal aortic aneurysm growth’, *PLoS ONE*. Public Library of Science, 12(11). doi: 10.1371/journal.pone.0187421.
- Swanson, W. M. and Clark, R. E. (1974) ‘Dimensions and Geometric Relationships of the Human Aortic Valve as a Function of Pressure’, *Circulation Research*. Lippincott Williams & Wilkins, 35(6), pp. 871–882. doi: 10.1161/01.RES.35.6.871.
- Tanaka, T. T. and Fung, Y.-C. (1974) ‘Elastic and inelastic properties of the canine aorta and their variation along the aortic tree’, *Journal of Biomechanics*, 7(4), pp. 357–370. doi: 10.1016/0021-9290(74)90031-1.

- Teng, Z., Feng, J., Zhang, Y., Huang, Y., Sutcliffe, M. P. F., Brown, A. J., Jing, Z., Gillard, J. H. and Lu, Q. (2015) 'Layer- and Direction-Specific Material Properties, Extreme Extensibility and Ultimate Material Strength of Human Abdominal Aorta and Aneurysm: A Uniaxial Extension Study', *Annals of Biomedical Engineering*. Springer US, 43(11), pp. 2745–2759. doi: 10.1007/s10439-015-1323-6.
- Vyas, M., Izzojr, J., Lacourciere, Y., Arnold, J., Dunlap, M., Amato, J., Pfeffer, M. and Mitchell, G. (2007) 'Augmentation Index and Central Aortic Stiffness in Middle-Aged to Elderly Individuals', *American Journal of Hypertension*. Oxford University Press, 20(6), pp. 642–647. doi: 10.1016/j.amjhyper.2007.01.008.
- Vychytil, J., Moravec, F., Kochová, P., Kuncová, J. and Svíglerová, J. (2010) Modelling of the mechanical behaviour of porcine carotid artery undergoing inflation-deflation test, *Applied and Computational Mechanics*.
- Wang, J.-J., Liu, S.-H., Kao, T., Hu, W.-C. and Liu, C.-P. (2006) 'Noninvasive determination of arterial pressure-dependent compliance in young subjects using an arterial tonometer', *Biomedical Engineering: Applications, Basis and Communications*, 18(03), pp. 111–118. doi: 10.4015/S1016237206000191.
- Weisbecker, H., Viertler, C., Pierce, D. M. and Holzapfel, G. A. (2013) 'The role of elastin and collagen in the softening behavior of the human thoracic aortic media'. doi: 10.1016/j.jbiomech.2013.04.025.
- Yu, X., Wang, Y. and Zhang, Y. (2018) 'Transmural variation in elastin fiber orientation distribution in the arterial wall', *Journal of the Mechanical Behavior of Biomedical Materials*, 77, pp. 745–753. doi: 10.1016/j.jmbbm.2017.08.002.
- Zeinali-Davarani, S., Wang, Y., Chow, M.-J., El Turcotte, R. € and Zhang, Y. (2015) 'Contribution of Collagen Fiber Undulation to Regional Biomechanical Properties Along Porcine Thoracic Aorta', *Journal of Biomechanical Engineering*, 137. doi: 10.1115/1.4029637.
- Zhang, J., Zhao, X., Vatner, D. E., McNulty, T., Bishop, S., Sun, Z., Shen, Y.-T., Chen, L., Meininger, G. A. and Vatner, S. F. (2016a) 'Extracellular Matrix Disarray as a Mechanism for Greater Abdominal Versus Thoracic Aortic Stiffness With Aging in Primates.', *Arteriosclerosis, thrombosis, and vascular biology*, 36(4), pp. 700–6. doi: 10.1161/ATVBAHA.115.306563.
- Zhang, J., Zhao, X., Vatner, D. E., McNulty, T., Bishop, S., Sun, Z., Shen, Y.-T., Chen, L., Meininger, G. A. and Vatner, S. F. (2016b) 'Extracellular Matrix Disarray as a Mechanism for Greater Abdominal Versus Thoracic Aortic Stiffness With Aging in Primates.', *Arteriosclerosis, thrombosis, and vascular biology*, 36(4), pp. 700–6. doi: 10.1161/ATVBAHA.115.306563.

# CHAPTER 7

## AN INVESTIGATION OF REPAIR TECHNIQUES ON THE BIOMECHANICS OF THE HUMAN AORTA



### **Abstract**

The effect of repair techniques on the biomechanics of the aorta is poorly understood resulting in significant levels of postoperative complications for patients worldwide. This study presents a computational analysis of the influence of Nitinol based devices on the biomechanical performance of a subject-specific human aorta. Simulations reveal that Nitinol stent-grafts stretch the artery wall so that collagen is stretched to a straightened high stiffness configuration. The high-compliance regime (HCR) associated with low diastolic lumen pressure is eliminated, and the artery operates in a low compliance regime (LCR) throughout the entire cardiac cycle. The slope of the lumen pressure-area curve for the LCR post-implantation is almost identical to that of the native vessel during systole. This negligible change from the native systole slope occurs because the stent-graft increases its diameter from the crimped configuration during deployment so that it reaches a low stiffness unloading plateau. The effective radial stiffness of the implant along this unloading plateau is negligible compared to the stiffness of the artery wall. Provided the Nitinol device unloads sufficiently during deployment to the unloading plateau, the degree of oversizing has a negligible effect on the pressure-area response of the vessel, as each device exerts approximately the same radial force, the slope of which is negligible compared to the LCR slope of the native artery. We show that 10% oversizing based on the observed diastolic diameter in the mid descending thoracic aorta results in a complete loss of contact between the device and the wall during systole, which could lead to an endoleak and stent migration. 20% oversizing reaches the dacron enforced area limit (DEAL) during the pulse pressure and results in an effective zero-compliance in the latter portion of systole. Finally, we show that open surgical repair (OSR) results in a profound change

in both the HCR and LCR slope, where a near zero compliance is observed throughout the entire cardiac cycle.

## 7.1 Introduction

Aortic disease is responsible for 47,000 deaths annually in the United States and a mortality rate following rupture of over 90% (Zimmerman *et al.*, 2016; Kent, 2014). In cases of surgical intervention, the 30 day postoperative mortality rate can be as high as 53% for endovascular aortic repair (EVAR) (Hinchliffe *et al.*, 2006) and 48% for open surgical repair (OSR) (Greenberg *et al.*, 2008). Several adverse events and postoperative complications associated with compliance mismatch have been reported in the literature including thrombosis (Abbott *et al.*, 1987), false aneurysm formation (Mehigan *et al.*, 1985) and cardiovascular complications that result in death of the patient (Nauta *et al.*, 2017). To date, the effect of aortic repair techniques on the biomechanical behaviour of the aorta is not well understood.

In the case of EVAR a stent-graft (Nitinol frame and a polytetrafluoroethylene or woven polyester graft) is deployed intravascularly with the aim of (i) reducing of stress in an aorta/aneurysm wall, or (ii) preventing further propagation of an aortic dissection and removing the false lumen. In the case of OSR the diseased section of the aorta is removed and replaced with a synthetic prosthetic vessel. The graft, generally fabricated from polyethylene terephthalate or Dacron, comprises of tightly woven or knitted fibres with high tensile strength (Sarkar *et al.*, 2006) and is sutured (proximally and distally) to the remaining native aortic tissue.

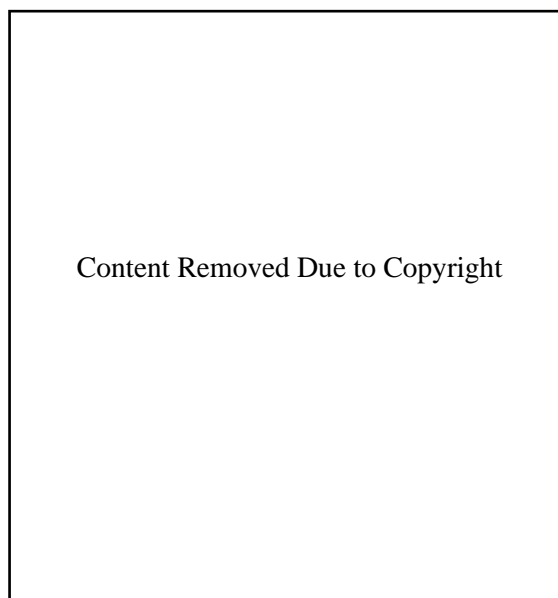


**Figure 7.1: Available treatment options for aortic disease. (A, B) Endovascular Aortic Repair (EVAR); (C, D) Open Surgical Repair (OSR). (A) shows a schematic of the EVAR procedure where a stent-graft is deployed intravascularly to the disease site (Figuroa and Zarins, 2011). (B) Postoperative CT scan showing proximal aortic and distal aortic stents (Sultan and Hynes, 2014). (C) shows a schematic of the OSR procedure where the healthy aorta proximal and distal to the diseased site are clamped, the diseased portion is cut open and a synthetic graft is sutured into the native vessels proximally and distally (Figuroa and Zarins, 2011). (D) Perioperative image of OSR of infrarenal aorta with Dacron graft (Baila *et al.*, 2016).**

It has not been established whether EVAR or OSR is the superior treatment option for patients with aortic aneurysm or dissection. A meta-analysis of 42 non-randomised studies evaluating EVAR versus OSR for descending thoracic aortic disease reported no significant difference between intervention groups in relation to stroke, reintervention and mortality beyond 12 months (Cheng *et al.*, 2010). A multi-centre prospective study comparing EVAR to OSR for a cohort of 341 thoracoabdominal aortic aneurysm patients and found no statistical difference between groups in relation to 30-day mortality or paraplegia (Tshomba *et al.*, 2017). Most recently, a study by Salata *et al.*, (2019) reports no statistically significant difference between outcomes after EVAR and OSR to repair abdominal aortic aneurysms in long-term mortality during more than 13 years of follow-up.

Experimental flat-plate compression and radial crimping of commercially available grafts has been reported by De Bock *et al.* (2013). Biaxial tension tests of graft materials demonstrate that stent-grafts are up to 25 times stiffer than the healthy aorta (Tremblay *et al.*, 2009). Pressure inflation tests also reveal that Dacron is significantly stiffer circumferentially than native aortic tissue (Ferrari *et al.*, 2019), while Bustos & Celentano, (2016) report a circumferential strain of less than 3% for dacron grafts subjected to a pressure of 240 mmHg. Singh & Wang, (2015) suggest that current commercially available stent-grafts act as a rigid non-distensible conduit and fail to replicate the natural deformation of the aorta.

This chapter presents a computational investigation of the effects of EVAR and OSR on the biomechanical behaviour of the aorta. The subject-specific MRI/FEA aortic model generated in Chapter 6, including elastin pre-strain, SMC contractility and collagen strain stiffening, is used as a platform to assess the alterations in the pressure-lumen area relationship due to clinical intervention. The study uncovers a number of fundamentally important, and previously unreported, insights that should be of critical concern for device design and clinical practice. Our simulations reveal that deployment of the stent-graft deforms the artery into a post-implantation equilibrium configuration with an expanded circumference. In this expanded configuration our model predicts that collagen is stretched beyond its transition strain (i.e. it is in a straightened high stiffness state) for the entirety of the cardiac cycle. Therefore the high compliance regime exhibited by the native aorta during diastole is eliminated by EVAR device deployment and the low-compliance systolic compliance occurs at all physiological pressures. Importantly, the device itself does not contribute to the vessel compliance because following deployment it operates on the near-zero stiffness nitinol unloading plateau. It merely stretches the artery, resulting in collagen strain stiffening during diastole. Similarly, we uncover that oversizing an EVAR device by 20%, 40% and 60% results in similar pressure-area curves, with all devices operating on the nitinol unloading plateau throughout the cardiac cycle following deployment. This result suggests that significantly over-sizing a device does not significantly affect the post-deployment effective compliance, while under-sizing a device can result in loss of contact with the vessel during systole, potentially leading to catastrophic failure due to device migration or endo-leaks. Finally, we show that open surgical repair results

in a dramatic change in aortic biomechanical behaviour, resulting in effective zero-compliance behaviour throughout the entire cardiac cycle.

## 7.2 Model Development

### 7.2.1 Mechanical behaviour of Aortic Stent-Grafts

*Homogenised effective Stent Membrane (ESM) modelling approach:* Owing to the considerable computational cost of modelling full stent geometries, we begin this study by assessing the feasibility of using a homogenised Stent-Graft (SG) model that can be calibrated such that the radial force (RF) versus displacement (U) relationship is identical to that of a full stent model. Firstly, we simulate the crimp and deploy of a commercially available SG ring and record the RF-U relationship (Figure 7.2(a)). A nitinol-type constitutive law is implemented in a user material subroutine (UMAT) so that the following features of a full device are accurately replicated: initial high stiffness regime during loading; the low-stiffness loading plateau; the initial unloading regime; the low stiffness unloading plateau. Details of this homogenised device model are provided in Appendix D, and the effective material properties are presented in Table 7.1. For the remainder of this chapter we refer to this homogenised device modelling approach as the Effective Stent Membrane (ESM).

*Identifying the reference stress-free device configuration:* Removal of the stitching which ties the Nitinol frame to the graft material reveals that the stent is not in a stress-free configuration when attached to a fully expanded dacron graft. Rather, removal of the graft results in a 24% increase in the effective diameter of the stent-ring (Figure 7.2(b)). This expanded nitinol stent geometry is taken to be the stress-free reference configuration of the stent. To accurately simulate such devices, it is important to base all calculations on this stress-free reference state. The device diameter indicated in the product catalogues is not the stress-free configuration; rather, it is the diameter that is enforced by the stiff graft material to which the stent is stitched. Throughout this chapter we refer to this configuration as the Dacron Enforced Area Limit (DEAL) or the Dacron Enforced Diameter Limit (DEDL).

The graft material only contributes mechanically once the DEAL is reached; during the crimp and deployment (up until the DEAL is reached) the graft is in a wrinkled/buckled state between the stent struts. The purpose of the graft in the case of aortic aneurysm/dissection repair is to relieve the stress from the arterial wall due to blood pressure. Due to the extremely high stiffness of the graft material (2.9 GPa (Santos *et al.*, 2012)), negligible axial deformation is incurred over the crimp/deploy step and hence we prescribe an effective device Poisson's ratio of zero to the ESM. A cylindrical orientation defines the circumferential, axial and normal direction of each M3D4 membrane element.

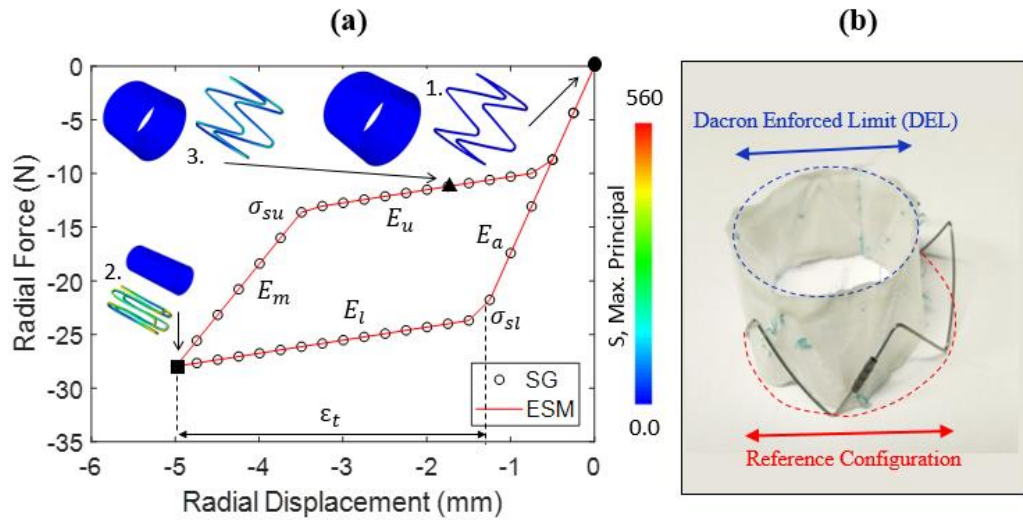


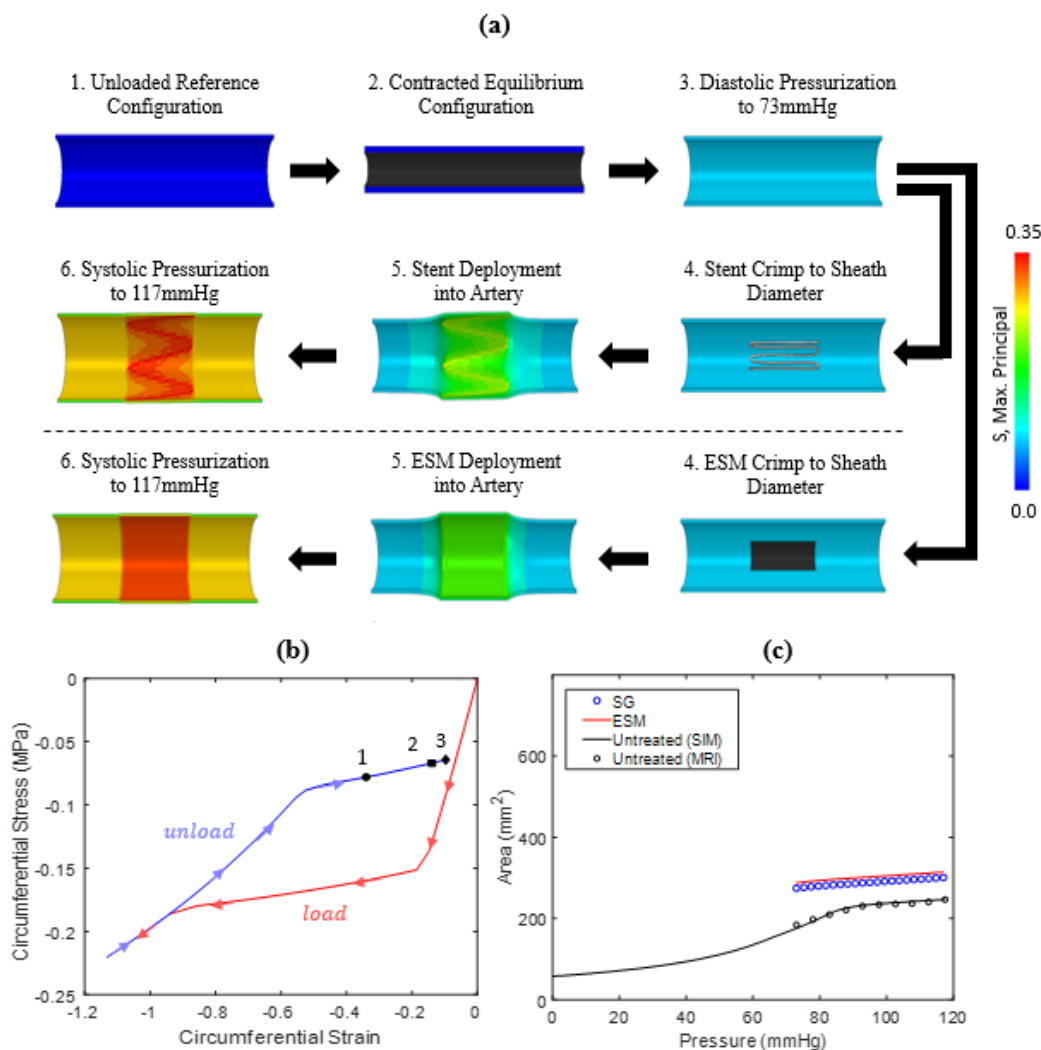
Figure 7.2: (a) Computational approach to modelling a BRANDNMAE aortic stent-graft, where the RF-U response of the stent-graft (SG) is fit using the Effective Stent Membrane (ESM) model. The ESM model results in an identical RF-U response throughout the crimp and deployment steps. The reference configuration (1.) (circle) is the configuration of the stent once it has been removed from the Dacron graft. Both the SG and ESM are then crimped to the internal diameter of the delivery sheath (2.) (square). During the deployment step, the implant expands until the Dacron Enforced Area Limit (DEAL) is reached, after which the implant has essentially a zero-compliance due to the stiffness of the Dacron. (b) By removing the stitches that attach the NiTi stent rings to the graft material we can observe that the diameter of the stent expands by a further 24%, to the true stress-free reference configuration. In-vivo, the DEAL prevents the implant from returning to this reference configuration.

Table 7.1: Parameters for ESM model. Each parameter is outlined in the schematic shown in Figure 7.2(a).

Parameter	Description
$E_a$	Austenite Elasticity
$E_m$	Martensite Elasticity
$E_l$	Transformation Loading Elasticity
$E_u$	Transformation Unloading Elasticity
$\sigma_{sl}$	Start of Transformation Loading
$\sigma_{su}$	Start of Transformation Unloading
$\epsilon_t$	Transformation Strain

### 7.2.2 Comparison of ESM and Stent-Graft on Artery Compliance

The solution procedure for the FE simulations is as follows. As described in Chapter 6, the equilibrium zero-pressure configuration due to elastin pre-stretch and smooth muscle cell (SMC) contractility is computed. The internal lumen surface is then loaded to a diastolic pressure of 73mmHg. The SG and ESM are then crimped to the internal diameter of the delivery sheath. Deployment of the SG and ESM is simulated by simply removing the crimp boundary condition. As the implant expands it comes into contact with the vessel wall, leading to a further increase in the vessel diameter until an equilibrium deployed configuration is achieved, whereby the outwards radial force of the device and the lumen pressure is in equilibrium with the inwards force due to the circumferential tensile stress in the stretched contractile artery wall. Finally, the lumen pressure is increased to the systolic value of 117 mmHg. As shown in Figure 7.3, results for the SG and ESM models are compared in terms of the max. Principal stress ( $S$ ) distribution in the artery wall, and in terms of the pressure-area relationship post-deployment. The ESM simulation exhibits an approximately uniform distribution of stress in the peri-implant artery wall. The SG simulation exhibits a similar stress state, but with higher stress concentrations in the regions where the struts directly contact the artery. The pressure-area curves computed for the SG and ESM are extremely similar. Both models predict that the lumen area is ~53% higher than the untreated artery at diastolic pressure, and ~24% higher than the untreated artery at peak systolic pressure. This indicates that the ESM model provides sufficient accuracy for assessment of a device induced compliance alteration. However, the ESM approach does not provide a detailed description of stress concentrations in the vessel wall due to complex geometries of stent struts. It should be noted, that in the open-cell stent design considered here, a low percentage of the overall device area consists of stent struts, generating high concentrations of stress in the regions of strut-vessel contact. In contrast, braided stent designs, or close-cell designs, such as those shown in Figure 7.1(a, b) are commonly used for aortic repair. The high area fraction of strut coverage for such designs suggests that the ESM modelling strategy will provide a very accurate description of the stress distribution in the vessel wall, in addition to accurately predicting of the effective vessel compliance.



**Figure 7.3:** (a) Flowchart for solution procedure. (1.) The unloaded reference configuration of the artery. (2.) The contractile elements within the arterial wall result in a reduction in area and a new equilibrium configuration. (3.) Diastolic pressure of 73 mmHg is applied to the internal lumen surface. (4.) The SG/ESM is crimped to the inner sheath diameter of the delivery device. (5.) The SG/ESM is deployed into the artery, which remains under the diastolic pressure load, and a new equilibrium area is reached. (6.) The system is pressurised with a pulse pressure to bring the total applied lumen pressure to 117 mmHg. (b) Circumferential Stress versus strain plot for the ESM model shows that the device come in contact with the arterial wall at (1) along the ‘unloading plateau’, which results in an increase in the diastolic equilibrium area (2). By applying the pulse pressure, the NiTi behaviour follows the high compliance stiffness of the unloading plateau, which is significantly less than the LCR stiffness of the aorta. (c) Both models (ESM and SG) predict that the lumen area is ~53% higher than the untreated artery at diastolic pressure, and ~24% higher than the untreated artery at peak systolic pressure. As the effective compliance of the implant is negligible compared to the high stiffness of the low compliance regime (LCR) of the aorta, a similar slope is observed in the pressure-area relationship between the untreated LCR and the area increase due to the pressure pulse post-implantation.

Both the SG and the ESM models predict that the characteristic bi-linear shape of the pressure-area of the untreated aorta is eliminated following to deployment of the device. Instead, a linear pressure-area curve is obtained following device deployment, the slope of which is similar to the slope of the low compliance regime (LCR) of the untreated artery in the systole pressure range. Analyses reveal that the primary effect

of deployment of the nitinol stent is to expand the artery so that collagen fibres are in the high stiffness regime throughout the entire cardiac cycle. The fact that the device does not significantly alter the pressure-area slope from the native LCR slope can be explained by considering the circumferential stress-strain path computed during the crimp-deployment history of the device, as shown in Figure 7.3(b). As the device is deployed (from its crimped state) it initially reduces its strain at a high modulus (the value of which is primarily governed by the martensite modulus of the NiTi stent). However, when the device reaches its equilibrium configuration at the diastolic pressure it deforms along the “unloading plateau”, which has an extremely low effective circumferential tangent stiffness of  $\sim 0.07$  MPa. The device unloading profile remains on this plateau up to the point of maximum systolic pressure. Given that the effective tangent modulus of the artery in the LCR is  $\sim 1$  MPa, the insertion of the device does not significantly change the effective compliance from the native vessel LCR. Rather, the only significant effect of the device is elimination of the native vessel high compliance regime (HCR) during diastole. Once again, we emphasize that this occurs simply because the device stretches the collagen in the vessel wall into a high stiffness regime for the entire cardiac cycle. The stiffness of the device becomes significant only if the DEAL is reached during physiological loading, in which case the device becomes extremely stiff compared to the native vessel, and the effective compliance of the treated section becomes zero for part of the cardiac cycle. In Section 7.2.3 below we investigate the critical issue of device over-sizing and the selection of an appropriate DEAL.

In Figure 7.4 we present a comparison of the SG and ESM models deployed in a subject-specific FE model of the aorta. In this case a longer stent graft, consisting of four stent rings, is considered. Figure 7.4(a, c) shows the max. Principal logarithmic stress ( $S$ ) plotted along the aorta for both the SG and ESM simulations, respectively. The ESM model provides a reasonable approximation of the stress state in the vessel wall, compared to the SG model. Once again, as shown in Figure 7.3(c), both devices provide similar predictions of the altered pressure-area relationship following implantation. As was the case in the idealised cylinder models described above, the device is found to stretch the subject-specific artery wall in the circumferential direction so that the collagen is stretched beyond the transition strain ( $\epsilon_t$ ) at all times during the cardiac cycle. This results in the elimination of the HCR of the pressure-area curve. Once again, the effective compliance of the stented section is extremely similar to that of the native vessel during systole because the device follows the relatively low unloading plateau during the increase of the lumen pressure from diastole to systole. The comparisons presented in Figures 7.3 and 7.4 suggest that the ESM modelling approach provides a reasonable approximation to the predicted behaviour of a full stent model – even for the low density open-cell geometry considered here.

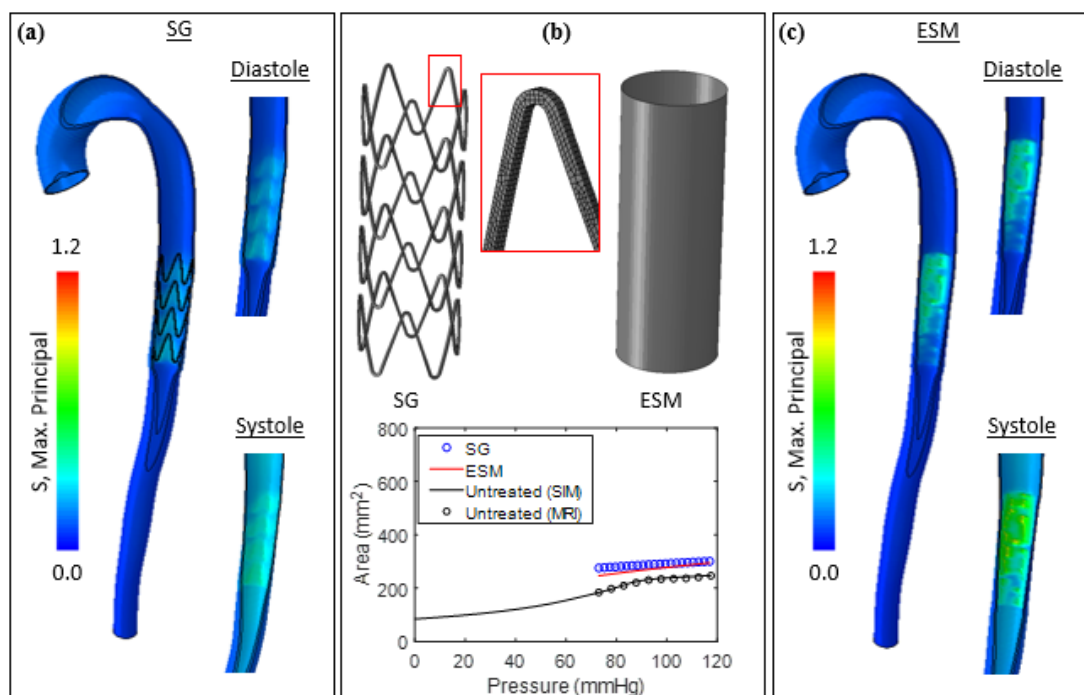


**Figure 7.4: Comparison of SG and ESM models in a subject-specific aorta. (a) Deployment of the SG results in stress concentrations in the regions where the struts directly contact the artery wall. (b) Both the SG and ESM models show a similar prediction of the implant induced compliance alteration on the pressure-area relationship. (c) The ESM simulation exhibits more uniform distribution of stress in the peri-implant artery wall, however the level of stress is similar to that of the SG model.**

### 7.2.3 Effect of Implant Oversizing and Positioning on Compliance

We next use the validated ESM modelling approach to investigate the influence of device over-sizing, device positioning, and native vessel stiffness on the post-implantation changes in the aortic pressure-area relationship.

*Influence of Oversizing – Model development:* The effect of EVAR device over-sizing on the pressure-area relationship at Plane 6 (mid descending thoracic aorta) is investigated using the subject-specific aortic model. Clinical guidelines recommend 10-20% oversizing for aortic stent-grafts (van Prehn *et al.*, 2009; Sher and Tadros, 2017). Here we consider three device designs in which the Dacron enforced diameter limit (DEDL) exceeds the diastolic vessel diameter by 20%, 40% and 60%, as illustrated in Figure 7.5. Based on commercially available designs, in all cases the diameter of the stent stress-free configuration is taken to be 24% greater than the dacron graft (i.e. the DEDL). Table 7.2 shows the diameter of the stress-free stent configuration, the DEDL and the crimped diameter for the three device designs under consideration. The crimp diameter is based on the use of a standard commercially available 22F delivery system (Ramanan *et al.*, 2015). In all cases the crimped device is deployed at Section 6 of the subject-specific aortic model, where the vessel diameter is 184 mm at the diastolic pressure of 73 mmHg and 247 mm at the peak systolic pressure of 117 mmHg. For each of the three stent designs, FE simulations of crimping and deployment are performed to determine the RF-U relationship. Corresponding

ESM models are then calibrated to replicate the stent RF-U relationship and deployed in the subject-specific artery.

**Table 7.2: Geometrical parameters for the 20%, 40% and 60% oversized implants.**

	Reference Configuration Diameter (mm)	DEDL (mm)	Crimp Diameter (mm)	Post- Operative Diastolic Area (mm <sup>2</sup> )	Post- Operative Systolic Area (mm <sup>2</sup> )
20%	22.8	18.4	7.1	248	273
40%	26.6	21.4	7.1	250	275
60%	30.4	24.5	7.1	252	276

*Influence of Oversizing – Results:* Figure 7.6(a) shows the post-implantation pressure-area curves at Section-6 of the subject-specific aorta for the 20%, 40% and 60% oversized devices. The DEAL for each case is also indicated on the figure. Nearly identical pressure-area curves are computed for all three designs, the only difference being that the 20% design reaches the DEAL at a pressure of 93 mmHg, after which the compliance is effectively zero. Post-implantation areas at the start of diastole and end of systole are listed in Table 7.2 for all three devices. The finding that the biomechanical outcome is essentially independent of the degree of device oversizing can be understood by considering the device effective circumferential stress-strain history during crimping and deployment, as shown in Figure 7.6(d). While the 60% oversized device reaches the highest compressive strain during crimping, as expected, all three devices are compressed to a strain that extends beyond the loading plateau. Therefore, all three devices follow the same unloading curve during deployment in the vessel. Furthermore, at the new diastolic equilibrium state, all three devices have reached the unloading plateau. Therefore, while the device diastolic strain is sensitive to the degree of oversizing (i.e. position along unloading curve), the circumferential stress of each device is similar, so therefore the effective radial force and the diastolic vessel diameter is similar for all three cases. Finally, all three devices remain on the unloading plateau as the pressure is increased to the end-systolic value. Therefore, the effective stiffness of the device is extremely low compared to the vessel, and the slope of the pressure-area curve throughout the cardiac cycle is essentially equal to the native vessel LCR slope for all three device designs.

The influence of the DEAL should be considered. As described above, the 20% oversized device reaches the DEAL at a lumen pressure of 93 mmHg, so the device becomes infinitely stiff and the vessel area remains constant as the pressure is increased to the end-systolic value (i.e. the compliance is zero in this regime). We recommend that the device should be sufficiently oversized so that the DEAL is not reached during physiological loading and a zero-compliance regime does not occur, as is the case for the 40% and 60% oversized devices. Excessive oversizing (>60%) may have two negative drawbacks; (i) the device may not reach the unloading plateau when deployed, in which case it will exhibit a higher tangent stiffness and the effective vessel compliance will be lower than the native LCR; (ii) the device may not fit in a standard delivery catheter, or it may fracture during crimping. However, insufficient oversizing may be catastrophic. As an example, we illustrate in Figure 7.6 that the DEAL associated with a 10% oversized device is lower than the lumen area during systole. This presents a significant risk of endoleak and device migration.

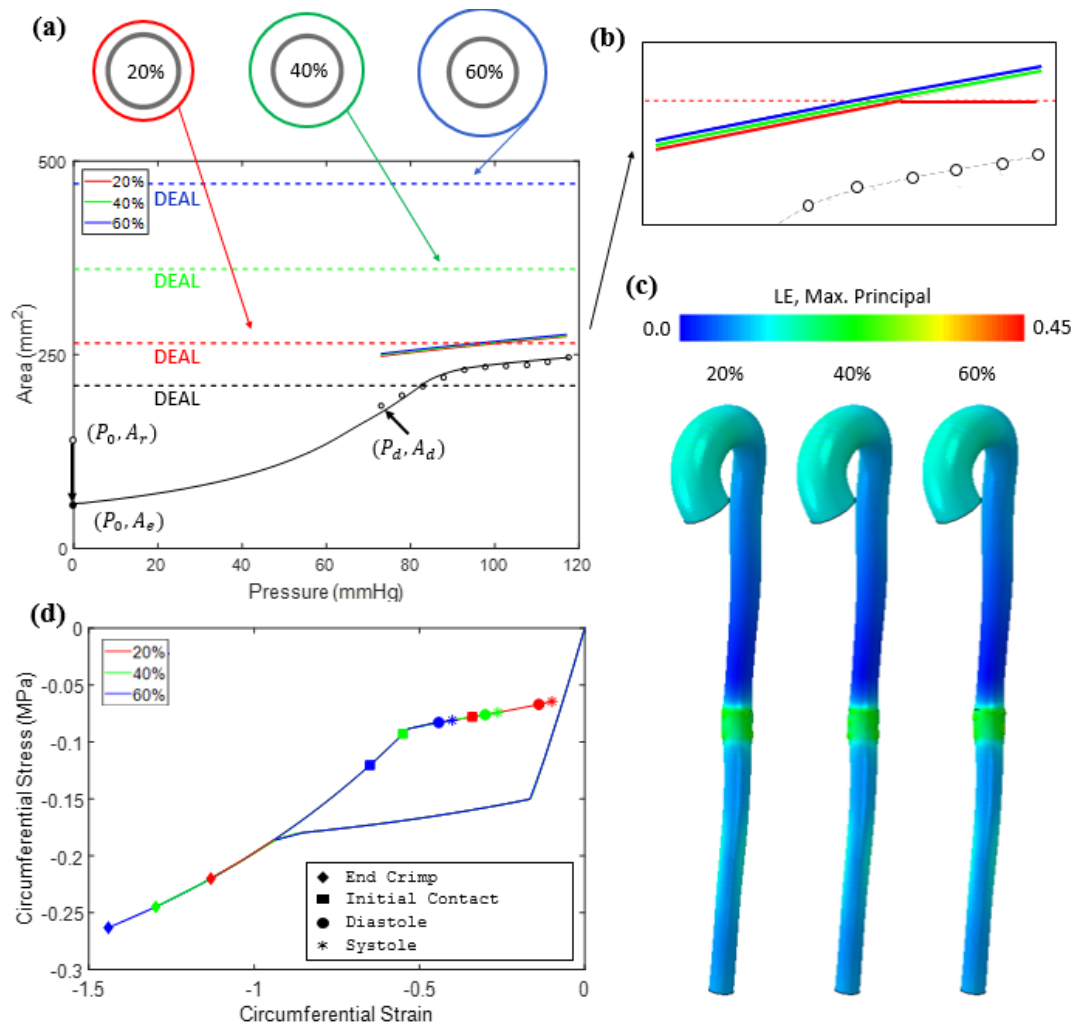


**Figure 7.6:** (a) The effects of ESM oversizing on the pressure-area relationship in Plane 6 of the human aorta. In each case the 20% (red), 40% (green) and 60% (blue) oversizing results in any area gain due to pulse pressure to follow the secondary stiffness slope of the aorta. (b) In the case of 20% oversizing, the DEAL is indicated by the dashed red line, below which the pressure-area response follows the secondary stiffness of the aorta. Once the DEAL is reached no further area gain is incurred for any further increase in pressure (as indicated by the change in slope of solid red line at ~93 mmHg). (c) Finite element contour plot of max. Principal logarithmic strain (LE), highlighting similar strain levels at the deployment site for each degree of oversizing. This can be explained by considering the device effective circumferential stress-strain history during crimping and deployment (d). In each case the diastolic equilibrium configuration lies on the unloading plateau where the stiffness of the nitinol is negligible compared to that of the secondary stiffness of the native aorta. With the application of the pulse pressure, each degree of oversizing remains on the unloading plateau and therefore exert approximately the same radial force on the arterial wall.

Figure 7.7 shows the effect of implant deployment on the pressure-area relationship in the human aorta proximally (7(a)) versus distally (7(b)). At the proximal section the effective compliance of the vessel post-implantation is similar to the LCR of the native vessel. It should be noted that the native vessel at this proximal section is the most compliant in the aorta. Therefore, the elimination of the extremely high compliance diastolic regime following device implantation results in a significant reduction in lumen area change during a cardiac cycle ( $\Delta A = 202 \text{ mm}^2$  for the native vessel, versus

$\Delta A=28 \text{ mm}^2$  post-implantation, representing an 86% reduction). Simulations also reveal the critical importance of device oversizing in highly compliant proximal sections: As shown in Figure 7.7, the DEAL for a 20% oversized device is lower than the end-systolic area of the native vessel, indicating a high risk of endoleak and migration. A 40% oversizing is required for this compliant proximal section.

Figure 7.7(b) shows the simulated behaviour for the distal section of the aorta. The compliance of the native vessel at this section is the lowest in the aorta. In this case a 20% oversized device does not reach the DEAL and the stented vessel exhibits a compliance similar in value to the native LCR for the entire duration of the cardiac cycle. In this case the reduction in area change during the cardiac cycle is not as significant as the effect proximally ( $\Delta A=38 \text{ mm}^2$  for the native vessel, versus  $\Delta A = 13 \text{ mm}^2$  post-implantation, representing an 65% reduction).

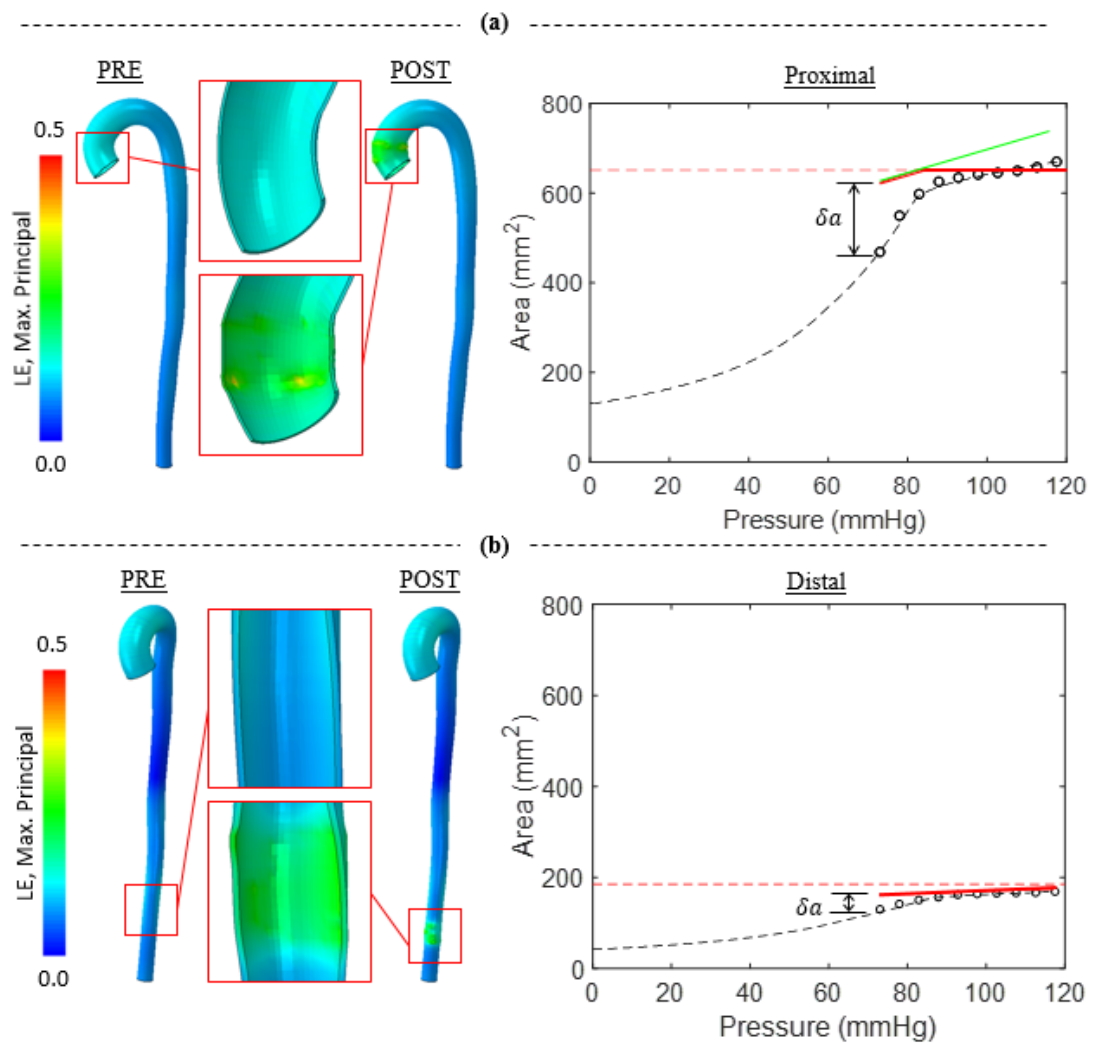
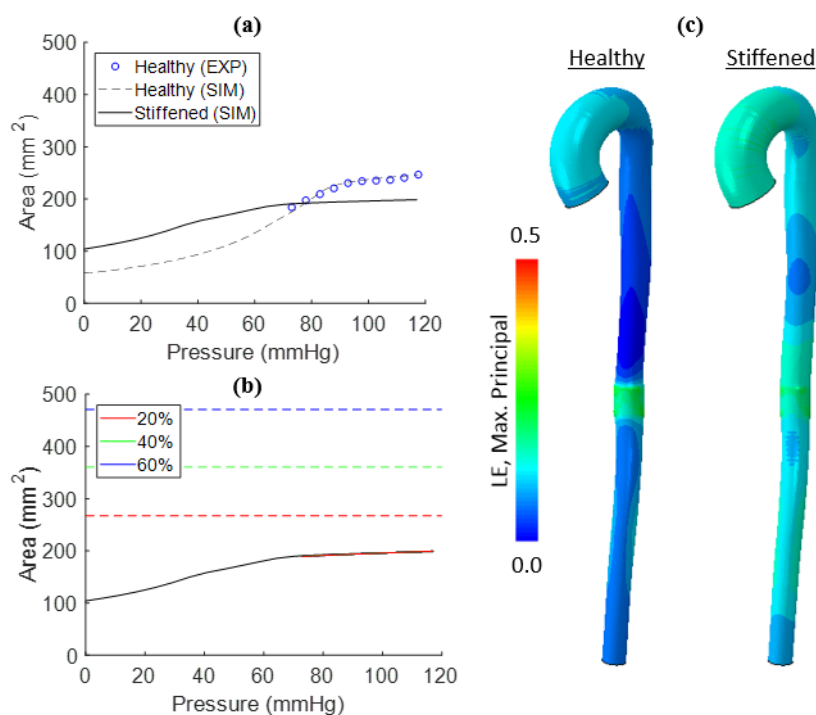


Figure 7.7: 20% oversized stent-graft in the (a) proximal aorta (Plane 2) and (b) distal aorta (Plane 9). Pre-operative pressure-area relationship is indicated by open circles and dashed line (fitted). Dotted line indicates the DEAL when the stent-graft is fully expanded, and no further area increase can be incurred for a given increase in pressure.

The relationship between vessel compliance and device design is further elucidated in Figure 7.8, in which we simulate age related arteriosclerotic stiffening of the aorta by reducing the volume fraction of elastin by 10% throughout the entire vessel (see equation 6.04 in our constitutive law in Chapter 6), based on the histological study of Hosoda *et al.*, (1984). We also reduce the transition strain at which collagen stiffening occurs (see equation 6.03 in our constitutive law in Chapter 6), based on reported biomechanical testing of aged and young aortic tissue (Vande Geest & Vorp, 2004). The stiffened aortic pressure-area relationship for Plane 6 is shown in Figure 7.8(a). Compared to a healthy young tissue the arteriosclerotic aorta does not exhibit a bi-linear pressure-area curve under the physiological range of lumen pressure due to the reduction of the collagen transition strain, i.e. an LCR-type regime occurs throughout the entire cardiac cycle. The reduction of elastin also increases the zero-pressure reference area, further adding to the linear shape of the pressure-area curve and the overall reduction in vessel compliance. For such a stiffened artery, the insertion of a stent-graft does not significantly alter the pressure-area curve of the vessel. The stiff vessel is already in the high stiffness collagen regime, so the area change and compliance change effected by device insertion is negligible, again because the deployed devices operate on the unloading plateau of the RF-U curve. In this case a 20% over-sizing is sufficient as the DEAL is not reached during the cardiac cycle.



**Figure 7.8:** (a) Healthy pressure-area relationship for Plane 6 as indicated by blue open circles, and FE fit (dashed black line) compared to Stiffened (solid black line). The stiffened aortic properties were achieved by reducing both the elastin volume fraction within the wall and the transition strain. (b) The effect of implant oversizing on the pressure-area relationship in a Stiffened aorta. 20%, 40% and 60% oversizing are indicated by the solid red, green and blue lines respectively. The DIAL for each percentage oversizing is indicated by the dashed red, green and blue lines respectively. (c) Finite element mesh of subject-specific aorta comparing healthy and pathologically stiffened properties in terms of max. Principal logarithmic strain (LE).

### 7.2.4 Investigation of Open Surgical Repair on Vessel Compliance

Finally, we investigate the effect of OSR on the biomechanics of the human aorta. Computationally, this is achieved by assigning separate material properties pertaining to a commercially available Dacron graft to a portion of ‘diseased’ aortic elements between the spinal levels of T11 and L2. The modulus of elasticity of Dacron was set as 1000 MPa and the material was assigned a Poisson’s ratio of 0.2 (Demanget & Favre, 2013). The thickness of the Dacron prosthesis was chosen to be the same as the wall thickness of the aorta, 1mm, (Gawenda *et al.*, 2003). Plane 6 and Plane 7 are within the bounds of the Dacron segment, while all other planes are assigned healthy fitted material parameters (Figure 7.9).

Figure 7.9 shows the deformation of the aorta throughout the cardiac cycle for an aorta that has undergone a segmental replacement with a Dacron prosthesis. The figure highlights the increased stiffness of the Dacron relative to the native aortic material properties, where the replaced segment incurs a negligible increase in max. Principal logarithmic strain (LE) with the application of the pulse pressure between diastole and systole. Figure 7.9(b) shows the pressure-area plot for a series of planes along the aorta analysed previously in Chapter 6. In Segments 6 and 7, the effect of the Dacron is evident in the effective-zero-compliance pressure-area relationship.

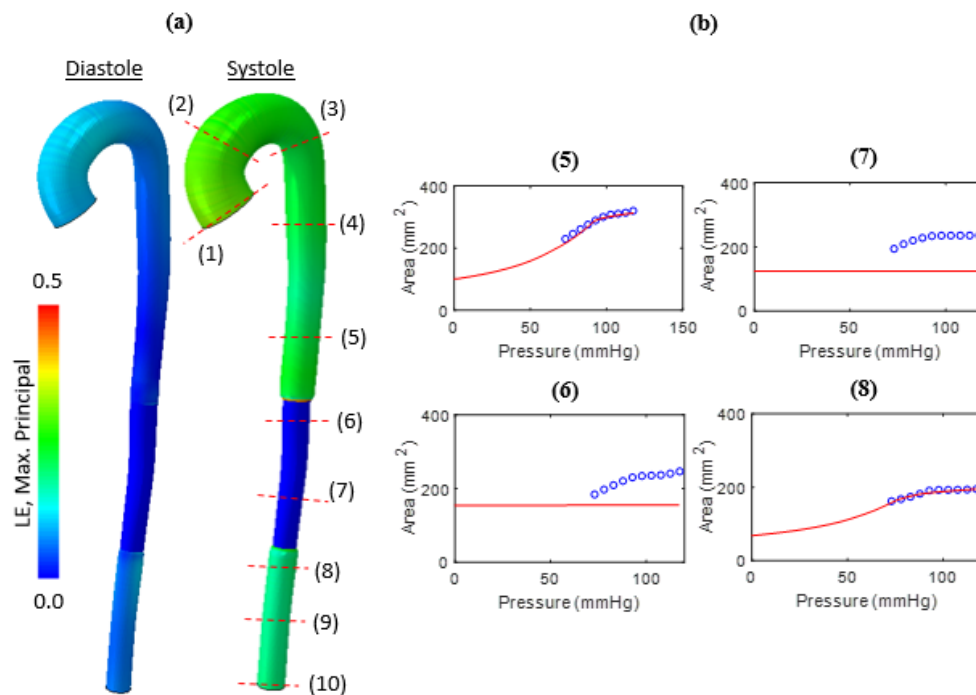


**Figure 7.9:** (a) Max. Principal logarithmic strain (LE) along the aorta at diastolic and systolic pressures following OSR of the aorta. When the segment between T11 and L2 is replaced with Dacron, the strain is significantly reduced compared to that which is observed in-vivo. (b) The area versus pressure curves for a series of locations along the aortic length adjacent to the Dacron region. When Segments 6 and 7 are replaced by Dacron the aorta exhibits an effective-zero-compliance pressure-area relationship between diastole and systole.

### 7.3 Discussion

This study presents a computational analysis of the influence of Nitinol based devices on the biomechanical performance of the aorta. Specifically, the influence of device implantation on the pressure-area curve of the vessel is analysed. The study uncovers a number of fundamentally important, and previously unreported, insights that should be of critical concern for device design and clinical practice.

- (i) The Nitinol stent-graft device expands the artery wall into a new equilibrium configuration which exceeds the transition strain of the vessel, meaning that the artery is now in the low compliance regime (LCR) where the high-stiffness of straightened collagen fibers governs the mechanical behaviour of the wall, and the high-compliance regime (HCR) at diastolic pressure is eliminated.
- (ii) The stent-graft unloads from the crimped configuration during deployment and operates along the unloading plateau between diastole and systole. The direct effective stiffness of the implant is negligible compared to the high stiffness of the artery wall in the LCR. As a result, the pressure-area relationship post-stenting between diastole and systole follows that of the local LCR slope of the aorta.
- (iii) Provided the Nitinol device increases its diameter sufficiently during deployment so that it reaches the unloading plateau, the degree of oversizing has a negligible effect on the pressure-area response of the vessel. Each oversized device considered in this study is found to exert approximately the same radial force because all devices reach the unloading plateau. Additionally, the radial compliance (the slope of the radial force-displacement curve) on the unloading plateau is negligible compared to the LCR slope of the native artery.
- (iv) We show that 10% oversizing based on the observed diastolic diameter in the mid descending thoracic aorta results in a complete loss of contact between the device and the wall during systole, which could lead to an endoleak and stent migration. 20% oversizing reaches the dacron enforced area limit (DEAL) during the pulse pressure and results in an effective zero-compliance in latter portion of systole. Furthermore, our study suggests that oversizing is more important proximally, while stiffer distal vessels do not require as much oversizing.
- (v) The implanted section follows the local LCR slope for the entire cardiac cycle, and as a result the effective compliance change in diastole is more pronounced in proximal sections where the difference between the HCR and LCR of the native vessel is greatest.
- (vi) Device deployment in a pathologically stiffened artery (in which the collagen content is increased and elastin content is decreased) does not strongly alter the lumen pressure-area curve. Furthermore, oversizing of the device has a negligible effect on the lumen pressure-area curve.

- (vii) Open surgical repair (OSR) results in a profound change in both the HCR and LCR slope, where a near zero compliance is observed throughout the entire cardiac cycle.

Following EVAR, the Nitinol implant expands the artery wall into a new equilibrium configuration whereby the outwards radial force of the device and the lumen pressure is in equilibrium with the inwards force due to the circumferential tensile stress in the stretched contractile artery wall. In this configuration, whereby the circumferential strain of the vessel wall exceeds the collagen transition strain, the artery operates in the low compliance regime (LCR) throughout the entire cardiac cycle. The high stiffness of the stretched/straightened collagen fibers governs the mechanical behaviour of the wall in both diastole and systole. Furthermore, as the implant unloads from the crimped configuration during the deployment step it operates along the unloading plateau between diastole and systole, and therefore the direct effective stiffness of the implant is negligible compared to the high stiffness of the artery wall in the LCR. As a result, the pressure-area relationship between diastole and systole follows that of the local LCR slope of the aorta. The deployment of the device merely expands the vessel diameter so that collagen in the vessel wall is in the high stiffness regime throughout the cardiac cycle and the compliance of the vessel itself is decreased during diastole. Several studies, both *in-vivo* and *in-vitro* report that the deployment of self-expanding stent-grafts reduces aortic wall compliance (Back *et al.*, 1994; Vernhet *et al.*, 2001; Morris *et al.*, 2016; Nauta *et al.*, 2017). However, to the author's knowledge, this study is the first to report the fundamental mechanism by which this occurs, and the first to report that device deployment alters the compliance only at low pressures during diastole.

Clinical guidelines recommend 10-20% oversizing for aortic stent-grafts based on the vessel diameter (van Prehn *et al.*, 2009; Sher and Tadros, 2017). However, we show in Chapter 5 that in the native aorta exhibits an area change between 15 and 65% from the start of systole to the end of systole. Other studies report similar levels of *in-vivo* area change during a cardiac cycle (Sonesson *et al.*, 1994; Sugitani *et al.*, 2012; Ferruzzi & Humphrey, 2013; Kim *et al.*, 2019) providing substantial evidence that clinicians cannot be certain that a 10% oversized device will maintain contact with the aortic wall throughout the entire cardiac cycle. Further uncertainty is introduced through the routine use of non-cardiac-gated imaging modalities for preoperative planning and device sizing, in that it is not known whether the pre-intervention imaging of the vessel shows the configuration at the start of diastole or at the end of systole, or at an unknown intermediate lumen pressure.

Provided the Nitinol device increases its diameter sufficiently during deployment to reach the unloading plateau, the degree of oversizing has a negligible effect on the pressure-area response of the vessel. Approximately the same radial force is generated by each device, provided that the unloading plateau is reached. Furthermore, the radial compliance (the slope of the radial force-displacement curve) on the unloading plateau is negligible compared to the LCR slope of the native artery, therefore the

device itself does not significantly contribute to the overall compliance of the section. Rather, the device merely stretches the collagen in the vessel wall into a straightened stiff configuration, thus eliminating the HCR associated with wavy collagen in diastole. Our study provides an explanation for the observations of an experimental study by Nauta *et al.*, (2017), where porcine aortae were connected to a mock circulatory loop and the radial strain was recorded following the deployment of three oversized stent-grafts (0-10%, 10-20%, and 20-30%). Experiments reveal that the device oversizing does not significantly affect the vessel radial strain.

Insufficient device oversizing has catastrophic consequences including device migration and endoleak, resulting in pulsation, dilation and rupture of the aneurysmal wall (Chuter, 2002). We show that 10% oversizing based on the observed diastolic diameter in the mid descending thoracic aorta results in a complete loss of contact between the device and the wall during systole. Our study suggests that significant oversizing is critical in proximally regions where the compliance of the native vessel is highest. Our findings are supported by the results of a clinical trial conducted by Donas *et al.*, (2019) who found that patients who received stent-grafts that were oversized by 14-20% had higher incidences of Type 1a (proximal) endoleaks requiring reintervention than patients that were oversized by 22-30%. Furthermore, the Eurostar data reports that the rate of endoleak decreases as the degree of oversizing increases from 0-20%, after which it is reported to plateau (Chuter, 2002). Our study suggests that a higher plateau of oversizing (>20) is appropriate for vessel sections that exhibit higher compliance, e.g. cases where devices must be deployed in proximal sections, or cases where devices must be deployed in younger subjects.

To the best of the author's knowledge this is the first study to report the Dacron enforced area limit (DEAL), and its implications on vessel biomechanics. The role of the graft is to; (i) de-pressurize the aneurysm wall leading to a reduced risk of rupture; (ii) hold the stent rings together; and (iii) act as a conduit for blood and pressure transfer. When the device is being deployed, the graft itself does not contribute mechanically until the DEAL is reached due to it being in a crimped/buckled configuration which provides no outwards radial force. Once the DEAL is reached however, the high stiffness of the Dacron material (~3 GPa) results in an effective zero-compliance of the device, whereby negligible area increase will occur for a given pressure increase. Guan *et al.*, (2016) report no significant difference in the diameter change of Dacron stent-grafts between the mid-ring region (where the struts are sutured to the Dacron) and inter-ring region (space between two consecutive axial stent rings) when subjected to an internal pressure, indicating the Dacron material governs the mechanical response of the device once the DEAL is reached. Overall the authors report a 0.02 mm radial displacement is reported following the application of internal lumen pressures up to 150 mmHg. It is worth noting that there is no DEAL on braided stents, and the proposed ESM methodology should be extremely suitable for modelling such devices where the Nitinol is uniformly distributed throughout the device with a higher area fraction than the open-cell design chosen here. Owing to the extensive computational costs in modelling braided stents, the ESM method may

provide an alternative approach in clinical-based FE modelling of devices where speed of simulation is critical.

As described previously, following deployment the implanted section follows the behaviour of the local low compliance regime (LCR) during the entire cardiac cycle. As a result, the effective change in diastole following device deployment is more pronounced in proximal sections than in distal sections distally. This is the case simply because the difference between the HCR and LCR is found to be highest in proximal sections. This finding is supported by the experimental study of Nauta *et al.*, (2017). Furthermore, clinical studies report incidences of cardiac events in 34-45% of patients that undergo stenting of the thoracic aorta (Martín *et al.*, 2008; Bischoff *et al.*, 2016; Beach *et al.*, 2017; Conrad *et al.*, 2017). Such incidences are considerably lower in abdominally stented patients 6-12% (Blankensteijn *et al.*, 1998; Barakat *et al.*, 2015; Atti *et al.*, 2018; Dakour Aridi *et al.*, 2018). The findings of our computational investigation provides a explanation for such clinical outcomes by demonstrating that proximal device deployment results in a more pronounced change in effective compliance in diastole that is the case for distal device deployment.

Our results show that device deployment in pathologically stiffened arteriosclerotic arteries results in a less pronounced effect on the pressure-area curve than the healthy control case. Furthermore, oversizing has a negligible effect on the pressure-area curve as the baseline stiffness in the arteriosclerotic aorta is higher resulting in an almost identical diastolic equilibrium configuration following deployment. This result provides an explanation for the observation by Nauta *et al.*, (2017) that the radial strain is similar both pre- and post-stenting in a naturally stiffer abdominal aorta. Finally, we show that open surgical repair (OSR) of the aorta results in a profound change to the pressure-area relationship with a near zero-compliance throughout the entire cardiac cycle. This result is in agreement with the experimental work of Tai *et al.*, (2000), who subjected a Dacron conduit to pressure inflation in a mock flow circuit and found that the diameter of the conduit increased by only 1.8% over a pressure pulse of 70 mmHg.

Several experimental studies, in addition to clinical trials, show that stent-grafts increase the pulse wave velocity (PWV) of the aorta (Kadoglou *et al.*, 2012, 2014; Morris, Stefanov and McGloughlin, 2013; de Beaufort *et al.*, 2017; Van Noort *et al.*, 2018), which is an independent risk factor for cardiac failure (Ben-Shlomo *et al.*, 2014). Importantly, the Windkessel effect is diminished following stenting (Nauta *et al.*, 2017, Belz, 1995). Increased PWV has been directly linked to cardiac death via a complex cascade of increased pulse pressure (Benetos *et al.*, 1997), increased left-ventricular afterload and decreased coronary flow (Zacharoulis *et al.*, 2007; Spadaccio *et al.*, 2016), and ultimately left ventricular hypertrophy (Kim *et al.*, 1995; Morita *et al.*, 2002).

In this study, the effect of stent-graft deployment in the young healthy aorta is investigated, where mechanical properties of the vessel are calibrated from Chapters 5 and 6. We show that oversizing is critical, particularly in the compliant proximal aorta, which is of significant clinical relevance given the fact that young subjects (<

30 years of age) are often treated for various aortic pathologies including aneurysm and dissection (Yoneyama et al., 2019; Marder & White, 2012; Sörelus, 2016; Hountis & Bolos, 2009; Tiryakioglu et al., 2009; Abbaszadeh & Nikparvar, 2019). We also simulate an arteriosclerotic aorta (Figure 7.8) by reducing the elastin content and transition strain based on previous experimental studies (Hosoda et al., 1984; Vande Geest & Vorp, 2004). Our results suggest that oversizing is less critical in stiffer vessels as the DEAL is less likely to be reached. In each case, stenting does not alter the local LCR of the aorta, provided the new diastolic equilibrium point is along the unloading plateau.

This computational investigation provides new insights into the mechanisms by which nitinol stent grafts alter the native biomechanis of the aorta. Our findings reveal that the effective radial compliance of the device itself is not significant compared to the native vessel, provide the device diameter increases sufficiently during deployment to reach the unloading plateau. Rather, the device deployment stretches the vessel wall so that the high compliance regime during diastole is eliminated due to the stretching to the collagen to a straightened stiff configuration. Our simulations demonstrate that device over-sizing has a negligible effect on the vessel diameter and compliance post-implantation, and we highlight the significant issues associated with insufficient oversizing so that the device reaches the DEAL. The test-bed developed in this study can be used to design next-generation devices and to guide clinical intervention to that post-operative complications including device migration and cardiac mortality can be reduced.

## 7.4 Bibliography

- Abbaszadeh, S., Eslami, M. and Nikparvar, M. (2019) Aortic Dissection in an 11-Year-Old Boy: Case Report Abbaszadeh et al Case Report Aortic Dissection in an 11-Year-Old Boy: Case Report Aortic Dissection in an 11-Year-Old Boy: Case Report, *Iranian Heart Journal*.
- Abbott, W. M., Megerman, J., Hasson, J. E., L'Italien, G. and Warnock, D. F. (1987) 'Effect of compliance mismatch on vascular graft patency.', *Journal of vascular surgery*, 5(2), pp. 376–82. Available at: <http://www.ncbi.nlm.nih.gov/pubmed/3102762> (Accessed: 16 September 2019).
- Atti, V., Nalluri, N., Kumar, V., Tabet, R., Yandrapalli, S., Edla, S., Tripathi, A., Patel, N. J., Dave, M., Aronow, W. S., Basir, M. B., Davis, T. P., Drachman, D. E. and Bhatt, D. L. (2018) 'Frequency of 30-Day Readmission and Its Causes After Endovascular Aneurysm Intervention of Abdominal Aortic Aneurysm (from the Nationwide Readmission Database)', *The American Journal of Cardiology. Excerpta Medica*. doi: 10.1016/J.AMJCARD.2018.12.006.
- Back, M., Kopchok, G., Mueller, M., Cavaye, D., Donayre, C. and White, R. A. (1994) 'Changes in arterial wall compliance after endovascular stenting', *Journal of Vascular Surgery*, 19(5), pp. 905–911. doi: 10.1016/S0741-5214(94)70017-6.
- Baila, S., Parnia, A., Panaite, C. and Salagean, M. (2016) Arterial bypass – a surgical method in treatment of peripheral arterial obstructive disease of the lower limbs |, *Romanian Journal of Cardiology*. Available at: <https://www.romanianjournalcardiology.ro/arhiva/arterial-bypass-a-surgical-method-in-treatment-of-peripheral-arterial-obstructive-disease-of-the-lower-limbs/> (Accessed: 18 October 2019).
- Barakat, H. M., Shahin, Y., McCollum, P. T. and Chetter, I. C. (2015) 'Prediction of organ-specific complications following abdominal aortic aneurysm repair using cardiopulmonary exercise testing', *Anaesthesia*, 70(6), pp. 679–685. doi: 10.1111/anae.12986.
- Beach, J. M., Kuramochi, Y., Brier, C., Roselli, E. E. and Eagleton, M. J. (2017) 'Durable outcomes of thoracic endovascular aortic repair with Zenith TX1 and TX2 devices.', *Journal of vascular surgery. Elsevier*, 65(5), pp. 1287–1296. doi: 10.1016/j.jvs.2016.11.029.
- de Beaufort, H. W., Conti, M., Kamman, A. V, Nauta, F. J., Lanzarone, E., Moll, F. L., van Herwaarden, J. A., Auricchio, F. and Trimarchi, S. (2017) 'Stent-Graft Deployment Increases Aortic Stiffness in an Ex&nbsp;Vivo Porcine Model', *Annals of Vascular Surgery*, 43, pp. 302–308. doi: 10.1016/j.avsg.2017.04.024.
- Ben-Shlomo, Y., Spears, M., Boustred, C., May, M., Anderson, S. G., Benjamin, E. J., Boutouyrie, P., Cameron, J., Chen, C.-H., Cruickshank, J. K., Hwang, S.-J., Lakatta, E. G., Laurent, S., Maldonado, J., Mitchell, G. F., Najjar, S. S., Newman, A. B., Ohishi, M., Pannier, B., Pereira, T., Vasani, R. S., Shokawa, T., Sutton-Tyrell, K., Verbeke, F., Wang, K.-L., Webb, D. J., Willum Hansen, T., Zoungas, S., McEniery, C. M., Cockcroft, J. R. and Wilkinson, I. B. (2014) 'Aortic Pulse Wave Velocity Improves Cardiovascular Event Prediction', *Journal of the*

- American College of Cardiology. *Journal of the American College of Cardiology*, 63(7), pp. 636–646. doi: 10.1016/j.jacc.2013.09.063.
- Benetos, A., Safar, M., Rudnichi, A., Smulyan, H., Richard, J. L., Ducimetière, P. and Guize, L. (1997) ‘Pulse pressure: a predictor of long-term cardiovascular mortality in a French male population.’, *Hypertension (Dallas, Tex. : 1979)*, 30(6), pp. 1410–5. doi: 10.1161/01.hyp.30.6.1410.
- Bischoff, M. S., Ante, M., Meisenbacher, K. and Böckler, D. (2016) ‘Outcome of thoracic endovascular aortic repair in patients with thoracic and thoracoabdominal aortic aneurysms’, *Journal of Vascular Surgery. Elsevier*, 63(5), p. 1170–1181.e1. doi: 10.1016/j.jvs.2015.11.045.
- Blankensteijn, J. D., Lindenburg, F. P., Van der Graaf, Y. and Eikelboom, B. C. (1998) ‘Influence of study design on reported mortality and morbidity rates after abdominal aortic aneurysm repair.’, *The British journal of surgery*, 85(12), pp. 1624–30. doi: 10.1046/j.1365-2168.1998.00922.x.
- De Bock, S., Iannaccone, F., De Beule, M., Van Loo, D., Vermassen, F., Verheghe, B. and Segers, P. (2013) ‘Filling the void: A coalescent numerical and experimental technique to determine aortic stent graft mechanics’, *Journal of Biomechanics*, 46(14), pp. 2477–2482. doi: 10.1016/j.jbiomech.2013.07.010.
- Bustos, C. A., García-Herrera, C. M. and Celentano, D. J. (2016) ‘Modelling and simulation of the mechanical response of a Dacron graft in the pressurization test and an end-to-end anastomosis’, *Journal of the Mechanical Behavior of Biomedical Materials. Elsevier Ltd*, 61, pp. 36–44. doi: 10.1016/j.jmbbm.2016.01.005.
- Cheng, D., Martin, J., Shennib, H., Dunning, J., Muneretto, C., Schueler, S., Von Segesser, L., Sergeant, P. and Turina, M. (2010) ‘Endovascular aortic repair versus open surgical repair for descending thoracic aortic disease a systematic review and meta-analysis of comparative studies.’, *Journal of the American College of Cardiology*, 55(10), pp. 986–1001. doi: 10.1016/j.jacc.2009.11.047.
- Chuter, T. A. M. (2002) ‘Stent-graft design: The good, the bad and the ugly’, *Cardiovascular Surgery. Elsevier Ltd*, pp. 7–13. doi: 10.1016/S0967-2109(01)00120-X.
- Conrad, M. F., Tucheck, J., Freezor, R., Bavaria, J., White, R. and Fairman, R. (2017) ‘Results of the VALOR II trial of the Medtronic Valiant Thoracic Stent Graft’, *Journal of Vascular Surgery. Mosby*, 66(2), pp. 335–342. doi: 10.1016/J.JVS.2016.12.136.
- Dakour Aridi, H. N., Locham, S., Nejm, B., Ghajar, N. S., Alshaikh, H. and Malas, M. B. (2018) ‘Indications, risk factors, and outcomes of 30-day readmission after infrarenal abdominal aneurysm repair.’, *Journal of vascular surgery*, 67(3), p. 747–758.e7. doi: 10.1016/j.jvs.2017.07.106.
- Demanget, N., Duprey, A. and Favre, J.-P. (2013) ‘Finite Element Analysis of the Mechanical Performances of 8 Marketed Aortic Stent-Grafts’, *Journal of endovascular therapy*.
- Donas, K. P., Usai, M. V., Taneva, G. T., Criado, F. J., Torsello, G. B., Kubilis, P., Scali, S. and Veith, F. J. (2019) ‘Impact of aortic stent-graft oversizing on

- outcomes of the chimney endovascular technique based on a new analysis of the PERICLES Registry.’, *Vascular*, 27(2), pp. 175–180. doi: 10.1177/1708538118811212.
- Ferrari, G., Balasubramanian, P., Tubaldi, E., Giovanniello, F. and Amabili, M. (2019) ‘Experiments on dynamic behaviour of a Dacron aortic graft in a mock circulatory loop’, *Journal of Biomechanics*. Elsevier Ltd, 86, pp. 132–140. doi: 10.1016/j.jbiomech.2019.01.053.
- Ferruzzi, J., Bersi, M. R. and Humphrey, J. D. (2013) ‘Biomechanical phenotyping of central arteries in health and disease: advantages of and methods for murine models.’, *Annals of biomedical engineering*, 41(7), pp. 1311–30. doi: 10.1007/s10439-013-0799-1.
- Figuroa, C. A. and Zarins, C. K. (2011) ‘Computational Analysis of Displacement Forces Acting on Endografts Used to Treat Aortic Aneurysms’, in *Biomechanics and Mechanobiology of Aneurysms. Studies in Mechanobiology, Tissue Engineering and Biomaterials*, pp. 221–246.
- Gawenda, M., Jaschke, G., Winter, S., Wassmer, G. and Brunkwall, J. (2003) ‘Endotension as a result of pressure transmission through the graft following endovascular aneurysm repair - An in vitro study’, *European Journal of Vascular and Endovascular Surgery*. W.B. Saunders Ltd, 26(5), pp. 501–505. doi: 10.1016/S1078-5884(03)00378-2.
- Geest, J. P. Vande, Sacks, M. S. and Vorp, D. A. (2004) ‘Age Dependency of the Biaxial Biomechanical Behavior of Human Abdominal Aorta’, *Journal of Biomechanical Engineering*. American Society of Mechanical Engineers, 126(6), p. 815. doi: 10.1115/1.1824121.
- Greenberg, R. K., Lu, Q., Roselli, E. E., Svensson, L. G., Moon, M. C., Hernandez, A. V, Dowdall, J., Cury, M., Francis, C., Pfaff, K., Clair, D. G., Ouriel, K. and Lytle, B. W. (2008) ‘Contemporary analysis of descending thoracic and thoracoabdominal aneurysm repair: a comparison of endovascular and open techniques.’, *Circulation*, 118(8), pp. 808–17. doi: 10.1161/CIRCULATIONAHA.108.769695.
- Guan, Y., Wang, L., Lin, J. and King, M. W. (2016) ‘Compliance study of endovascular stent grafts incorporated with polyester and polyurethane graft materials in both stented and unstented zones’, *Materials*. MDPI AG, 9(8). doi: 10.3390/ma9080658.
- Hinchliffe, R. J., Bruijstens, L., MacSweeney, S. T. R. and Braithwaite, B. D. (2006) ‘A randomised trial of endovascular and open surgery for ruptured abdominal aortic aneurysm - results of a pilot study and lessons learned for future studies.’, *European journal of vascular and endovascular surgery : the official journal of the European Society for Vascular Surgery*, 32(5), pp. 506-13; discussion 514–5. doi: 10.1016/j.ejvs.2006.05.016.
- Hountis, P., Dedeilias, P. and Bolos, K. (2009) ‘Acute aortic dissection in a young patient without Marfan fibrillinopathy: a case report’, *Cases Journal*, 2(1), p. 7076. doi: 10.1186/1757-1626-2-7076.

- Hosoda, Y., Kawano, K., Yamasawa, F., Ishii, T., Shibata, T. and Inayama, S. (1984) 'Age-Dependent Changes of Collagen and Elastin Content in Human Aorta and Pulmonary Artery', *Angiology*. Sage PublicationsSage CA: Thousand Oaks, CA, 35(10), pp. 615–621. doi: 10.1177/000331978403501001.
- Kadoglou, N. P. E., Moulakakis, K. G., Papadakis, I., Ikonmidis, I., Alepaki, M., Lekakis, J. and Liapis, C. D. (2012) 'Changes in aortic pulse wave velocity of patients undergoing endovascular repair of abdominal aortic aneurysms', *Journal of Endovascular Therapy*, 19(5), pp. 661–666. doi: 10.1583/JEVT-12-3916MR.1.
- Kadoglou, N. P. E., Moulakakis, K. G., Papadakis, I., Ikonmidis, I., Alepaki, M., Spathis, A., Karakitsos, P., Lekakis, J. and Liapis, C. D. (2014) 'Differential effects of stent-graft fabrics on arterial stiffness in patients undergoing endovascular aneurysm repair.', *Journal of endovascular therapy: an official journal of the International Society of Endovascular Specialists*, 21(6), pp. 850–8. doi: 10.1583/14-4772MR.1.
- Kent, K. C. (2014) 'Clinical practice. Abdominal aortic aneurysms.', *The New England journal of medicine*, 371(22), pp. 2101–8. doi: 10.1056/NEJMcp1401430.
- Kim, J., Cocciolone, A. J., Staiculescu, M. C., Mecham, R. P. and Wagenseil, J. E. (2019) 'Captopril treatment during development alleviates mechanically induced aortic remodeling in newborn elastin knockout mice', *Biomechanics and Modeling in Mechanobiology*. Springer Science and Business Media LLC. doi: 10.1007/s10237-019-01198-2.
- Kim, S. Y., Hinkamp, T. J., Jacobs, W. R., Lichtenberg, R. C., Posniak, H. and Pifarré, R. (1995) 'Effect of an inelastic aortic synthetic vascular graft on exercise hemodynamics', *Annals of Thoracic Surgery*, 59(4), pp. 981–989. doi: 10.1016/0003-4975(95)00068-V.
- Marder, V. J., Aird, W. C. and White, G. C. (2012) *Hemostasis and Thrombosis: Basic Principles and Clinical Practice*.
- Martín, C. E., Forteza, A., Pérez, E., López, M. J., Centeno, J., Blázquez, J. A., de Diego, J., García, D. and Cortina, J. M. (2008) 'Predictors of Mortality and Reoperation in Acute Type-A Aortic Dissection Surgery: 18 Years of Experience', *Revista Española de Cardiología (English Edition)*. Elsevier, 61(10), pp. 1050–1060. doi: 10.1016/S1885-5857(09)60008-6.
- Mehigan, D., Fitzpatrick, B., Browne, H. and Bouchier-Hayes, D. (1985) 'Is compliance mismatch the major cause of anastomotic arterial aneurysms? Analysis of 42 cases', *J Cardiovasc Surg*, 26(2), pp. 147–150.
- Morita, S., Asou, T., Kuboyama, I., Harasawa, Y., Sunagawa, K. and Yasui, H. (2002) 'Inelastic vascular prosthesis for proximal aorta increases pulsatile arterial load and causes left ventricular hypertrophy in dogs', *Journal of Thoracic and Cardiovascular Surgery*. Mosby Inc., 124(4), pp. 768–774. doi: 10.1067/mtc.2002.124244.
- Morris, L., Stefanov, F., Hynes, N., Diethrich, E. B. and Sultan, S. (2016) 'An Experimental Evaluation of Device/Arterial Wall Compliance Mismatch for Four Stent-Graft Devices and a Multi-layer Flow Modulator Device for the Treatment

- of Abdominal Aortic Aneurysms.’, *European journal of vascular and endovascular surgery : the official journal of the European Society for Vascular Surgery*, 51(1), pp. 44–55. doi: 10.1016/j.ejvs.2015.07.041.
- Morris, L., Stefanov, F. and McGloughlin, T. (2013) ‘Stent graft performance in the treatment of abdominal aortic aneurysms: The influence of compliance and geometry’, *Journal of Biomechanics*, 46(2), pp. 383–395. doi: 10.1016/j.jbiomech.2012.11.026.
- Nauta, F. J. H., de Beaufort, H. W. L., Conti, M., Marconi, S., Kamman, A. V., Ferrara, A., van Herwaarden, J. A., Moll, F. L., Auricchio, F. and Trimarchi, S. (2017) ‘Impact of thoracic endovascular aortic repair on radial strain in an ex vivo porcine model’, *European Journal of Cardio-Thoracic Surgery*. Oxford University Press, 44(4), p. ezw393. doi: 10.1093/ejcts/ezw393.
- Van Noort, K., Holewijn, S., Schuurmann, R. C. L., Boersen, J. T., Overeem, S. P., Jebbink, E. G., Vermeulen, J. J. M., Reijnen, M. M. P. J., Slump, C. H. and De Vries, J. P. P. M. (2018) ‘Effect of abdominal aortic endoprostheses on arterial pulse wave velocity in an in vitro abdominal aortic flow model’, *Physiological Measurement*. Institute of Physics Publishing, 39(10). doi: 10.1088/1361-6579/aae195.
- Palmiere, Cristian, et al. "Thoracic aortic dissection associated with cocaine abuse." *Forensic Science International*, 10 May 2004, p. 137+. Gale Academic OneFile
- van Prehn, J., Schlösser, F. J. V, Muhs, B. E., Verhagen, H. J. M., Moll, F. L. and van Herwaarden, J. A. (2009) ‘Oversizing of aortic stent grafts for abdominal aneurysm repair: a systematic review of the benefits and risks.’, *European journal of vascular and endovascular surgery : the official journal of the European Society for Vascular Surgery*, 38(1), pp. 42–53. doi: 10.1016/j.ejvs.2009.03.025.
- Ramanan, B., Fernandez, C. C., Sobel, J. D., Gasper, W. J., Vartanian, S. M., Reilly, L. M., Chuter, T. A. M. and Hiramoto, J. S. (2015) ‘Midterm Results of the Use of Low Profile Multibranched Thoracoabdominal Aortic Stent Grafts’, *Journal of Vascular Surgery*. Elsevier BV, 62(2), pp. 527–528. doi: 10.1016/j.jvs.2015.06.013.
- Salata, K., Hussain, M. A., de Mestral, C., Greco, E., Aljabri, B. A., Mamdani, M., Forbes, T. L., Bhatt, D. L., Verma, S. and Al-Omran, M. (2019) ‘Comparison of Outcomes in Elective Endovascular Aortic Repair vs Open Surgical Repair of Abdominal Aortic Aneurysms’, *JAMA Network Open*. American Medical Association (AMA), 2(7), p. e196578. doi: 10.1001/jamanetworkopen.2019.6578.
- Santos, I. C. T., Rodrigues, A., Figueiredo, L., Rocha, L. A. and Tavares, J. M. R. S. (2012) ‘Mechanical properties of stent-graft materials’, *Proceedings of the Institution of Mechanical Engineers, Part L: Journal of Materials: Design and Applications*, pp. 330–341. doi: 10.1177/1464420712451065.
- Sarkar, S., Salacinski, H. J., Hamilton, G. and Seifalian, A. M. (2006) ‘The Mechanical Properties of Infrainguinal Vascular Bypass Grafts: Their Role in Influencing Patency’, *European Journal of Vascular and Endovascular Surgery*, pp. 627–636. doi: 10.1016/j.ejvs.2006.01.006.

- Sher, A. and Tadros, R. O. (2017) 'Endograft Sizing for Abdominal Aortic Aneurysms', in *Aortic Aneurysm*. InTech. doi: 10.5772/66369.
- Singh, C., Wong, C. S. and Wang, X. (2015) 'Medical Textiles as Vascular Implants and Their Success to Mimic Natural Arteries.', *Journal of functional biomaterials*. Multidisciplinary Digital Publishing Institute, 6(3), pp. 500–25. doi: 10.3390/jfb6030500.
- Sonesson, B., Länne, T., Vernersson, E. and Hansen, F. (1994) 'Sex difference in the mechanical properties of the abdominal aorta in human beings', *Journal of Vascular Surgery*, 20(6), pp. 959–969. doi: 10.1016/0741-5214(94)90234-8.
- Spadaccio, C., Nappi, F., Al-Attar, N., Sutherland, F. W., Acar, C., Nenna, A., Trombetta, M., Chello, M. and Rainer, A. (2016) 'Old Myths, New Concerns: the Long-Term Effects of Ascending Aorta Replacement with Dacron Grafts. Not All That Glitters Is Gold', *Journal of Cardiovascular Translational Research*. Springer New York LLC, pp. 334–342. doi: 10.1007/s12265-016-9699-8.
- Sugitani, H., Hirano, E., Knutsen, R. H., Shifren, A., Wagenseil, J. E., Ciliberto, C., Kozel, B. A., Urban, Z., Davis, E. C., Broekelmann, T. J. and Mecham, R. P. (2012) 'Alternative splicing and tissue-specific elastin misassembly act as biological modifiers of human elastin gene frameshift mutations associated with dominant cutis laxa.', *The Journal of biological chemistry*, 287(26), pp. 22055–67. doi: 10.1074/jbc.M111.327940.
- Sultan, S. and Hynes, N. (2014) 'When Not to Implant the Multilayer Flow Modulator: Lessons Learned From Application Outside the Indications in Patients With Thoracoabdominal Pathologies', *J ENDOVASC THER*, 21.
- Tai, N. R., Salacinski, H. J., Edwards, A., Hamilton, G. and Seifalian, A. M. (2000) 'Compliance properties of conduits used in vascular reconstruction', *British Journal of Surgery*, 87(11), pp. 1516–1524. doi: 10.1046/j.1365-2168.2000.01566.x.
- Tiryakioglu, S. K., Tiryakioglu, O., Turan, T. and Kumbay, E. (2009) 'Aortic dissection due to sildenafil abuse', *Interactive CardioVascular and Thoracic Surgery*. Oxford University Press (OUP), 9(1), pp. 141–143. doi: 10.1510/icvts.2009.205849.
- Tremblay, D., Zigras, T., Cartier, R., Leduc, L., Butany, J., Mongrain, R. and Leask, R. L. (2009) 'A Comparison of Mechanical Properties of Materials Used in Aortic Arch Reconstruction', *Annals of Thoracic Surgery*, 88(5), pp. 1484–1491. doi: 10.1016/j.athoracsur.2009.07.023.
- Tshomba, Y., Leopardi, M., Ferrer, C., Cao, P., De Rango, P., Verzini, F., Melissano, G., Coscarella, C. and Chiesa, R. (2017) 'Aneurysms of the Thoraco-abdominal Aorta: A Comparison with Propensity Score between Endovascular Repair and Open Surgery', *Annals of Vascular Surgery*. Elsevier BV, 38, pp. e16–e17. doi: 10.1016/j.avsg.2016.07.033.
- Vernhet, H., Demaria, R., Juan, J. M., Oliva-Lauraire, M. C., Sénac, J. P. and Dautat, M. (2001) 'Changes in wall mechanics after endovascular stenting in the rabbit aorta: Comparison of three stent designs', *American Journal of Roentgenology*.

American Roentgen Ray Society, 176(3), pp. 803–807. doi: 10.2214/ajr.176.3.1760803.

Zacharoulis, A. A., Arapi, S. M., Lazaros, G. A., Karavidas, A. I. and Zacharoulis, A. A. (2007) ‘Changes in Coronary Flow Reserve following Stent Implantation in the Swine Descending Thoracic Aorta’, *Journal of Endovascular Therapy*, 14(4), pp. 544–550. doi: 10.1177/152660280701400417.

Zimmerman, K. P., Oderich, G., Pochettino, A., Hanson, K. T., Habermann, E. B., Bower, T. C., Gloviczki, P. and DeMartino, R. R. (2016) ‘Improving mortality trends for hospitalization of aortic dissection in the National Inpatient Sample’, in *Journal of Vascular Surgery*. Mosby Inc., p. 606–615.e1. doi: 10.1016/j.jvs.2016.03.427.

# CHAPTER 8

## CONCLUDING REMARKS



### 8.1 Summary of Key Contributions

#### Chapter 4:

##### *Novel technical contributions*

- The spatial heterogeneity in microarchitecture along the length of the human aorta is characterised using histological and stereological techniques.
- The collagen fiber distributions are characterized along the axial and radial dimensions of the aorta and it is shown that a von Mises mixture model is required to accurately fit the complex, non-symmetric distributions observed.

##### *Novel scientific insights*

- The volume fraction of elastin within the aortic wall decreases with distance from the heart, while the volume fractions of both of collagen and smooth muscle cells increase.
- The orientation of collagen fibers is highly heterogeneous along the length of the aorta and throughout the individual layers of the wall, and the presence of two equally dominant and symmetric fiber families is absent.

#### Chapter 5:

##### *Novel technical contributions*

- A novel dual-VENC 4D Flow MRI protocol is developed and implemented in a commercial scanner, which is capable of capturing the true deformation and flow along the entire aorta throughout the full cardiac cycle.

- A composite dataset approach is proposed which negates the need for phase unwrapping algorithms, minimizing post-processing time and resulting in superior accuracy in regions of low flow in diastole compared to mono-VENC acquisitions.

*Novel scientific insights*

- The dual-VENC protocol is implemented in a commercial scanner on a healthy volunteer and the compliance of the aorta, defined as the change in area divided the diastolic area, decreases with distance from the heart, while the pulse wave velocity (PWV) increases.
- By plotting the instantaneous pressure versus area relationship at each of the 10 planes analysed, the non-linearity in compliance can be observed where the aorta is highly compliant at low pressures and stiffens at higher pressures.

**Chapter 6:**

*Novel technical contributions*

- A novel physically motivated constitutive law is developed, and the pressure-area relationship observed *in-vivo* in Chapter 5 is fit using the MRI/FEA framework.
- A framework for the generation of patient-specific finite element meshes directly from medical imaging datasets such as that described in Chapter 5, is generated.

*Novel scientific insights*

- Internal vessel contractility, due to pre-stretched elastin fibres and actively generated smooth muscle stress, must be incorporated into the artery constitutive law, along with collagen strain stiffening, in order to accurately predict the non-linear pressure-area relationship uncovered by our MRI investigations in Chapter 5 and the stress-strain response from experiments.
- Our modelling approach is shown to capture the key features of elastin and SMC knockout experiments.
- The framework leads to the prediction that collagen and smooth muscle volume fractions increase distally, while elastin volume fraction decreases distally. This finding is supported by the histological analyses presented in Chapter 4.
- The strain at which collagen transitions from low to high stiffness is lower in the abdominal aorta, again supporting the histological finding that collagen waviness is lower in this region.

**Chapter 7:***Novel technical contributions*

- The effect of the two main treatment options for aortic disease on the *in-vivo* pressure-area relationship are investigated in the subject-specific FE model generated in Chapter 6; (i) Endovascular aortic repair (EVAR) where an intravascular device is deployed into the aorta, and (ii) open surgical repair (OSR), where a segment of the aortic wall is replaced with Dacron.
- The framework developed can serve as a test-bed for the design of next-generation stent-grafts and replacement synthetic materials for aortic repair.

*Novel scientific insights*

- It is shown that EVAR results in the aorta reaching a new equilibrium configuration due to the outward force of the implant being balanced by increased tension in the vessel wall. This additional strain being imparted on the aortic wall results in the material transition from the high compliance regime into the low compliance regime.
- The stent-graft unloads from the crimped configuration during deployment and operates along the unloading plateau between diastole and systole. The direct effective stiffness of the implant is negligible compared to the high stiffness of the artery wall in the LCR. As a result, the pressure-area relationship post-stenting between diastole and systole follows that of the local LCR slope of the aorta.
- The implanted section follows the local LCR slope for the entire cardiac cycle, and as a result the effective change in diastole is more pronounced proximally versus distally where the bi-linearity of the pressure-area curve is more pronounced.
- Open surgical repair (OSR) results in a profound change in both the HCR and LCR slope, where a near zero compliance is observed throughout the entire cardiac cycle.

## 8.2 Future perspectives

The work presented in this thesis has addressed several key topics in relation to aortic heterogeneity and arterial mechanics. These contributions have implications for related areas in biomechanics and the design of medical devices. This section provides a discussion of future perspectives.

In Chapter 4 we show for the first time in humans that the elastin content decreases while the collagen content increases with distance from the heart. Although considerably more difficult in terms of availability, the approach could be extended to younger cadavers in order to investigate the effect of ageing on the trends observed in this work. It is shown that collagen fiber orientations cannot be simplistically represented by two equally dominant and symmetric families (Roy *et al.*, 2014; Grytsan & Holzapfel, 2015), and that a von Mises mixture model is required to accurately represent the complex distributions that exist throughout the wall. A possible next step would be to develop a mixture dispersion model with varying terms that could better replicate the data. For each location along the aorta, the orientation of elastin and SMCs could also be quantified, which would feed into a more accurate representation of the true angles of these constituents in such material laws as that developed in Chapter 6.

In Chapter 5 a novel dual-VENC 4D Flow MRI framework is proposed as a methodology for characterizing aortic mechanical properties *in-vivo*. This offers a powerful clinically feasible means of evaluating patients preoperatively with regards to stent-graft sizes and postoperatively allowing visualisation of endoleaks, perfusion of branch vessels and the effect of various devices on kinematics and haemodynamics. The framework could also be used in ageing studies to capture the degree of stiffening that occurs over time in the aorta or indeed for monitoring aneurysm development. Furthermore, the 4D Flow MRI protocol can serve as direct input into patient-specific FSI models of unprecedented detail (Miyazaki *et al.*, 2017; Soudah *et al.*, 2017; Saitta *et al.*, 2019).

The novel constitutive law developed in Chapter 6 allows for the regional characterization of aortic mechanical properties based on the deformation of the system *in-vivo* and the microstructural constituents within the wall. The importance of incorporating the contractile components of the artery is highlighted in order to accurately replicate both the pressure-area and stress-strain response of the material. This model could be implemented in coronary/peripheral vascular applications, as incorporation of the contractile elastin and SMCs will influence the mechanical behaviour of the tissue into which stents are deployed (Shadwick, 1999; Ebrahimi, 2009; Chow and Zhang, 2010). Furthermore, a smooth transition region could be added to better fit experimental data that exhibits a slower transition from low to high stiffness. The framework for the generation of patient-specific FE models developed also in Chapter 6, is of significant value to the field of computational biomechanics. The method is entirely automated and results in a well-structured hexahedral mesh for

simulations, which could also be extended to coronary, cerebral and even orthopaedic applications.

The implantation of stent-grafts or the replacement of arterial segments with Dacron are routine procedures in almost every medical centre today around the world, however the impact of such procedures on the biomechanics of the native vessel or system is not well understood. In Chapter 7 both treatment options are shown to significantly alter the pressure-area response of the aorta compared to preoperative conditions. The next stage of this work should be to extend the current platform to optimize new synthetic materials and devices to better capture the native biomechanics of the aorta and reduce postoperative complications.

### 8.3 Bibliography

Chow, M.-J. and Zhang, Y. (2010) 'Changes in the Mechanical and Biochemical Properties of Aortic Tissue due to Cold Storage', *Journal of Surgical Research*. doi: 10.1016/j.jss.2010.04.007.

Ebrahimi, A. P. (2009) 'Mechanical properties of normal and diseased cerebrovascular system.', *Journal of vascular and interventional neurology*, 2(2), pp. 155–62. Available at: <http://www.ncbi.nlm.nih.gov/pubmed/22518247> (Accessed: 19 October 2019).

Grytsan, A., Watton, P. N. and Holzapfel, G. A. (2015) 'A thick-walled fluid-solid-growth model of abdominal aortic aneurysm evolution: application to a patient-specific geometry.', *Journal of biomechanical engineering. American Society of Mechanical Engineers*, 137(3), p. 031008. doi: 10.1115/1.4029279.

Miyazaki, S., Itatani, K., Furusawa, T., Nishino, T., Sugiyama, M., Takehara, Y. and Yasukochi, S. (2017) 'Validation of numerical simulation methods in aortic arch using 4D Flow MRI', *Heart and Vessels. Springer Tokyo*, 32(8), pp. 1032–1044. doi: 10.1007/s00380-017-0979-2.

Roy, D., Holzapfel, G. A., Kauffmann, C. and Soulez, G. (2014) 'Finite element analysis of abdominal aortic aneurysms: geometrical and structural reconstruction with application of an anisotropic material model', *IMA Journal of Applied Mathematics. Oxford University Press*, 79(5), pp. 1011–1026. doi: 10.1093/imamat/hxu037.

Saitta, S., Pirola, S., Piatti, F., Votta, E., Lucherini, F., Pluchinotta, F., Carminati, M., Lombardi, M., Geppert, C., Cuomo, F., Figueroa, C. A., Xu, X. Y. and Redaelli, A. (2019) 'Evaluation of 4D flow MRI-based non-invasive pressure assessment in aortic coarctations', *Journal of Biomechanics. Elsevier Ltd*. doi: 10.1016/j.jbiomech.2019.07.004.

Shadwick, R. E. (1999) 'Mechanical design in arteries', *The Journal of Experimental Biology*, 202, pp. 3305–3313. Available at: <http://jeb.biologists.org/content/jexbio/202/23/3305.full.pdf> (Accessed: 14 June 2018).

Soudah, E., Casacuberta, J., Gamez-Montero, P. J., Pérez, J. S., Rodríguez-Cancio, M., Raush, G., Li, C. H., Carreras, F. and Castilla, R. (2017) 'Estimation of wall shear stress using 4D flow cardiovascular MRI and computational fluid dynamics', *Journal of Mechanics in Medicine and Biology. World Scientific Publishing Co. Pte Ltd*, 17(3). doi: 10.1142/S0219519417500464.

